



DISSERTATION

Three-dimensional super-resolution microscopy of the immunological synapse

Ausgeführt zum Zwecke der Erlangung des akademischen Grades eines Doktors der technischen Wissenschaften

unter der Leitung von

Univ. Prof. Dipl.-Ing. Dr. techn. Gerhard J. Schütz

Institut für Angewandte Physik, E134

eingereicht an der Technischen Universität Wien Fakultät für Physik

von

Mgr. Lukáš Veľas

11739137

Zusammenfassung

T-Zellen sind Teil unseres adaptiven Immunsystems und für die Erkennung von Antigenen in unserem Körper verantwortlich. Durch Binden des T-Zell Rezeptors (TCR) an ein Antigen, welches durch den Haupthistokompatibilitätskomplex (MHC) an der Zellmembran von antigenpräsentierenden-Zellen (APC) präsentiert wird, werden T-Zellen aktiviert. Gemäß dem kinetischen Segregationsmodell der T-Zell-Aktivierung spielt die Topographie immunologischen Synapse eine große Rolle im Antigen-Erkennungsprozess. Aufgrund von Größenausschlusseffekten beeinflusst die Topographie der Synapse die Rezeptorbindungsraten und die Segregation von Proteinen. Daher ist es wichtig, die 3D-Topographie der Synapse mit hoher Präzision zu bestimmen. Aktuelle Methoden liefern nur recht grobe Bilder der Proteinverteilung innerhalb der Synapse. Darüber hinaus ist die Erfassung der Verteilung von Proteinen in allen drei Dimensionen noch herausfordernder als in zwei, da die Auflösung entlang der optischen Achse von Mikroskopen gering ist.

Wir haben eine 3D-Superauflösungsmethode entwickelt, die stochastische optische Rekonstruktionsmikroskopie (STORM) mit defokussierter Mikroskopie kombiniert, welche Effekte der Fluoreszenzemission im superkritischen Winkel auf die Form der Punktbildfunktion ausnutzt. Die Methode lässt sich leicht in für die Einzelmolekül-Lokalisationsmikroskopie ausgestatteten Aufbauten implementieren. Wir haben das Arbeitsprinzip an einer Reihe verschiedener Proben mit bekannter Struktur validiert, wie z. B. fluoreszenz-beschichtete Glaskugeln, 30 nm lange DNA-Origami-Nanostrukturen und Kernporenkomplexe, und konnten die zugrunde liegenden Strukturen erfolgreich auflösen.

Schließlich haben wir die Methode auf T-Zellen angewandt, um die räumliche Organisation des T-Zell-Rezeptors innerhalb der Synapse zu untersuchen. Experimente wurden an hybriden Synapsen zwischen primären T-Zellen und funktionalisierten Lipidmembranen durchgeführt. Wir erreichten eine isotrope Lokalisierungspräzision unter 15 nm. Wir quantifizierten die Membranfluktuationen auf der T-Zelle sowie den Abstand des TCRs in Bezug auf die Lipidmembran. Unsere Daten zeigen durchschnittliche Abstände von 18 nm bis 31 nm für aktivierende bzw. nicht-aktivierende Lipidmembranen. Zusätzlich korrelierten wir die 3D-Superauflösungsbilder mit beugungsbegrenzten Bildern der Immunsynapse, die durch Interferenzreflexionsmikroskopie zur Kreuzvalidierung der beiden Techniken erhalten wurden.

Abstract

T cells are part of our adaptive immune system and are responsible for recognition of antigens in our bodies. T cell activation is triggered upon binding of the T cell receptor (TCR) to the major histocompatibility complex loaded with antigenic peptide (pMHC), which is presented on the surface of antigen presenting cells (APC). According to the kinetic segregation model of T cell activation, topography of the immunological synapse plays a large role in the antigen recognition process. The synapse topography affects receptor binding rates and the mutual segregation of proteins due to size exclusion effects. It is hence important to determine its 3D topography with high precision. Current methods provide only rather coarse images of the protein distribution within the synapse. Moreover, capturing the distribution of proteins in all three dimensions is even more challenging as the resolution along the optical axis of microscopes is lower.

We have developed a 3D super-resolution method that combines stochastic optical reconstruction microscopy (STORM) with defocused imaging which exploits effects of the supercritical angle fluorescence on the shape of the point spread function. The method is easily implementable in setups already equipped for single molecule localization microscopy. We have proven the working principle on a number of different samples with known ground truth, such as fluorescently coated glass spheres, 30 nm long DNA origami nanorulers and Nuclear Pore Complexes, successfully resolving the underlying structures.

Finally, we have applied the method to T cells to study the spatial organization of the T cell receptor within the synapse. Experiments were performed on hybrid synapses between primary T cells and functionalized glass-supported lipid bilayers. We achieved isotropic localization precision below 15 nm. We quantified membrane fluctuations and the cleft size within the synapse by mapping the position of the TCR with respect to the supported lipid bilayer. Our data show average distances of 18 nm up to 31 nm for activating and non-activating bilayers, respectively. Additionally, we correlated the 3D superresolution images with diffraction limited images of the immune synapse obtained by interference reflection microscopy for crossvalidation of the two techniques.

Eidesstattliche Erklärung

Ich erkläre an Eides statt, dass ich die vorliegende Arbeit selbständig verfasst, andere als die angegebenen Quellen nicht benutzt, und die den benutzten Quellen wörtlich und inhaltlich entnommenen Stellen als solche kenntlich gemacht habe. Das in TISS der TU Wien hochgeladene Textdokument ist mit der vorliegenden Dissertation ident.

Wien, am 8. September 2022

Unterschrift

Acknowledgements

My deepest gratitude belongs to my supervisor Prof. Gerhard Schütz for his exceptional support throughout my PhD studies. Thank you, Gerhard, for believing in me, giving me the opportunity and freedom to pursue my research interests, for stimulating my curiosity and thinking through many of our discussions and for your patience and understanding while waiting for the results of my work.

Huge thanks belong to all the members of the Biophysics group, which has become my second home. Thank you for all the fun in the office, in the lab, during the lunches, coffees, ice creams, at conferences, barbeques, picknicks, badmintons... It has been a great ride and I couldn't imagine a better working environment. I am happy to have you all.

I would also like to thank all the PIs and PhD students of the ENACTI2NG training network. I felt really privileged to be part of this community and learned a lot from everyone. Thank you for all our amazing and unforgettable trips across Europe.

My work wouldn't be possible without the help of Dr. Alexander Jesacher and Dr. Philipp Zelger. Thank you, Alex, for our wonderful collaboration, for having me in Innsbruck, and for teaching me about super-resolution microscopy. Thank you, Philipp, for coming to Vienna every time I needed you, for helping me with building the microscope, for answering my never-ending questions about the software, but also, for sharing about life and parenting hacks with me.

Finally, I would like to thank my wonderful family, my wife Liliana and our daughter Julia, for always being there for me, for their unconditional love and for creating a real home here in Vienna. To my parents and my sisters for their love and support at all times. Ďakujem a ľúbim vás!

Table of Content

Zusamm	enfassung	i
Abstract		iii
Eidessta	ttliche Erklärung	V
Acknowl	edgements	vii
Table of	Content	viii
Chapter	0: Preface	1
Motiva	ation of the research	2
Publish	ned articles	4
Chapter	1: Background	5
1.1	Immunology	6
1.1.1	o.	
1.1.2	•	
1.1.3	Antigen recognition by T cells	12
1.1.4	4 T cell signaling	14
1.1.	5 Immunological synapse	16
1.1.6	6 Models of T cell activation	17
1.1.	7 The role of membrane topography in T cell activation	23
1.1.8	8 Model membrane systems for T cell studies	25
1.2	Microscopy	28
1.2.3	1 Fluorescence	28
1.2.2	2 Fluorescence microscopy	30
1.2.3	• • • • • • • • • • • • • • • • • • • •	
1.2.4	4 Super-resolution microscopy	33
1.2.	Single molecule localization microscopy	35
1.2.6	3D Single molecule localization microscopy	40
1.2.	7 Fluorophores for single molecule localization microscopy	46
1.2.8	8 Labeling strategies for single molecule localization microscopy	49
1.2.9	9 Interference reflection microscopy	50
Chapter	2: Materials and Methods	55
2.1	Reagents and proteins	56
2.2	Microscopy systems	56
2.3	Sample preparation and imaging	57
2.4	Data Analysis	61
2.5	Simulations	67
Chapter	3: Results and Discussion	69
3.1	3D Single molecule localization microscopy via defocused imaging	70
3.1.3	.,	
3.1.2		

3.1.3	Precision calculations	72
3.1.4	Design of the experimental setup	74
3.1.5	5 Stability	77
3.1.6	6 Aberrations	79
3.2	Proof of principle measurements	83
3.2.1	1 Glass sphere	83
3.2.2	2 DNA origami nanorulers	84
3.2.3	Nuclear pore complex	87
3.3	3D SMLM of the Immunological synapse	90
3.3.1	1 Introduction	90
3.3.2	2 Correlative 3D SMLM and Interference Reflection Microscopy	91
3.3.3	Correlative IRM, TIR and 3D SMLM of the immunological synapse	92
3.3.4	4 Quantitative Analysis of T cell surface topography within the immunological	al synapse
		103
3.3.5	5 Discussion	106
3.4	Conclusion	108
Chapter 4	4: Appendix	111
Supple	mentary Gallery	112
List of	Abbreviations	148
List of Figures		150
Bibliog	raphy	153
Curricu	ılum Vitae	167

Chapter 0: Preface

Motivation of the research

Fluorescence microscopy has been widely used over the past decades to address questions in molecular and cell biology. The main advantage of fluorescence over other microscopy techniques is its selectivity and sensitivity, as one can label a specific protein of interest and detect it in small concentrations among a plethora of other unlabeled proteins (Lakowicz 2013). Especially with the advance of sensitive cameras capable of detecting only few photons, it has become possible to observe the sample at the single molecule level. The single molecule approach brings the advantage of analyzing individual proteins, and not only averaging over the entire population, enabling to study local processes and heterogeneities in living cells (Moerner and Fromm 2003). For example, brightness of the single molecules can be used to learn about protein stoichiometry (Moertelmaier et al. 2005). Förster resonance energy transfer allows to sensitively measure distances between two molecules on the scale of a few nanometers and characterize their interaction lifetimes (Roy, Hohng, and Ha 2008; Huppa, Axmann, Mörtelmaier, et al. 2010). Furthermore, the position of single molecules can be determined with a much better precision than the diffraction limit, allowing for super-resolution microcopy (Rust, Bates, and Zhuang 2006). Finally, tracking of single proteins over time allows to learn about its diffusional behavior (Schmidt et al. 1996).

Our group has been developing and applying fluorescence microscopy techniques to address various aspects of early T cell signaling. T cells play a major role in adaptive immunity by recognizing infected or tumor cells in the body and by mounting an effective immune response against them. Understanding their function is therefore essential for understanding diseases of the immune system and for designing novel immunotherapies. Despite a great effort in the past decades, fundamental questions related to the first steps of T cell activation have remained unanswered (Courtney, Lo, and Weiss 2018). Especially, the unprecedented sensitivity and selectivity with which the T cell receptor (TCR) recognizes its antigenic peptide bound to Major Histocompatibility Complex (pMHC) on the surface of antigen presenting cell (APC) is not fully understood. There are several models which partially explain some of the observed phenomena, but a model providing a comprehensive picture is still missing (Platzer and Huppa 2020).

Studying T cell - APC interactions with high spatial resolution is challenging due to the random orientation of the cell – cell contact in respect to the optical axis. Therefore, supported lipid bilayers (SLBs) equipped with stimulatory and adhesion proteins are often used as mimicry of the APC surface (Groves and Dustin 2003). These artificial systems offer simplification of the imaging geometry but still preserve the main characteristics of the T cell activation such as increase of the intracellular calcium, formation of a supramolecular activation cluster and release of cytokines. Since the immune synapse formed between the T cell and the SLB is in a close proximity to the coverslip, this setting facilitates the use of total internal reflection fluorescence (TIRF) microscopy to boost the signal of single molecule fluorescence and to suppress the cellular background.

Up to this point, most fluorescence microscopy investigations on T cells were carried out in two dimensions (2D), as it would be inherently more difficult to capture the z direction. However, cells are three-dimensional (3D) objects and measurements of the 2D projections might lead to misinterpretation of the results. For example, a molecule diffusing along a microvillus in z direction would appear as immobilized in 2D projection (Adler et al. 2010). Furthermore, 3D information is required to study the topography of cells. Recent studies suggest an important role

of microvilli in the first steps of T cell activation as they form initial contacts between T cells and APCs (Cai et al. 2017). Furthermore, the topography of the immunological synapse influences receptor-ligand binding rates and promotes segregation of different receptor-ligand pairs due to their size. (Weikl et al. 2009). This is emphasized in the kinetic segregation model of T cell activation (Davis and van der Merwe 2006). Here, the TCR-pMHC binding leads to the formation of tight contacts with a distance of 15 nm between T cell and APC and results in the exclusion of the bulky tyrosine phosphatase CD45, thereby promoting T cell activation.

In contrast, contacts mediated by adhesion molecules, lead to only slightly larger distances of ~40 nm. To study such small distance differences, state-of-the-art techniques with high spatial resolution need to be implemented. SMLM has been commonly used to resolve structures in 2D on the scale of 20-50 nm (Lelek et al. 2021). However, achieving high and isotropic localization precision in all three dimensions is challenging and often comes with the cost of high complexity of the experimental setup. Common techniques include astigmatic or biplane imaging, point spread function engineering, interference or supercritical angle fluorescence-based methods (von Diezmann, Shechtman, and Moerner 2017). These methods differ from each other in the achievable localization precision and the applicable z range.

An advantage of using SLBs is that fluorophores close to the coverslip emit supercritical angle fluorescence (SAF) which is highly dependent on the distance of the fluorophore to the coverslip. The SAF contribution can be exploited in order to boost the achievable localization precision along the optical axis. By splitting the optical path and separating the SAF component from the rest of the signal, similar localization precision could be obtained along the optical axis as in the lateral plane (Bourg et al. 2015; Deschamps, Mund, and Ries 2014). This setting is however not ideal as it requires a more complex two channel imaging path, and separation of the SAF component which is connected with losses of fluorescence signal. Therefore, a novel method that optimally leverages the SAF effect is needed.

Topography of the immune synapse can be also studied via interference reflection microscopy (IRM) which is diffraction-limited in the lateral direction but very sensitive in z. The method relies on the interference of light beams reflected from the coverslip-buffer and buffermembrane interface and the resulting brightness of the images relates to the distance of the membrane to the coverslip. However, quantitative studies in cells are hampered due to problems with titled membranes, multiple membrane layers and higher order interference maxima/minima (Limozin and Sengupta 2009). Cross-validation of the IRM with 3D SMLM would be useful to clarify the extent of these problems and the reliability of IRM images in reporting on the true distances.

Knowing the topography of the immune synapse would also help to clarify the physical reason for the observation of TCR microclusters in TIRF upon T cell activation (Campi, Varma, and Dustin 2005). It has been recently proposed that TCR microclusters start as contact points between T cells microvilli and the SLB and their observed brightness could be a consequence of proximity of these regions to the coverslip in exponentially decaying excitation and not the molecular enrichment (Cai et al. 2017). Measuring the z position of the microclusters in the TIRF field would enable to quantify this contribution and disentangle it from the contribution caused by the molecular enrichment.

In summary, based on the above-mentioned research motives, this thesis had several goals. The first goal was to develop a method that efficiently exploits the effect of SAF on the localization precision in a simple single channel setting without the need of SAF separation. Such Chapter 0 Preface

implementation would facilitate the use 3D SMLM on any microscopy setup already equipped for a 2D SMLM and would therefore be highly beneficial for the community. The second goal was to apply the method to precisely map the 3D positions of the TCR within the immunological synapse in activating and non-activating conditions and measure the synaptic cleft size to identify the tight contacts. The third goal was to closely characterize the TCR microclusters and disentangle the molecular enrichment from the brightness increase due to their proposed proximity to the coverslip. Finally, the fourth goal was to correlate the 3D SMLM data of the T cell topography with IRM images to study how well can these images be used to report on the distances between the cells and SLBs.

Published articles

The content of this thesis is part of the following publications:

Velas, L., Brameshuber, M., Huppa, J. B., Kurz, E., Dustin, M. L., Zelger, P., Jesacher, A., & Schütz, G. J. (2021). Three-Dimensional Single Molecule Localization Microscopy Reveals the Topography of the Immunological Synapse at Isotropic Precision below 15 nm. Nano letters, 21(21), 9247-9255

Zelger, P., Bodner, L., Velas, L., Schütz, G. J., & Jesacher, A. (2020). Defocused imaging exploits supercritical-angle fluorescence emission for precise axial single molecule localization microscopy. *Biomedical optics express*, 11(2), 775-790.

Related publications:

Zelger, P., Bodner, L., Offterdinger, M., Velas, L., Schütz, G. J., & Jesacher, A. (2021). Threedimensional single molecule localization close to the coverslip: a comparison of methods exploiting supercritical angle fluorescence. *Biomedical Optics Express*, 12(2), 802-822.

Zelger, P., Kaser, K., Rossboth, B., Velas, L., Schütz, G. J., & Jesacher, A. (2018). Three-dimensional localization microscopy using deep learning. Optics express, 26(25), 33166-33179



Immunology 1.1

Our bodies are constantly under attack of pathogens including viruses, bacteria, fungi and parasites. Yet, thanks to our immune system, we only rarely get sick. The immune system is a fascinating machinery of several organs, tissues and billions of individual cells working together in an orchestrated way to defend the organism against pathogens and tumors. Its two main components are innate and adaptive immunity (Figure 1). The innate immunity forms the first line of defense. It is composed of anatomical barriers, specialized phagocytic cells and the complement system. It can respond quickly to an infection but is limited in the variety of pathogens it can recognize. On the other hand, the adaptive immunity is able to specifically target any antigen possible, due to its huge repertoire of antigen specific receptors. It has two major ways of function: humoral immunity provided by B lymphocytes producing antibodies and cellmediated immunity provided by T lymphocytes. The response of the adaptive immunity is, however, slower and it takes a couple of days until it can effectively combat the pathogen. Nevertheless, once infected with a pathogen, the adaptive immunity also develops an immunological memory which helps the body to react quickly to future reinfections.

In this chapter, I provide an overview of the components and functions of the innate and adaptive immune system and their interplay when combating infection by pathogens. For a more detailed reading I recommend Janeway's Immunobiology and Cellular and Molecular

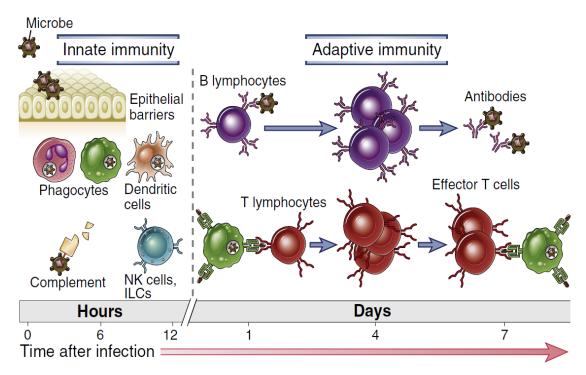


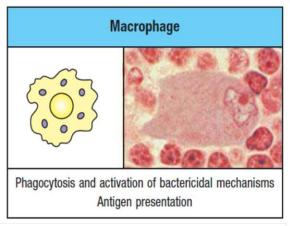
Figure 1: Overview of the Immune system. The immune system has two main components: Innate and adaptive immunity. Innate immunity is composed of epithelial barriers, specialized phagocytic and effector cells and the complement system. The response of the innate immunity is initiated quickly after infection. Adaptive immunity is composed of B and T lymphocytes. B lymphocytes produce antibodies against specific antigens. T lymphocytes differentiate into effector T cells with cytotoxic or helper activity. The response of the adaptive immunity is initiated later in the infection. Taken from (Abbas, Lichtman, and Shiv 2015).

Immunology, which are two excellent sources for the immunological background (Murphy and Weaver 2016; Abbas, Lichtman, and Shiv 2015). Later I will focus in more detail on T cells and the T cell receptor, which are the main subjects of this thesis. I review different models of T cell activation and studies, which attempt to explain the role of immunological synapse topography in early T cell signaling.

1.1.1 Innate immune system and its function

A first and very effective way of the innate immune system to stop pathogens from entering the organism are anatomical barriers such as skin and mucosal surfaces. In addition to posing a physical barrier to pathogens, mucosal surfaces also produce antimicrobial proteins which act as natural antibodies and further inhibit the possibility of pathogens to invade the body. This strategy of the immune system is called avoidance and prevents the infection in the first place (Murphy and Weaver 2016).

However, if the barriers are breached and pathogens succeed in invading the organism, different components of the innate immune system come into play. These breaches are often accompanied by inflammatory inducers, which are molecules normally not present in the host, such as molecular components of bacteria and viruses, bacterial lipopolysaccharides or extracellular ATP. These substances alarm the cellular response of the innate immune system. There are several types of innate immune cells present in the organism including macrophages, dendritic cells, neutrophils, eosinophils, basophils and mast cells. Macrophages and dendritic cells are phagocytic cells, which can engulf the pathogens into intracellular vesicles and destroy them by fusing the vesicles with lysosomes or cytoplasmic granules containing degradative enzymes (Figure 2). Macrophages are rather large cells which are commonly present in almost all tissues. Apart from phagocytosis, they are important in orchestrating the immune response by production of inflammatory mediators, which activate other immune cells or attract them to the site of infection. Dendritic cells are also phagocytic cells which engulf particulate matter and ingest large amounts of extracellular fluids by a process called micropinocytosis. Their main role, however, is not the killing of the pathogens but their degradation into small parts, which are later



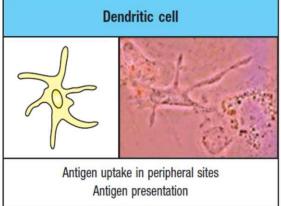


Figure 2: Macrophages and dendritic cells are phagocytic cells of the innate immune system. They play an important role in antigen presentation. The figure shows a schematic and a microscopy image of the macrophage and the dendritic cell. Taken and adapted from (Murphy and Weaver 2016).



presented to the cells of the adaptive immune system. The molecules capable of inducing an immune response are called antigens and therefore dendritic cells are often called professional antigen presenting cells (Murphy and Weaver 2016).

Additional support to the cellular innate immune system is provided by a variety of roughly 30 proteins forming the complement system. Its role is to recognize pathogens present in the extracellular space and to tag them for easier ingestion by the phagocytic cells of the innate immune system, or to directly destroy them by forming pores in their membranes (Abbas, Lichtman, and Shiv 2015).

To distinguish between pathogens and host cells, cells of the innate immune system use a limited number of receptors called pattern recognition receptors (PRRs), which recognize common patterns or molecules present on the pathogens. These receptors often target molecules which have been preserved during the evolution and don't change significantly. The target group of molecules include mannose-rich oligosaccharides, peptidoglycans, lipopolysaccharides of the bacterial cell wall and unmethylated CpG DNA, which is common to many pathogens (Murphy and Weaver 2016).

Many mediator molecules are produced by the activated cells of the innate immune system in order to alarm other cells and induce inflammation at the site of the infection. These inflammatory mediators can be divided into two main categories: cytokines and chemokines. Cytokines are a large group of proteins secreted by the immune cells whose role is to affect the behavior of the nearby cells with complementary receptors. Typically, they induce or enhance the effector functions of the target cells. Chemokines are chemoattractants, responsible to attract other immune cells such as neutrophils and monocytes to the site of the infection (Murphy and Weaver 2016).

1.1.2 Adaptive immune system and its function

Even though the innate immune system is a powerful weapon against pathogens, it is limited in the number of antigens it can recognize, and therefore some pathogens succeed to establish a lasting infection. However, our bodies evolved the adaptive immune system which can target arbitrary antigens it encounters thanks to antigen-specific receptors. There are two main categories of adaptive immune cells responsible for the humoral and cell-mediated immunity: B lymphocytes, also called B cells, and T lymphocytes, also called T cells (Figure 3) (Abbas, Lichtman, and Shiv 2015).

The name B cells comes from bone marrow, which is the place where B cells originate and mature. B cells carry a B cell receptor (BCR) on their surface which can be also secreted in the form of antibodies. Antibodies are also known as immunoglobulins, so the BCR is sometimes called membrane or surface immunoglobulin. When an antigen binds to its specific BCR on the surface of a naïve, antigen unexperienced B cell, the B cell activates, proliferates, and differentiates into a plasma cell. Plasma cells are the effector cells of the B cells which produce large amounts of antibodies which can bind to their specific antigens found in the extracellular space (Murphy and Weaver 2016).

There are three main effector roles of antibodies. First, antibodies simply bind to the surfaces of extracellular pathogens, making it difficult for them to interact with or enter the host cells. This is called neutralization and is very effective against viruses and bacterial toxins. Second, by coating the surfaces of extracellular pathogens, antibodies facilitate the recognition of the

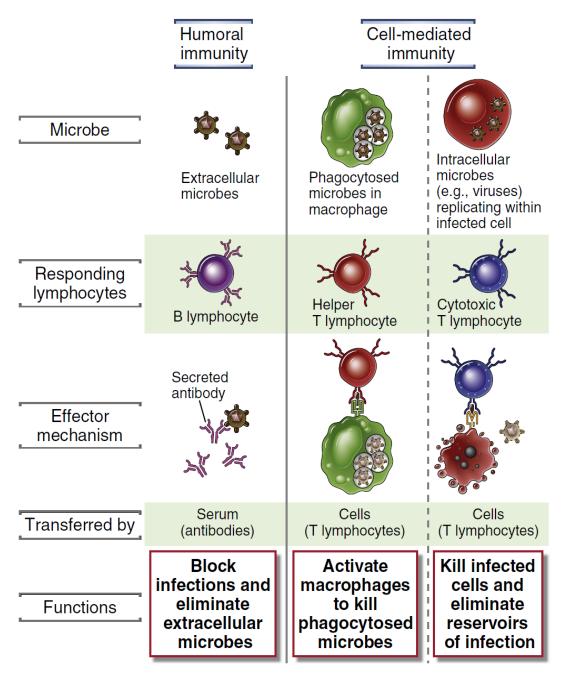


Figure 3: Overview of adaptive immunity. B lymphocytes are responsible for reacting to extracellular pathogens by secreting antibodies with neutralizing effects. T cells aim at intracellular microbes by killing the infected cells or activating macrophages to kill the phagocytosed pathogens. Taken from (Abbas, Lichtman, and Shiv 2015)

pathogen by cells of the innate immune system. This effect is called opsonization. Third, many proteins of the complement system recognize constant regions of antibodies. This leads to complement activation where the bacteria can be directly destroyed by the complement system or tagged for further phagocytosis (Abbas, Lichtman, and Shiv 2015).

T cells originate in the bone marrow but mature in the thymus. They carry a membrane protein called T cell receptor (TCR). The T cell receptor is related to immunoglobulins but is quite different in its structure and function. There is also no secreted version of the T cell receptor. The



TCR is only capable of binding to its antigen when the antigen is already bound to a major histocompatibility complex (MHC) molecule on the surface of antigen presenting cells. Therefore, the main role of T cells is to identify whether other cells contain their specific antigen. There are three subtypes of T lymphocytes which differ in their effector function. Cytotoxic T cells – also called CD8+ T cells for expressing the CD8 co-receptor - kill cells which are infected by an intracellular pathogen which carries their specific antigen. Helper T cells – also called CD4+ T cells for expressing the CD4 co-receptor - activate macrophages to destroy phagocytized pathogens or activate B cells to produce antibodies. Regulatory T cells inhibit the function of other lymphocytes in order to control the extent of the immune response and prevent damage to the host. Eventually, some B and T cells differentiate into memory cells after activation, which is the reason for immunological memory (Murphy and Weaver 2016).

As mentioned, the antigen presentation to the T cells is closely associated with MHC molecules. There are two types of MHC molecules: MHC class I and MHC class II. MHC class I can interact with the TCR and the CD8 co-receptor expressed on the surface of cytotoxic T cells. It is therefore expressed on cells of almost all tissues. MHC class II can interact with TCR and CD4 coreceptors on the surface of helper T cells. They are expressed mainly on dendritic cells, macrophages and B cells. Dendritic cells presenting a specific antigen to helper T cells activate the T cells to proliferate and produce cytokines. Macrophages and B cells presenting the antigen can be activated by helper T cells to kill the intracellular pathogens or produce antibodies (Murphy and Weaver 2016).

The structure of antibodies and the T cell receptor is quite distinct but shares some similarity (Figure 4). Antibodies have two functionally distinct parts: a constant and a variable region. The constant region, or Fc, can take only five different forms based on five different classes of antibodies. This region can be easily recognized by the cells of the innate immune system, for which they carry corresponding receptors. The variable region, or Fv, on the other hand, can take a vast number of forms which allows it to bind to an equally vast number of antigens. Practically, for virtually every antigen molecule there exists an Fv which can bind to it. From the structural point of view, antibodies are composed of two identical heavy chains and two identical light chains. The variable regions of one light and one heavy chain together form an antigen-binding

Schematic structure of an antibody molecule

variable region (antigenbinding site) constant region (effector function)

Schematic structure of the T cell receptor

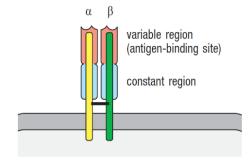


Figure 4: Schematic structure of an antibody molecule and the T cell receptor. An antibody molecule consits of a constant and a variable region with two antigen-binding sites. The T cell receptor is composed of a constant and a variable region with only one antigen-binding site. The T cell receptor resembles a fragment of the antibody molecule. Taken and adapted from (Murphy and Weaver 2016).

site which determines the antigen-binding specificity of the antibody. Since the two heavy and the two light chains are identical, the full molecule of the antibody provides two identical antigenbinding sites. Contrary to that, the T cell receptor is composed of two non-identical chains, an α and a β chain, each of which has a variable and a constant region. The variable regions of the two chains together form one antigen-binding site (Murphy and Weaver 2016).

Every B and T cell carries a receptor with a specific antigen specificity which is determined by the variable regions. Antigen-receptor genes are assembled by somatic gene rearrangements from incomplete receptor gene segments. In this way, a small number of gene segments can give rise to a huge number of different antigen-receptors. In addition to this combinatorial diversity, other mechanisms of adding or deleting nucleotides during the gene segment joining provides further junctional diversity. Moreover, every antigen-recognition site is composed of two variable regions which arise from independent gene rearrangements. Since the above-mentioned process of gene recombination is to a large extent random, it is common that self-reactive antigen-receptors are produced. If not taken care of, such cells would end up attacking the host itself. Therefore, lymphocytes that show any reactivity to the host tissue during the maturation process in the bone marrow or the thymus are removed from the final lymphocyte receptor repertoire in a process called clonal deletion. Only this can ensure the reactivity of the remaining lymphocyte clones only to foreign substances coming from pathogens or tumors (Murphy and Weaver 2016).

The final number of different antigen-receptors in the repertoire of a human being is estimated to 108. However, for every antigen there are only a few hundred cells in our body capable of responding to it. In order to provide a strong immune response, after binding of the antigen to its respective antigen-receptor, the lymphocyte activates and undergoes many rounds of division. The progeny then contains the same clone of the antigen-receptor that can further recognize the antigen. This process is called clonal expansion.

Lymphocytes can be commonly found circulating in the blood or being present in the lymphoid organs. There are two types of lymphoid organs: central or primary and peripheral or secondary lymphoid organs. Central lymphoid organs involve bone marrow and thymus, the places where the lymphocytes originate or mature. The peripheral lymphoid organs include lymph nodes, spleen, and many mucosal tissues. Lymphatic vessels interconnect the different lymph nodes into a large network. The peripheral lymphoid organs contain large amounts of mature lymphocytes waiting to encounter their antigen. After infection, dendritic cells are triggered to migrate into the peripheral lymphoid organs in order to present the antigen to the T cells. Also B cells encounter their antigens in this place but need an additional stimulation from T cells in order to fully activate. The peripheral lymphoid organs are therefore places where the adaptive immune response is initiated (Murphy and Weaver 2016).

It is therefore evident that the effector mechanisms of adaptive immunity strongly depend on and involve components of innate immunity. Adaptive immunity brings, however, specificity in the fight against pathogens. Additionally, since some activated lymphocytes differentiate into memory cells, adaptive immunity provides immunological memory which ensures that the same pathogen will be recognized much quicker in a subsequent infection.



Background Chapter 1

1.1.3 Antigen recognition by T cells

Every T cell carries a special clone of the TCR; in total there are around 30 000 TCR molecules per cell (Murphy and Weaver 2016). Most T cells express αβ TCRs, which are heterodimers of TCRα and TCR β chains. There is a minor population of T cells which carry $\gamma\delta$ TCRs and have different antigen recognition properties, which are still not fully understood (Nielsen, Witherden, and Havran 2017). Both α and β chains consist of a variable region, a constant region, a short stalk segment, a transmembrane region, and a short cytoplasmic tail (Figure 5). The two chains are connected via disulfide bonds in the stalk segment. The two variable regions form the antigenbinding site at the tip of the TCR. At this place, hypervariable loops of amino acids form complementarity-determining regions (CDRs), which determine the binding specificity of the TCR (Dong et al. 2019; Murphy and Weaver 2016).

On the membrane of T cells, the T cell receptor is part of a larger TCR-CD3 complex, where TCR is responsible for antigen recognition and CD3 for signaling (Meuer et al. 1983; Oettgen et al. 1986) (Figure 5). The CD3 complex consists of CD3 γ , CD3 δ , CD3 ϵ and ζ chains. It is thought that the α chain of the TCR interacts with a CD3δ:CD3ε heterodimer and a CD3ζ:CD3ζ homodimer, while the β chain of the TCR interacts with a CD3 γ :CD3 ϵ heterodimer. The intracellular parts of the CD3 chains carry immunoreceptor tyrosine-based activation motifs (ITAMs), whose phosphorylation is the first step in the T cell signaling. Each TCR-CD3 complex carries 10 ITAMs, one for each γ , δ , and ϵ chain and three for each ζ chain (Dong et al. 2019; Murphy and Weaver 2016).

The TCR recognizes its antigen in a different way than antibodies do. Antibodies bind to a specific location on the surface of the antigen molecule called epitope. For the T cell receptor, the antigenic protein has to be unfolded and only a small peptide is loaded on the major histocompatibility complex (MHC) molecule for interaction with the TCR. Therefore, the T cell receptor recognizes amino acid sequences that can be buried deep in the tertiary structure of the antigen protein (Abbas, Lichtman, and Shiv 2015).

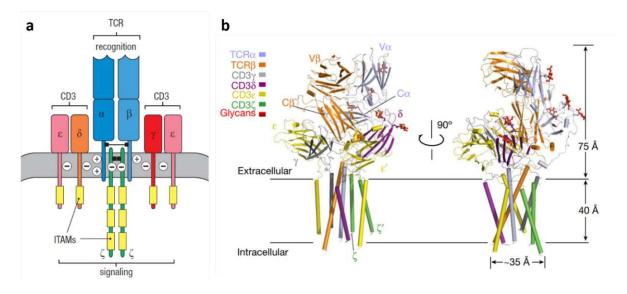


Figure 5: Structure of the TCR-CD3 complex. A schematic of the TCR-CD3 complex with TCRα, TCRβ, two CD3 ε , CD3 γ , CD3 δ and two ζ chains with ITAMs indicated in yellow in (a). Cryo-EM structure of the TCR-CD3 complex in (b). Taken and adapted from (Dong et al. 2019; Murphy and Weaver 2016)



There are two classes of MHC molecules, MHC class I and MHC class II (Figure 6). MHC class I is composed of two polypeptide chains, the α chain and the β_2 -microglobulin. The α chain is anchored to the membrane and is formed by three domains α_1 , α_2 and α_3 . The fourth domain of the MHC class I molecule, the β_2 -microglobulin, is non-covalently associated with the α chain. The α_1 and α_2 domains together form the peptide-binding cleft. MHC class II is composed of two polypeptide chains α and β , which interact non-covalently with each other and are anchored both to the membrane. In the case of MHC class II, the binding-cleft is formed by α_1 and β_1 domains. MHC molecules are highly polymorphic and they vary especially at the site of the binding-cleft, which means that different individuals will have MHC molecules able to bind different sets of peptides (Murphy and Weaver 2016).

The binding-cleft of MHC must be able to facilitate binding of a large variety of different peptides. MHC class I can bind peptides that are composed of 8 to 10 amino acids. The two main anchor points are the amino and the carboxy termini of the peptide. The binding-cleft also provides additional anchor points for the peptides. In the case of MHC class II, the binding grove

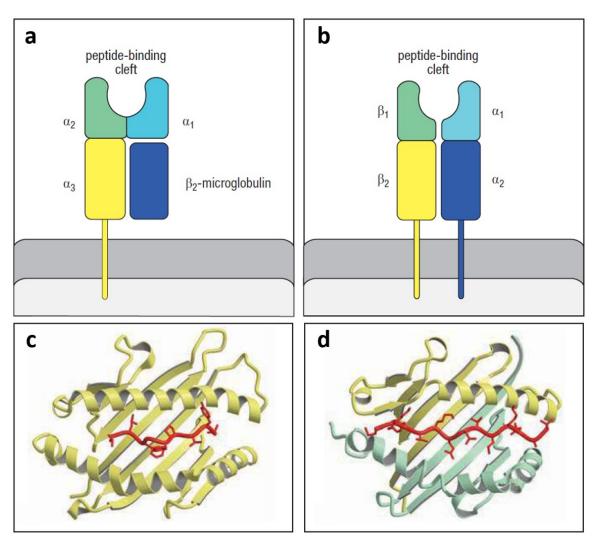


Figure 6: Schematic structure of MHC class I (a) and MHC class II (b) molecules. Peptide binding clefts of MHC class I and class II molecules with an inserted peptide (red) in (c) and (d). Taken and adapted from (Murphy and Weaver 2016)

can accommodate peptides which are at least 13 amino acids long and there is no upper limit (Murphy and Weaver 2016).

The T cell receptor doesn't only interact with the peptide but also with parts of the MHC molecule. Therefore, the specificity of the T cell recognition involves both the peptide and the MHC molecule. This defines the MHC restriction of the T cell responses; T cells respond differently to the same peptide presented by different MHC molecules (Murphy and Weaver 2016).

The different classes of MHC additionally provide binding sites for co-receptors that are expressed on the surface of T cells, and their binding is required to produce an effective response to antigen. Cytotoxic T cells express the CD8 co-receptor, which recognizes MHC class I. CD8 is a heterodimer of α and β chains which consist of one Ig like domain and are linked together by a disulfide bond. CD8 is anchored to the membrane via a long peptide that is extensively glycosylated in order to keep the co-receptor in the extended conformation and protects it against proteases. The CD8 co-receptor binds weakly to the α_3 subunit of MHC class I.

Helper T cells express the CD4 co-receptor which recognizes MHC class II. CD4 is a single chain protein formed by four Ig-like subunits grouped in two parts that are connected with a flexible hinge region. It binds weakly to a hydrophobic region formed between the α_2 and β_2 domains of MHC class II. Both CD4 and CD8 co-receptors are able to bind the kinase Lck at their cytoplasmic tails, which is important in the activation of T cells.

MHC class I and II acquire their peptides in different compartments of the cells, which reflect their functionality. MHC class I presents peptides from proteins that are produced in the cytosol, such as during viral infection of the cell. The viral proteins are degraded by proteasomes in the cytosol, transported to the endoplasmic reticulum and loaded on MHC class I which is synthesized in this location. From there, stable pMHC (peptide:MHC) complexes are transported to the membrane for presentation to cytotoxic T cells. MHC class II is also synthesized in the endoplasmic reticulum but is not loaded with peptides there. Instead, a CLIP protein is inserted to block the peptide-binding cleft. These complexes are then transported to an acidic endosomal compartment where the CLIP dissociates and peptides that entered the vesicular compartments can bind. MHC class II molecules therefore present peptides from proteins that have been phagocytosed by macrophages, dendritic cells or B cells (Murphy and Weaver 2016).

1.1.4 T cell signaling

The exact mechanism of how the signal from binding of the TCR to the antigen gets transduced across the membrane is still not fully understood. Here, I summarize the consensus signaling cascade that takes part on the intracellular side. After binding of the TCR to the pMHC, the coreceptor CD4 or CD8 can also bind the MHC molecule (Courtney, Lo, and Weiss 2018) (Figure 7). This brings the kinase Lck, which is associated with the cytoplasmic tails of the respective coreceptor, into close proximity with the ITAMs. Activated Lck can phosphorylate the ITAMs which then serve as binding sites for the tyrosine kinase ZAP-70. ITAM-bound ZAP-70 can then be phosphorylated by Lck and get activated (van Oers, Killeen, and Welss 1994; Thill, Weiss, and Chakraborty 2016). Activated ZAP-70 phosphorylates the membrane associated scaffold protein LAT (linker for activated T cells) and the adaptor protein SLP-76. LAT and SLP-76 are linked together via the adaptor protein Gads and form LAT: Gads: SLP-76 complexes, which play a central role in T cell activation (Balagopalan et al. 2010; Wange 2000). The signaling cascade is depicted in Figure 8. Activation of ZAP-70 is also followed by recruitment and activation of PI₃-kinase,



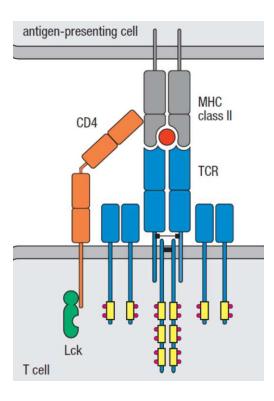


Figure 7: Schematic structure of the TCR-CD3 (blue) complex and CD4 co-receptor (orange) binding to peptide (red) loaded MHC class II molecule (gray). The Lck kinase (green) associated with the CD4 coreceptor phosphorylates ITAMs of the CD3 chains. Taken and adapted from (Murphy and Weaver 2016)

however, the mechanism of this is currently unclear. The formation of LAT:Gads:SLP-76 complexes and the activation of PI₃-kinase is followed by different downstream signaling pathways (Courtney, Lo, and Weiss 2018). Briefly, activation of PLC-y affects transcription, activation of the kinase Akt affects metabolism, and recruitment and activation of ADAP and Vav affects cell adhesion (Murphy and Weaver 2016).

In more detail, one of the pathways triggered by PLC-γ activation results in an increase in intracellular calcium, which further activates the transcription factor NFAT involved in the production of the cytokine IL-2. Increase of the intracellular calcium is often considered a marker of T cell activation (Trebak and Kinet 2019). In this pathway, the activated PLC-γ catalyzes the breakdown of the membrane lipid PIP2 into lipid diacylglycerol and membrane unbound inositol 1,4,5-triphosphate (IP₃). IP₃ diffuses through the cytosol and opens calcium channels on the membrane of the endoplasmic reticulum (ER) and enables the release of ER-stored calcium. The decrease in the ER calcium levels triggers aggregation of STIM1 which then interacts with a CRAC channel on the plasma membrane. Opening of the CRAC channels allows entry of extracellular calcium and replenishment of the ER calcium levels (Murphy and Weaver 2016).

One of the proteins involved in the regulatory pathway of T cell activation is the tyrosine phosphatase CD45 (Koretzky et al. 1991). CD45 belongs to the most abundant proteins in the T cell plasma membrane and has both positive and negative regulatory roles in T cell activation (Courtney, Lo, and Weiss 2018). The positive regulatory role of CD45 lies in the dephosphorylation of Lck on its inhibitory C-terminal tail (Mustelin, Coggeshall, and Altman 1989). In the loss of CD45 activity, Lck is hyperphosphorylated on this place, which leads to its

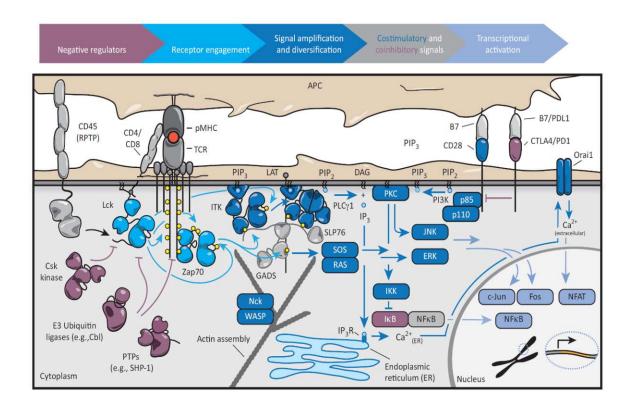


Figure 8: Scheme of signaling events that result from a productive binding of the T cell receptor to antigenic peptide:MHC. The kinase Lck phosphorylates ITAMs on the CD3 chains, which leads to recruitment and activation of ZAP-70. This leads to phospohorylation of further downstream signaling components and results in modified metabolism, cell adhesion and transcription. Taken from (Courtney et al. 2018).

autoinhibition. The negative regulatory role of CD45 is caused by its ability to dephosphorylate signaling components like the ITAMs on the TCR-CD3 complex (Furukawa et al. 1994).

1.1.5 Immunological synapse

An important step in the activation of T cells is the formation of the immunological synapse between the T cells and antigen presenting cells (Platzer and Huppa 2020). The integrin LFA-1 on non-activated T cells binds its ligand ICAM-1 on the surface of antigen presenting cells with low affinity. After TCR stimulation, LFA-1 undergoes a transition into a high affinity state which helps to stabilize the cell-cell interaction. After activation, the T cell also reorganizes its actin cytoskeleton (Fritzsche et al. 2017) which supports integrin aggregation and synapse stabilization. In this pathway, Vav binds to membrane bound PIP3 and the LAT:Gads:SLP-76 complex. This leads to recruitment of WASP and later to actin polymerization (Murphy and Weaver 2016).

Communication between T cells and antigen presenting cells takes place within the immunological synapse (Norcross 1984). It is also the place where the initial TCR triggering and subsequent membrane associated reactions of the downstream signaling take place (Platzer and Huppa 2020). Formation of the immunological synapse is strictly dependent on the recognition of agonist pMHC and can last up to 24 hours after initial signaling (Huppa et al. 2003). Most of the immunological synapses show the form of a bull's eye (Monks et al. 1998), but other structures

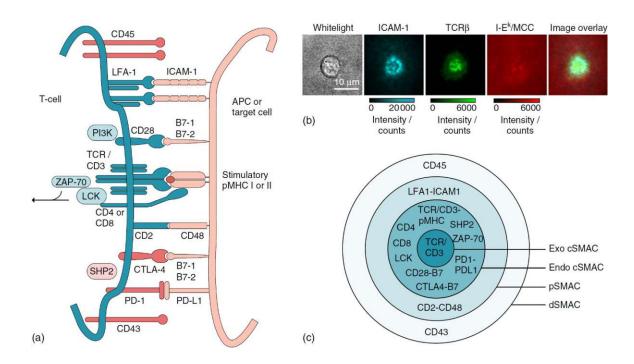


Figure 9: Formation of immunological synapse (IS) and the bull's eye structure. Interaction between adhesion and stimulatory proteins in the IS (a). Fluorescence microscopy images of ICAM-1, TCR and MHC molecule distributions in the IS of activated T cell (b). Schematic of the bull's eye with cSMAC, pSMAC and dSMAC (c). Taken and adapted from (Platzer and Huppa 2021).

have been observed as well (Thauland and Parker 2010; Fritzsche and Dustin 2018). In the bull's eye pattern model, shown in Figure 9, the center of the synapse called central supramolecular activation cluster (cSMAC) is enriched in TCR, CD28 and the protein kinase PKC0. The surrounding ring, also termed peripheral SMAC (pSMAC), is mainly enriched in LFA-1. The most distal part of the immunological synapse, also termed distal SMAC (dSMAC), contains the bulky tyrosine phosphatase CD45 (Grakoui et al. 1999).

Prior to the formation of a mature immunological synapse, TCR microclusters have been observed on T cells interacting with antigen decorated supported lipid bilayers (SLBs) via total internal reflection fluorescence (TIRF) microscopy (Campi, Varma, and Dustin 2005). These TCR microclusters are further enriched in the signaling molecules Lck, Zap-70 and LAT, but exclude CD45 (Su et al. 2016). They are formed a few seconds after initial contact of the T cell with SLBs and are transported to the cSMAC via a retrograde flow of actin and microtubules (Campi, Varma, and Dustin 2005; Fritzsche et al. 2017). Lck inhibition revealed TCR microclusters to be a result of and not a cause for initial TCR triggering (Varma et al. 2006). TCR microclusters are thought to serve as platforms for primary and transient signaling of T cells, while in their final destination, the cSMAC, the signaling is largely terminated (Lee et al. 2002).

1.1.6 Models of T cell activation

Binding of the T cell receptor to an antigenic pMHC results in phosphorylation of the ITAMs on the intracellular chains of CD3 and subsequent T cell activation. However, how the binding event is translated into this phosphorylation is yet not fully understood and there is a number of models that attempt an explanation (Courtney, Lo, and Weiss 2018). The most challenging phenomenon



to explain is the extraordinary sensitivity and selectivity of the T cell receptor, as T cells are able to recognize single antigenic pMHC molecules in a vast excess of endogenous pMHC molecules (Huang et al. 2013; Sykulev et al. 1996; Irvine et al. 2002; Purbhoo et al. 2004). Furthermore, there is only a small difference between foreign and self pMHC molecules when considering their affinity and kinetics of TCR binding (Daniels et al. 2006).

Kinetic proofreading model:

The kinetic proofreading model was proposed after early experiments suggested that strongly stimulating pMHCs exhibit a longer binding lifetime than non-stimulating ligands (McKeithan 1995). In order to explain the selectivity of the TCR, the kinetic proofreading model proposes the existence of a number of biochemical reactions that take place before ligand unbinding to trigger the downstream signaling cascade. Binding of self pMHC does not last sufficiently long to allow all the necessary steps to happen. A schematic of the kinetic proofreading with co-receptor binding is depicted in Figure 10. Furthermore, these reactions must be driven out of equilibrium, for example by using ATP energy. That is the case for a number of phosphorylation reactions in the initial phase of TCR signaling. On the other hand, this model doesn't clarify the sensitivity of T cells, as the signal from a single T cell receptor might be too weak to trigger activation. One of the possible explanations can be a cooperativity of downstream signaling, as for example observed in the LAT signalosome, that would amplify a weak input signal. Recent findings also revealed that in addition to the number and kinetics of sequential signaling steps, a key determinant of discriminatory capability is spatial localization of a minimum number of these steps to the engaged TCR (Ganti et al. 2020).

Serial triggering model:

The model of serial TCR triggering proposes an explanation for the high sensitivity of T cells. In this model, a single antigenic pMHC can serially bind and trigger multiple TCRs (Valitutti et al. 1995). Therefore, a small number of pMHC complexes can achieve a high TCR occupancy which

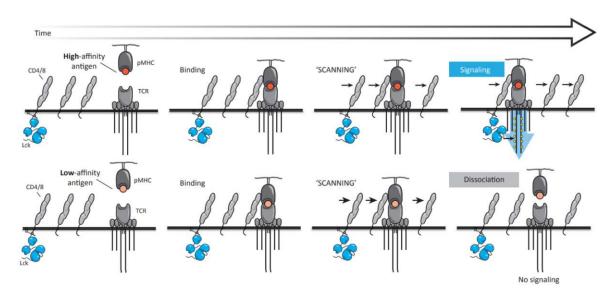


Figure 10: Schematic of the kinetic proofreading model: High-affinity antigen provides stable TCRpMHC bonds which last long enough to induce signaling. In the case of low-affinity antigen, the dissociation of the TCR-pMHC bond occurs before the phosphorylation of CD3 cytoplasmic tails and does not lead to signaling. Taken and adapted from (Courtney, Lo, and Weiss 2018).

is proportional to the T cell's biological response. However, in a contradiction to the kinetic proofreading model, a larger off-rate would be beneficial for this model, as more TCRs could be engaged in a given amount of time (Chakraborty and Weiss 2014). Furthermore, experimental data suggest that there is no optimal off rate and that stronger binding promotes stimulation (Holler and Kranz 2003).

Co-receptor binding model:

The co-receptors CD4 and CD8 were firstly thought to stabilize TCR-pMHC binding and prolong their binding lifetime (Chakraborty and Weiss 2014). However, based on further experiments and simulations this has not been confirmed (Huppa, Axmann, Mörtelmaier, et al. 2010). Both coreceptors have a high off-rate from their ligand MHC class I and class II, and only CD8 has been shown to slightly increase the binding time of TCR-pMHC class I interactions (Luescher et al. 1995; Wooldridge et al. 2005). Furthermore, CD8 has been shown to be critical for the recognition of low affinity pMHC, but the absence of CD8 binding did not show any significant difference for the recognition of higher affinity ligands (Laugel et al. 2007). On the other hand, it seems reasonable to assume that the co-receptors play a role in TCR triggering as their cytoplasmic tails are associated with the kinase Lck, and their binding to the TCR-pMHC complex recruits Lck for phosphorylation of the ITAMs on the CD3 chains. Based on further experiments, a model has been proposed describing the role of the co-receptors in amplification of the signal when T cells are stimulated by a small number of antigenic pMHCs (Hoerter et al. 2013). In this model, following TCR binding to an antigenic pMHC, Lck is recruited to the TCR complex and activated, representing a crucial step in the kinetic proofreading mechanism. Binding of the endogenous pMHC to the TCR is too weak to enable activation of Lck. Following the activation of Lck and phosphorylation of the TCR's ITAMs, the co-receptor bound to activated Lck can diffuse away and trigger TCRs bound to endogenous pMHCs. This amplification step can be further facilitated by the formation of TCR microclusters (Varma et al. 2006; Yokosuka et al. 2005).

Kinetic segregation model:

The kinetic segregation model is based on perturbing the balance between phosphorylation and dephosphorylation of the TCR via segregation of the phosphatase CD45 from the signaling complexes (Davis and van der Merwe 2006) (Figure 11). Binding of the TCR to pMHC in the immunological synapse creates a spacing of approximately 15 nm between the two opposing membranes (Dustin and Cooper 2000). This narrow gap is too small to accommodate CD45 and leads to its segregation from the ligated TCRs (Chang et al. 2016). On the other hand, the kinase Lck which has no extracellular domain retains access to TCR phosphorylation and can therefore trigger downstream signaling.

In support of this model are experiments where the extracellular domain of CD45 was shortened and no segregation and activation was observed (Cordoba et al. 2013). Consistently, increasing the length of pMHC and therefore widening of the immunological synapse led to reduced sensitivity of the T cells towards antigen (Choudhuri et al. 2005). However, some experimental results challenge the proposed model. In a cell free model with reconstituted parts of the TCR signaling machinery, it was shown that CD45 was excluded from LAT signaling microclusters, suggesting that size might not be the only determinant of segregation (Su et al. 2016). Furthermore, a puzzling fact is that CD45 has a positive role on the T cell activation by inhibiting the inactive state of the kinase Lck by its dephosphorylation (Koretzky et al. 1991). Following this dual nature of CD45, a recent study reported the exclusion of CD45 from the tips

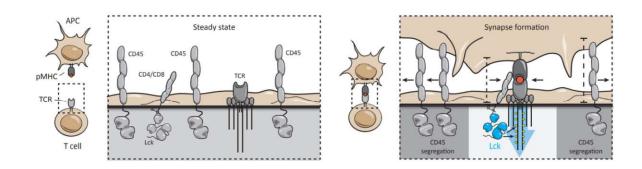


Figure 11: Schematic of the kinetic segregation model: In the steady state, phosphorylation of the CD3 cytoplasmic tails by the intracellular kinase Lck is in balance with their dephosphorylation by the bulky membrane phosphatase CD45. Binding of the TCR to pMHC brings the opposing membranes into close proximity which results in exclusion of CD45 from this region and phosphorylation of the TCR complex by Lck. Taken and adapted from (Courtney, Lo, and Weiss 2018)

of pMHC-engaging microvilli while the proximity of the CD45 was necessary for optimal stimulation of T cells (Razvag et al. 2018). In conclusion, there is no doubt that kinetic segregation takes place in the immunological synapse due to T cell scanning of the surface of the antigen presenting cells, however, its significance in the earliest phase of TCR triggering remains unclear (Platzer and Huppa 2020).

Conformational change model:

Probably the most straight forward model of signal transduction through the membrane would involve a conformational change in the structure of the T cell receptor after antigenic pMHC ligation (Figure 12). Indeed, there is supporting evidence involving a conformational change in the A-B loop of the α chain and H3 helix of the β chain which interact with the extracellular domain of the CD3 (Kjer-Nielsen et al. 2003; Natarajan et al. 2017). Moreover, a conformational change has been described on the intracellular side involving an exposure of a proline-rich sequence on CD3ɛ that can bind Nck and facilitate downstream signaling (Borroto et al. 2014; Gil et al. 2002). However, the model of a mere conformational change of the TCR is in contradiction with the fact that ligation of the TCR with a soluble antigenic pMHC does not lead to T cell activation (Xie et al. 2012). Furthermore, many crystal structures of ligated TCRs did not show significant structural differences when compared to the free TCR (Khan et al. 2011).

ITAM sequestration model:

It has also been questioned, why phosphorylation of ITAMs by Lck does not happen irrespective of TCR binding to pMHC. An explanation was proposed in which the positively charged intracellular chains would interact with negatively charged lipids at the cytoplasmic leaflet of the plasma membrane and would therefore be shielded from the access of Lck (Xu et al. 2008) (Figure 13). This model is, however, contradicted by a study where membrane shielding was prevented in a mutant chimera and still no phosphorylation was found in the basal state (Fernandes et al. 2010). In this study, a cluster of positively charged residues in the membrane-proximal aminoterminal region of the cytoplasmic domain of CD3 ϵ was mutated, which reduced the association of CD3E cytoplasmic domain with the membrane as detected by the FRET assay. Furthermore, the fact that ITAMs are partially phosphorylated in the basal state of T cells also doesn't support this hypothesis (Van Oers et al. 1993).

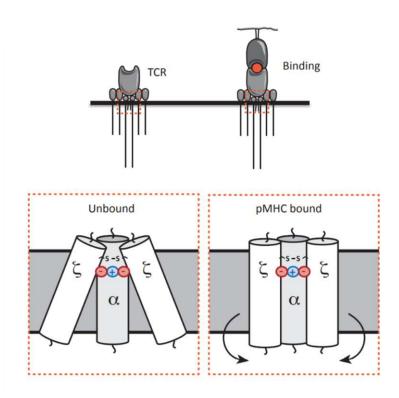


Figure 12: Schematic of conformational change model: Upon binding of the TCR to the pMHC a conformational change occurs in the cytoplasmic region which allows for phosphorylation and signaling. Taken and adapted from (Courtney, Lo, and Weiss 2018)

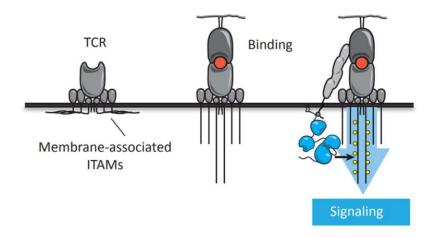


Figure 13: Schematic of ITAM sequestration model: In the unbound state of the TCR, the ITAMs of the CD3 cytoplasmic chains are associated with the membrane and extend to the cytoplasm upon binding of the pMHC. Taken and adapted from (Courtney, Lo, and Weiss 2018).

Mechanosensor model:

In the context of T cells scanning the surface of APCs for antigen, forces act on bound TCR:pMHC complexes. It is therefore conceivable that a TCR could act as a mechanosensor that is able to distinguish between endogenous and agonist pMHC based on the forces it is experiencing (Figure

Background Chapter 1

14). It has been shown that free monomeric pMHC molecules were not able to activate T cells unless they were anchored to a lipid bilayer (Ma et al. 2008). Furthermore, low densities of agonist pMHC failed to activate T cells without supportive ICAM-1 mediated adhesion. More direct evidence for the influence of pulling forces on T cell activation was provided by experiments which involved non-agonist anti-CD3 antibody coated beads, which were pulled across T cells via optical tweezers. In these experiments, calcium signaling was detected upon reaching 50 pN forces (Kim et al. 2009). A model has been proposed, in which deformation of the TCR-CD3 complex due to mechanical forces induces intracellular signaling. Indeed, T cell-exerted forces were observed in studies involving DNA-based force sensors coupled to pMHC, showing 10-20 pN forces (Liu et al. 2016; Ma et al. 2016), and single molecule peptide-based FRET sensors, yielding forces of up to 6 pN (Göhring et al. 2021).

Destabilization of the TCR-pMHC binding via forces might lead to an increased capacity of the TCR to distinguish between endogenous and agonist ligands (Klotzsch and Schütz 2013). Experimental evidence for such mechanism was observed by (Liu et al. 2014). In this experiment, T cells were brought into contact with pMHC functionalized beads and pulled apart. The results led to the observation that under force the lifetime of the bond between TCR and antigenic pMHC increased while for endogenous pMHC it decreased. Based on these experiments, it was postulated that agonist pMHCs form 'catch bonds' with the TCR while the self pMHCs form 'slip' bonds. Catch bonds are type of bonds which become stronger upon application of an external force and resist breaking. On the contrary, slip bonds, which represent the vast majority of biological and chemical bonds, dissociate faster when subjected to a force (Prezhdo and Pereverzev 2009). The structural reason behind these different bonds, however, remains unknown (Platzer and Huppa 2020). In opposition to this model is a study where slip bonds were found also for antigenic pMHC, indicating that catch bonds are not an intrinsic property of antigenic pMHC-TCR interactions (Limozin et al. 2019). A consensus in the field is that forces do act on the TCR:pMHC complexes, however, more research needs to be done to clarify their role in the proximal TCR signaling (Platzer and Huppa 2020).

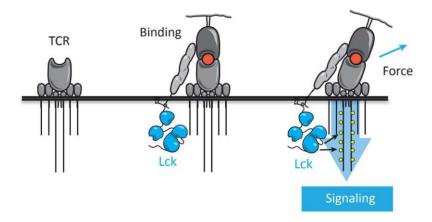


Figure 14: Schematic of mechanosensor model: Phosphorylation of the CD3 cytoplasmic tails is enabled after exertion of a force on the TCR – pMHC bond. Taken and adapted from (Courtney, Lo, and Weiss 2018).

Background Chapter 1

Lipid interaction model:

The role of the lipid composition of the T cell membrane has also been discussed as it may influence the spatial organization of T cell receptor on the surface of T cells. It has been shown that addition of cholesterol and cholesterol sulfate inhibit the phosphorylation of ITAMs through their interaction with the β chain of the TCR (Swamy et al. 2016; Wang et al. 2016). According to the study by Swamy, cholesterol locks the TCR-CD3 complex in an inactive conformation which serves as a fine-tuning tool for T cell sensitivity. The nanoscopic lipid environment was also argued to serve as a platform for TCR clustering. On the contrary, single molecule microscopy studies have failed to detect TCR clustering on the membrane of resting T cells (Brameshuber et al. 2018; Rossboth et al. 2018).

In conclusion, no single model presented up to date provides a good explanation for the phenomena accompanying TCR triggering and T cell activation. The solution most likely lies in a combination of the mentioned models. Especially a combination of kinetic proofreading, kinetic segregation and mechanosensory models looks promising. Data with high spatial and temporal resolution would be needed to address the issue at the single molecule level.

1.1.7 The role of membrane topography in T cell activation

Cell adhesion is mediated by binding of receptor molecules on one membrane to their ligands on the opposing membrane, and thereby influences the membrane topography. In the case of a receptor-ligand length mismatch attractive and repulsive interactions between proteins can be observed due to changes in the overall bending energy of the two membranes. These interactions depend mainly on the size of the receptor-ligand complexes in the adhesion zone (Weikl et al. 2009).

T cell adhesion is mediated via receptor-ligand complexes with different lengths. In this case, the membrane curvature caused by the length mismatch is unfavorable and at critical concentrations of different receptor-ligand complexes we can observe spatial segregation based on the length. A good example of this segregation upon T cell adhesion is the separate patterns formed of short length TCR-pMHC complexes and long ICAM-LFA integrin complexes (Monks et al. 1998). In T cell adhesion, the integrin LFA-1 binds to its ligand ICAM-1 and forms a 40 nm long trans-dimer. Much shorter trans-dimers of 15 nm are formed due to binding of TCR to pMHC as well as CD28 to B7-1 (Dustin and Cooper 2000). After 15 to 30 minutes of spreading, a clear separation of the two complexes with different lengths can be observed (Figure 15Aa and Figure 15B) (Grakoui et al. 1999). However, in the initial phase of cell adhesion a different pattern can arise with small TCR clusters in the pool of integrin molecules (Figure 15Ad) or integrin complexes concentrated in the middle and a ring of TCR surrounding it (Figure 15Ac). It is known that active transport of TCR mediated via actin cytoskeleton rearrangement is responsible for the final shape of the immunological synapse with TCR molecules residing in the central SMAC (Super Molecular Activation Cluster) and integrin molecules in the peripheral SMAC (Figure 15C) (Murphy and Weaver 2016).

Monte Carlo simulations have been used to study the segregation of TCR-pMHC transdimers from LFA-1/ICAM-1 trans-dimers during cell adhesion upon conditions without active transport. These results show that without coupling of TCR to the actin cytoskeleton, the resulting



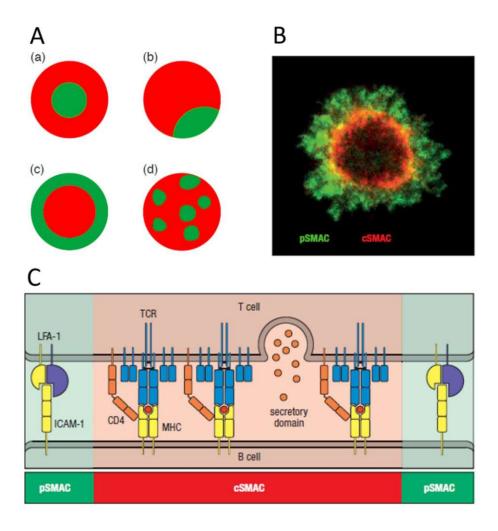


Figure 15: Simulated patterns in the adhesion zone for two different receptor-ligand complexes (A). The sub-panels show: (a) the final pattern of T cell activation with central TCR domain (green) surrounded by an integrin domain (red), (b) simulated final pattern without an active transport, (c) and (d) show intermediate patterns for high and low TCR-pMHC concentrations. Fluorescence microscopy image of the final pattern of the immunological synapse upon T cell activation with TCR in red and LFA-1 in green (B). Scheme of protein segregation in the immunological synapse into central and peripheral Super Molecular Activation Clusters (SMACs) (C). Taken and adapted from (Weikl et al. 2009; Murphy and Weaver 2016).

shape of the immunological synapse would show segregation of the complexes at the edge of the cell (Figure 15Ab) since this situation minimizes the line tension. The intermediate patterns within these simulations with clusters or inversed TCR and integrin patterns resemble those ones occurring during cell adhesion at early time points. For high TCR-pMHC concentrations see Figure 15Ac and for smaller concentrations see Figure 15Ad (Weikl and Lipowsky 2004).

T cell adhesion and formation of the early immunological synapse is important to provide a stable zone for TCR-pMHC interaction. This is ensured by LFA-1 binding to ICAM-1 on the surface of antigen presenting cells. This interaction is capable of squeezing a large glycocalyx layer on the cell surface and bringing the opposing membranes to a distance of about 40 nm (Platzer and Huppa 2020). Furthermore, there has been a number of recent studies describing



the role of microvilli in the process of T cell activation. Microvilli are finger-like dynamic membrane protrusions supported by the actin cytoskeleton. They are varying in size from 100 nm to micrometers in length, 70 to 500 nm in width, and are largely present on the surface of T cells (Polliack et al. 1973; Jung et al. 2016). Microvilli have been shown to be enriched in TCR, costimulatory and signaling molecules, providing therefore a possible signaling hub for T cell activation (Jung et al. 2016). Further studies have shown an active role of microvilli in scanning the surface of antigen presenting cells and establishing contacts (Cai et al. 2017). These established contacts are also thought to have a relation with the TCR microclusters, as the TCR microclusters on the tips of microvilli were moved centripetally into the cSMAC (Cai et al. 2017). It has been questioned whether these micro-synapses formed by microvilli could lead to the exclusion of CD45 and TCR triggering in the context of the kinetic segregation model. Indeed, some studies reported exclusion of the CD45 a few seconds after contacts were established (Chang et al. 2016; Razvag et al. 2018; Fernandes, Ganzinger, Tzou, Jonsson, et al. 2019) and there is also recent evidence for CD45 pre-exclusion from the microvilli tips prior to contact formation (Jung et al. 2021).

1.1.8 Model membrane systems for T cell studies

T cells interact with antigen presenting cells (APCs) and form immunological synapses, which are sites for interaction of a number of different proteins and exhibit complex topographies. In order to be able to control the interaction taking place in the IS and facilitate microscopy imaging, it is common to use supported lipid bilayers (SLBs) functionalized with proteins, which act as surrogates of APCs (Huppa, Axmann, Mörtelmaier, et al. 2010; Grakoui et al. 1999; Groves and Dustin 2003). This experimental design brings a couple of advantages:

- 1. It enables the addition of particular proteins, with full control over their densities and mobility
- 2. It preserves the essential hallmarks of T cell signaling, including the formation of an immunological synapse, the recruitment of the kinase ZAP-70 and other downstream signaling effectors, the increase in intracellular calcium and the release of cytokines.
- 3. It aligns the synapse perpendicular to the optical axis, allowing for high-resolution fluorescence microscopy
- 4. It brings the synapse to a close proximity to the glass coverslip, enabling the use of total internal reflection fluorescence (TIRF) microscopy.

The development of SLBs, which could capture key features of natural membranes such as mobility of the lipids and the associated ligands was pioneered by McConnell and co-workers in the 80s (Tamm and McConnell 1985; Brian and McConnell 1984). Nowadays, there is a number of different methods how to create SLBs such as the Langmuir-Blodgett/Langmuir-Schäfer technique, spin-coating or vesicle fusion (van Weerd, Karperien, and Jonkheijm 2015). In the case of vesicle fusion, a solution of unilamellar lipid vesicles or proteoliposomes is used, which under certain conditions interact with the surface to form the SLB. Such vesicles can be prepared either by extrusion or sonication. Standard procedures of vesicle preparation include drying the lipid mixture dissolved in an organic solvent by nitrogen flow, rehydration, vortexing and sonication or extrusion. While extrusion provides vesicles with narrower size distribution in comparison with the sonication (Ruozi et al. 2011), it can result in loss of material in the extrusion device (van



Background Chapter 1

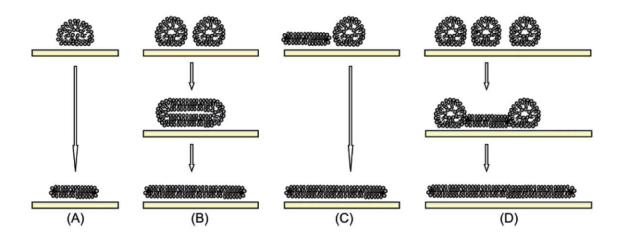


Figure 16: Formation of a supported lipid bilayer, mechanisms of vesicle rupture. (A) An isolated adsorbed vesicle ruptures spontaneously. (B) Neighboring vesicles fuse and rupture. (C) The active edge of an SLB patch induces rupture of neighboring vesicles. (D) The cooperative action of several neighboring vesicles leads to the rupture of a first vesicle and the patch edge triggers the rupture of adjacent vesicles. Taken from (Richter, Bérat, and Brisson 2006)

Weerd, Karperien, and Jonkheijm 2015). Upon incubation of the prepared vesicles with solid substrates such as glass, mica or silica, SLBs are formed under certain conditions regarding the ionic strength and pH. The formation of SLBs proceeds in two steps (Figure 16):

- 1. Vesicle adsorption onto the solid support and vesicle rupture.
- 2. The formation of bilayer patches and their fusion to form a continuous SLB.

Formation of an SLB is an energetically favorable process (van Weerd, Karperien, and Jonkheijm 2015). The polar heads align to face the aqueous environment and the hydrophobic tails cluster together. The water released from the ruptured vesicles further increases the entropy of the system. Additional interactions, such as van der Waals interactions and electrostatic effects also play a role in the formation and organization of the SLB. After formation of the SLB a thin hydration layer of 6-20 Å can be found between the bilayer and the substrate (Kiessling and Tamm 2003).

Physical properties of the SLBs are affected by their lipid composition and surface properties of the substrates (van Weerd, Karperien, and Jonkheijm 2015). Predominantly, the acyl chains of the lipids determine the mobility, phase behavior and segregation in lipid bilayers. Lipids bearing saturated acyl chains tend to pack more tightly, increasing their transition temperature and resulting in reduced lateral mobility. Different temperature-dependent states can be distinguished with different phase behavior such as liquid-disordered, liquid-ordered and solid phase. The coupling of the SLB to its substrate can further influence the properties of the bilayer. For example, the lateral diffusion of lipids in the proximal leaflet of the SLB on a mica substrate is slower than for the distal leaflet (Scomparin et al. 2009).

In order to mimic a cell membrane, SLBs can be modified to carry a particular ligand or a whole protein. This can be achieved by a variety of modification strategies, e.g. using lipid headgroups bearing maleimide, NHS, biotin, Ni-NTA or azide functionalities allowing for both reversible or irreversible binding of the ligand (Yu and Groves 2010; van Weerd, Karperien, and



Jonkheijm 2015). In particular, SLBs containing lipids with Ni-NTA head-groups provide a convenient strategy for binding His-tag proteins. The Ni-NTA head-group displays high selectivity and moderate affinity towards His-tags with association constants around 104 M-1 (Gizeli and Glad 2004). In order to provide stable attachment and proper orientation of the protein, multiple histidine residues can be introduced into the ligand of interest. This attachment strategy has been used in various T cell studies where His₁₂-tagged MHC and His₁₀-tagged ICAM-1 molecules were presented on mobile SLBs to the T cells and induced the formation of immunological synapse (Figure 17) (Nye and Groves 2008; Groves and Dustin 2003). Binding of the His-tagged proteins to Ni-NTA functionalized SLB is reversible and can be removed either by addition of a competitor such as imidazole or by depletion of Ni²⁺ by ethylenediaminetetra-acetic acid (EDTA) (van Weerd, Karperien, and Jonkheijm 2015).

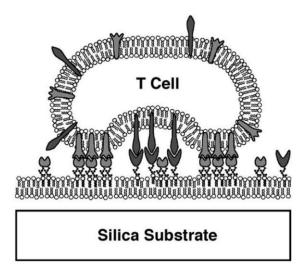


Figure 17: Scheme of a T cell interacting with a supported lipid bilayer functionalized with MHC (light gray) and ICAM-1 (dark gray). Taken from (Groves and Dustin 2003; Murphy and Weaver 2016)



1.2 **Microscopy**

The first microscopes were invented in the late 16th century and have opened the doors to the world of the small things and led to discovery of microorganisms. Nowadays, microscopes are a necessary equipment in many medical, biological and industrial applications. Throughout the history, people have been developing microscopes to bring higher magnification, contrast and resolution. Over the years, fluorescence microscopy has become the best method for high contrast imaging. Fluorescence microscopy utilizes specific light-absorbing and -emitting compounds called fluorophores. Further use of fluorescently labelled antibodies has brought high specificity and sensitivity to the labelling which has revolutionized the field and has led to a plethora of new microscopy techniques and advancements in cell biology. However, for many years, the resolution of microscopes has been limited to a few hundreds of nanometers due to diffraction of light, as described by Abbe in 1873 (Abbe 1873). This has changed recently with the development of super-resolution fluorescence techniques for which the 2014 Nobel Prize in Chemistry was awarded to Eric Betzig, Stefan W. Hell and William E. Moerner. Nowadays the best techniques can achieve resolution on the scale of a few nanometers (Dobrucki and Kubitscheck 2017).

In this chapter I will describe theoretical fundaments for understanding two techniques used in this work: Super-resolution fluorescence microscopy and Interference reflection microscopy. Further I will focus deeper on single molecule localization techniques and its recent applications to all 3 dimensions.

1.2.1 Fluorescence

Fluorescence is a phenomenon in which a fluorophore absorbs light of a given wavelength and subsequently emits light of a longer wavelength. Fluorophores are mostly nanocrystals or molecules which have delocalized electrons. To fully understand the properties of fluorescence, it is useful to explain them with Jablonski diagram, which describes the energy states of fluorescent molecules (Figure 18). The energy levels of the molecule are given by its electronic and vibrational states. The lowest energy state of the molecule is the lowest vibrational state of the ground electronic state S₀. In this state, also called single state, the electrons have antiparallel spins. When the molecule absorbs light in the form of a photon, it undergoes a transition to a higher vibrational state of the electronic state S_1 or S_2 . S_1 and S_2 are the first and the second excited electronic state of the molecule with antiparallel electron spins. This transition is very fast and takes only a few femtoseconds. In addition, the energy is conserved by the fact that the energy difference between the excited and the ground state equals the energy of the absorbed photon. Shortly after absorption, the higher vibrational energy of the molecule is dissipated by collisions of the molecule with the surrounding solvent molecules, and the molecule undergoes a transition to the lowest vibrational state of the S₁ electronic state. From there, the fluorophore can undergo three possible transitions. The first one is fluorescence, in which the molecule emits a photon and transits to a vibrationally excited state of the ground electronic state S₀. Typical time scale of fluorescence emission is a few nanoseconds. The second option is a nonradiative decay, in which the molecule transits to the ground electronic state S₀ and the energy is dissipated in the form of heat. The third transition is the least probable one, in which the excited electron flips its spin and the molecule ends up in an excited triplet state T₁. This transition is also called intersystem crossing. During the deexcitation of the triplet state of the molecule, the electron must flip its spin again and the molecule undergoes either a nonradiative or a radiative transition, also called



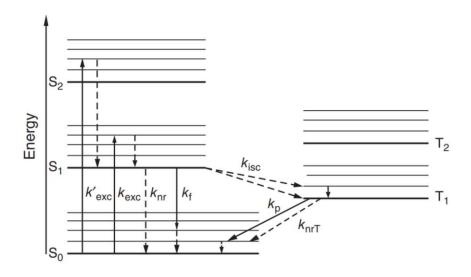


Figure 18: Jablonski diagram of a fluorophore. The energy levels of a molecule can be described by singlet and triplet electronic states (S_0 , S_1 , S_2 and T_1 , T_2), and vibrational states. The solid line arrows indicate absorption (k_{exc}) or emission of a photon (k_f – fluorescence, k_p – phosphorescence). The dashed line arrows indication nonradiative transitions of the fluorophore (k_{nr} – nonradiative, k_{isc} – intersystem crossing). Taken from (Dobrucki and Kubitscheck 2017)

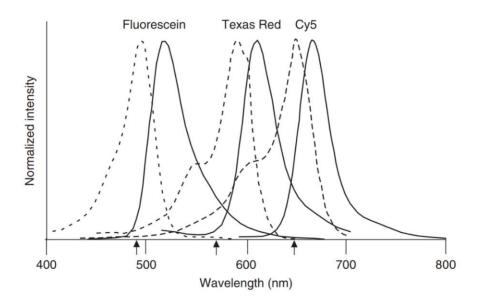


Figure 19: Excitation (dashed line) and emission (solid line) spectra of three fluorescent dyes: Fluorescein, Texas Red and Cy5. The difference between the peaks of emission and excitation spectra is described by Stokes shift. Taken from (Dobrucki and Kubitscheck 2017)

phosphorescence, to the ground state S₀. Since spin flipping is involved in the phosphorescence, the times for emitting a photon are on the scale of microseconds to hours (Dobrucki and Kubitscheck 2017; Lakowicz 2013).

The fact that the emission of a fluorescent photon is always preceded by the dissipation of the molecules' vibrational energy results in the red-shifted, lower energy photon, compared to the photon that was absorbed. This effect is also called Stokes shift. Even if the molecule was excited to the lowest vibrational level of the S₁ electronic state, reorientation of the solvent molecules prior to the emission of the fluorescent photon, would lower the energy level of the state S₁. This phenomenon is called solvent relaxation. Excitation and emission spectra of a few fluorophores are depicted in Figure 19. The excitation spectrum represents a wavelength dependent probability of the photon absorption by a fluorophore, whereas the emission spectrum shows the probability of the photon emission. At room temperature, the spectra show continuous bands rather than single lines due to additional rotational and translational energies of the molecules (Lakowicz 2013; Dobrucki and Kubitscheck 2017).

1.2.2 Fluorescence microscopy

Most of the fluorescence microscopes are based on an inverted optical microscope configuration (Figure 20a). This configuration allows to study specimens like cells, that reside at the bottom of the petri dish or similar chambers. Since the fluorescence is only triggered after absorption of photons at a specific wavelength, excitation light sources are important part of microscopes. These usually include either gas or solid-state lasers with specific excitation wavelengths, LEDs (light emitting diodes), mercury or halogen lamps. Stability and homogeneity of illumination are important factors in the fluorescence microscopy (Dobrucki and Kubitscheck 2017).

Another important part of the fluorescence microscopes are optical filters. Excitation filters transmit only wavelengths suitable for excitation of the fluorophores. Emission filters ideally transmit only the fluorescent light from the sample to the detector. Thanks to the Stokes shift between excitation and emission spectra, dichroic mirrors are used to spectrally separate between excitation light - which is reflected to the specimen - and fluorescence - which is transmitted to the detector. The spectral separation between excitation and emission light results in high contrast of the fluorescence images. The working principle of dichroic mirrors is depicted in Figure 20b and the transmission graph of the whole system (excitation filter, dichroic mirror, emission filter) is depicted in Figure 20c. The intensity of fluorescence is orders of magnitude smaller than the intensity of the excitation light. Therefore, another advantage of the inverted microscope is that the excitation light is not directed to the detector as it would be in the case of dia-illumination, which only relies on the blocking of the excitation light from reaching the detector by optical filters (Dobrucki and Kubitscheck 2017).

The most important imaging instrument of the fluorescence microscope is the objective. Parameters such as magnification, numerical aperture, collection efficiency and type of immersion medium should be considered when choosing the right objective for fluorescence microscopy. Magnification influences the size of the point spread function (PSF) on the detector. For optimal single molecule localization microscopy, the full width at half maximum (FWHM) of the PSF should be matched with the pixel size of the detector. Resolution of the microscope is given by the numerical aperture (NA) of the objective. The higher the NA the smaller the PSF on the detector. Furthermore, objectives with NA larger than the refractive index of the sample allow for objective-based total internal reflection fluorescence (TIRF) microscopy and collection of supercritical angle fluorescence, thereby increasing the collection efficiency. Water- or oilimmersion of the objective increases the NA by allowing detection of fluorescence emitted at steeper angles. However, use of the oil-immersion objectives yields spherical aberrations when



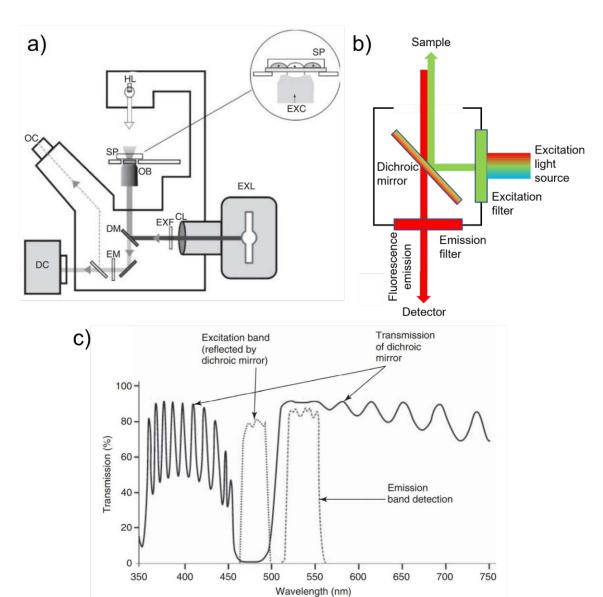


Figure 20: Schematic of an inverted fluorescence microscope in (a). Excitation light passes through the excitation filter and is reflected by a dichroic mirror towards the sample. Collected fluorescence passes through the dichroic mirror and emission filter towards the detector (b). Transmission spectra of dichroic mirror, excitation and emission filters (c). Taken and adapted from (Dobrucki and Kubitscheck 2017)

imaging deeper into aqueous solution which has to be considered for 3D imaging (Dobrucki and Kubitscheck 2017).

The last requirement of a fluorescent microscope is a detector capable of detecting weak fluorescence signals, such as electron-multiplying charge-coupled devices (EM-CCD) or scientific complementary metal-oxide semiconductors (sCMOS). EM-CCDs are particularly suited for low photon counts as they allow for detection of single photons with low read-out noise. sCMOS cameras are less sensitive in comparison to EM-CCDs in the low light settings and produce inhomogeneous read-out noise which needs to be corrected for. However, sCMOS cameras can be

manufactured with larger chip sizes and have much shorter read-out times than EM-CCDs (Lelek et al. 2021).

1.2.3 Total internal reflection fluorescence microscopy

Total internal reflection fluorescence (TIRF) microscopy is a microscopy technique in which only a thin layer of the sample in the vicinity of a coverslip is excited with an evanescent field. To generate the evanescent field, the excitation light is directed to the sample at an angle larger than the critical angle for total internal reflection. This can be achieved by using a prism or the objective itself. In the case of objective based TIRF, the same objective is used for illumination as well as collection of the fluorescence (Figure 21B). High NA objectives are needed to achieve such steep angles of excitation. Since only a thin layer of the sample near the glass slide is illuminated, this approach brings the advantage of suppressing the out of focus fluorescence, which is the main source of background in fluorescence microscopy. TIRF is widely used to observe the interface between biological samples and glass coverslips and achieves great contrast for single molecule fluorescence microscopy applications (Mashanov et al. 2003).

Propagation of the light between two media with refractive indices n_1 and n_2 is governed by Snell's law:

$$n_1 \sin \theta_1 = n_2 \sin \theta_2 \,, \tag{1}$$

where θ_1 and θ_2 are the angles of the incident and the refracted beam, respectively (Dobrucki and Kubitscheck 2017). In many microscopy applications, the first medium is represented by a glass coverslip with $n_1 = 1.52$ and the second medium is represented by a sample in an aqueous environment with $n_2 = 1.33$. Since $n_2 < n_1$, Equation (1) implies that the angle of the refracted beam will be larger than the angle of the incident beam. The incident angle can be increased to a level when the refracted beam propagates parallel to the coverslip with $\theta_2 = \pi/2$. Such incident angle is called critical angle θ_c and depends only on the values of the two refractive indices:

$$\sin\theta_c = \frac{n_2}{n_1}.\tag{2}$$

Given Equation (2), the value of the critical angle for a glass-water interface is 50,13°. Increasing the incident angle beyond the critical angle leads to total internal reflection (TIR). In TIR settings, an evanescent excitation wave is created on the sample side with the following properties:

1. The excitation intensity I decreases exponentially with the distance from the coverslip z,

$$I = I_0 e^{-\frac{Z}{\delta}},\tag{3}$$

where I_0 denotes the excitation intensity at the coverslip and δ specifies the decay length as follows:

$$\delta = \frac{\lambda}{4\pi} (n_1^2 \sin^2 \theta_1 - n_2^2)^{-\frac{1}{2}},\tag{4}$$

with λ denoting the wavelength of light.



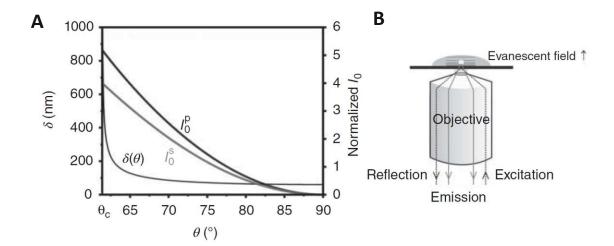


Figure 21: Penetration depth δ and normalized intensity at the coverslip I_0^p for p- and I_0^s for s- polarized light in dependece of the angle of angle of illumination (A). Scheme of objective based TIR illumination (B). Taken and adapted from (Dobrucki and Kubitscheck 2017)

- 2. The excitation intensity I_0 at the surface depends on the incidence angle θ_1 . At the critical angle, $\theta_1 = \theta_c$, it is 5 or 4 times higher than the incident intensity for p- or s- polarized light, respectively (Figure 21a).
- 3. Linear polarization is preserved for s-polarized incident light. For p-polarized incident light it is converted to an elliptically polarized evanescent field with the ellipse parallel to the plane of incidence.

The first of the above stated properties of the evanescent wave yields the advantage of illuminating just a thin layer of the sample close to the coverslip and suppressing the out of focus fluorescence. The second property gives a boost to the excitation intensity of the fluorophores in the vicinity of the coverslip. These two advantages make it possible to observe single molecules of fluorophores with outstanding signal to noise ratio. Furthermore, the third property enables the excitation of molecules with absorption dipoles parallel to the optical axis, which is difficult to achieve with standard means (Dobrucki and Kubitscheck 2017).

In practice, TIR illumination can be achieved by focusing the incident light into the back focal plane of a high NA objective off-centrally, which results in a tilted collimated beam leaving the front lens of the objective. To achieve angles beyond the critical angle the NA of the objective has to be larger than the refractive index of the sample n_2 . For cell samples with the refractive index of the cytoplasm of 1.38, objectives with NA > 1.4 are required.

1.2.4 Super-resolution microscopy

One central limitation to fluorescence microscopy in the past was the resolution limit caused by diffraction of light. Due to diffraction the image of any point source is given by the point spread function (PSF). The dimensions of the PSF are much larger than the imaged fluorophore. The size of the PSF depends on the wavelength of the emitted light λ and the numerical aperture of the objective *NA*, which is a measure of the range of light rays that contribute to the image formation. It is defined as



Background Chapter 1

$$NA = n \sin \alpha \,, \tag{5}$$

where n is the refractive index of the medium between the source and the objective and α is the maximum angle at which light enters the objective. If the fluorophores are in close proximity to each other, their corresponding PSFs may overlap, which hampers the ability to resolve them as separate spots (Figure 22) (Gray 2009). The critical distance, known as diffraction limit, was described by Abbe (Abbe 1873) as

$$d_{Abbe} = \frac{\lambda}{2NA} = \frac{\lambda}{2n\sin\alpha}.$$
 (6)

For an experimental setup with an objective of NA = 1.33 and fluorescence emitted at 650 nm, the diffraction limit yields $d_{Abbe} = 244$ nm. This number is two orders of magnitude larger than the fluorophore itself and demonstrates the difficulty of imaging structures that are smaller than a few hundreds of nanometers.

However, multiple techniques - termed super-resolution microscopy - have been developed to overcome the diffraction limit and yield 10 to 100 times better resolution. The biggest family of super-resolution microscopy methods is single molecule localization microscopy (SMLM). SMLM techniques take advantage of the fact that the center of single nonoverlapping PSFs can be localized with a high precision on the scale of a few nanometers (Smith et al. 2010). The trick of SMLM lies in the temporal separation of the fluorophore emission in such a way, that in every image only a small subset of non-overlapping PSFs is detected. Each image hence allows the localization of a subset of fluorophores. The whole super-resolved image can then be reconstructed from a sequence of images. SMLM includes techniques such as

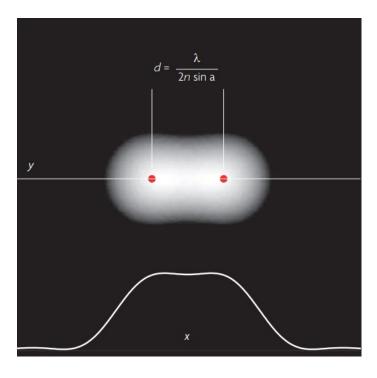


Figure 22: Abbe's diffraction limit. Two fluorophores cannot be distinguished because of their overlapping PSFs if they are closer to each other than the diffraction limit. Taken from (Gray 2009).



photoactivated localization microscopy (PALM) (Betzig et al. 2006), fluorescence photoactivation localization microscopy (FPALM) (Hess, Girirajan, and Mason 2006), stochastic optical reconstruction microscopy (STORM) (Rust, Bates, and Zhuang 2006) and direct stochastic optical reconstruction microscopy (dSTORM) (Heilemann et al. 2008).

Other methods enable the separation of neighboring fluorophores by the generation of a light pattern that excites a subset of fluorophores at any given time point while preventing emission from other fluorophores. These methods include stimulated emission depletion (STED) (Hell and Wichmann 1994) and structured illumination microscopy (SIM) (Gustafsson 2000). Furthermore, super-resolution optical fluctuation imaging (SOFI) (Dertinger et al. 2009) analyzes temporal fluorescence fluctuations of fluorophores and is therefore suitable to applications where larger densities of fluorophores are used.

1.2.5 Single molecule localization microscopy

Single molecule localization microscopy (SMLM) is a super-resolution technique based on extracting the coordinates of single fluorophores from their point spread functions (PSF) with a high precision. This is possible only if the fluorophore's PSF does not overlap with the PSF of a neighboring fluorophore. Therefore, SMLM super-resolution microscopy relies on the separation of fluorescent emission from distinct molecules in time.

The temporal separation is most commonly achieved by a phenomenon called photoswitching, in which dye molecules can switch between a fluorescent "on" state and a nonfluorescent "off" state. The fluorophore's photoswitching can be induced by irradiation with light of a specific wavelength or by its chemical environment. For example, fluorescence photoactivated localization microscopy (PALM) utilizes fluorescent proteins that can be switched to the "on" state via a pulse of UV laser light (Hess, Girirajan, and Mason 2006), while stochastic optical reconstruction microscopy (STORM) relies on synthetic dyes that randomly photoswitch in the presence of a blinking buffer (Heilemann et al. 2008). On the contrary, methods such as point accumulation in nanoscale topography (PAINT) do not require fluorophore photoswitching but utilize the fluorophores' binding to a target as a means of switching between an "on" state characterized by the ligated target, and an "off" state corresponding to the unligated target (Sharonov and Hochstrasser 2006).

By selection of fluorophores with short-lived "on" states and long-lived "off" states, one can achieve fluorophore blinking, where at any given time point only a small portion of the fluorophores in the sample emit fluorescence. Such fluorescence signal sparsity provides nonoverlapping PSFs, which can be precisely localized by fitting a model function to the measured signal. The localization precision depends mostly on the signal to noise ratio (SNR), therefore bright fluorophores capable of emitting large amounts of photons in a short amount of time are necessary. The acquisition of a super-resolved image via SMLM involves recording thousands of subsequent image frames with sparsely distributed PSFs, in which ideally every fluorophore appears at least once. All the localizations are collected to form the final image.

In more detail, there are three main steps in recording a super-resolved image via SMLM: detection of single molecules, their localization and the super-resolution image rendering (Figure 23). In the first step, the approximate positions of the fluorophores are found in the diffraction limited images, for example, by finding the local maxima. The diffraction limited images are often pre-processed to remove heterogeneous background, for example by wavelet filtering, rolling ball



Background Chapter 1

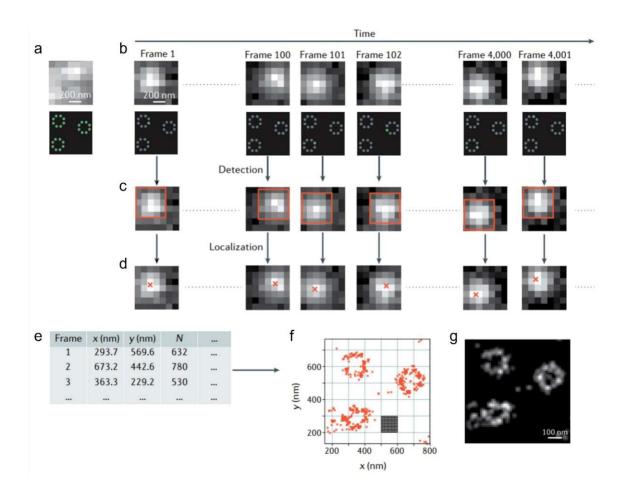


Figure 23: Process of SMLM. Diffraction limited image of an underlying structure if all fluorophores are in the ON state (a). Recording many frames of the diffraction limited images of blinking fluorophores (b). Selecting ROIs containig single molecule images (c). Localizing the molecules with a model function (d). Aquiring a list of all localizations with fitted parameters (e). Plotting the localizations in scatter plot (f) and rendering of the super-resolved image (g). Taken and adapted from (Lelek et al. 2021).

algorithm (Ovesný et al. 2014) or simply by subtracting the mean background from the whole image sequence (Cheng and Hsieh 2017). This detection step results in a set of small regions of interest (ROIs) containing the identified molecules. However, it may be that a portion of the signals gets identified wrongly as false positives or negatives if the signal to noise ratio is low in the diffraction limited image (Kay 1998).

In the second step, the previously produced set of single molecule images is used to perform the sub-pixel localization (Figure 24). The task of the localization algorithm is to precisely and accurately estimate the parameters of the emitters position x, y, z with a known imaging model *H* that give rise to the observed image *I* on the detector

$$I(u,v) = H(x,y,z,N_{sig},N_{bg}) = H(\theta),$$
(7)

where u, v are the coordinates in the imaging plane, N_{sig} are the total signal photons and N_{bg} is a constant background per unit area (von Diezmann, Shechtman, and Moerner 2017). Accuracy and precision are the two main quality parameters of the localization algorithm (Figure 25). If the position of the emitter is measured multiple times, the localization precision describes the spread



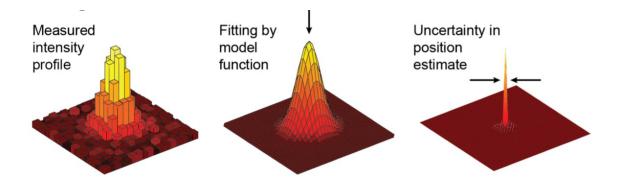


Figure 24: Fitting of the pixelated measured signal of a single molecule on the detector with a model function results in a position estimate with a high precision. Taken and adapted from (von Diezmann, Shechtman, and Moerner 2017).

of the position estimates around their mean value. The localization accuracy describes the deviation of the mean of the measured positions from the true position of the emitter (Deschout et al. 2014). In practice, the image on the detector is pixelated and subjected to noise, producing a signal n_k at every pixel w_k of the ROI. Simple approaches to solve the problem are, for example, maximum value estimator or centroid estimator. The maximum value estimator returns the position of the brightest pixel, which is computationally easy but rather imprecise since it is sensitive to noise and depends on the pixel size. The centroid estimator on the other hand returns the position of the weighted average of all pixels in the ROI, but it is biased toward the center of the ROI by the background in outlying pixels (von Diezmann, Shechtman, and Moerner 2017).

Better results can be achieved by assuming a model of the PSF with radial symmetry (Parthasarathy 2012) and by implementation of unbiased localization algorithms such as leastsquares (LS) fitting and maximum likelihood estimation (MLE) (Cheezum, Walker, and Guilford 2001). In the case of LS fitting, the square error S between the PSF model $\mu(\theta)$ and the data n is minimized:

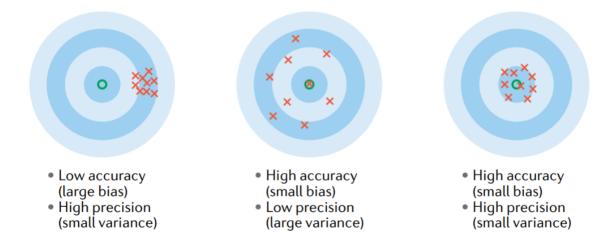


Figure 25: Localization accuracy and precision: Accuracy describes bias of the fitting algorithm from the true emitters position. Precision describes the variance of localized emitters position from repeated measurements. Taken from (Lelek et al. 2021).



Background Chapter 1

$$S = \sum_{k=1}^{N} [n_k - \mu_k(\theta)]^2 , \qquad (8)$$

yielding the optimized parameters θ . However, LS fitting assumes that the noise in each observed pixel value n_k is normally distributed, which is a priori not known (Abraham et al. 2009). Further assuming that the fluorophore emits light isotropically without polarization, the PSF image of infocus fluorophores yields an Airy function (Gibson and Lanni 1991):

$$I(u,v) = C \left(\frac{J_1(kNA\rho)}{kNA\rho}\right)^2, \tag{9}$$

where J_1 is the first order Bessel function, $k=2\pi/\lambda$ is the wavenumber, ρ is the radial distance from the emitter in the image plane, NA is the numerical aperture of the objective and C reflects the total integrated signal. For computational reasons it is convenient to approximate the airy function with a Gaussian function (Zhang, Zerubia, and Olivo-Marin 2007)

$$I(u,v) = \frac{N_{sig}}{2\pi\sigma^2} \exp\left(-\frac{\rho^2}{2\sigma^2}\right) + N_{bg}, \qquad (10)$$

where σ is the width of the Gaussian function. LS fitting with a Gauss model estimator avoids bias and achieves localization precision described by

$$\sigma^2 = \frac{\sigma_{PSF}^2 + a^2/12}{N_{sig}} \left(\frac{16}{9} + \frac{8\pi N_{bg} (\sigma_{PSF}^2 + a^2/12)}{N_{sig} a^2} \right),\tag{11}$$

where σ_{PSF} is the width of the PSF and a^2 is the pixel area on the camera (Mortensen et al. 2010). The above stated formula can be simplified assuming low background to the well-known inverse proportionality between the localization precision and the number of detected photons; in other words, the more photons one can collect, the better is the achieved localization precision

$$\sigma \propto \frac{1}{\sqrt{N_{sig}}}. (12)$$

The golden rule for localization algorithms is maximum likelihood estimation (MLE) which approaches the best achievable localization precision (Ober, Ram, and Ward 2004). MLE attempts to estimate a set of parameters of a given image formation model that give rise to the measured signal, accounting for the noise statistics. In other words, MLE finds the parameters for which the observed PSF is the most probable. This is done by maximizing the likelihood function $\mathfrak{L}(\theta|n)$, or equivalently the log-likelihood function, by varying the parameters θ (Enderlein 1995). Assuming that the Poisson noise is dominant, the log-likelihood function is

$$\mathfrak{Q}(\theta|n) = \sum_{k=1}^{N} \left[n_k \ln(\mu_k(\theta)) - \mu_k(\theta) \right], \tag{13}$$

where n_k are the measured pixel values and $\mu_k(\theta)$ is the imaging model (Ober, Ram, and Ward 2004). Achieving good localization precision implies the use of the correct PSF model. This can be



achieved via calculating the PSF shapes based on optical theories while also considering the effects of optical aberrations caused by imperfections of the imaging system. Such aberrations can be easily measured by recording a stack of images of fluorescent beads along the optical axis (Li et al. 2018). In praxis, algorithms exploiting experimentally measured PSFs commonly outperform algorithms that use idealized PSFs (Sage et al. 2019).

To assess and compare different localization algorithms, one can calculate the best achievable localization precision. Since localization of an emitter is a parameter estimation problem, tools from estimation theory can be used to analyze it (von Diezmann, Shechtman, and Moerner 2017). For example, Fisher information provides a mathematical measure of sensitivity of a given observable quantity, such as the image, to the changes of its underlying parameters, e.g. the emitter's position (Chao, Ward, and Ober 2016). The more the image changes upon changing the emitter's position, the more information about its position is contained in the image and, therefore, the localization algorithm can achieve better localization precision. A mathematical expression of Fisher information, given the dominance of Poisson noise and spatially uniform background, yields

$$I(\theta) = \sum_{k=1}^{N} \frac{1}{\mu_k + \beta} \left(\frac{\partial \mu_k}{\partial \theta}\right)^{\mathrm{T}} \left(\frac{\partial \mu_k}{\partial \theta}\right),\tag{14}$$

where μ_k is the model of PSF in pixel k, β represents the number of background photons per pixel and T denotes the transpose operation (von Diezmann, Shechtman, and Moerner 2017). The inverse of the Fisher information is the Cramér-Rao lower bound (CRLB)

$$CRLB(\theta) = \frac{1}{I(\theta)},\tag{15}$$

which states the lower bound on the variance with which the parameters θ can be estimated by using any unbiased estimator (Kay 1998). CRLB therefore represents an optimal localization precision that can be achieved for a given imaging method, signal, noise and background, and has been shown to be approachable in practice (Smith et al. 2010). The CRLB can be utilized to find the optimal performance when designing new microscopy methods, for example in PSF engineering of 3D SMLM.

In the last step of SMLM, all the localizations produced by the localization algorithm can be further processed and rendered to obtain the super-resolved image. In the post-processing step it is common to filter out all suboptimal localizations, e.g. based on the signal, CRLB thresholds, or the match between the fitted image and the PSF model (Lelek et al. 2021). Overcounting artifacts, stemming from the emitters that are detected several times during the recording, can also be reduced by merging the localizations that appeared in subsequent frames within the localization precision (Platzer et al. 2021). If ignored, overcounting can give rise to artificial clustering (Annibale et al. 2011).

Moreover, localizations need to be corrected for drift of the sample during the recording. Such sample drift stems from a variety of sources including vibrations and mechanical relaxation of the microscope, and is often difficult to avoid (Deschout et al. 2014). A common approach is to introduce fiducial markers to the sample which are tracked during the whole recording and used for correction (Lee, Baday, et al. 2012). Fiducials should be bright enough to allow for better localization precision than for the imaged molecules, however they should also not increase the

background of the sample. This problem can be avoided by using spectrally separated fiducial markers. Another approach to drift correction which avoids using fiducial markers is based on spatial correlation between the subsequent super-resolution images (Geisler et al. 2012). In super-resolved image rendering, the results can be visualized e.g. as scatter plots (Figure 23f) or, more commonly, on a grid with small bin sizes on the scale of the localization precision; the number of localizations per bin is then translated to the pixels intensity (Figure 23g) (Lelek et al. 2021).

The instrumentation of SMLM is relatively simple compared to the instrumentation of STED or SIM techniques. SMLM utilizes wide-field fluorescence microscopes with high NA objectives for efficient collection of photons and sensitive cameras with low noise, such as EM-CCD or sCMOS camera (von Diezmann, Shechtman, and Moerner 2017).

1.2.6 3D Single molecule localization microscopy

There is a huge need in fluorescence microscopy to be able to observe samples in all three dimensions since relying on the measurements of merely a 2D projection is not sufficient as they can lead to misinterpretation of the results. For example, free diffusional motion of a particle on the surface of a sphere, if visible only as a 2D projection, would be observed as confined diffusion (Adler et al. 2010).

The main challenge in 3D fluorescence microscopy is that the PSF of a standard fluorescence microscope changes only slightly with an axial shift of the emitter relative to the focal plane. The diffraction limit for the axial direction is approximately two times larger than for the lateral direction:

$$d_z \approx \frac{n\lambda}{NA^2}$$
, (16)

where λ is the wavelength of light, n is the refractive index of the medium and NA is the numerical aperture of the imaging system (Blom and Widengren 2017). For example, a typically achievable resolution for standard microscopy is around 250 nm in lateral and 600 nm in axial direction (Liu et al. 2018). The insensitivity of the PSF to the emitter's shifts in axial direction is equivalent to a low Fisher information and, hence, poor precision in determining the z coordinate of the emitter.

There is a number of microscope modifications for SMLM that overcome this problem by achieving a high Fisher information for the localization in both lateral and axial direction allowing for robust 3D super-resolution imaging. These methods can be divided into several groups based on the principle of how they achieve 3D localizations: Multifocal imaging, PSF engineering methods and methods based on interference-, interface- or intensity-sensing (von Diezmann, Shechtman, and Moerner 2017). Shortly, in multifocal imaging, the PSF is measured at different focal planes. In PSF engineering methods, the shape of the PSF is manipulated to encode the axial coordinate of the emitter. In the interference-, interface- and intensity-sensing methods, the position of the emitter is measured in relation to features in the imaging geometry instead of fitting the PSF shape. All of these methods have their strengths and weaknesses regarding the amount of signal, background, noise, axial range and speed and are suitable for applications under different conditions (Liu et al. 2018). A selection of the methods will be discussed in this chapter.



Multifocal imaging:

Multifocal or multiplane imaging is based on recording in-focus as well as defocused images of the same emitter resulting in an enhanced 3D localization precision. The in-focus image yields good lateral precision while the defocused images yield good axial precision. The simplest form of this method is biplane imaging with two focal planes (Figure 26A), but multiplane imaging with up to 4 planes was also demonstrated (Prabhat et al. 2006). The biplane imaging can be realized with a beam splitter in the imaging path and two cameras (Prabhat et al. 2004), or one camera divided into two channels (Ram et al. 2008). The shift between the focal planes can be achieved either by axially displacing one of the cameras or one of the tube lenses. The optimal off-set between the focal planes can be calculated by Fisher information analysis (Tahmasbi et al. 2014). 3D localization in multiplane imaging is performed by simultaneous MLE or LS fitting of the set of the measured PSF images from different planes with a theoretically or experimentally derived model (Mlodzianoski et al. 2009). The advantage of multiplane imaging is superior performance of the localization precision in comparison with one-plane imaging (Figure 26C), high temporal resolution, relatively simple optical setup and a usable axial range of around 1,5 µm. Among the disadvantages are poorer SNR due to division of photons into multiple imaging pathways as well as emergence of spherical aberrations which worsen the axial precision caused by misplacement of the camera or the tube lens (Botcherby et al. 2007). Multiplane imaging has been applied to

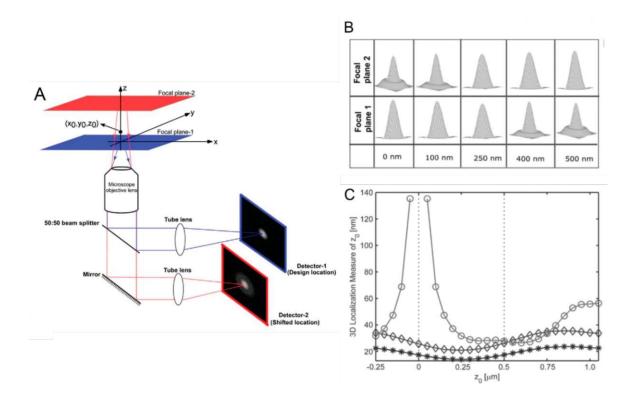


Figure 26: Experimental setup for biplane imaging (A). Fluorescence is collected via an objective and the emission is split and imaged on two detectors with a relative shift in focus. PSF of a single emitter as it appears on the two detectors depending on its z position in the sample (B). Achievable localization precision for single plane imaging (0), biplane imaging (0) and biplane imaging with 2 times longer exposure time improved by a factor $\sqrt{2}$ (*). Taken and adapted from (von Diezmann, Shechtman, and Moerner 2017).



Background Chapter 1

super-resolution microscopy in thick samples (Juette et al. 2008) as well as 3D single-particle tracking (Ram et al. 2012).

PSF engineering:

PSF engineering methods are based on encoding the axial position of the emitter into the shape of PSF. With this approach, it is possible to localize the emitter in all three dimensions just by fitting single images. The z position of the emitter is linked to the shape of the PSF via some intrinsic parameter such as orientation, size or a combination of different features. While the principle of all PSF engineering methods is the same, the resulting shapes of the PSF vary in their applicability to different conditions. For example, a particular PSF shape can deliver high localization precision in all three directions but only for a small range of axial positions. On the other hand, a different PSF can yield somewhat worse but consistent localization precision over a large z range (Liu et al. 2018).

Encoding of the emitter's depth to the shape of the PSF can be achieved by introducing phase aberrations into the imaging pathway (Figure 27) (von Diezmann, Shechtman, and Moerner 2017). For example, introducing a cylindrical lens in front of the camera causes astigmatism which results in an elliptical shape of the PSF. A more general way of introducing phase aberration into the imaging pathway is by placing a phase modulator in the plane which is conjugated with the back focal plane of the objective. Such phase modulators include deformable

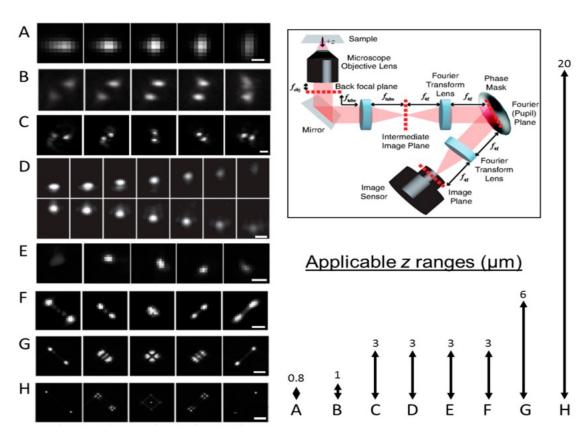


Figure 27: Overview of PSF engineering methods with astigmatism (A), phase-ramp (B), double helix (C), accelerating beam (D), corkscrew (E), 3 μm range Tetrapod (F), 6 μm range Tetrapod (G) and 20 μm Tetrapod (H). PSF engineering methods are based on the modulation of phase at the Fourier plane with a phase mask. Taken and adapted from (von Diezmann, Shechtman, and Moerner 2017).



mirrors (Izeddin et al. 2012), liquid crystal spatial light modulators (Pavani et al. 2009) or a lithographically etched dielectrics (Gahlmann et al. 2013). The relation between the image I(u,v)in the imaging plane and the back focal plane is given by a Fourier transformation:

$$I(u, v; x, y, z) \propto |\mathcal{F}\{E(x', y'; x, y, z) \cdot P(x', y')\}|^2,$$
 (17)

where E(x', y') is the electrical field in the back focal plane caused by the emitter at (x, y, z), P(x', y') is the phase modulation introduced into the back focal plane by a phase modulator and \mathcal{F} denotes the 2D Fourier transform (Goodman 2005). The principle of PSF engineering methods is to choose a phase pattern P(x', y') which makes the estimation of the emitter's z position from the image I(u, v) easier. Such PSF designs usually rely on eccentricity (Figure 27a), relative position of two lobes (Figure 27b-d), lateral translation (Figure 27e) or a combination of these features (Figure 27f-h) (von Diezmann, Shechtman, and Moerner 2017).

In the case of astigmatism, the z coordinate is encoded in the eccentricity and direction of the ellipse (Figure 27a) (Kao and Verkman 1994). In order to restore the axial position, the width of the PSF along the x and y axis can be fitted by two Gaussian functions, yielding a pair (σ_x, σ_y) which is then compared with a theoretical model or an experimentally derived calibration curve. The performance of astigmatic imaging in relation to a standard PSF and other engineered PSFs is compared in the Figure 28. Clearly, astigmatic PSF brings a superior localization precision in axial direction over the standard PSF and is suitable for a z-range of around 1 µm. Beyond this range, the size of the PSF increases, which significantly decreases the signal to noise ratio as well as the localization precision. The small size of the astigmatic PSF is also advantageous, as higher emitter densities per frame without overlapping PSF can be tolerated, therefore decreasing the recording time. As an application example, astigmatic imaging has been applied together with STORM to study the 3D morphology of nanoscopic cellular structures achieving 20 nm lateral and 50 nm axial resolution (Huang, Wang, et al. 2008).

In order to achieve larger axial ranges, a double-helix point spread function using a spatial light modulator was designed (Greengard, Schechner, and Piestun 2006). The shape of the doblehelix PSF exhibits two lobes which rotate with changing axial position of the emitter (Figure 27c). The lateral localization is estimated from the mid-point between the two lobes and the axial position from the orientation of the line connecting them. The larger axial range of the method comes from the fact that translation of the emitter along the optical axis does not impact the overall size of the PSF, only the orientation changes. This yields superior localization precision compared to astigmatic PSF over an axial range of 3 µm (Figure 28). The double-helix point spread function was used to localize molecules in a polymer sample with 10 to 20 nm resolution (Pavani et al. 2009) as well as in biological structures with 20 to 30 nm resolution in lateral and axial direction, respectively (Lee, Sahl, et al. 2012). One of the disadvantages of this method comes from the use of the spatial light modulator, which has a lower photon transfer efficiency due to the ability to modulate only one polarization of light. This fact results in a photon loss of up to 50%, hampering low photon applications (Grover et al. 2011). However, solutions to this problem implementing a polarization beam splitter and half-wave plate to modulate all polarization components have been proposed (Pavani, DeLuca, and Piestun 2009).

As mentioned above, the measure of the best achievable localization precision for a given PSF lies in the Fisher information. One can design an optimal PSF by maximizing the Fisher information for a specific axial range and under different experimental conditions including photon numbers, background, noise, magnification, and pixel size (Shechtman et al. 2014). Using



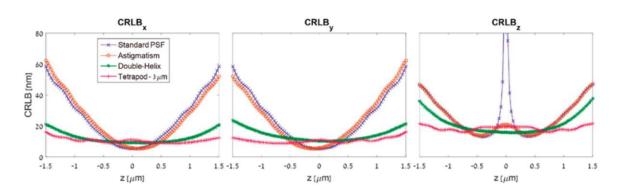


Figure 28: Comparison of CRLB in x, y and z direction for standard, astigmatic, double-helix, and tetrapod PSFs. Taken and adapted from (von Diezmann, Shechtman, and Moerner 2017).

this method, a tertrapod PSF also known as saddle-point PSF was designed for conditions of high background level and an axial range of 3 µm (Figure 27f). The saddle-point PSF features two strong side lobes, whose orientation and distance change as a function of emitters axial position. Such a design of a PSF provides a more consistent CRLB over the range of 3 µm than the doublehelix PSF (Figure 28) (von Diezmann, Shechtman, and Moerner 2017). Further tetrapod PSFs were designed by maximizing the Fisher information for 6 and 20 µm ranges (Figure 27g-h) and applied to tracking lipid molecules on the surface of living, thick mammalian cells (Shechtman et al. 2015). A disadvantage of tetrapod PSFs is that they have a larger size which limits the localization density in a single frame. Furthermore, neural networks have been utilized recently to design an optimal PSF for the case of dense SMLM with overlapping fluorophores' signals (Nehme et al. 2020).

Generally, the best way how to use all the information encoded in the shape of the PSF is to fit it with a theoretical or experimentally derived model using MLE which uses information from dim pixels more correctly (von Diezmann, Shechtman, and Moerner 2017). PSF engineering can be further utilized not only to encode the axial position of the emitter but also its 3D orientation (Backer et al. 2013) or its emission wavelength (Smith et al. 2016), demonstrating the robustness of this approach.

Intensity sensing methods:

All above-described methods rely on the shape of the PSF to determine the axial position of the emitter. However, the z position of the emitter can also be encoded in the emitter's image by other means. One example is to illuminate the sample with a z-dependent excitation gradient such as an evanescent wave in the case of TIRF microscopy. Assuming constant fluorescence quantum yield and absorption cross-section of the emitter, the z position of the fluorophore can be extracted from the detected fluorescence intensity (Dickson et al. 1996). In the case of TIRF, the excitation intensity decays exponentially leading to bright signals with good localization precision for the emitters close to the coverslip, but faint signals with poor localization precision for emitters further away from the coverslip. Better results can be achieved by sequential illumination of the sample with evanescent fields with different penetration depths (Fu et al. 2016). In such cases the z position of the molecule is extracted from the intensity ratio obtained from the two sequential images.

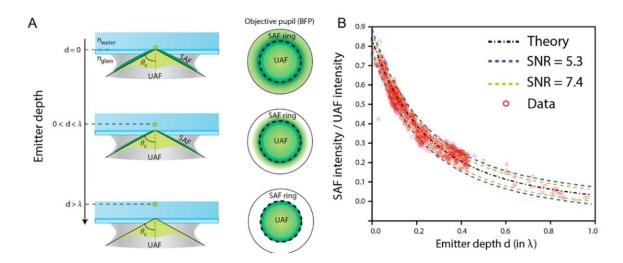


Figure 29: Principle of supercritical angle fluorescence emission. The superctitical angle fluorescence (SAF) appears when a fluorophore is closer to the coverslip than wavelength of the emission. SAF is spatially separated from the undercritical angle fluorescence (UAF) in the objective pupil (A). Ratio SAF/UAF intensity as a function of the emitter's z position (B). Taken and adapted from (Bourg et al. 2015)

Interface sensing methods:

The axial position of a fluorophore can also be estimated from its interaction with a coverslip that has a different refractive index than the sample. If the emitter is in the vicinity of a glass coverslip, a part of the fluorophore's near field fluorescence gets coupled into the coverslip as supercritical angle fluorescence (SAF), which can be collected by a high NA objective (Ruckstuhl and Verdes 2004). The amount of SAF depends exponentially on the emitters axial position and disappears for distances larger than the wavelength of the fluorescence light (Figure 29A). Since the SAF travels to the objective under an angle that is beyond the critical angle for TIRF microscopy, it is spatially separated from the undercritical angle fluorescence (UAF) in the back focal plane of the objective. The z dependent SAF and z independent UAF can be discriminated by placing an annular filter into a plane conjugated to the back focal plane, and the ratio SAF/UAF can be used to determine the emitter's axial position (Figure 29B). In practice, the emission path is split into two channels, where the SAF light is blocked in one of them by an aperture. The ratio (SAF+UAF)/UAF is used for calculation of the emitter's z position (Deschamps, Mund, and Ries 2014). This technique has been demonstrated with DNA-origami nanostructures as well as with single molecule imaging in cells (Bourg et al. 2015; Deschamps, Mund, and Ries 2014).

Interference methods:

A different approach to determine the molecule's axial position is to utilize the self-coherence of the emitted fluorescence. In this case, fluorescence is collected by two opposing objectives. Interference is used to sense phase shifts between the two optical paths resulting from the emitter's z position (Hell and Stelzer 1992). In order to avoid the need of scanning the sample to obtain the interferogram, one can measure the resulting intensity in different channels with additional phase delays. In the case of two channels, a simple 50:50 beam splitter can be used to recombine the signal from the two objectives and form the interference on two detectors (von Diezmann, Shechtman, and Moerner 2017). However, the axial range of two channel approaches



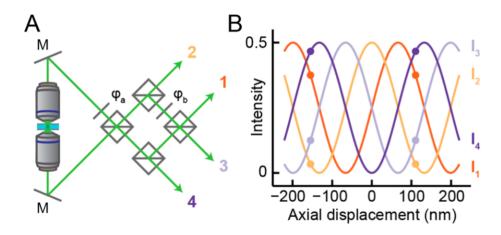


Figure 30: Schematic of four channel interference microscope utilizing two objectives and four beam splitters (A). The resulting intensities on the four detectors as a function of emitters z position (B). Taken and adapted from (von Diezmann, Shechtman, and Moerner 2017)

is limited to $\lambda/4n$, where n is the refractive index of the media. A better axial range of $\lambda/2n$ can be achieved by sampling the intensity onto more channels, for example three in the iPALM method (Shtengel et al. 2009) or four in 4Pi-SMS (Middendorff et al. 2008) (Figure 30). Interferometric approaches are capable of achieving a superior localization precision of 10 nm laterally and 5 nm axially, however, at the cost of complexity of alignment and maintenance (von Diezmann, Shechtman, and Moerner 2017).

1.2.7 Fluorophores for single molecule localization microscopy

Fluorescent labelling of the sample can be achieved by using synthetic dyes or fluorescent proteins. For the purpose of SMLM, the fluorophores need to exhibit blinking behavior between ON- and OFF-states, which allows recording images of single molecules without overlapping PSFs. There are five different mechanisms how to achieve such a transition between ON- and OFFstates: photoswitching, photoactivation, photoconversion, spontaneous blinking and temporary binding, depicted in Figure 31 (Lelek et al. 2021).

Photoswitching:

Photoswitching is a reversible transition between an ON- and an OFF-state, which results in many blinks of each photoswitchable fluorophore during the acquisition time. The transition occurs upon irradiation of the fluorophore at a suitable wavelength and with the use of a blinking buffer consisting of PBS, 10-100 mM thiol and optionally an enzymatic oxygen scavenging system (van de Linde et al. 2011). During the ON-state, the fluorophore resides in the singlet ground state and is able to emit fluorescence upon excitation. In the OFF-state, the fluorophore is in a reduced state due to the thiol in the buffer, which can last from hundreds of milliseconds to several seconds. The return of the fluorophore from the OFF-state to the ON-state takes place after interaction of the reduced fluorophore with the residual oxygen in the buffer (van de Linde et al. 2011). Irradiation of the sample with UV (405 nm) can further shorten the duration of the OFF-state and therefore increase the number of bright fluorophores per image. The duration of the ON-state can be influenced by the irradiation density, or by the concentration of thiol or pH of the buffer (Lin et al. 2015). All these parameters should be optimized for a given sample and the used dye, while

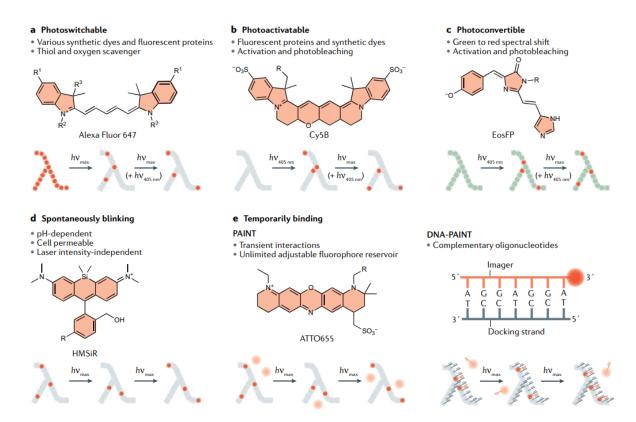


Figure 31: Mechanisms of transitions between ON- and OFF-states for different dyes. Photoswitchable dyes undergo a reversible transition between ON- and OFF-state upon irradiation at a suitable wavelength and in the presence of a blinking buffer (a). Photoactivatable dyes require an activation pulse to undergo an irreversible transition from OFF- to ON-state (b). Photoconvertible dyes undergo a shift in their emission spectrum upon irradiation with a specific wavelength (c). Spontaneously blinking dyes (d). Temporarily binding dyes utilize transient interactions such as complementary binding of short nucleotides in DNA-PAINT (e). Taken and adapted from (Lelek et al. 2021).

keeping in mind that low laser intensities and longer illumination times generally lead to lower photobleaching and increased resolution (Diekmann et al. 2020). In the beginning of the SMLM experiment, most of the fluorophores are in the ON-state and can be driven to the OFF-state by illumination with high excitation intensity of 10-30 kWcm⁻². During the experiment, a lower excitation intensity of 1-3 kWcm⁻² is used to image single molecules and ensure blinking of the dyes (Lelek et al. 2021). The most common synthetic dyes are carbocyanine dyes like Cy5 and Alexa Fluor 647, rhodamine and oxazine dyes such as other Alexa Fluor and ATTO dyes (Klein, Proppert, and Sauer 2014). In the case of fluorescent proteins, Dronpa can undergo photoswitching upon excitation with a wavelength of 488 nm and an activation wavelength of 405 nm without the need of a special buffer (Andresen et al. 2007). Photoswitchable fluorophores are the key players in the case of STORM (Rust, Bates, and Zhuang 2006) and dSTORM (Heilemann et al. 2008) experiments. Toxicity of the blinking buffers mostly limits the application of photoswitchable dyes to experiments with fixed cells. However, since cells contain the thiol glutathione at millimolar concentrations some synthetic dyes can be used also for dSTORM in live cells (Heilemann et al. 2009; Wombacher et al. 2010).

Photoactivation:

Photoactivation is an irreversible transition of a fluorophore from an OFF-state to an ON-state, which can occur upon irradiation with UV light or spontaneously in an aqueous environment. The transition from the ON- to the OFF-state takes place by photobleaching with the excitation light during the recording of the single molecule signals. No special buffer is needed and therefore photoactivatable fluorophores are suitable also for live cell imaging (Lelek et al. 2021). Synthetic photoactivatable dyes include photochromic rhodamine amides (Bossi et al. 2008), the silicon rhodamine PA Janelia Fluor 646, the azetidinyl rhodamine PA Janelia Fluor 549 (Grimm et al. 2016) and the bridged carbocyanine Cy5B (Michie et al. 2017). Among the fluorescent proteins are PAmCherry, PA-TagRFP, PAmKate, and PA-GFP (Lukyanov et al. 2005), which have been used for PALM experiments in fixed (Betzig et al. 2006) as well as live cells (Manley et al. 2008).

Photoconversion:

Photoconversion is another irreversible transition, in which the fluorophore undergoes a shift in its emission spectrum upon irradiation with a specific wavelength. For example, the transition can occur between a green and a red fluorescence state. In such case, the green fluorescence state is considered as OFF-state and can be spectrally filtered. The red fluorescence state is then considered as ON-state and is used for imaging of the single molecule signals. Eventually, the transition from ON- to OFF-state is achieved by photobleaching. Photoconvertible fluorescent proteins include Eos, Dendra2 (Turkowyd, Virant, and Endesfelder 2016) and mMaple (McEvoy et al. 2012).

Spontaneous blinking:

Some fluorophores blink spontaneously in aqueous solution without the need of a special blinking buffer. Such blinking is driven by pH dependent chemical reactions in the sample and it is suitable for live cell imaging (Uno et al. 2014). Spontaneously blinking dyes include HMSiR (Takakura et al. 2017), HEtetTFER (Uno et al. 2018) and FRD (Macdonald et al. 2018).

Temporary binding:

A different approach how to achieve switching between ON- and OFF-states is to let fluorophores bind temporarily to the target structure. In such cases, the bound, immobilized state is considered as ON-state, in which the molecule can be localized. The OFF-state is represented by the unligated receptor; freely diffusing, unbound fluorophores do not lead to localizations but just increase the background fluorescence of the sample. This approach is named point accumulation in nanoscale topography (PAINT) (Sharonov and Hochstrasser 2006). The most popular variant of this method is DNA-PAINT, in which transient immobilization is achieved by hybridization of DNA strands (Jungmann et al. 2010). Shortly, in DNA-PAINT the target molecule is labelled via a short nucleotide called docking strand. The fluorescent label is attached to a complementary oligonucleotide called imaging strand that is freely diffusing in the solution. The binding kinetics can be influenced by the length of the nucleotide sequence and the concentration of the imaging strands in the solution. The longer the imaging strand, the longer the ON-state due to its stability, and the higher the concentration of the imaging strands, the shorter the OFF-state. Typically, the binding lifetime of an 8 base pairs long duplex is around 500 ms (Jungmann et al. 2010).



Background Chapter 1

1.2.8 Labeling strategies for single molecule localization microscopy

In order to image the molecules of interest in the sample, they have to be labeled with a fluorophore. There are multiple labeling strategies including genetic fusion of a fluorescent protein to the target protein, immunostaining with dye-conjugated antibodies, genetic fusion with a protein that can be tagged to a synthetic fluorophore, direct labeling of the target protein via amino-acid residues or using transiently binding molecules carrying fluorophores (Figure 32) (Lelek et al. 2021). An ideal labeling strategy should meet the following criteria: yielding a minimal linkage error, achieving high labeling densities and preserving the physiological function and localization of the target molecule.

Genetic fusion of fluorescent proteins to the target proteins has been demonstrated with PALM (Betzig et al. 2006; Manley et al. 2008). Cells can be transiently or stably transfected to express the fluorescently labeled protein, but expression levels can vary largely among the cells (Thorn 2017). Fluorescent proteins are 2-5 nm large and hence produce a rather small linkage error. However, genetic fusion can result in perturbation of the physiological function of the target protein (Rodriguez et al. 2017).

Immunostaining is the most common approach to label proteins with synthetic dyes in fixed cells (Lelek et al. 2021). In direct immunostaining a dye-conjugated antibody is used to label the target protein. However, fluorescent modification of the antibody can lead to lower binding affinity to the target protein. Therefore, in indirect immunostaining, dye-conjugated secondary antibodies are used to bind to an unlabeled primary antibody. In this way, more secondary antibodies can bind to the primary antibody which leads to signal amplification. The disadvantage of immunostaining is the large size of antibodies and therefore the linkage error ranging from 10 nm for direct labeling to 20 nm for indirect labeling. Therefore, smaller molecules such as 2-4 nm nanobodies are a good alternative to full antibody labeling (Ries et al. 2012).

Genetic fusion of tag proteins allows for highly specific labeling with low linkage error, using synthetic dyes. The tag protein is expressed together with the protein of interest and covalently binds the fluorescently labeled ligand. The most commonly used protein tags are

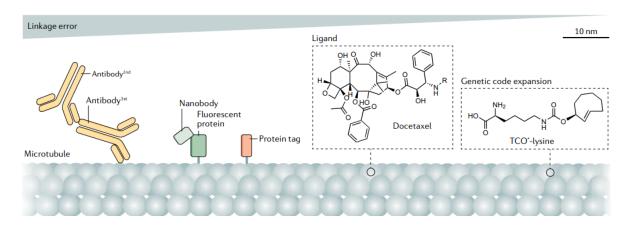


Figure 32: Overview of labeling strategies with indicated corresponding linkage error. From left: Indirect immunostaining, nanobody labeling, genetic fusion of fluorescent proteins, genetic fusion of protein tags, direct labeling via a fluorescent ligand and incorporation of unnatural amino acid for click chemistry. Taken and adapted from (Lelek et al. 2021)



SNAP- and Halo-tags (Yan and Bruchez 2015; Liss et al. 2015). Tag proteins can be used also in live cell imaging with membrane permeable fluorescent ligands.

Direct labeling via dye-coupled peptides or drugs is available for some biological substrates like actin and microtubule filaments (Xu, Zhong, and Zhuang 2013). Proteins can also be labeled site specifically via a single amino acid residue. However, such approaches often lead to perturbation of the physiological function of the molecule of interest. Genetic expansion enables incorporation of TCO*-lysine into the expressed proteins, which can be bound to a synthetic dye via fluorogenic click reaction without perturbing the functionality of the proteins and enabling live cell imaging (Neubert et al. 2018; Lang and Chin 2014).

Transiently binding molecules carrying fluorophores are used in the PAINT approach (Sharonov and Hochstrasser 2006). For example, the DNA-paint approach involves labeling the target molecule with a short oligonucleotide called docking strand. Usually, the short nucleotide is attached to a secondary antibody that binds to a primary antibody bound to the target molecule (Schnitzbauer et al. 2017).

1.2.9 Interference reflection microscopy

In order to study interactions between two surfaces, it is necessary to accurately measure their separation. Interference reflection microscopy (IRM) offers an easy to implement and label free approach to study adhesion of cells to the substrate by using interference of light (Curtis 1964). It relies on the interference of reflected light rays from the glass-buffer and the buffer-sample interface. With known sample properties and interference models this method can yield great accuracy; for example, beads can be tracked with 10 nm lateral and 1 nm axial precision (Schilling et al. 2004). However, such precise height measurements are hampered in cells as the cell shape and refractive index is not known a priori (Limozin and Sengupta 2009). Nevertheless, IRM is often used to qualitatively study the adhesion of cells; it is also used for cross-validation with different techniques, such as fluorescence microscopy (Bunnell et al. 2003).

IRM is usually performed with a standard inverted microscope, an incoherent light source and a detector, such as a CCD or CMOS camera. The illumination path is set up according to Köhler illumination to allow for homogeneous illumination and the ability to adjust the illumination numerical aperture of the system. Since IRM highly relies on the reflection from the sample, any additional reflections within the optical path can obstruct the final image. To overcome this issue, a closely related technique to IRM called reflection interference contrast microscopy (RICM) utilizes a set of two polarizers and an anti-flex objective with a quarter-wave plate (Figure 33). RICM can greatly enhance the contrast of the image, however, requires a special objective to be used (Limozin and Sengupta 2009).

The principle of IRM is shown in Figure 34. A monochromatic incident ray I_0 is partially reflected from a glass-medium interface resulting in a reflected ray I_1 and a transmitted ray. The transmitted ray continues further through the medium until it is reflected from the sample, producing ray I_2 . The rays I_1 and I_2 interfere with each other and give rise to the final intensity on the detector *I* which depends on the distance of the sample to the coverslip:

$$I = I_1 + I_2 + 2\sqrt{I_1 I_2} \gamma_{12} \cos[2kh(x, y) + \phi], \qquad (18)$$



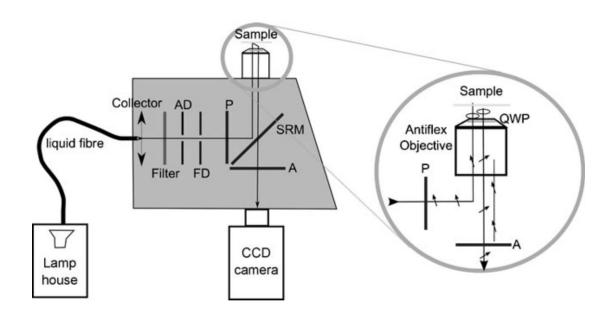


Figure 33: Schematic of a RICM setup. Light from a light source is coupled into the microscope via a liquid fiber and adjusted for Köhler illumination. Then the light passes through a polarizer and is reflected by a semi-reflective mirror to the sample. Objective contains a quarter wave plate which produces circularly polarized light that is reflected from the sample. The reflected light passes through another polarizer which filters out reflections caused by elements in the optical path and is imaged on a camera. Taken from (Limozin and Sengupta 2009).

where $k = 2\pi n_1/\lambda$, ϕ is a phase shift usually equal to π , h(x,y) is the distance of the sample to the coverslip at the position x, y, and γ_{12} is the mutual degree of coherence (Born and Wolf 2013). The intensities of the reflected rays are governed by Fresnel laws with $I_1 = r_{01}^2 I_0$, $I_2 =$ $(1-r_{01}^2)r_{12}^2I_0$ and $r_{ij}=(n_i-n_j)/(n_i+n_j)$. For example, for the glass-water interface we obtain $r_{01}^2 = 0.005$, for the water-lipid interface $r_{12}^2 = 0.003$. These small values show the need for avoiding any reflection within the microscope.

Coherence of the light source also plays a large role in the quality of the final image. In the case of an incoherent light source only rays coming from the same point of the source lead to a stable interference pattern. This creates a rather small coherently illuminated volume at the focal plane in the sample, given by the coherence length of the illumination light. The higher the coherence the larger the volume of the sample that contributes to the interference fringes. Therefore, using an incoherent light source is important to limit the contributions to the interference fringes from structures further away from the focal plane (Limozin and Sengupta 2009).

In Köhler illumination, the NA of the light source is defined by the aperture diaphragm, which is a disk with a radius ρ . The illumination numerical aperture INA is then defined as INA = $n\rho/D = n\sin\alpha$, with refractive index n, source-image distance D and the angle of the cone of light emerging from the objective α . The maximal distance x_c between two coherently illuminated positions in the sample corresponds to $x_c = 0.16 \lambda / INA$ (Limozin and Sengupta 2009). Therefore, high INA imposes a reduced coherence, in particular along the optical axis, which limits the depth of focus. High INA is especially useful when studying adhesion of cells close to the substrate, as it can prevent problems arising from multiple reflections within the cell sample (Geiger et al. 1984).

Background Chapter 1

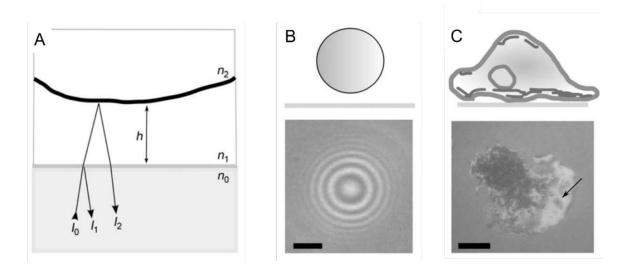


Figure 34: Principle of IRM; light rays reflected from the glass – buffer interface and buffer – membrane interface interfere with each other based on the distance h (A). IRM image of a 10 μm diameter polystyrene bead, scale bar 2 μm (B). IRM image of a spreading monocyte, lamellipodium indicated with an arrow, scale bar 5 μm (C). Taken and adapted from (Limozin and Sengupta 2009).

The intensity in the IRM image can be used to calculate the distance between the sample and the substrate. Let us define the maximum and minimum intensity from Equation (18), assuming the degree of coherence $\gamma_{12} = 1$: $I_{max} = I_1 + I_2 + 2\sqrt{I_1I_2}$ and $I_{min} = I_1 + I_2 - 2\sqrt{I_1I_2}$. Furthermore, let us define sum *S* and difference *D* of these intensities: $S = I_{max} + I_{min}$ and $D = I_{max} + I_{min}$ $I_{max} - I_{min}$. Using $\phi = \pi$, the image intensity I can be rewritten into the form

$$2I = S - D\cos\left(\frac{4\pi n_1}{\lambda}h\right),\tag{19}$$

with S and D as experimentally measurable parameters (Limozin and Sengupta 2009). However, this simple equation ignores the effects of illumination numerical aperture, presence of multiple interfaces, and tilt or curvature of the interface (Figure 35).

Considering the effect of illumination numerical aperture *INA* on the high measurements from the image intensity, one can express the following formula (Rädler and Sackmann 1993)

$$2I = S - D \frac{\sin y}{y} \cos \left\{ \frac{4\pi n_1}{\lambda} \left[h \left(1 - \sin^2 \left(\frac{\alpha}{2} \right) \right) \right] \right\}, \tag{20}$$

with $y=2kh\sin^2(\alpha/2)$, where α is the half angle of the illumination cone and n_1 is the medium's refractive index. Equation (20) shows two effects on the dependence of the intensity on the height (Figure 35A): first, the fringe visibility decreases with increasing height and second, the fringe spacing stretches. The higher the *INA*, the more prominent these effects become.

If multiple interfaces occur (Figure 35B), the intensity results from the interference of all reflected rays. The following formula can be expressed that reflects the height-intensity relation (Limozin and Sengupta 2007)

$$2I = S - 2D\cos\{2k[h(x, y) - h_0]\}, \tag{21}$$



where $h_0=\frac{-\lambda}{4\pi n_1} \arctan\frac{\gamma \sin\delta}{1+\gamma \cos\delta}$, $\gamma=\frac{r_{23}}{r_{12}}(1-r_{12}^2)$ and $\delta=4\pi n_2 d_m/\lambda$, d_m is the membrane thickness. Therefore, the presence of two interfaces leads to a shift h_0 to the interference fringes, which depends on the refractive indices and the spacing of the two layers (Figure 35B).

Reflecting surfaces may also be tilted or curved, which leads to a displacement of the reflected rays (Figure 35C). In such cases, one has to calculate the contribution of all reflected rays which reach a given point in the image plane (Kühner and Sackmann 1996). The numerically calculated radial profile of the interference fringes for a sphere is shown in Figure 35C. One can see that the curved surface results in decreased inter-fringe distances with decreasing visibility. The ability to detect the reflection from highly tilted surfaces is limited by the illumination numerical aperture as well as the numerical aperture of the detection.

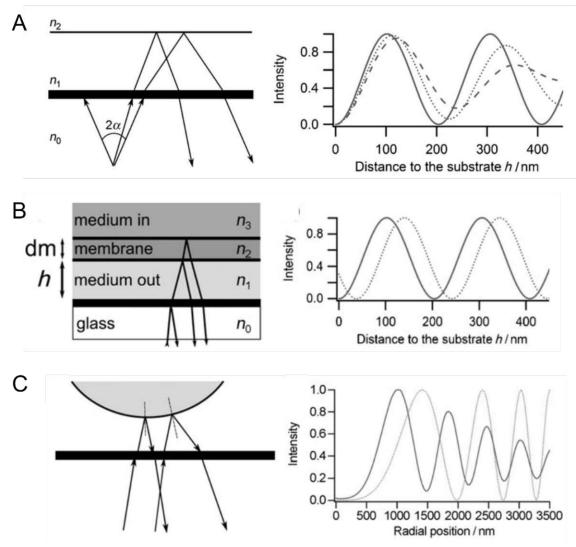


Figure 35: Effects of illumination numerical aperture, multiple interfaces and curved surfaces on the height-intensity relation. (A) The effect of illumination aperture (INA = 0, solid line; INA = 0.8, dotted line; INA = 1, dashed line). (B) The presence of multiple interfaces leads to a shift of the interference fringes (dashed line) compared to the reference (solid line). (C) The effect of curved surfaces calculated for a sphere with 5 μm radius (solid line) compared to a sphere surface with horizontally oriented segments. Taken and adapted from (Limozin and Sengupta 2009).



All these above-mentioned effects hamper quantitative measurements of the distance of the cell surface from the substrate as precise orientations, refractive indices and presence of multiple layers are not known a priori to construct an adequate model of interference (Limozin and Sengupta 2009).

Chapter 2: Materials and Methods

Reagents and proteins 2.1

For a better overview, reagents and proteins are sorted according to experiments in which they were used.

Buffers: Phosphate buffer saline with 1x or 10x salt concentration (PBS or 10xPBS) and Hanks' balanced salt solution (HBSS) were purchased from Sigma Aldrich (Germany).

Fluorescent labeling of glass spheres (section 3.2.1): Glass spheres were from Schott (d=2mm, Germany). Biotin labeled bovine albumin (BSA-biotin) was purchased from Sigma Aldrich (Germany). Streptavidin-AF647 was from Thermo Fischer Scientific (USA).

Preparation of nuclear pore complexes (section 3.2.3): Dulbecco's Modified Eagle Medium (DMEM), FCS, non-essential amino acids (NEAA) and GlutaMax were from Gibco (USA). Triton X-100, NH₄Cl were purchased from Sigma Aldrich (Germany). BG-AF647 from New England Biolabs (USA). ImageIT FX Signal Enhancer and DTT was from Thermo Fisher Scientific (USA).

Fluorescent labeling of ICAM-1 (section 3.3): Alexa 488 - NHS and Zeba Spin Desalting Column (7K MWCO) were from Thermo Fisher Scientific (USA), NaHCO₃ from Sigma Aldrich (Germany).

Preparation of supported lipid bilayers (section 3.3): 1,2-dioleoyl-sn-glycero-3-phosphocholine (DOPC), 1,2-dipalmitoyl-sn-glycero-3-phosphocholine (DPPC) and 1,2-dioleoyl-sn-glycero-3-[(N-(5-amino-1-arboxypentyl)iminodiacetic acid)succinyl] (nickel salt) (Ni-NTA-DGS) were from Avanti Polar Lipids (USA). B7-1 and ICAM-1 were from Sino Biological (China). I-Ek and MCC peptide were prepared and labeled as described previously (Huppa, Axmann, Mortelmaier, et al. 2010). Chloroform was from Sigma Aldrich (Germany).

Preparation of T cells (section 3.3): Fetal bovine serum (FCS) and Histopaque-1119 were purchased from Sigma Aldrich (Germany). Cell medium RPMI 1640, penicillin, streptomycin, glutamate, sodium pyruvate, 1x non-essential amino acids and mercaptoenthanol were from Gibco, Life Technologies (USA). IL-2 from Thermo Fischer Scientific (USA). H57-scFv was expressed in inclusion bodies, refolded, site-specifically labeled with maleimide functionalized AF647 (Thermo Fisher Scientific, USA), and purified as described in (Huppa, Axmann, Mortelmaier, et al. 2010).

Ratiometric calcium imaging (section 3.3): FURA-2AM was from Thermo Fisher Scientific (USA), DMSO from Sigma Aldrich (Germany).

Cell fixation (sections 3.2.3 and 3.3): Formaldehyde was from Thermo Fischer Scientific (USA) and glutaraldehyde from Serva (Germany).

Gloxy STORM buffer for super-resolution imaging (sections 3.2.1, 3.2.3 and 3.3): Glucose, glucose oxidase, catalase and cysteamine were purchased from Sigma Aldrich (Germany).

2.2 Microscopy systems

2.2.1 System for combined SMLM and IRM

A detailed description of the new setup will be given in section 3.1.4. Here, I provide a brief summary of the major components. All SMLM and IRM experiments were performed on a homebuilt experimental setup based on an Olympus IX73 (Japan) microscope body equipped with a



high NA objective (Carl Zeiss, alpha-plan apochromat, 1.46 NA, 100x, Germany). Samples were illuminated with 405, 488 or 640 nm laser light (100 mW nominal laser power, OBIS Laser box, Coherent, USA) coupled by an optical fiber into a high-speed galvo back focal scanner (iLas², Visitron Systems, Germany). The iLas² system was used for rapid spinning of the laser in the back focal plane of the objective (spinning TIR configuration), yielding a maximal excitation intensity of 1 kW/cm² at the sample. Finally, lasers were reflected to the specimen and filtered from the fluorescence signal by a quad dichroic mirror (Di01-R405/488/532/635, Semrock, USA) and an emission filter (ZET405/488/532/642m, Chroma, USA) placed in the upper deck of the microscope body. The same dichroic mirror was used for coupling in light from a blue LED (455 nm, Thor Labs, USA) for IRM imaging. An additional shortpass beamsplitter (HC BS 750 SP, Semrock, USA) was placed in the lower deck of the microscope for coupling in a home-built focus hold system based on a 785 nm laser diode (LM9LP, Thor Labs, USA), a camera (ac640-750um, Basler, Germany) and an objective piezo stage (P721.SL2, Physik Instrumente, Germany). Finally, the specimen was imaged on a camera (EM-CCD Ixon Ultra, Andor, UK). Illumination and image acquisition was operated by VisiView (Visitron Systems, Germany).

2.2.2 System for calcium imaging

Ratiometric calcium imaging in section 3.3 was performed on an Axiovert 200M microscope (Carl Zeiss, Germany) equipped with a 10x objective (UPlanFL N 10x/0.30 NA, Olympus, Japan) and a monochromatic light source (Polychrome V, TILL Photonics, Germany) to allow sequential illumination at 340 and 380 nm. The emission was filtered via a long pass filter (T400lp, Chroma, USA) and an emission filter (510/80ET, Chroma, USA) and imaged on a camera (EM-CCD iXon Ultra, Andor, UK). The system was operated via Live Acquisition software (TILL Photonics, Germany)

2.3 Sample preparation and imaging

2.3.1 Preparation of fluorescent beads

Fluorescent beads attached to glass slides were used for characterization of drift in section 3.1.5 as well as for aberrations measurements in section 3.1.6. Glass slides (MENZEL-Gläser Deckgläser 24 x 60 mm #1.5, Thermo Fisher Scientific, USA) were plasma cleaned for 10 minutes (PDC-002, Plasma Cleaner Harrick Plasma, USA) and glued on 8-well chambers (Nunc Lab-Tek, Thermo Fisher Scientific, USA). 100 nm large TetraSpeck Microspheres (Thermo Fisher Scientific, USA) were sonicated (ultrasound bath USC500TH, VWR, England) in the original tube for 5 min and incubated with the glass slide (1-10 µl of the stock solution in 100 µl of water) for 10 minutes. Next, 100 µl of poly-D-lysine (0.1 mg/ml, Sigma Aldrich, Germany) was added to the chambers for 10 min to ensure immobilization of the beads. Finally, the sample was washed with 20 ml of water and was ready for imaging.

2.3.2 Drift measurement

For characterization of drift in section 3.1.5, a sample with well separated fluorescent beads was imaged at epi-configuration with 640 nm laser light at a rate of 1 frame per second for a total time of 1 hour.

2.3.3 Aberrations measurement

For aberrations measurements in section 3.1.6, a sample with a low density of fluorescent beads was prepared so that the separation between the neighboring beads was at least 50 pixels (1 pixel=146.6 nm). A single fluorescent bead was imaged at different focal planes from -1600 nm to +1600 nm with a step of 200 nm. 100 images were acquired and averaged per focal plane position to ensure good signal to noise ratio. The recorded z-stack consisting of 17 images (51x51 pixels) was then used for phase retrieval and characterization of aberrations in the optical system.

2.3.4 Preparation of Gloxy STORM buffer

Gloxy buffer was used for STORM measurements on glass spheres (section 3.2.1), nuclear pore complexes (section 3.2.3) and T cells (section 3.3). Aliquots of glucose, glucose oxidase and cysteamine were stored at -20°C and catalase was stored at 4°C (all from Sigma Aldrich, Germany). The Gloxy STORM buffer was prepared fresh prior to every experiment by mixing 500 μl of 20% glucose, 200 μl of 10xPBS, 230 μl of ultra-pure water, 50 μl of 1 M cysteamine with pH adjusted to 7.5, 10 μ l of 50 mg/ml glucose oxidase and 10 μ l of 12.6 mg/ml catalase. The buffer was used for imaging for up to 2 h.

2.3.5 Glass sphere

Glass spheres were used for proof of principle experiments in section 3.2.1. Glass spheres (2mm diameter, Schott, Germany) were plasma-cleaned (PDC-002, Plasma Cleaner Harrick Plasma, USA) for 10 minutes and incubated with 5 % BSA-biotin (Sigma Aldrich, Germany) for 60 minutes. The spheres were then washed with PBS and incubated with 1 µg/ml Streptavidin-AF647 (Thermo Fisher Scientific, USA) for 30 minutes. Afterwards, spheres were rinsed with PBS and placed into 8-well chambers (Nunc Lab-Tek, Thermo Fisher Scientific, USA) with plasma cleaned glass coverslip (MENZEL-Gläser Deckgläser 24 x 60 mm #1.5, Thermo Fisher Scientific, USA). Prior to imaging, PBS was replaced with Gloxy STORM buffer. The 3D SMLM data were recorded using dSTORM approach in combination with defocused imaging. The defocus magnitude was adjusted to 500 nm, the sample was imaged in epi configuration with 640 nm laser light, 20 ms illumination time and 10 ms delay. A total of 20000 frames was recorded. For the IRM image of the glass sphere, 300 images were recorded with the 455 nm LED illumination and averaged to produce a good signal to noise ratio image.

2.3.6 DNA-origami nanorulers

DNA-origami nanorulers were used for proof of principle experiments in section 3.2.2. GATTA-PAINT 3D 30R Ultimate Line sample was purchased from GATTAQUANT (Germany). The sample was imaged in TIRF with 640 nm excitation laser upon defocusing the objective 500 nm into the sample. Blinking of the molecules was ensured via PAINT approach. 20000 frames were acquired with illumination time of 100 ms and delay of 10 ms.

2.3.7 Nuclear pore complex

Nuclear pore complex was used for proof of principle experiments in section 3.2.3. U₂OS cells expressing Nup96-SNAP-tag (Thevathasan et al. 2019) were a kind gift from Jonas Ries (EMBL



Heidelberg, Germany). The cells were cultured in DMEM medium supplemented with 10% FCS, NEAA and GlutaMax (Gibco, USA). A day before the imaging, the cells were split and seeded into 8-well chambers (Nunc Lab-Tek, Thermo Fisher Scientific, USA) with plasma cleaned coverslips (MENZEL-Gläser Deckgläser 24 x 60 mm #1.5, Thermo Fisher Scientific, USA). All following steps took place at room temperature. After 24 hours the cells were washed 2 times with HBSS (Sigma Aldrich, Germany) and pre-fixed with 200 µl of 2.4% PFA (Thermo Fisher Scientific, USA) for 30 s. Then the cells were permeabilized with 200 µl of 0.4% Triton-X100 (Sigma Aldrich, Germany) for 3 min. Next, the cells were fixed with 200 µl of 2.4% PFA for 30 min. The fixation was quenched by incubating cells with 200 μl of 50 mM NH₄Cl (Sigma Aldrich, Germany) for 5 min. T cells were then washed 2 times with PBS and incubated with two drops of ImageIT Signal Enhancer (Thermo Fisher Scientific) for 30 min. Labeling was performed by incubating cells with 1 μM BG-AF647 (New England Biolabs, USA) in 0.5 % BSA (Sigma Aldrich, Germany) and 1 μ M DTT (Thermo Fisher Scientific, USA) for 2 h. In the end the cells were rinsed 3 times with PBS and stored at +4 °C until imaged on the same or the next day. Prior to imaging, PBS was exchanged for the Gloxy STORM buffer. The 3D SMLM data were recorded using dSTORM approach in combination with defocused imaging. The defocus magnitude was adjusted to 500 nm, the sample was imaged in TIRF configuration with 640 nm laser light, 20 ms illumination time and 10 ms delay. A total of 65000 frames was recorded.

2.3.8 Fluorescent labeling of ICAM-1

ICAM-1 was fluorescently labeled in order to determine its surface density on a supported lipid bilayer in section 3.3. 50 µg of mouse ICAM-1 protein (His Tag) (Sino Biological, China) was dissolved in ultrapure water to a final concentration of 1 mg/ml and 10 µl of 1 M NaHCO₃ (Sigma Aldrich, Germany) was added. Next, Alexa488-NHS (Thermo Fisher Scientific, USA) was added at 20x molar excess to ICAM-1 and incubated for 1 h at room temperature. Afterwards, the protein was purified from the unbound dye in Zeba Spin Desalting Column (7K MWCO, Thermo Fisher Scientific, USA) and the final concentration of the protein and the degree of labeling was measured by microplate reader (Synergy H1, Agilent, USA). The protein was stored in -20°C in PBS with 50% glycerol (Sigma Aldrich, Germany) to prevent crystallization.

2.3.9 Supported lipid bilayers (SLBs)

Supported lipid bilayers were prepared for T cell experiments in section 3.3. 1,2-dioleoyl-sn-(DOPC) 1,2-dioleoyl-sn-glycero-3-[(N-(5-amino-1glycero-3-phosphocholine and arboxypentyl)iminodiacetic acid)succinyl] (nickel salt) (Ni-NTA-DGS) (both Avanti Polar Lipids, USA) were dissolved in chloroform and mixed in a glass tube at a molar ratio of 98 (DOPC): 2 (Ni-NTA-DGS), and subsequently dried under N₂ flow for 20 minutes. Next, the lipid mixture was resuspended in 1 ml of PBS and sonicated for 10 minutes (ultrasound bath USC500TH, VWR, England) to form small unilamellar vesicles (SUVs). Glass slides (MENZEL-Gläser Deckgläser 24 x 60 mm #1.5, Thermo Fisher Scientific, USA) were plasma cleaned for 10 minutes and glued on 8well chambers (Nunc Lab-Tek, Thermo Fisher Scientific, USA). To form supported lipid bilayers, the freshly cleaned glass slides were incubated with SUVs for 20 min and washed extensively with PBS. Next, SLBs were incubated with His-tag proteins (Activating conditions: 10 ng I-Ek/MCC, 50 ng B7-1 and 30 ng or 0.3 ng ICAM-1; resting conditions: 30 or 0.3 ng ICAM-1) for 1 hour, and extensively rinsed with PBS. B7-1 and ICAM-1 were from Sino Biological (China), I-Ek and MCC peptide were prepared and labeled as described previously in (Huppa, Axmann, Mörtelmaier, et al. 2010). Before seeding the cells, PBS was exchanged for HBSS (Sigma Aldrich, Germany). Immobile SLBs for field aberrations measurement in section 3.1.6 were prepared identically, except for the following changes: we used a lipid mixture of 98 % 1,2-dipalmitoyl-sn-glycero-3phosphocholine (DPPC) and 2 % Ni-NTA-DGS. For sonication the ultrasound bath was preheated to 50 °C and coverslips were incubated with SUVs on a hot plate (65°C). Finally, SLBs were incubated with 10 ng of I-Ek/MCC-AF647.

2.3.10 Determination of ligand densities on SLBs

In order to determine the density of ligands on the supported lipid bilayer (SLB) in section 3.3, fluorescent variants of the proteins, ICAM-1-AF488 and I-Ek/MCC-AF647 were used at the same concentrations as their unlabeled counterparts used for the T cell experiments. To find out the fluorescence intensity of a single molecule, SLBs with low density of ligands were prepared and imaged in TIRF configuration with 488 or 640 nm laser excitation. For high density bilayers with unknown ligand concentration, a single image of SLB containing ICAM-1-AF488 or I-Ek/MCC-AF647 was taken in TIRF with the same intensity and exposure time as for the single molecule recording.

2.3.11 T cells

T cells were used in experiments in section 3.3. T cells were obtained from transgenic 5c.c7 mice as described previously (Huppa et al. 2003). Briefly, T cells were isolated from lymph nodes and stimulated with 2 µM HPLC-purified moth cytochrome C (MCC) peptide (ANERADLIAYLKQATK, Intavis Bioanalytical Instruments) in a T cell medium (RPMI 1640 containing 10% FCS (Sigma Aldrich, Germany), 100 U/mL penicillin/streptomycin, 2mM glutamate, 1 mM sodium pyruvate, 1x non-essential amino acids, and 50 μM-Mercaptoenthanol (Gibco, USA)). Culture volume was doubled and 100 U/mL IL-2 (Thermo Fisher Scientific, USA) was added on day 2. On days 3 and 5, T cell cultures were expanded in a ratio of 1:1. On day 6, dead cells were removed by centrifugation trough a Histopaque-1119 cushion (Sigma Aldrich, Germany). T cell experiments were performed on days 7–9 after initial stimulation.

2.3.12 Animal model and ethical compliance statement

5c.c7 αβ TCR-transgenic mice bred onto the B10.A background were a kind gift from Michael Dustin (University of Oxford, UK). Both 8-12 weeks old male and female mice were randomly selected and sacrificed for isolation of T cells from lymph nodes and spleen, which was evaluated by the ethics committees of the Medical University of Vienna and approved by the Federal Ministry of Science, Research and Economy, BMWFW (BMWFW-66.009/0378-WF/V/3b/2016). Animal husbandry, breeding and sacrifice of mice was performed in accordance to Austrian law (Federal Ministry for Science and Research, Vienna, Austria), the guidelines of the ethics committees of the Medical University of Vienna and the guidelines of the Federation of Laboratory Animal Science Associations (FELASA), which match those of Animal Research: Reporting in vivo Experiments (ARRIVE). Further, animal husbandry, breeding and sacrifice for T cell isolation was conducted under Project License (I4BD9B9A8L) which was evaluated by the Animal Welfare and Ethical Review Body of the University of Oxford and approved by the Secretary of State of the UK Home Department. They were performed in accordance to Animals (Scientific Procedures) Act 1986, the guidelines of the ethics committees of the Medical Science of University of Oxford and



the guidelines of the Federation of Laboratory Animal Science Associations (FELASA), which match those of Animal Research: Reporting in vivo Experiments (ARRIVE).

2.3.13 T cell imaging

Experiments with T cells are described in section 3.3. In order to label the T cell receptor, appr. 106 T cells were washed twice by centrifugation (300 RCF for 3 min) with 2 ml of HBSS containing 2% FCS (Sigma Aldrich, Germany). Next, T cells were incubated with H57-scFv conjugated with AF647 at saturating conditions for 20 min on ice (H57-scFv was expressed in inclusion bodies, refolded, site-specifically labeled with maleimide functionalized AF647 (Thermo Fisher Scientific, USA), and purified as described in (Huppa, Axmann, Mortelmaier, et al. 2010)). After incubation the cells were washed twice by centrifugation with 2 ml of HBSS + 2% FCS at 4°C. The cells were then immediately seeded on the prepared SLBs and fixed after 5-15 minutes of spreading with 4% formaldehyde (Thermo Fisher Scientific, USA) + 0.2% glutaraldehyde (Serva, Germany) for 10 min. Afterwards, the fixing solution was rinsed with PBS. Finally, PBS was exchanged with Gloxy STORM buffer for dSTORM. To acquire 3D SMLM data of T cell receptor we used dSTORM with defocused imaging as described in (Zelger et al 2020). Before the experiment, single molecules adhered to the glass coverslip next to the cells were brought into focus, and the objective was displaced by 500 nm towards the sample by the piezo stage (P721.SL2, Physik Instrumente, Germany). For the dSTORM experiment, 20.000 frames at 20 ms illumination time and 9 ms delay time were recorded for each analyzed image. After 10.000 frames a 405 nm UV laser was added to the illumination sequence (1 mW laser power, OBIS Laser box, Coherent, USA). The distance of the objective to the coverslip was maintained by the focus hold system for the entire recording of the cells. In order to acquire the IRM image of the T cell, the sample was illuminated via 455 nm LED. The final IRM image was constructed as an average of 100 recorded images of the same spot for better signal to noise ratio.

2.3.14 Ratiometric calcium imaging

Ratiometric calcium imaging on T cells was performed in section 3.3. Appr. 106 T cells were washed by centrifugation (300 RCF for 3 min) with 2 ml of imaging buffer composed of HBSS + 2% FCS (Sigma Aldrich, Germany). The supernatant was removed and 0.5 μl of FURA-2AM (1 mg/ml in DMSO, Thermo Fisher Scientific, USA) was added to the cell suspension and incubated at room temperature for 30 min. Next, the cells were washed twice by centrifugation with the imaging buffer. Finally, the pellet was resuspended in 100 µl of imaging buffer and 15 µl of the cell suspension was added per chamber. The cells were imaged from the very beginning of their contact with the SLB. The imaging was performed by sequentially illuminating the sample with 340 and 380 nm at 1 Hz for at least 10 min.

Data Analysis 2.4

2.4.1 Localization of single molecules

The single molecule coordinates x, y, and z, the single molecule brightness (B) and the background signal (bg) were determined by maximum likelihood fitting of the calculated PSF model on a 21 by 21 pixel subregion around the signal, as previously described (Zelger et al.



2018). Shortly, we assumed a Poissonian probability for the number of photons n_k detected in pixel k:

$$P_{k}(n_{k}|\mu_{\theta,k}) = e^{-\mu_{\theta,k}} \frac{\mu_{\theta,k}^{n_{k}}}{n_{k}!}.$$
(22)

The expectation values $\mu_{\theta,k}$ depend on the parameter vector $\theta = (bg, B, x, y, z)$ and the PSF model *h*:

$$\mu_{\theta,k} = bg + Bh_k(x, y, z). \tag{23}$$

The PSF model was based on vectorial imaging theory described in (Axelrod 2012). For every recorded image, the parameter vector $\hat{\theta}$ is estimated by finding a minimum of the total negative log-likelihood function using the MATLAB tool *fminunc*:

$$\hat{\theta} = \arg\min_{\theta} \sum_{k} [\mu_{\theta,k} - n_k \ln(\mu_{\theta,k})] . \tag{24}$$

The initial parameter values required for the minimum search were provided by fitting a Gaussian model plus offset to the raw data.

2.4.2 Aberrations

The PSF model includes optical aberrations of the experimental setup retrieved from z-stack measurements of 100 nm fluorescent beads (TetraSpeck Microspheres, Thermo Fisher Scientific, USA) described in section 3.1.6. We refine the PSF model by taking phase aberrations in the objective pupil into account, which we express in a Zernike mode basis using Noll coefficients (Noll 1976) ranging from 2 (tip) to 37 (3rd order spherical) plus the 4th order spherical mode Z_{56} :

$$\phi = \sum_{i=2}^{37} a_i Z_i + a_{56} Z_{56} \,, \tag{25}$$

where a_i represent the magnitudes of the Zernike modes Z_i . Furthermore, the transmission function of the objective is modeled using a circular polynomial:

$$P = \sum_{n=1}^{5} q_n (x'^2 + y'^2)^n, \qquad (26)$$

where q_n are the coefficients of the transmission function, x' and y' are coordinates in the back focal plane of the objective. In the first step, a focus stack I_{exp} of a single 100 nm bead is recorded. All images are laterally centered according to the centroid of the in-focus image. Subsequently, all images are cropped to a size of 40×40 pixels, with one pixel measuring 146.6 nm in the focal plane. Finally, constant background values are subtracted. A matching image stack I_{sim} is simulated using a vectorial model (Axelrod 2012). This simulated point response is convolved with the shape of the bead (Hanser et al. 2004) as well as with an additional Gaussian kernel ($\sigma = 0.5$ pixels, empirically determined), to closer match the experimental images. For the monochromatic



simulation we assume the maximum emission wavelength (measured to be 680 nm) as well as unpolarized emission. The phase retrieval algorithm compares the simulated 3D model stack $I_{sim}(i,j,k)$ with the experimental data $I_{exp}(i,j,k)$ by calculating the differences and summing up their absolute values:

$$E = \sum_{i=1}^{n_x} \sum_{j=1}^{n_y} \sum_{k=1}^{n_z} |I_{sim}(i,j,k) - I_{exp}(i,j,k)|, \qquad (27)$$

where n_x , n_y and n_z denote the respective dimensions. We empirically found this metric to yield robust results in conjunction with the MATLAB function fminunc. By varying the Zernike mode coefficients of the simulation and the coefficients of the transmission function, the algorithm fits the model to the experimental stack. After those Zernike magnitudes which minimize the error E have been found, the coefficients a_2 , a_3 (corresponding to tip and tilt) are set to zero and high-NA defocus (Botcherby et al. 2007) is subtracted in order to center the PSF model on the computational grid. The final PSF model h is obtained by calculating one last focus stack using the updated Zernike coefficients and normalizing it to an integral value of one.

2.4.3 Cramér-Rao lower bound calculations

The Cramér-Rao lower bounds (CRLBs) for parameter uncertainties are given by the corresponding diagonal elements in the inverse Fisher information matrix, which is calculated as follows (Chao, Ward, and Ober 2016):

$$FI_{m,n} = \sum_{k=1}^{K} \frac{1}{\mu_{\theta,k}} \frac{\Delta \mu_{\theta,k}}{\Delta \theta_m} \frac{\Delta \mu_{\theta,k}}{\Delta \theta_n}.$$
 (28)

The CRLB for parameter θ_u then corresponds to:

$$CRLB_u = FI_{u,u}^{-1} . (29)$$

The signal and background photon numbers required for CRLB calculation were provided by the maximum likelihood estimates.

2.4.4 Analysis of drift

Fluorescent beads measured in section 3.1.5 were localized in 3D and localizations corresponding to a single bead were grouped by a tracking algorithm (Trackpy, (Allan et al. 2021)). The trajectories of single beads were then averaged in x, y and z direction to obtain a single, more precise trajectory of the whole sample drift. To test the performance of cross-correlative drift correction on the bead sample, the localizations were then drift corrected using the ImageJ plugin ThunderStorm (Ovesný et al. 2014).

2.4.5 SMLM corrections of field aberrations and offset

It is necessary to correct for field-dependent aberrations, as they would introduce bias into the determined z-positions of the localized signals. For this purpose, we imaged immobile supported lipid bilayers functionalized with I-Ek/MCC AF647-as a ground truth sample (section 3.1.6), in



which all dye molecule should be located in the same z-plane. The localizations were fitted with a planar surface, which was then subtracted from all localizations for correction. To find the z =0, average z position of the molecules adsorbed to the glass in the sample of interest was subtracted.

2.4.6 Analysis of glass spheres

Glass sphere experiments are described in section 3.2.1. Single molecule signals were localized in 3D and corrected for the field aberrations. Localizations with very low (B < 500) or very high (B > 2500) photon numbers were filtered out. The localizations were then drift corrected in xy plane by calculating cross correlations using ImageJ plugin ThunderStorm (Ovesný et al. 2014).

The SMLM data were then fitted with a sphere surface of 1 mm radius to find the contact point of the sphere with the coverslip and to find the z offset of the SMLM data which was eventually subtracted. The expected distance z₀ of the glass sphere from the coverslip was calculated via

$$z_0 = R - \sqrt{R^2 - r_0^2} \,, \tag{30}$$

where R = 1 mm is the radius of the sphere and r_0 is the radial distance to the contact point.

For the correlative SMLM and IRM imaging on the glass sphere the contact point of the sphere to the glass coverslip was determined by fitting a 2D second-order polynomial to the IRM intensity profile in Figure 52b between the central intensity minimum and the first intensity maximum. The dependence of the normalized IRM intensity on the expected distance of the sphere to the coverslip z₀ was fitted with

$$IRM = \alpha_1 e^{-\alpha_2 z_0} \cos\left(2\pi \frac{z_0}{\alpha_3}\right) + \alpha_4 \,, \tag{31}$$

yielding $\alpha_1 = -0.54$, $\alpha_2 = 0.0036$ nm⁻¹, $\alpha_3 = 188,42$ nm, $\alpha_4 = 0.56$.

For Figure 52d we put the origin of the z-coordinates to the surface of the glass coverslip, to which we referenced all obtained z-positions. In Figure 52e the distance of the localizations to the coverslip z_{SMLM} was correlated with the IRM intensity of the corresponding pixels and overlaid with the fit from Equation (31). The Cramér-Rao lower bounds shown as dashed lines were calculated considering the localizations' brightness, background level, z position and the PSF model including aberrations.

2.4.7 Analysis of DNA nanorulers

DNA nanorulers experiments are described in section 3.2.2. Single molecule signals were localized in 3D and corrected for the field aberrations. Localizations with very low (B < 1500) or very high (B > 15000) photon numbers were filtered out. The localizations were then drift corrected in xy plane by calculating cross correlations using ImageJ plugin ThunderStorm (Ovesný et al. 2014).

To identify the labeled positions on the nanorulers two rounds of clustering were performed with DBSCAN algorithm (Ester et al. 1996). Shortly, DBSCAN is an algorithm for density-based clustering, capable of discovering clusters of different shapes and sizes from a large amount of data containing also noise and outliers. Advantage of DBSCAN is that a total number of clusters does not have to be specified. The algorithm uses two parameters: the minimum number of points minPts clustered together for a region to be considered dense and a distance measure eps. A point p is considered a core point if at least minPts points are within distance eps of it (including p). A point q is reachable from p if point q is within distance eps from core point p. All points which are not core nor reachable are noise points. In the first step, localizations were clustered with eps = 20 nm and minPts = 40, thereby identifying localizations belonging to single nanorulers. In the second step, the localizations belonging to a single nanoruler were further clustered with eps = 10 nm and minPts = 10, thereby identifying the two labeled positions on the nanoruler. The parameters were determined empirically. Only nanorulers with two identified sub clusters were considered for further analysis. Lastly, from the mean position of the localizations per sub-cluster, the length and the angle with the horizontal plane were calculated for every nanoruler.

To analyze the achieved localization precision, the 3D localizations were merged by a tracking algorithm Trackpy into groups (parameters: 100 nm radius and 5 allowed gaps) and a standard deviation in x, y and z direction was calculated from the localizations for each group.

2.4.8 Analysis of NPC

Experiments on nuclear pore complexes are described in section 3.2.3. Single molecule signals were localized in 3D and corrected for field aberrations. The localizations were then drift corrected in xy plane by calculating cross correlations using ImageJ plugin ThunderStorm (Ovesný et al. 2014). The data were then manually searched for single NPCs.

To analyze the achieved localization precision, the 3D localizations were merged by a tracking algorithm Trackpy into groups (parameters: 100 nm radius and 5 allowed gaps) and a standard deviation in x, y and z direction was calculated from the localizations for each group. We additionally calculated the dependence of the x, y and z standard deviations on the average zposition of the localizations within each group.

2.4.9 SLB ligand density

Ligand densities on bilayers were characterized for experiments in section 3.3. Single molecule brightness B was analyzed from SLBs with a low concentration of the fluorescent ligand by fitting the single molecule signals with a 2D Gaussian function using ImageJ plugin ThunderStorm (Ovesný et al. 2014) in a small region of interest (128x128 pixels). Background per pixel bg was estimated from the recording after all fluorescent molecules bleached. To estimate the density of ligands on a densely labeled SLB we measured the average fluorescence intensity per pixel I in the ROI using ImageJ. The ligand density was then calculated as follows:

$$D = \frac{I - bg}{BA},\tag{32}$$

where $A = 0.0215 \,\mu\text{m}^2$ is the pixel area. In the case of sparsely occupied SLBs with distinguishable single molecules, the number of observed molecules was divided by the area of ROI.



2.4.10 Analysis of T cells

SMLM corrections: Single molecule signals from TCR in section 3.3 were localized in 3D and corrected for field aberrations. All z-positions were referenced against z-positions determined from signals observed around the cells, which correspond to traces of fluorescent H57-scFv molecules adsorbed to the glass surface. In order to correct for overcounting artifacts, localizations were merged by a tracking algorithm (Trackpy) (Allan et al. 2021), yielding the average three-dimensional position and the average single molecule brightness. Parameters of Trackpy were the three-dimensional search radius, and the maximally allowed size of gaps within a given trajectory which may occur due to molecular blinking or fitting problems. Both parameters should be chosen sufficiently large to include most blinks originating from the same molecule, and sufficiently small to avoid connecting blinks from different molecules. To identify an appropriate choice of the three-dimensional search radius and the maximally allowed gap size, we analyzed the standard deviation of all determined z-coordinates σ_z . Beyond a search radius of 60 nm and a gap size of 5 we observed a plateau in σ_z (Figure 63a); in the following we hence analyzed all data with a search radius of 60 nm and a gap size of 5. To find out whether the obtained values of σ_z correspond to the underlying surface roughness we simulated 3D-SMLM experiments (Figure 63b), using experimentally derived single molecule blinking statistics and localization precision. For a simulated surface roughness of 26 nm we found high quantitative agreement between our simulations and data recorded on T cells seeded on activating supported lipid bilayers. For the selected values of 60 nm search radius and 5 gaps we overestimated the surface roughness only by 1.5 nm. Finally, localizations were filtered for the single molecule brightness B (500 < B < 4000) in order to avoid fitting of camera noise or of strong signals arising from overlapping molecules.

Correlative SMLM and IRM: In Figure 54c, localizations were plotted versus the IRM intensity I_{IRM} of the corresponding pixels; the localizations with z_{SMLM} < 100 nm were fitted with

$$z_{SMLM} = \frac{\beta_1}{2\pi} \arccos\left(\frac{I_{IRM}}{\beta_2} - \beta_3\right),\tag{33}$$

yielding $\beta_1 = -0.50$, $\beta_2 = 225.69$ nm, $\beta_3 = 0.39$.

The z histogram of the lamellipodium shown in Figure 54b (ii) was fitted with a sum of 2 Gaussian functions with center positions at 68 and 228 nm (Figure 56).

Localization precision: To determine the localization precision for x, y and z direction (Figure 53) we first calculated the standard deviation of localizations from signals occurring in subsequent frames within a three-dimensional distance of 60 nm and a maximum gap size of 5, yielding the single frame localization precision $\sigma_{1,i}$ for molecule i. Merged localizations show an improved localization precision $\sigma_{2,i}=\sigma_{1,i}/\sqrt{N_i}$, with N_i the number of observations per molecule. The overall localization precision is then given by $\sigma = \sqrt{\alpha \cdot \langle \sigma_{1,i}^2 \rangle_i + (1-\alpha) \cdot \langle \sigma_{2,i}^2 \rangle_i}$, where α denotes the fraction of molecules observed only once. CRLBs were calculated from the estimates for each single molecule observation, CRLB_i, accordingly. The histograms in Figure 53 show the weighted sums of the normalized histograms of $\sigma_{1,i}$ and $\sigma_{2,i}$.

Reconstruction of diffraction-limited images: To reconstruct diffraction-limited images from SMLM recordings (Figure 57 ii), localizations were convolved with the PSF model taking into account the single molecule brightness B and the z position. The PSF model was calculated for a focus position at z = 0 and included the aberrations of our optical setup.

TCR microclusters: For specific analysis of TCR microclusters, we ascribed pixels to TCR microclusters based on intensity thresholding of the diffraction limited images of activated T cells (threshold: MC intensity per pixel > 1.5-times mean intensity per pixel of the whole cell) (see Figure 59 for an example). Localizations were assigned either to microcluster pixels (termed "in") or to the complementary pixels (termed "out"). The ratio in/out of the single molecule brightness values was calculated based on the single molecule brightness B. The density ratio was calculated from counting the number of localizations, N, per IN and OUT area.

2.5 **Simulations**

2.5.1 Simulations of overcounting

Simulations were performed to estimate parameters for overcounting correction in section 3.3. To produce a continuous, rough surface we first generated a random 3D surface on a 10 nm grid with a size of 10 x 10 μm² by placing normally distributed z-coordinates on every grid-point; the normal distribution was centered around zero with a standard deviation of 26 nm. Next, a Gaussian smoothing with a standard deviation of 0.5 µm (in x/y) was applied, and the zcoordinates were rescaled to preserve a standard deviation of 26 nm in z. Finally, the resulting surface was shifted along the z-axis so that the lowest point of the surface yielded z=0 nm. Onto this surface, we placed 1000 molecules randomly distributed in the x/y plane. For each molecule a blinking sequence of on- and off-states was generated (total of 20000 frames), using the single molecule blinking statistics determined by analyzing the blinking kinetics of AF647 in underlabeled T cells. We observed a slight z-dependence of the mean on-time $\bar{t}_{on} = k_1 + k_2$. z_{SMLM} , with $k_1 = 1.5$ frames and $k_2 = 0.01$ frames/nm, which was taken into account by including each molecule's z-position; the off-time $\bar{t}_{off} = 5000 frames$ was largely independent of the z-coordinate. Both on- and off-times were assigned using exponential distributions with the corresponding mean values \bar{t}_{on} and \bar{t}_{off} . Localizations were assigned to each molecule's position in the on-periods according to the determined localization errors of 12 nm in x and y direction. In case of localization errors along the z-direction we took into account the decreased excitation along the optical axis upon using TIR excitation, which was determined from sparsely labeled cells; we obtained $\sigma_z = k_3 + k_4 \cdot z_{SMLM}$, with $k_3 = 12 \ nm$ and $k_4 = 0.05$. The final data set was used for merging analysis via Trackpy with the different search radii and gap sizes (see Figure 63b).



Chapter 3: Results and Discussion

3D Single molecule localization microscopy via defocused imaging

This chapter is based on the following publication: Zelger, P., Bodner, L., Velas, L., Schütz, G. J., & Jesacher, A. (2020). Defocused imaging exploits supercritical-angle fluorescence emission for precise axial single molecule localization microscopy. *Biomedical optics express*, 11(2), 775-790.

3.1.1 Introduction

Single molecule localization microscopy (SMLM) is a powerful method for obtaining superresolved images of fluorescent samples with a spatial resolution on the order of <50 nm (Rust, Bates, and Zhuang 2006). This is achieved by temporal separation of the signals from the fluorescent molecules and fitting their positions. Early SMLM experiments focused mainly on localizing the fluorophores in x and y direction, however, with the 3D nature of biological samples it has soon become necessary to provide tools for localization of molecules along the optical axis with a similar precision. Unfortunately, the point spread function (PSF) of the optical microscope is stretched in z-direction, resulting in a poorer localization precision. I discussed several approaches in the 3D SMLM chapter, which have been applied to overcome this problem including multifocal imaging, PSF engineering, intensity or interface sensing methods and interference methods. All these methods have different advantages and disadvantages such as the complexity of the optical path, the achievable localization precision and the z-range.

In a special case, when the region of interest lies within a wavelength of the fluorescence light from the coverslip, alternative information becomes accessible to improve the axial position estimates. One example is the dependence of the fluorescent lifetimes on the distance of the fluorophore from a dielectric or metallic surface (Enderlein and Böhmer 2003). Alternatively, if the fluorophore is in a close vicinity to the coverslip, a part of its non-propagative near field fluorescence turns into propagating waves inside a nearby material with higher refractive index than the solvent. This part of light is called supercritical angle fluorescence (SAF) and its amount shows a strong dependence on the distance between the fluorophore and the coverslip (Ruckstuhl et al. 2000).

SAF has been exploited in order to obtain z-information about the sample by various techniques including scanning confocal microscopy (Ruckstuhl and Verdes 2004), widefield fluorescence microscopy (Axelrod 2001) and STED (Sivankutty et al. 2020). In the context of SMLM, the amount of SAF is typically measured by splitting the detection path into two channels and blocking the SAF contribution in one of them. The ratio of the photon counts in the two channels is then used to estimate the z position of individual fluorophores. This technique has been published simultaneously by two groups who called it either supercritical angle localization microscopy (SALM) (Deschamps, Mund, and Ries 2014) or direct optical nanoscopy with axially localized detection (DONALD) (Bourg et al. 2015).

We show that the effect of SAF can be exploited in a simple defocused imaging which doesn't require emission path splitting and provides localization precision in z-direction that is superior to SALM/DONALD. Our findings are supported by the calculation of the corresponding Cramér-Rao lower bounds (CRLB) and SMLM measurements via dSTORM on a number of different samples.

3.1.2 Method

The SALM/DONALD approach takes advantage of the fact that the SAF and UAF (undercritical angle fluorescence) are spatially separated in the back focal plane (BFP) of the objective. This allows to filter out the contribution of the SAF in one of the imaging channels by placing a circular aperture to a plane conjugated to the BFP. The z-position of the fluorophore can then be estimated from the signal ratio between the two images (Figure 36a).

A different approach needs to be taken in the case of a single channel method. One possibility would be to place a specific phase contrast filter into the BFP of the objective, which would introduce a phase shift of π between the SAF and UAF components. Such phase shift would result in a destructive interference of the SAF and UAF in the center of the PSF whenever a SAF contribution would appear, thus turning the presence of SAF into a visible PSF change on the camera. Interestingly, we found that a similar phase shift between the SAF and UAF in the BFP can be achieved by defocusing the objective less than a wavelength towards the sample. Upon defocusing, the PSF becomes very sensitive to the emitters z-position. Precise z-position can be estimated from fitting a calculated PSF model to the recorded single molecule images using a maximum likelihood estimation. The main advantage of defocused imaging is that only one emission path is needed for a precise z-position estimation, which facilitates its application on a regular wide-field fluorescence microscope. A comparison between the SALM/DONALD and offfocus imaging is shown in Figure 36 panel (a) and (b), respectively.

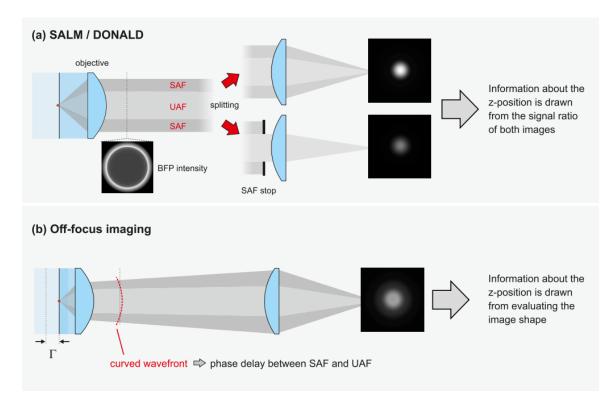


Figure 36: Comparison of SALM/DONALD and Off-focus imaging exploiting the SAF for localization microscopy. (a) SALM/DONALD uses beam splitting of the emission path and SAF stop to block the SAF in one channel. The z-position of the fluorophore is drawn from the signal ratio of both images. (b) Offfocus imaging introduces a phase-shift between the SAF and UAF which results in a PSF highly sensitive to the z-position of the fluorophore. Γ denotes the defocus magnitude. Taken and adapted from (Zelger et al. 2020).

The defocus magnitude Γ is an important parameter in the defocused imaging which influences the localization precision for x, y and z directions. It is defined as the distance over which the objective lens is moved towards the sample, starting from the position where the coverslip surface is in focus. The defocus magnitude is a freely selectable parameter and can be chosen either for a balanced x, y and z localization precision or a particularly good z-performance as discussed in the following chapter.

3.1.3 Precision calculations

In order to find the optimal defocus magnitude Γ we have calculated the Cramér-Rao lower bounds for the 3D localization uncertainties $\sigma_{x,y}$ and σ_z (Chao, Ward, and Ober 2016). The PSF model was based on a vectorial imaging theory (Axelrod 2012). In the calculations we have assumed a sample immersed in an aqueous medium with a refractive index of 1.33, an objective with a NA of 1.7 or 1.49, an ideal detector with no readout and dark noise but including shot noise,

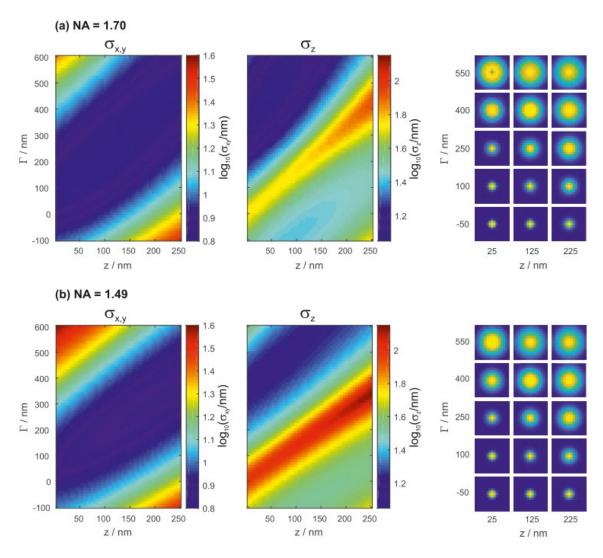


Figure 37: Calculated dependency of the localization precision in x, y and z direction on the defocus magnitude Γ and the z-position of the fluorophore. (a) shows results for NA 1.7 objective, (b) shows results for NA 1.49 objective. PSF images for various combinations of Γ and z positions are shown on the right. Taken and adapted from (Zelger et al. 2020).

an effective pixel size of 115 nm, an emission wavelength of 670 nm and single molecule images with a size of 15x15 pixels. The number of collected photons was set to 2000 and the background level was 100 photons per pixel, rendering realistic experimental conditions. The resulting dependence of the localization uncertainties on the defocus magnitude Γ and the z-position of the fluorophore are shown in Figure 37, panel (a) for the objective with NA 1.7 and panel (b) for the objective with NA 1.49. Images of the PSF are also shown for various combinations of Γ and zposition. From the resulting uncertainty maps it is clear that the best achievable localization precision for the x, y direction can be obtained by matching the defocus magnitude Γ with the zposition of the fluorophore, however, higher values of Γ are necessary to obtain good localization precision in z-direction. For the objective with the NA of 1.7, $\Gamma \approx 500$ nm provides a good compromise for the xyz localization precision. Increasing the Γ slightly beyond 500 nm leads to improving the localization precision in z direction but at the same time decreasing the xy performance due to a large PSF footprint. Similarly, $\Gamma \approx 400$ nm offers a good compromise for the xyz localization precision in the case of NA 1.49 objective.

As the next step we compared the performance of defocused imaging with the SALM/DONALD approach assuming the same experimental conditions as previously and a 1.7 NA objective. It is important to note that in our calculations we define a number of photons collected by the objective and not a number of photons detected by the camera. The difference between these two numbers can be significant, as using the SAF stop in one of the channels of the SALM/DONALD approach blocks up to 25% of the total signal. Similarly for the defocused imaging, in the case of PSF with a large footprint, a portion of photons lands outside of the analyzed 15x15 pixel region and is therefore not detected. Additionally, we propose a new approach based on the DONALD/SALM principle, in which not only the photon numbers but also the PSF shapes in the two channels are analyzed in order to boost the localization precision and denote it as SALM/DONALD+. The results of the calculated localization precisions for defocused imaging with $\Gamma = 500$ nm, the original SALM/DONALD approach and the newly proposed SALM/DONALD+ approach are compared in Figure 38. In the case of xy-precision, all three approaches yield similar performance; the SALM/DONALD(+) approach has a slight advantage for lower z-positions of the fluorophore and off-focus imaging performs better at higher z values (Figure 38a). Regarding the z-precision, the off-focus imaging clearly performs better than the other two approaches up to the z-position of 200 nm (Figure 38b). Moreover, we can see a clear

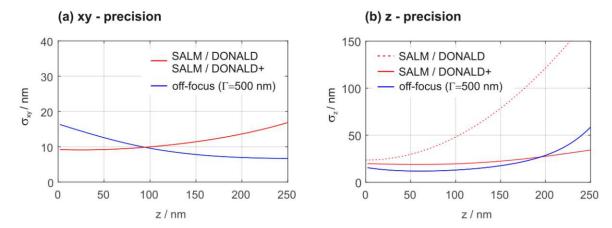


Figure 38: Comparison of xy (a) and z (b) localization precisions between defocused imaging, SALM/DONALD and an improved version SALM/DONALD+. Taken and adapted from (Zelger et al. 2020).

advantage in the additional analysis of the PSF's shape for the SALM/DONALD+ approach as it significantly outperforms the original SALM/DONALD.

3.1.4 Design of the experimental setup

Performing 3D super-resolution imaging on the scale of tens of nanometers requires a robust and stable experimental setup. Within this project we have designed and built a microscopy system based on an Olympus IX73 (Japan) inverted microscope. A scheme of the setup is depicted in Figure 39. To minimize the vibrations of the system, the whole experimental setup was placed on an air damped table (SMART table UT2, Newport, USA). Additionally, all components which could cause vibrations, such as fan cooled lasers and controllers were decoupled from the table. The camera was water-cooled and the internal fan was switched off.

The microscope was equipped with a high NA objective, either a 1.7 NA Olympus objective (NA 1.7 APON100xHOTIRF, Japan) or a 1.46 NA Zeiss objective (alpha-plan apochromat, 1.46 NA, 100x, Germany), to allow for TIRF excitation and collection of supercritical angle fluorescence. With the two different objectives, immersion oils with refractive indices 1.78 (Cargille Labs, USA) or 1.52 (Immersol 518 F, Carl Zeiss, Germany) were used, respectively, matching the refractive index of the used coverslips; the high refractive index coverslip (HIGHINDEX-CG, Olympus, Japan) and the standard coverslip (MENZEL-Gläser Deckgläser 24 x 60 mm #1.5, Thermo Fisher Scientific, USA). While the higher NA of the 1.7 NA objective brings the advantage of better localization precision it requires special immersion oil and coverslips with high refractive indices. We found it to be more practical to use the regular coverslips and immersion oil with the 1.46 NA objective, despite the slightly worse localization precision. The sample was resting on a micro-

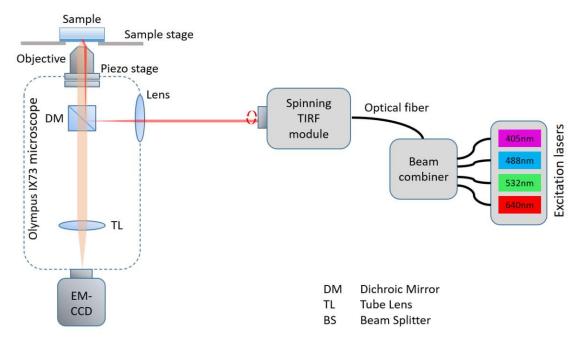


Figure 39: Design of the experimental setup for 3D SMLM via off-focus imaging. Excitation lasers with wavelengths at 405, 488, 532 and 640 nm are coupled into a single optical fiber via beam combiner and directed into a spinning TIRF module. The laser beams are then reflected towards the sample via a dichroic mirror. The sample is illuminated in TIRF by a high NA objective. The fluorescence is collected via the objective and imaged on an EM-CCD camera.

positioning sample stage (MicroStage, Mad City Labs, USA) to allow for precise sample positioning and minimizing the sample drift. Furthermore, the objective was mounted on a piezo stage (P721.SL2, Physik Instrumente, Germany) to allow for defined positioning of the objective along the optical axis in a nanometer range.

The excitation part consisted of an OBIS laser box (Coherent, USA) with four different lasers, 405 nm, 488 nm, 532 nm and 640 nm. The lasers were first coupled into individual optical fibers and eventually combined to a single optical fiber in a beam combiner. The optical fiber was then attached to a spinning TIRF module (iLas2, Visitron Systems, Germany), consisting of collimator lens, beam expanding lenses, alignment mirrors and two galvo mirrors which were placed closely to the conjugated plane with the sample plane. The role of the two galvo mirrors was to create a circular laser pattern in the back focal plane of the objective resulting in a spinning TIRF configuration. The advantage of the spinning TIRF is that the resulting illumination pattern on the sample is more homogeneous and without interference stripes which can occur in TIRF. The collimated excitation laser was then focused into the back focal plane of the objective by a built-in lens. For illumination, the excitation laser was reflected towards the sample via a quad dichroic mirror (Di01-R405/488/532/635, Semrock, USA).

The fluorescence signal collected via the objective passed the quad dichroic mirror and quad emission filter (ZET405/488/532/642m, Chroma, USA) and was focused via a tube lens on the EM-CCD camera (Ixon Ultra, Andor, UK). The exact distance of the camera to the tube lens was adjusted by shining a collimated LED light through the tube lens and finding the focal spot. This step was important to minimize spherical aberrations of the system. The camera was cooled to -60 °C to minimize the dark noise and water cooled to prevent vibrations from fan cooling. Triggering of the lasers and the camera, as well as the adjustment of the TIRF angle and the spinning frequency was controlled via VisiView software (Visitron Systems, Germany).

A critical parameter for off-focus imaging is the defocus magnitude, which influences the localization precision and is the prerequisite for calculating the correct PSF model. Therefore, the defocus magnitude must remain constant during the whole SMLM recording. Defocusing is a common problem during long measurements due to a mechanical drift of the objective or the sample along the optical axis. In order to solve this problem, we have implemented a focus hold system which maintains the distance between the objective and the sample on the scale of few nanometers. Implementation of the focus hold system to our experimental setup is depicted in Figure 40. It is based on the total internal reflection of a 785 nm laser beam (LM9LP, Thor Labs, USA) from the sample coverslip, its collection and detection by a CMOS camera (ac640-750um, Basler, Germany). The separation of the 785 nm laser from the fluorescence is achieved via a dichroic mirror (HC BS 750 SP, Semrock, USA). In such a configuration, any change in the distance between the objective and the sample results in a shift of the reflected beam which is detected on the camera. In order to keep the distance between the sample and the objective constant, changes in the position of the reflected beam are detected and used for adjustment of the piezo stage via a feedback loop. Measurement of the beam position on the camera as well as the feedback loop are operated with LabView software.

Additionally, we have equipped the experimental setup with a module allowing for interference reflection microscopy (IRM), shown in Figure 41. This is important to allow for direct comparison of the acquired 3D SMLM images with IRM images on the same cells and within a

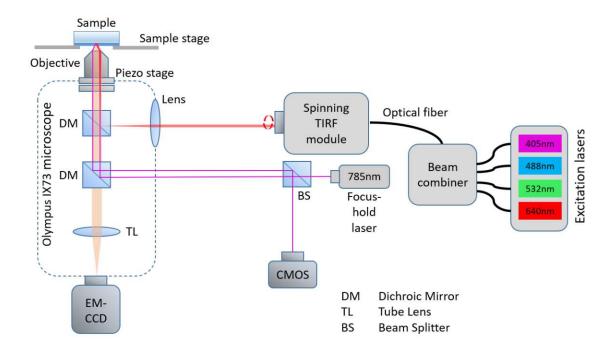


Figure 40: Addition of a focus hold system for stabilization of z-drift. A 785 nm laser beam is reflected from a secondary dichroic mirror towards the sample. The back reflection from TIR is collected by the objective and imaged onto a secondary CMOS camera. Changes in the distance between the objective and the sample result in shifts of the reflected beam which are detected by the camera. In order to maintain a constant distance between the sample and the objective, the objective is moved along the optical axis by a piezo stage.

short time frame. The IRM module consisted of 455 nm LED (Thor Labs, USA) illumination which was focused on a plane conjugated with the back focal plane of the objective. In this plane a circular aperture was placed for the adjustment of the illumination numerical aperture. The illumination beam was then collimated and coupled into the excitation pathway via a dichroic mirror (zt 473 RDCXT, AHF, Germany). The illumination beam was then focused into the back focal plane of the objective and reflected via the quad dichroic mirror towards the sample. An important parameter of the quad dichroic mirror is that it partially reflects the LED light towards the sample but also transmits the reflected light from the sample towards the camera. The sample was illuminated via the objective and the reflected light was imaged on the EM-CCD camera.



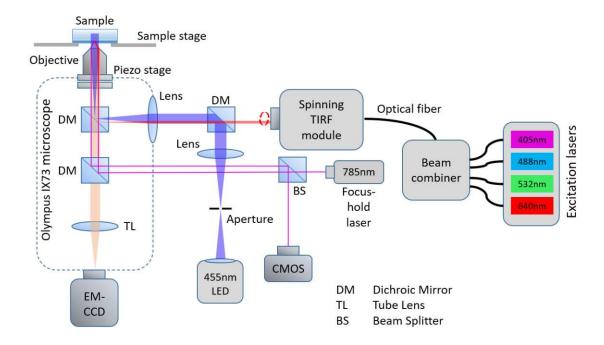


Figure 41: Addition of Interference reflection microscopy to the experimental setup. The light beam from the 455 nm LED is focused into a plane conjugated with the back focal plane of the objective. An aperture at this place is used to control the illumination numerical aperture. The light beam is collimated and coupled into the excitation pathway by a dichroic mirror. The light beam is then partially reflected towards the sample and the reflected beam is imaged on the EM-CCD camera.

3.1.5 Stability

Acquisition of the super-resolved images via SMLM takes time on the order of >10 minutes. Any drift of the sample, or of the experimental setup within this time frame leads to smeared images. Especially in 3D SMLM, drift along all three axes is problematic. In order to assess the stability of our experimental setup we have tracked 100 nm fluorescent beads over a period of 1 hour, which represents the higher end of the duration of the 3D SMLM data acquisition. To limit the bleaching of the fluorescence beads over such a long time, the sample was imaged with a reduced frame rate of 1 fps. Also, the sample was illuminated via EPI illumination and not in TIR configuration, as this would lead to biased bleaching of fluorophores closer to the coverslip. For the first 30 minutes, the beads were tracked with an active focus hold system, which was then turned off. The drift was calculated for every bead in respect to its initial position and then averaged over all beads. The result is shown in Figure 42. In this measurement, the experimental system has shown a substantial and continuous drift along the x- and y-axis with average speeds of 2.5 and 1.4 nm/min, respectively. In addition to the long-term drift of the system we could also observe fluctuation on short time scales. Regarding the z axis, no z drift was observed while the focus hold system was in operation. After the focus hold system was turned off, the system continuously drifted along the z axis with an average speed of 1.4 nm/min, also showing fluctuations in the z position. No substantial change in the x- and y-drift was observed after the focus hold system was turned off.

This measurement clearly demonstrates the need for the drift correction in SMLM experiments. While the z-drift could be successfully prevented by the active focus-hold system,

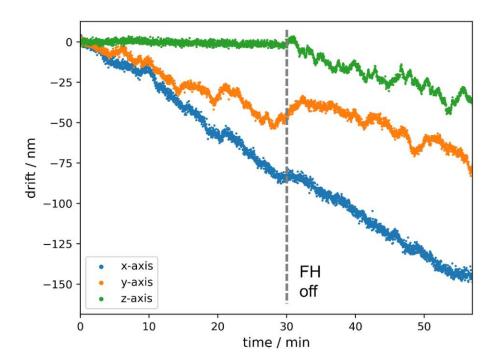


Figure 42: Drift measurement of fluorescent beads along the x, y and z axis. The focus hold (FH) system was switched off after 30 minutes. Drift in x and y direction was continuous and showed fluctuations on shorter time scales. The active focus hold system prevented the drift in z direction in the first 30 minutes. After the focus hold system was turned off, the drift along the z-axis was continuous.

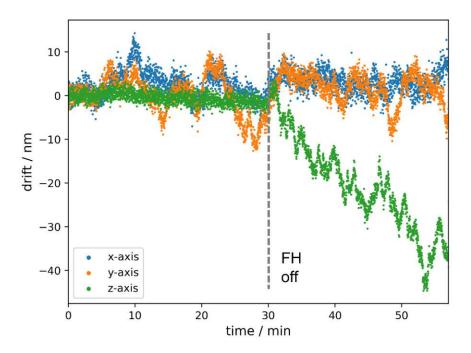


Figure 43: Drift of the fluorescent beads after application of an x/y cross-corelative drift correction. The long term x/y drift was corrected, but fluctuations up to 10 nm in amplitude remained.



the x, y-drift remained problematic. A number of solutions to this problem is available which involve post-processing of the SMLM data, including cross-correlative drift correction and fiducial markers (Geisler et al. 2012). Figure 43 shows an application of a 2D cross-correlative drift correction to our measurement using the ThunderStrom plugin of Image (Ovesný et al. 2014). Clearly, the long term x, y drift was removed, however, the fluctuations on the order of few nanometers remained uncorrected.

It is important to note that the drift of the experimental system is hardly predictable and not reproducible. It depends on multiple factors such as sample mounting, previous movement of the stage, temperature equilibrium of the setup, air flow in the laboratory and external factors such as vibrations within the building. The aim of this measurement was to show the importance of the active focus hold system and the application of post-processing drift correction methods.

3.1.6 Aberrations

In order to achieve optimal localization precision in 3D SMLM, an accurate PSF model needs to be fitted to the recorded SM signals. We have chosen to employ the PSF model based on a vectorial imaging theory (Axelrod 2012). However, optical systems often suffer from aberrations such as spherical aberrations, coma and astigmatism which arise either from non-ideal optical components or their misalignment and distort the aberration-free PSF. Therefore, we have decided to refine the PSF model by taking phase aberrations in the objective pupil into account.

NOLL ZERNIKE TERM EXPANSION ABERRATION RADIAL PISTON Polynomial ORDER ordering number WVF 0 map TILT VALLEY HORIZONTAL VERTICAL 1 PRIMARY ASTIGMATISM DEFOCUS 2 cosine OBLIQUE VERTICAL 2 PRIMARY COMA TREFOIL 5 VERTICA sine 3 SECONDARY ASTIGMATISM QUADRAFOII 10 cosine VERTICAL VERTICAL OBLIQUE OBLIQUE SECONDARY SECONDARY COMA PENTAFOIL TREFOIL 12 cosine cosine 19 sir 20 cosine 17 sine 5 2 3 ANGULAR MERIDIONAL FREQUENCY

Figure 44: Noll Zernike term expansion for characterization of optical aberrations in the back focal plane of the objective. The colormap denotes the phase profile in the objective pupil for a given Zernike mode. Taken and adapted from (Sacek 2006).



Aberrations in the objective pupil can be expressed in a Zernike mode basis using Noll coefficients (Noll 1976) as shown in Figure 44. We have used the coefficients ranging from 2 (tilt) to 37 (3rd order spherical) plus the 4th order spherical mode:

$$\phi = \sum_{i=2}^{37} a_i Z_i + a_{56} Z_{56},\tag{34}$$

where a_i represent the magnitudes of the Zernike modes Z_i .

We have implemented a phase retrieval method related to previous work on this topic (Quirin, Pavani, and Piestun 2012; Hanser et al. 2004). In the first step, a z-stack of 100 nm fluorescent bead was imaged, ranging from -1.6 μm to 1.6 μm with 200 nm steps, yielding a stack I_{exp} consisting of 17 images. The laser intensity was increased for the out of focus images to maintain good signal to noise ratio. The images were cropped to 51x51 pixels and constant background value was subtracted. Next, a matching image stack I_{sim} was simulated using a vectorial model (Axelrod 2012). The simulated point response was convolved with the shape of the bead to closer match the experimental images. The objective transmission function was also taken into account as described in Methods, section 2.4.2 (Zelger et al. 2018). The phase retrieval algorithm then fitted the simulated stack I_{sim} to the experimental stack I_{exp} by varying the Zernike mode coefficients and the transmission function of the objective.

The experimentally measured, fitted and aberration-free stacks are shown in Figure 45, panel (a). From their comparison it is clear that aberrations were present in our imaging path. Probably most apparent is the presence of slight astigmatism as the PSF appears elongated along the vertical axis at -1.6 μm and along the horizontal axis at +1.6 μm. Further Zernike coefficients from the phase retrieval are shown in Figure 45b. Apparently, the Zernike modes Z_6 (astigmatism), Z_{11} (1st order spherical), Z_{22} (2nd order spherical), Z_{37} (3rd order spherical), Z_{56} (4th order spherical) are dominant and non-negligible. Retrieved phase and transmission are shown in Figure 45c. We have calculated the CRLB for the retrieved PSF and compared it with the aberration-free PSF in Figure 46. Clearly the aberration-free PSF performs better in all three dimensions. However, the aberrated-PSF shows an advantage for the z-precision in the range above 200 nm and the astigmatism is responsible for slightly worse performance along the ydirection.

Aberrations can slightly vary over the field of view due to imperfections in the optical pathway, the presence of optical elements and misalignments. Our PSF model is, however, measured only at the center of the field of view and therefore does not account for these deviations. Presence of field aberrations can lead to biased estimates of z positions. Especially, astigmatism and coma are the dominant field aberrations when imaging away from the center of the objective's field of view. Furthermore, slight tilt of the sample or the camera can result in a somewhat different defocus magnitude over the field of view. In order to determine the z position bias over the field of view, we have imaged a fluorescently labeled planar supported lipid bilayer as a sample with a known ground truth. In more detail, a glass coverslip was coated with a gel phase SLB consisting of 98% DPPC and 2% DGS-NTA, which was functionalized via His-tag binding with AF647 labeled pMHC. Hence, the z distance of the fluorophores to the glass coverslip is constant over the whole sample. The resulting image is shown in Figure 47a with color coded z-position estimates. The localizations clearly show a tilt in z-direction, starting at 20 nm at the top of the image and ending at 120 nm at the bottom of the image. We assume that this behavior

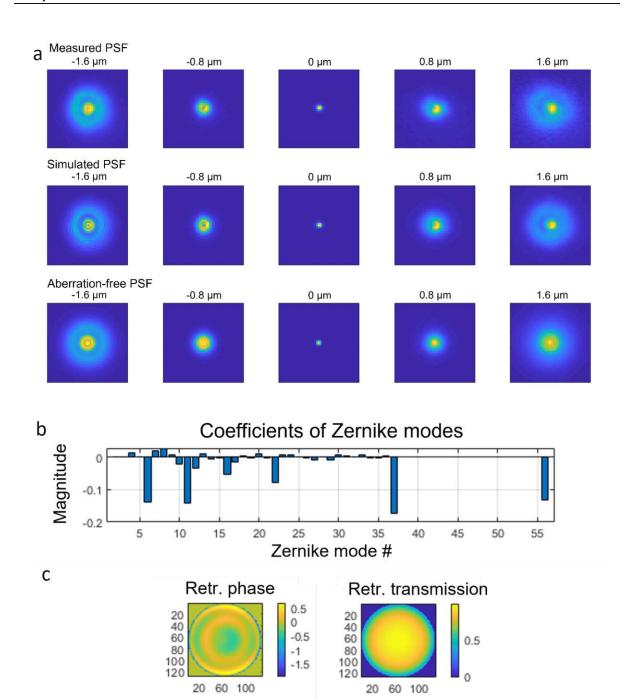


Figure 45: Characterization of the aberrations of the experimental setup. Comparison of the experimentally measured PSF of a fluorescent bead, the fitted simulated PSF and the aberration-free PSF (a). A z-stack of 5 images is shown ranging from -1.6 μm to +1.6 μm. Retrieved coefficients of Zernike modes (b). Retrieved phase profile in the objective pupil and retrieved transmission of the objective (c).

was caused by a joint effect of field aberrations and a slight tilt of the sample, the camera or the objective with respect to the optical axis. In order to correct for this field curvature, we fitted a 1st order polynomial surface to the data and subtracted it to achieve a flat z-distance over the field of view, shown in Figure 47b. Obviously, correction of the field curvature is critical for accurate evaluation of 3D SMLM data. We recommend correcting the data by recording a calibration



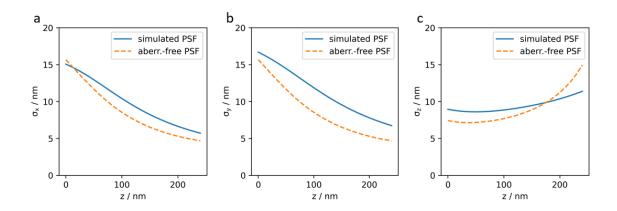


Figure 46: Comparison of the achievable localization precisions for the simulated PSF retrieved from the measured data and the aberration-free PSF. Z-position dependence of the localization precision based on the CRLB calculation for x (a), y (b) and z (c) direction are shown. The simulated PSF shows slightly worse precision than the aberration-free PSF for all three directions.

sample with a known ground truth as was demonstrated here or use the localizations of fluorophores attached to the coverslip within the sample of interest if possible.

The overall z-offset in the SMLM data in Figure 47a is largely due to a not precisely known value of the defocus magnitude Γ with which the experiment was carried out because its accuracy depends on the ability of the experimenter to focus on the surface of the glass coverslip in order to define z = 0. Manual focusing usually brings an error on the scale of 100 nm. However, systematic errors in the defocus magnitude cause to a very good approximation only an axial shift of the SMLM data, which is tolerable for most applications (Zelger et al. 2021). In applications, where an accurate distance from the coverslip is desired, localizations of molecules attached to the glass coverslip can be used to set the z = 0.

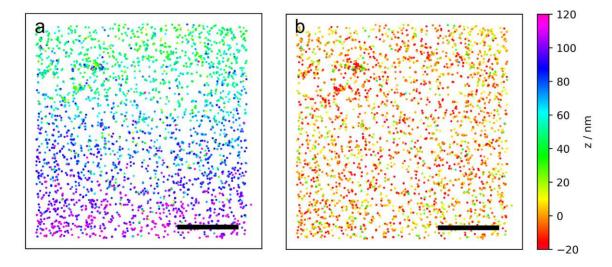


Figure 47: Correction of z-bias caused by field aberrations. Uncorrected 3D SMLM image of fluorescently labeled proteins attached to a supported lipid bilayer (a). 3D SMLM image corrected by subtracting a fitted surface to the original data (b). Scale bar 5 μm

Proof of principle measurements 3.2

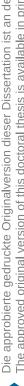
In order to test the performance of defocused imaging and its potential biases I performed a number of 3D SMLM experiments on samples with a known ground truth. These experiments included a glass sphere labeled with fluorescent dyes on the surface, which has previously been proposed as a calibration sample for 3D SMLM (Cabriel et al. 2018), DNA-origami nanorulers with a defined spacing between two labelled positions (Schmied et al. 2013) and nuclear pore complexes which provide a well-known structure within a cellular environment (Thevathasan et al. 2019).

3.2.1 Glass sphere

Glass spheres represent a suitable calibration sample for 3D SMLM, as the distance z_0 of its surface from the coverslip can be easily calculated as a function of the distance r_0 from the contact point between the sphere and the coverslip (Figure 48 panel a), yielding

$$z_0 = R - \sqrt{R^2 - r_0^2} \,, \tag{35}$$

where *R* is the radius of the sphere. For our experiment, we have chosen a sphere with a radius R=1 mm, as it covers z distances up to 200 nm for r_0 up to 20 μ m. The sphere was incubated with BSA-biotin and labeled with streptavidin-AF647. The glass coverslip was additionally coated with unlabeled streptavidin in order to minimize Brownian motion of the glass sphere in the buffer. Imaging via dSTORM was performed in classical epi-illumination, since TIR excitation led to coupling of the evanescent field into the glass sphere and caused a high background signal. High background signals were observed also in epi-illumination as fluorophores on the whole glass sphere surface were excited. Additionally, the vicinity of the sphere's surface to the fluorophores captures a portion of the near field fluorescence which - in consequence - is not collected by the objective. Even though the high background level and dimmer fluorescence signal compromitted the achievable localization precision, this experiment is useful to evaluate the possible z distance biases coming from unaccounted aberrations or refractive index mismatch between the buffer and the glass. The acquired localizations corrected for the field curvature are shown in Figure 48b. A sphere surface was fitted to the localizations in order to find the contact point $r_0 = 0$ and to identify the set-point z = 0. We have plotted all z-positions over the distance r_0 , which clearly follows the calculated sphere surface z_0 (Figure 48c). We have additionally binned the localizations along r_0 with a bin size of 100 nm and calculated their mean z position to visualize the agreement of the experimental result with the ground truth. The measurement reveals no strong bias effects in the z direction. Figure 48d shows the acquired localization precision σ for x, y and z direction in this experiment. The localization precision was calculated as the standard deviation of localizations which appeared in subsequent frames within a radius of 200 nm. The mean localization precisions are 23, 24 and 34 nm for x, y and z direction, respectively. The slight inequality of x and y localization precisions comes from the astigmatism of the PSF.



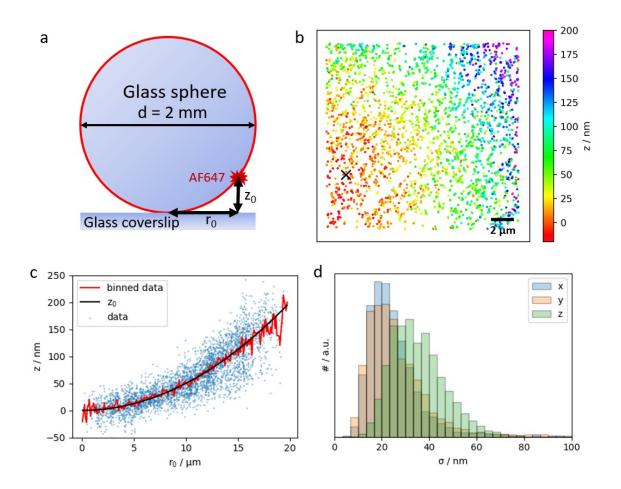


Figure 48: 3D SMLM on a glass sphere. The glass sphere with d=2mm was coated with AF647 and imaged via dSTORM (a). The distance of the sphere's surface z_0 to the coverslip is known due to the known sphere's shape. Panel (b) shows the 3D localization map. The contact point of the sphere with the coverslip is indicated with a cross. Panel (c) shows the z position of the single molecule localizations with respect to their distance to the sphere's contact point r_0 . The black line indicates the ground truth and the red line shows the mean z position of binned localization data along r_0 . Panel (d) shows a histogram of the measured localization precision for x, y and z direction with the mean values of 23, 24 and 34 nm, respectively.

3.2.2 DNA origami nanorulers

To test the limits of our method we have imaged a DNA origami sample. In our case, we used DNA origami nanorulers with a rod-like shape, which contain two rings of ssDNA docking strands on both ends of the rod separated by 30 nm. One end of the nanorulers was attached to the coverslip while the other end was freely oriented in space, therefore covering all possible z positions between 0 to 30 nm. This sample is therefore well suited to study the resolution capabilities of our method in all three dimensions. The docking strands allow for transient binding of ssDNA imaging strands conjugated to ATTO655, which freely diffuse in the sample's buffer. We used DNA-PAINT for acquisition of the super-resolution data, where the dye blinking kinetics is defined by the base pairing of the imaging and docking strand. We imaged the sample in TIRFM



configuration as this led to a lower fluorescent background from the freely diffusing imaging strands. In total, 20000 frames were acquired with an illumination time of 100 ms.

The results are shown in Figure 49. Panel (a) shows a schematic of DNA nanorulers attached to a coverslip with length L_{NR} and angle θ_{NR} and two labelled positions. To make the search for the nanorulers more effective we used density based clustering algorithm DBscan (Ester et al. 1996). The algorithm uses two parameters: the minimum number of points minPts clustered together for a region to be considered dense and a distance measure eps. A point p is considered a core point if at least *minPts* points are within distance *eps* of it (including *p*). A point q is reachable from p if point q is within distance eps from core point p. Core and reachable points are considered part of the cluster and all points which are not core nor reachable are noise points. The DBscan was applied on our data in two steps. The first step aimed at identifying all nanorulers. For this, we clustered the 3D localization data with eps = 20 nm and minPts = 40localizations, yielding 296 clusters in the field of view. The second step aimed at finding the two ends of the nanorulers. Here, we performed a secondary clustering on the previously clustered data with eps = 10 nm and minPts = 10 localizations. This has resulted in 1 or more subclusters for every primary cluster. For further analysis, we considered only those localizations which gave rise to 2 subclusters, yielding 46 nanorulers in the field of view.

The localizations belonging to the identified nanorulers are shown in Figure 49b. Panel (c) shows exemplary images of two distinct nanorulers, with lengths 29 and 33 nm and tilt angles 86° and 31°, and the two subclusters in red and blue color. Next, we have plotted the length versus angle for all resolved nanorulers in Figure 49d, with the red line indicating the distance between the two imaged positions as specified by the manufacturer. Clearly the measured distances agree well with the ground truth, yielding the mean nanoruler length of 32.6 nm and a standard deviation of 6.1 nm. The distribution of angles appears to be biased towards small angles, despite the manufacturer's prediction of equally distributed angles of nanorulers in the sample. This has two possible explanations. First, unspecific binding of the imaging strands to the coverslip surface can result in localization clusters that can be misinterpreted as nanorulers, adding to the portion of nanorulers with angles close to 0. Secondly, due to a slightly poorer localization precision in z direction of 11.2 nm in comparison to x and y direction with 7.4 and 6.6 nm (Figure 49e), it might be more difficult for the clustering algorithm to resolve the upright standing nanorulers as two sub-clusters, thereby reducing the number of nanorulers with higher angles.

In conclusion, defocused imaging performed very well in resolving DNA origami nanorulers structures as small as 30 nm oriented freely along all three dimensions. The method benefited from a number of advantages in this experiment. Firstly, the position of the fluorophores on the DNA origami is within a range of 30 nm from the coverslip, boosting the sensitivity of the method due to high contribution of the SAF component. Secondly, the background of the sample was relatively low, especially when using TIRF microscopy. Thirdly, the DNA-PAINT method allows to localize the same position on the nanoruler multiple times due to constant rebinding of fresh imaging strands without the problem of photobleaching.

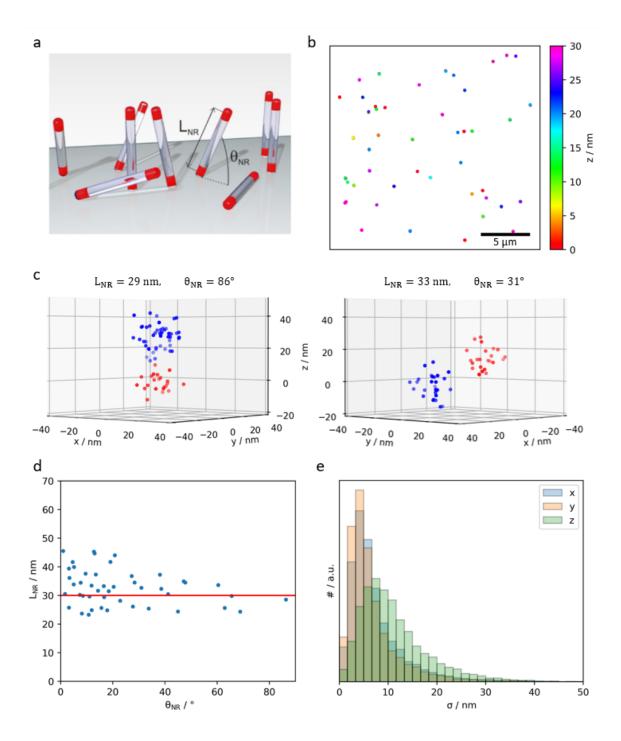


Figure 49: 3D SMLM on 30 nm DNA origami nanorulers. A sketch of DNA origami nanorulers with two labeled positions (a). L_{NR} denotes the nanoruler's length and θ_{NR} its angle with respect to the coverslip. Panel (b) shows filtered localizations belonging to the resolved nanorulers. Panel (c) shows two exemplary images of nanorulers with 29 and 33 nm length and an angle of 86 and 31°. The blue and red color denote two different subclusters in the localization data corresponding to the two labeled positions on the nanoruler. Panel (d) shows the length versus angle dependence for the resolved nanorulers. Red line indicates the ground truth. Panel (e) shows a histogram of the measured localization precision for x, y and z direction with the means of 7.4, 6.6 and 11.2 nm, respectively.

3.2.3 Nuclear pore complex

Several biologically relevant control samples have been used to test and benchmark the quality of different super-resolution imaging techniques, including histones (Betzig et al. 2006), mitochondria (Huang, Jones, et al. 2008), microtubules (Huang, Wang, et al. 2008) and nuclear pore complexes (Thevathasan et al. 2019). An ideal reference sample for 3D super-resolution microscopy should fulfill the following criteria: it is abundant in cells, has a well-preserved structure which features distances resolvable by the technique, and spans all three dimensions. Nuclear pore complexes (NPCs) fulfill all these criteria. They are abundantly present on the nuclear membrane of cells fulfilling the role of selective transporters of macromolecules. The structure of the NPCs has been solved by electron microscopy (Von Appen et al. 2015). NPCs are made of around 30 different proteins providing a great variety for fluorescent labelling. One of the commonly labelled proteins is a nucleoporin Nup96, which is present in 32 copies per NPC, forming two concentric rings on the cytoplasmic and nucleoplasmic side with a diameter of 107 nm and a separation of 50 nm. Each ring consists of 8 corners separated by 42 nm and the two rings are registered, conserving the 8-fold symmetry of the whole structure. Each corner is formed by two copies of Nup96 with a separation of 12 nm (Figure 50a).

High labeling efficiency is a prerequisite to successful imaging of NPCs. We have used a cell line where the nucleoporin Nup96 was endogenously tagged with SNAP-tag (Thevathasan et al. 2019). Cells were cultured in the imaging chambers for 2 days, fixed and labeled with AF647. The lower side of the nuclear membrane was sufficiently close to the coverslip, allowing for TIRF microscopy. The sample was imaged via dSTORM. The resulting 3D localization map is shown in Figure 50b. Hundreds of NPCs appeared in a 10x10 µm field of view ranging from 50 to 300 nm in z position along the surface of the nuclear membrane. We have selected two regions of interest, region (i) with NPCs located at distance >250 nm from the coverslip surface, and region (ii) with NPCs located at a distance <150 nm from the coverslip surface.

Panel (c) shows the region (i) with well resolved ring structures of the NPCs. Within the region, we have selected a single NPC where the 8-fold symmetry can be clearly seen and the localizations form a ring with a diameter of 107 nm, indicated with the red circle. However, the z projection of this NPC does not show the two rings separated by 50 nm. The histogram of z positions is shown in Figure 50d. The observed characteristic was similar for all NPCs within this region. Region (ii) is shown in Figure 50e with NPCs clearly showing a ring structure. In contrast to the region (i), the 8-fold symmetry of the NPC cannot be resolved anymore. On the other side, the z projection of the selected NPC shows two distinct planes separated by 50 nm, as shown also in the histogram in Figure 50f. Similar characteristic was also observed for other NPCs within region (ii).

This phenomenon can be explained by differences in the achieved localization precision. We have analyzed the standard deviation of localizations which appeared in subsequent frames within 100 nm radius. Histograms of these standard deviations are shown in Figure 51a, with mean values of 8.4, 8.8 and 10.9 nm for x, y and z direction, respectively. Additionally, we have plotted the standard deviation of the repeating localizations versus their mean z position in Figure 50b. Interestingly, the localization precision in x and y is worse for molecules close to the coverslip due to the large PSF footprint and improves with the higher z position as the PSF footprint is getting smaller. The localization precision in z shows an opposite trend with the best localization precision close to the coverslip, as the SAF component is then largest. Furthermore,

the data agree with the theoretically calculated localization precisions based on the calculation of CRLB.

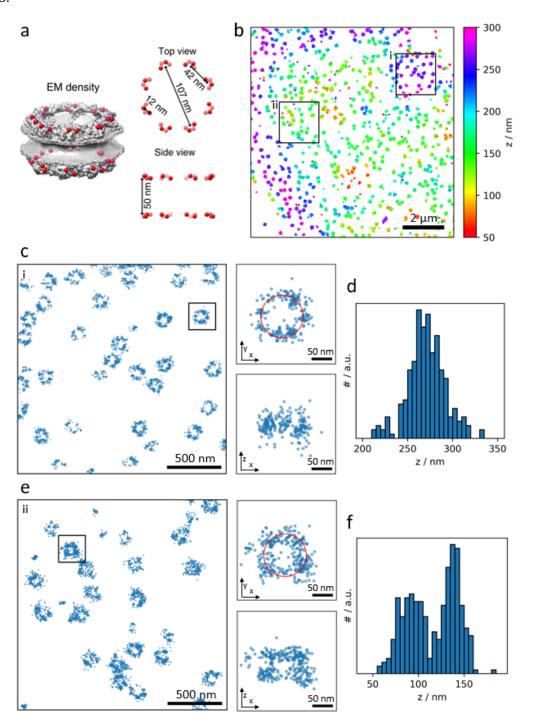


Figure 50: 3D SMLM on nuclear pore complexes. Nup96 protein was labeled with AF647 and imaged with dSTORM via defocused imaging. Panel (a) shows the NPC structure based on electron microscopy with C termini of Nup96 indicated in red. Panel (b) shows a 3D localization map of a 10x10 μm cell nucleus region with two selected regions (i) and (ii). Panel (c) shows the region (i) with well resolved NPCs in the x/y plane. (d) shows a histogram of z positions from the selected NPC. Panel (e) shows the region (ii) with well resolved NPCs in z direction. (f) shows a histogram of z positions from the selected NPC. Panel (a) taken and adapted from (Thevathasan et al. 2019)

From the analysis of the z dependency of the localization precision it is clear that NPCs located close to the coverslip show a localization precision of around 13 nm in x and y and 9 nm in z direction. This allows to resolve the two planes of the NPC but not the 8 corners. NPCs located further away from the coverslip achieve a localization precision of around 6 nm in x and y and 15 nm in z direction. This allows to resolve the 8 corners of the NPC but not the two planes.

In summary, the defocused imaging has succeeded in resolving the structure of the NPC, visualizing the ring shape with a diameter of 107 nm and the two planes of the NPC with a separation of 50 nm. However, we didn't observe NPCs with good resolution simultaneously in all three dimensions. This is due to the dependence of the localization precision on the z position of the NPC. The desired localization precision for resolving the NPC structure would be around 6 nm for x and y direction and 9 nm for z direction. This could probably be achieved by further optimization of the imaging parameters and increase of the labeling efficiency.

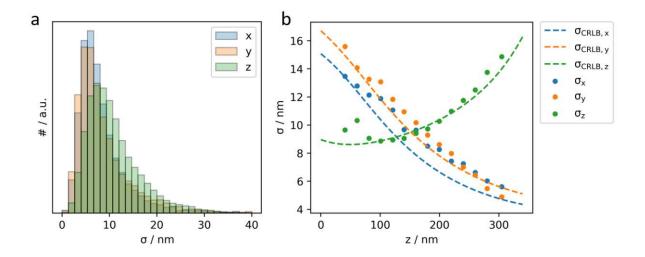


Figure 51: Histogram of localization precision in x, y and z direction (a). Panel (b) shows the dependence of the localization precision on the z position of the fluorophores. Points represent the experimentally measured localization precisions; the dashed lines represent the calculated CRLBs for the corresponding signals and background.

3D SMLM of the Immunological synapse 3.3

This chapter is based on the following publication: <u>Velas, L.</u>, Brameshuber, M., Huppa, J. B., Kurz, E., Dustin, M. L., Zelger, P., Jesacher, A., & Schütz, G. J. (2021). Three-Dimensional Single Molecule Localization Microscopy Reveals the Topography of the Immunological Synapse at Isotropic Precision below 15 nm. *Nano letters*, 21(21), 9247-9255

3.3.1 Introduction

Understanding the topography of cellular interfaces is central for addressing many cell biological questions. The distance between the two juxtaposing cell surfaces not only regulates the affinity of protein-protein trans-interactions (Hu, Lipowsky, and Weikl 2013; Dustin et al. 1997), but the extension of the intercellular cleft also affects the spatial distribution of membrane proteins with differently-sized ectodomains (Cartwright, Griggs, and Davis 2014). A prominent example is the size-exclusion of the large phosphatase CD45 upon contact formation between a T cell and an antigen-presenting cell (APC), which is suspected to represent an important regulatory mechanism for the phosphorylation of the T cell receptor (TCR) (Davis and van der Merwe 2006); according to this model, shifting the balance between Lck-mediated phosphorylation and CD45mediated dephosphorylation induces downstream signaling.

A common way to study antigen-specific T cell activation involves the use of functionalized glass-supported lipid bilayers (SLBs) as surrogates of APCs (Grakoui et al. 1999; Huppa, Axmann, Mörtelmaier, et al. 2010; Groves and Dustin 2003). This experimental design has several advantages when it comes to the application of high-resolution microscopy techniques, while still preserving the essential hallmarks of T cell signaling, including the formation of an immunological synapse, the recruitment of the kinase ZAP-70 and other downstream signaling effectors, the increase in intracellular calcium and the release of cytokines.

First, interfacing cells with a glass coverslip further allows for exploiting the interference of light reflected from the glass-water interface and light reflected from the cell membrane for imaging purposes (Curtis 1964; Limozin and Sengupta 2009). This technique, termed interference reflection microscopy (IRM), yields high precision information on the separation of the cell surface from the surface of the glass coverslip, eventually limited only by the signal-tonoise ratio of the data and by the knowledge of the interference model (Limozin and Sengupta 2009). IRM has been frequently applied to qualitatively assess the homogeneity of T cell adhesion to activating or inert surfaces (Smith et al. 2008; Grakoui et al. 1999; Balagopalan et al. 2011; Cai et al. 2017), often yielding patches of close contact next to areas of substantial elevation of the T cell surface. Quantitative interpretation of the data, however, is often hampered by unknowns of the interference model (Limozin and Sengupta 2009). For example, tilted membranes or the presence of second or third order interferences are difficult to account for. In addition, multiple reflections from different layers of varying refractive index induce phase shifts in the IRM intensity profiles, thereby impeding absolute distance measurements. In fact, protein ectodomains and the glycocalyx contribute to the change in refractive index between the aqueous environment and the cell, rendering the plane of reflection rather poorly-defined. Finally, IRM images are of diffraction-limited spatial resolution, and thereby yield averages of the interference contrast over a few 100 nm. Fluctuations at smaller scales would hence be averaged out.

As a second advantage of hybrid synapses, they facilitate the application of total internal reflection (TIR) excitation to accentuate the signal of dyes proximal to the glass surface over intracellular background (Axelrod, Burghardt, and Thompson 1984). Using TIR excitation, researchers discovered for example the formation of TCR microclusters upon T cell activation (Hashimoto-Tane and Saito 2016; Yokosuka et al. 2005; Varma et al. 2006).

A third advantage relates to the use of single molecule localization microscopy (SMLM) for studying the organization of signaling molecules in the course of T cell activation (Rossy et al. 2013; Pageon et al. 2016; Rossboth et al. 2018; Simoncelli et al. 2020; Jung et al. 2016; Jung et al. 2021). SMLM achieves superior spatial resolution by precisely localizing well separated single molecule signals that can be obtained from blinking chromophores (Sauer and Heilemann 2017). While a two-dimensional localization precision below 20 nm was frequently reported, it is difficult to achieve similar precision along the optical axis (Hajj et al. 2014). In this context, the presence of the glass coverslip in the vicinity of the fluorophores of interest allows for using the supercritical angle fluorescence as a parameter for determining the distance between the dye molecule and the glass surface (Oheim, Salomon, and Brunstein 2020; Bourg et al. 2015). We have demonstrated that, when combined with defocused imaging, supercritical angle threedimensional SMLM (3D SMLM) achieves isotropic localization precision down to ~10 nm in all three dimensions (Zelger et al. 2020).

Here, we used 3D SMLM based on supercritical angle microscopy to study the topography of the immunological synapse formed between primary murine CD4+ T cells and functionalized SLBs at isotropic localization precision below 15 nm. The obtained TCR localization maps were correlated with IRM images of the same synapse, thereby allowing not only cross-validation of the two approaches, but also the identification of artifacts inherent to IRM images. From the TCR z-coordinates we quantified the roughness of the T cell surface within the synapse, as well as its separation from the SLB: Both for activating and non-activating conditions we observed multiple TCR-proximal spots of close contact, which would qualify for CD45 exclusion. We finally quantitatively compared 3D-SMLM images with diffraction-limited TIR fluorescence microscopy of T cell synapses to disentangle different contributions to the appearance of TCR microclusters.

Correlative 3D SMLM and Interference Reflection Microscopy

In order to evaluate the correlation between 3D SMLM and IRM data we used a system with known separation of the detected single dye molecules from the glass surface. We opted for an AlexaF647-coated glass sphere of 2 mm diameter adhered to a glass coverslip, which yielded zdistances of up to 200 nm within the field of view of 22 x 22 µm², depicted in Figure 52a. Figure 52b shows an IRM image recorded next to the contact point between the sphere and the glass surface. Concentric interference fringes are clearly visible. When plotting the recorded IRM intensity values versus the distance of the according pixels from the glass surface, z_0 , we observed the characteristic cosine-dependence (Figure 52c). In this case, three branches of the IRM intensity can be distinguished, corresponding to different orders of the interference pattern. The first branch covers z_{SMLM} values up to 90 nm, the second 90-180 nm, and the third values above 180 nm. A slight decrease in amplitude and wavelength of the recorded IRM curve is noted for increasing IRM interference orders, which is a consequence of reflections on the curved surface (Limozin and Sengupta 2009). In Figure 52b we also included the recorded 3D SMLM data, with the color-code indicating the calculated displacement from the glass surface, z_{SMLM} . When plotted



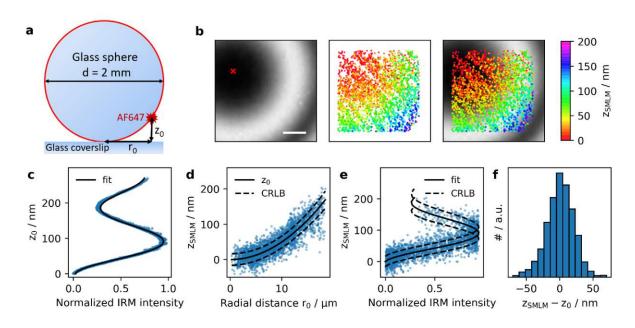


Figure 52: Control experiment on a fluorescently labeled glass sphere. A glass sphere of 2 mm diameter was labeled with BSA-Biotin-Streptavidin-AF647. Based on the known size of the sphere, the distance of the AF647 to the coverslip z₀ was calculated from the measured radial distance r₀ from the contact point of the sphere with the coverslip (a). (b) IRM and SMLM images were recorded next to the contact point of the sphere with the coverslip (red cross). (c) We plotted the z_0 corresponding to the center of the respective pixel against the normalized IRM intensity and fitted with Eq. (31). (d) The measured distances z_{SMLM} of all localizations were plotted against their radial distance r_0 . The solid line indicates the expected behavior for a spherical surface Eq. (30), dashed lines indicate the square root of the Cramér-Rao lower bound. (e) Dependence of z_{SMLM} on the normalized IRM intensity. Solid line indicates fit results from panel (c), dashed lines the square root of the Cramér-Rao lower bound. (f) The difference between the measured values z_{SMLM} and the calculated values z_0 showed a standard deviation of 21 nm. Scale bar 5 µm. Taken from (Velas et al. 2021).

against the radial distance from the sphere's contact point, r_0 , the measured single molecule displacements z_{SMLM} follow closely the surface of the sphere (Figure 52d). We further correlated z_{SMLM} with the IRM intensity values recorded on the corresponding pixels (Figure 52e), yielding very good agreement of the two data sets. The solid black line shows the calibration curve obtained in Figure 52c, the dashed lines indicate the expected Cramér-Rao lower bound (CRLB) (Ober, Ram, and Ward 2004; Zelger et al. 2020). To obtain a quantitative measure of the method's z-precision we calculated for each localization the difference between z_{SMLM} and the theoretical z_0 (Figure 52f). The determined standard deviation of 21nm agrees well with the Cramér-Rao lower bound of 17nm.

Correlative IRM, TIR and 3D SMLM of the immunological synapse

Next, we applied the method to image the 3-dimensional topography of the immunological synapse formed between CD4+ murine 5c.c7 TCR-transgenic T cells and stimulatory or inert surfaces. To visualize the position of the TCR, T cells were labeled with an AlexaF647-conjugated single chain antibody fragment (Huppa, Axmann, Mörtelmaier, et al. 2010) against the TCR β

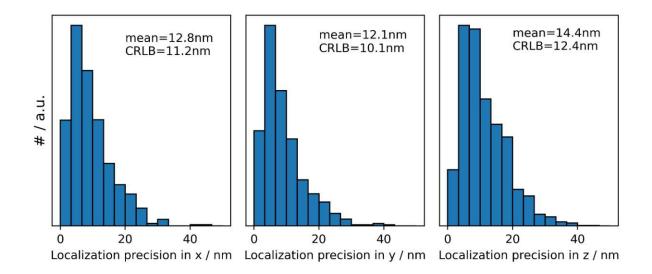


Figure 53: Histogram of localization precision in x, y and z direction. Localization precision was calculated as the standard deviation of localizations of the same molecule appearing in consecutive frames. The mean localization precision and the CRLB are indicated for the different dimensions. Taken from (Velas et al. 2021).

subunit. An isotropic mean precision of 12.7 nm, 12.0 nm, and 14.6 nm was determined for single molecule localization along the x, y, and z axis, respectively (Figure 53).

We first addressed the three-dimensional organization of the TCR in activated T cells. To this end, T cells were seeded onto fluid SLBs functionalized with MCC-loaded I-Ek at a surface density of 100 ± 30 molecules/ μ m², which is known to stimulate intracellular calcium release (Hellmeier et al. 2021); in addition, bilayers contained the adhesion molecule ICAM-1 and the costimulatory molecule B7-1 (Figure 54a). For all applied conditions, T cell activation was controlled via ratiometric calcium imaging by using FURA-2 dye (Figure 55). An increase in the FURA-2 ratio reflects an increase in the intracellular calcium levels upon T cell activation. Prior to conducting imaging experiments, T cells were fixed at specific time points (here 5 minutes) after their seeding onto the SLBs, and imaged both via IRM and 3D SMLM. The IRM images show substantial contrast fluctuations (Figure 54b), indicating corresponding fluctuations in the distance of the T cell membrane from the SLB. This is supported by the 3D SMLM data, where the determined TCR z-positions spread between 0 nm and 300 nm. Plotting z_{SMLM} versus the IRM intensity revealed a good correlation between the two data sets for the first branch of the IRM signal (Figure 54c, solid black line). This correlation vanished, however, for higher order IRM branches. We attribute this lack of correlation to additional parameters affecting the measured IRM contrast such as unknown angles of the reflecting surfaces or the occurrence of multiple interferences, which particularly disturbs IRM signals originating from reflections at larger distances from the glass surface. We therefore did not fit those regions of the IRM curves. In addition, different resolutions of the two methods impede direct comparison of the two data sets: While 3D-SMLM data report on z-distances specific for 2D coordinates that can be determined with a precision below the diffraction-limit, IRM images are limited by diffraction and hence provide average values over areas given by the size of the 2D point spread function.



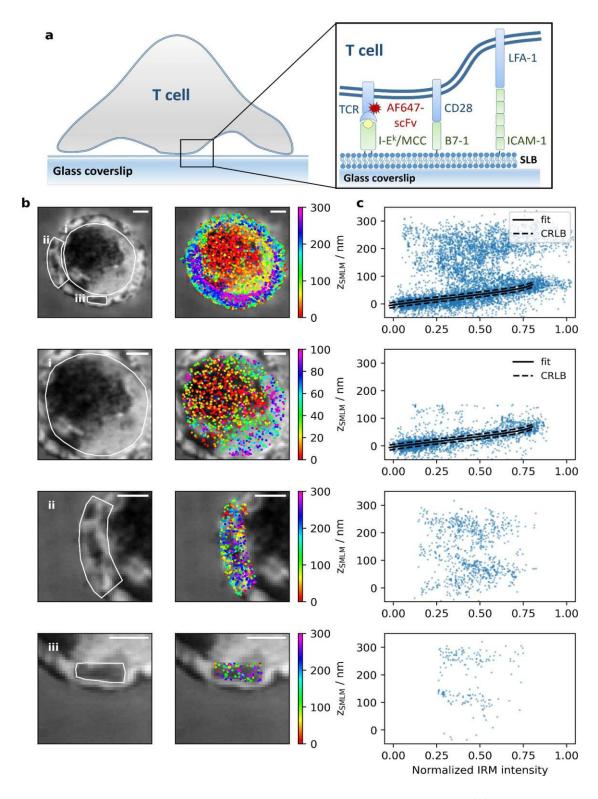


Figure 54: Correlative 3D SMLM and IRM within the immunological synapse. (a) Experiments were performed on a T cell adhering to an SLB functionalized with I-E^k/MCC, B7-1 and ICAM-1; the TCR was labeled via AF647-conjugated H57-scFv. (b) IRM (left) and SMLM/IRM overlay images (right) of the immunological synapse. The areas i, ii and iii are shown in magnification below. (c) Correlation plots between z_{SMLM} and the normalized IRM intensity for the areas indicated in panel (b). Data points with z_{SMLM} < 100 nm were fitted with Eq. (33) (solid line). The dashed lines indicate the square root of the Cramér-Rao lower bound. Scale bars 2 μm. Taken from (Velas et al. 2021).

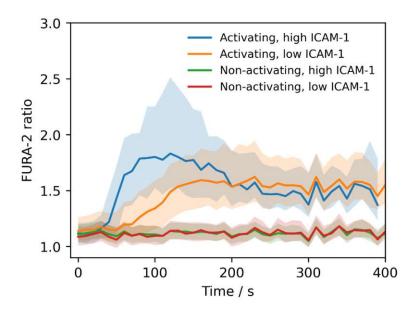


Figure 55: Release of intracellular calcium assessed via the median FURA-2 ratio. Data are shown as a function of time post seeding for T cells subjected to activating and non-activating conditions while employing the ICAM-1 at indicated densities. Taken from (Velas et al. 2021).

For detailed assessment we selected in region i) of Figure 54b the cell center, in which the left half of the region was well adhered to the SLB surface while the right half featured a separation of ~60 nm from the SLB. Here, results obtained with the two imaging modalities are in very good agreement. In region ii) showing the cell edge, where the T cell formed a narrow lamellipodium, we observed two distinct clusters in the z_{SMLM} data, one reflecting the bottom, the

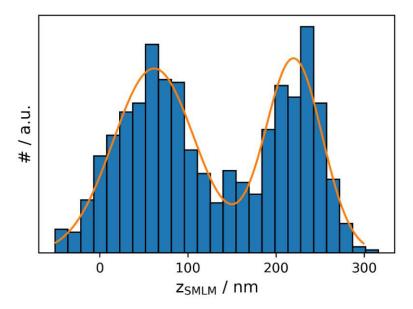


Figure 56: Histogram of zSMLM positions in the area of the lamellipodium shown in Figure 54b (ii), yielding 2 peaks at a mutual distance of 160 nm. Taken from (Velas et al. 2021).



other the top membrane of the lamellipodium. The two clusters were separated by ~ 160 nm (Figure 56), which corresponded to the thickness of the lamellipodium (Abraham et al. 1999).

Interestingly, the z-positions of this particular region hardly correlated with the IRM patterns, likely due to high inclinations of the reflecting membrane at the lamellipodium edge possibly causing additional interferences in the IRM image. In region iii), another feature of membrane topography became apparent: the central dark IRM area did not indicate an area of close contact, but instead showed rather distal lamellipodium regions reflected by z_{SMLM} coordinates more than 100 nm away from the glass surface. Also in this region, the separation of the two lamellipodia membranes of ~160 nm became apparent from two well-separated localization clusters in the z_{SMLM} data.

It is also instructive to compare the obtained 3D SMLM and IRM images with conventional diffraction-limited TIR fluorescence microscopy images as shown in Figure 57 (see also Figure 58 for an additional example of a T cell seeded on an activating bilayer with low ICAM-1 density and Supplementary Gallery in Appendix). In this particular example, the cell had been fixed just before the formation of the central supramolecular activation cluster (cSMAC), when TCR microclusters were observed in a ring-like structure around the cell center (Figure 57i). This image hence presumably reflects a snapshot of the directional microcluster transport towards the cSMAC (Hashimoto-Tane et al. 2011). While TCRs in the ring itself showed tight contact with the glass surface - likely due to binding to the cognate pMHC -, 3D SMLM revealed that the engulfed circular membrane patch contained TCRs substantially elevated by ~100nm (Figure 57 iii & ix), in agreement with the observation that the cSMAC is a site of TCR endocytosis (Onnis and Baldari 2019). In addition, some of the SLB engaged TCR in the cSMAC reside in ~ 100 nm extracellular microvesicles that elevate the non-engaged TCR bearing plasma membrane by ~100 nm above the SLB (Choudhuri et al. 2014), potentially contributing to the two layers of TCR in the cSMAC.

We next analyzed TCR microclusters in more detail. In principle, TCR microcluster contrast is not only determined by protein enrichment, but also by the closer proximity of the fluorophores to the glass surface, yielding both increased excitation intensity in the evanescent field as well as increased detection efficiency due to the collection of supercritical angle fluorescence. Since our method allows for disentangling single molecule fluorescence brightness, z-position, and local clustering, we addressed the different contributions to the diffractionlimited TIR images. For this, we compared the diffraction-limited TIR images (Figure 57i) with data obtained from 3D SMLM. The single molecule brightness indeed showed some correlation with the positions of microclusters in the diffraction-limited image (Figure 57vii), which was also reflected in a map of the single molecule z-positions (Figure 57ix). Furthermore, single molecule localizations were strongly clustered at the positions of the microclusters (Figure 57viii). We sought to reconstruct the diffraction-limited image by convolving the single molecule localization map with the brightness-weighted point spread function (PSF) (Figure 57ii). The reconstructed image agreed well with the original diffraction-limited image, down to the level of the individual TCR microclusters.



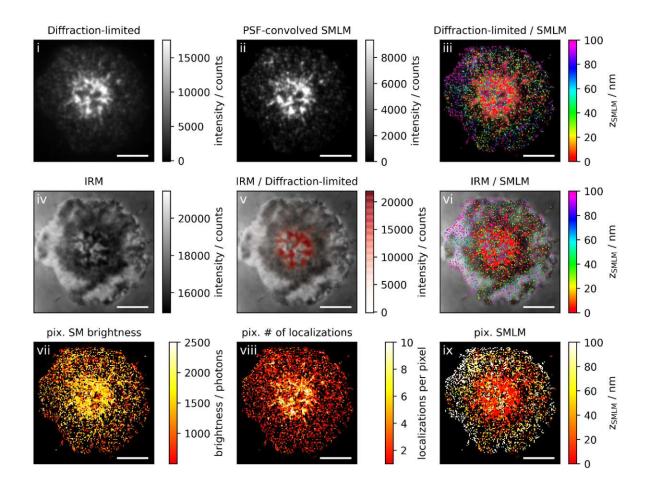


Figure 57: Correlative 3D SMLM, IRM, and diffraction-limited TIR microscopy of the immunological synapse. T cells were activated on a SLB functionalized with I-E^k/MCC, B7-1 and high density of ICAM-1 (125 \pm 22 molecules/ μ m²), and fixed 10 minutes post seeding. The T cell was imaged with IRM and fluorescence microscopy: (i) Diffraction-limited TIR image of the T cell. (ii) Reconstruction of the diffraction-limited image by convolving the 3D SMLM image with the corresponding PSF. (iii) Overlay of the diffraction-limited TIR image with the 3D SMLM image. The color-code indicates distances to the coverslip z_{SMLM} . (iv) IRM image. (v) Overlay of the IRM image with the diffraction-limited image. (vi) Overlay of the IRM and the 3D SMLM image. Bottom row images were generated by calculating the pixel-wise average of the 3D SMLM images (pixel size of 146 nm is consistent with diffraction-limited image) according to pixelated mean single molecule (SM) brightness (vii), pixelated number of localizations (viii) and pixelated mean z_{SMLM} (ix). Scale bars 5 μm. Taken from (Velas et al. 2021).

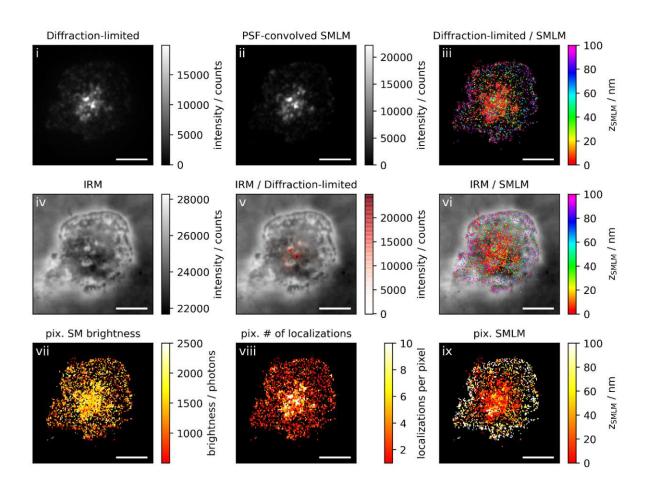


Figure 58: Correlative 3D SMLM, IRM, and diffraction-limited TIR microscopy of the immunological synapse. T cells were activated on a SLB functionalized with I-E^k/MCC, B7-1 and low density of ICAM-1 $(4 \pm 2 \text{ molecules/}\mu\text{m}^2)$, and fixed 10 minutes post seeding. The T cell was imaged with IRM and fluorescence microscopy: (i) Diffraction-limited TIR image of the T cell. (ii) Reconstruction of the diffraction-limited image by convolving the 3D SMLM image with the corresponding PSF. (iii) Overlay of the diffraction-limited TIR image with the 3D SMLM image. The color-code indicates distances to the coverslip z_{SMLM}. (iv) IRM image. (v) Overlay of the IRM image with the diffraction-limited image. (vi) Overlay of the IRM and the 3D SMLM image. Bottom row images were generated by calculating the pixel-wise average of the 3D SMLM images (pixel size of 146 nm is consistent with diffraction-limited image) according to pixelated mean single molecule (SM) brightness (vii), pixelated number of localizations (viii) and pixelated mean z_{SMLM} (ix). Scale bars 5 μm. Taken from (Velas et al. 2021).

To quantitatively disentangle the different contributions, we identified TCR microclusters by intensity-thresholding the diffraction-limited images (Figure 59), and analyzed the single molecule properties separately for localizations coinciding with the TCR microcluster regions versus localizations outside of TCR microclusters. Figure 60 shows the ratios of single molecule brightness and number of single molecule localizations per pixel, which were obtained from multiple cells. While the brightness levels in microclusters increased only by 20%, we observed about 3-fold enrichment of localizations. The product of the two ratios quantitatively matched the average brightness ratios of pixels corresponding to microclusters versus pixels of outside

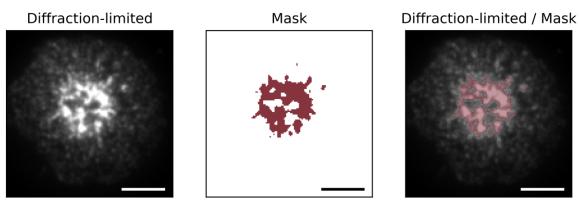


Figure 59: Intensity thresholding was applied to the diffraction-limited images of T cells to identify TCR microclusters. Pixels with an intensity exceeding the mean intensity of the cell by a factor of 1.5 were considered as part of microclusters ("in"), all other pixels as outside of the microclusters ("out"). Scale bar 5 μm. Taken from (Velas et al. 2021).

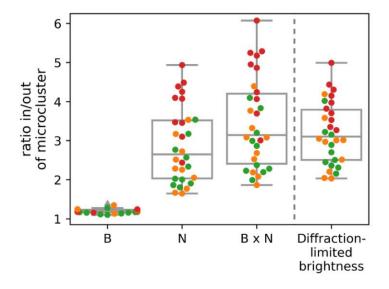


Figure 60: Disentangling single molecule brightness and molecular enrichment in TCR microclusters: We quantified the average single molecule brightness, B, and the number of localizations, N, in pixels corresponding to TCR microclusters ("in") and the complementary regions of the synapse ("out"). Plotted are the ratios in / out for B, N, the product B x N, and the average diffraction-limited brightness per pixel. Each data point corresponds to the average ratio per cell. Colors indicate the time point of fixation post seeding (orange: 5-10 minutes, green: 10 minutes, red: 10-15 minutes). (n=30 cells). Taken from (Velas et al. 2021).



regions obtained from the diffraction-limited images. Importantly, as this analysis was based on pixel-wise discrimination of microclusters in the diffraction-limited images, it was not affected by residual overcounts in the SMLM images. Taken together, we conclude that the increased brightness of TCR microclusters in diffraction-limited images is mainly explained by enrichment of TCR molecules. Of note, we observed the expected increased brightness of microclusters fixed at late time-points (red data points) compared to those fixed at early time-points (orange data points) (Varma et al. 2006); also this effect is explained by an increase in the number of single molecule localizations.

We further studied T cells contacting SLBs that were functionalized with the adhesion molecule ICAM-1 only, so that no calcium signal was triggered (see Figure 55 for ratiometric calcium analysis). Exemplary image for high ICAM-1 density is shown in Figure 61 and for low ICAM-1 density in Figure 62 (Additional images are shown in Supplementary Gallery in Appendix). As expected, we did not observe the formation of bright TCR microclusters as in the activated state. While in general the cells spread well on such substrates, areas of close contact appeared more fragmented than in the activated situation. This effect was more pronounced when we reduced the density of the adhesion molecule ICAM-1 in the SLB from 125 \pm 22 molecules/ μ m² to 4 ± 2 molecules/ μ m².

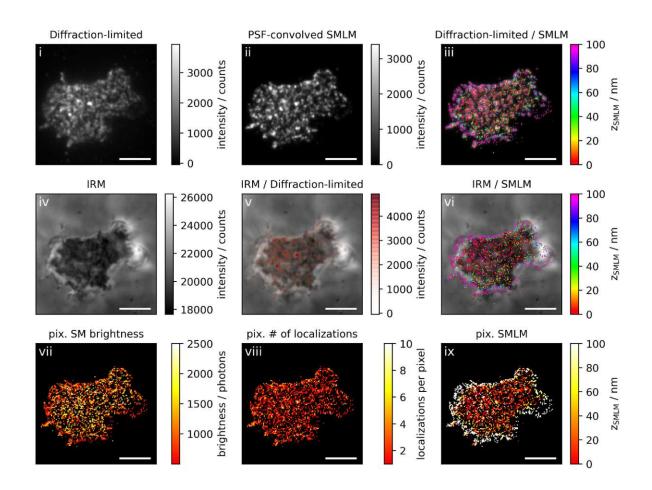


Figure 61: Correlative 3D SMLM, IRM, and diffraction-limited TIR microscopy of the immunological synapse. T cells were seeded on a SLB functionalized with high density of ICAM-1 ($125\pm$ 22 molecules/ μ m²), and fixed 10 minutes post seeding. The T cell was imaged with IRM and fluorescence microscopy: (i) Diffraction-limited TIR image of the T cell. (ii) Reconstruction of the diffraction-limited image by convolving the 3D SMLM image with the corresponding PSF. (iii) Overlay of the diffraction-limited TIR image with the 3D SMLM image. The color-code indicates distances to the coverslip z_{SMLM} . (iv) IRM image. (v) Overlay of the IRM image with the diffraction-limited image. (vi) Overlay of the IRM and the 3D SMLM image. Bottom row images were generated by calculating the pixel-wise average of the 3D SMLM images (pixel size of 146 nm is consistent with diffraction-limited image) according to pixelated mean single molecule (SM) brightness (vii), pixelated number of localizations (viii) and pixelated mean z_{SMLM} (ix). Scale bars 5 μm. Taken from (Velas et al. 2021).

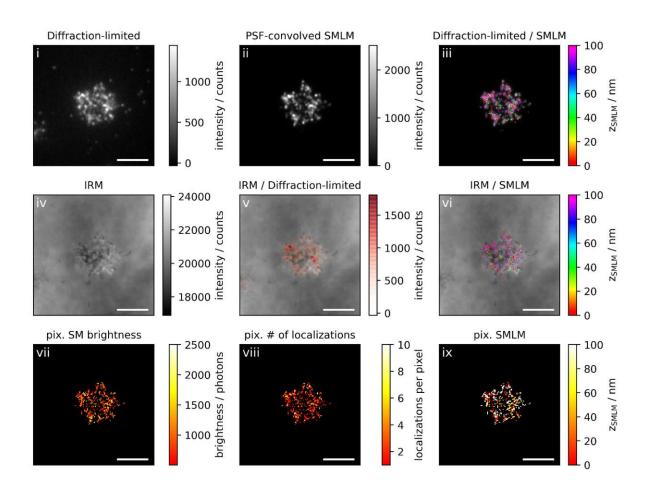


Figure 62: Correlative 3D SMLM, IRM, and diffraction-limited TIR microscopy of the immunological synapse. T cells were seeded on a SLB functionalized with low density of ICAM-1 (4 \pm 2 molecules/ μm^2), and fixed 10 minutes post seeding. The T cell was imaged with IRM and fluorescence microscopy: (i) Diffraction-limited TIR image of the T cell. (ii) Reconstruction of the diffraction-limited image by convolving the 3D SMLM image with the corresponding PSF. (iii) Overlay of the diffraction-limited TIR image with the 3D SMLM image. The color-code indicates distances to the coverslip z_{SMLM}. (iv) IRM image. (v) Overlay of the IRM image with the diffraction-limited image. (vi) Overlay of the IRM and the 3D SMLM image. Bottom row images were generated by calculating the pixel-wise average of the 3D SMLM images (pixel size of 146 nm is consistent with diffraction-limited image) according to pixelated mean single molecule (SM) brightness (vii), pixelated number of localizations (viii) and pixelated mean z_{SMLM} (ix). Scale bars 5 μm. Taken from (Velas et al. 2021).

3.3.4 Quantitative Analysis of T cell surface topography within the immunological synapse

For quantification, we determined the roughness of the T cell surface within the immunological synapse. To prevent the inclusion of data originating from the top membrane of lamellipodia we only considered localizations with z_{SMLM} < 100 nm. Before analysis, all 3D SMLM images were corrected for overcounts, which eventually allowed us to obtain a valid estimation of the surface roughness, as overcounting increases the standard deviation of z_{SMLM} . The correction method was based on merging localizations appearing from a single emitter in subsequent frames within a given 3D radius and with a number of maximally allowed gaps. To find the optimal set of parameters we have calculated the standard deviation σ_z of z_{SMLM} from all localization obtained after merging using the indicated 3D search radius and maximally allowed gaps (Figure 63a). Increasing the search radius in the range of 0-40 nm led to a decrease in σ_z and further increase did not result in a significant change of σ_z . Similarly, a decrease in σ_z was observed for increasing the maximally allowed gaps from 0 to 5, and further increase did not result in a significant change. Therefore, we chose the search radius of 60 nm and maximally 5 allowed gaps as optimal parameters for the correction of overcounting. We further supported this selection by analyzing simulated data via the same approach Figure 63b. The simulated 3D SMLM data followed a surface with a roughness of 26 nm with experimentally derived single molecule blinking statistics and localization precision (see Methods, section 2.5.1 for details).

At non-activating conditions and low ICAM-1 densities we observed substantial fluctuations of the recorded z-positions (Figure 64a). For quantitative determination of the

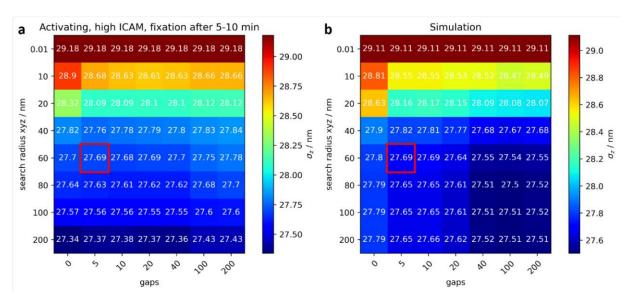


Figure 63: Selecting the appropriate parameters for correction of overcounts. a) 3D SMLM experiments were performed on T cells recorded under activating conditions as described for experiments shown in Figure 57. We determined the standard deviation of z_{SMLM} , σ_z , of all localization obtained after merging using the indicated three-dimensional search radius and maximally allowed gaps. The chosen value is highlighted by the red square. b) For comparison, we analyzed simulated 3D SMLM data via the same approach. The simulation was based on experimentally derived single molecule blinking statistics and localization precision (see Methods for details). For the simulations we assumed a surface roughness of 26nm. Taken from (Velas et al. 2021).

surface roughness, we compared the obtained variances $\sigma_{z, TCR}^2$ with values obtained for fluorescently labeled SLB-anchored I-E^k/MCC, $\sigma_{z,MHC}^2$, according to $\sigma = \sqrt{\sigma_{z,TCR}^2 - \sigma_{z,MHC}^2}$, yielding a standard deviation of $\sigma = 37$ nm. Fluctuations decreased to 29 nm when we increased the density of the adhesion molecule ICAM-1 in the lipid bilayer. Upon activation via higher densities of I-Ek/MCC, T cells adhered more smoothly to the surface, as indicated by reduced overall zfluctuations of 19 nm. Also, in case of activation we observed the T cell surface flattening out to a considerable extent with ICAM-1 present at higher densities.

According to the kinetic segregation model, the axial dimension of the intercellular cleft determines the accessibility of the large phosphatase CD45. We hence quantified the absolute distance of the TCR from the SLB, when compared to fluorescently labeled SLB-anchored I-E^k/MCC. Generally, we observed similar trends as for the standard deviations: with increasing densities of I-Ek/MCC and ICAM-1 the TCR was observed to be closer to the SLB surface (Figure 64b). The separation varied between 18 nm at high densities of I-Ek/MCC and ICAM-1 up to 31 nm for scanning T cells recorded at low densities of ICAM-1. When selecting only signals corresponding to TCR microclusters for our distance analysis, we observed the expected close contact between TCR and I-Ek/MCC, with a calculated separation of 5 nm. The residual separation reflected in all likelihood the distance separating the dye site-specifically conjugated to the single chain antibody fragment and the dye coupled to the MCC peptide's C-terminus as presented by I-E^k (Huppa, Axmann, Mörtelmaier, et al. 2010).

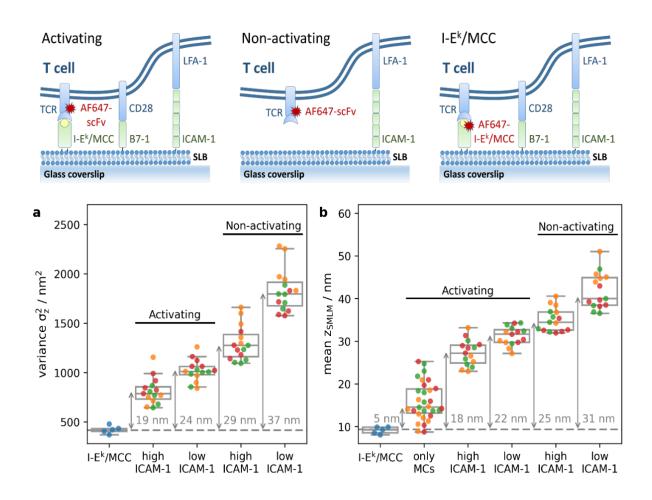


Figure 64: Contact analysis for T cells recorded under activating and non-activating conditions: T cells were seeded on SLBs either functionalized with I-E^k/MCC, B7-1 and ICAM-1 (termed "activating") or with ICAM-1 only (termed "non-activating"). To vary adhesive strength, we used 125 ICAM-1 molecules per μm² (termed "high ICAM-1") or 4 ICAM-1 molecules per μm² (termed "low ICAM-1"). T cells were allowed to spread on SLBs and were fixed after 5-10 (orange), 10 (green) or 10-15 (red) minutes post seeding. As a control, unlabeled T cells were seeded on SLBs containing I- E^k/MCC labeled with AF647. The recorded localizations were filtered for z_{SMLM} < 100 nm in order to exclude contributions from the upper surface of lamellipodia. (a) The variance of z_{SMLM} per cell was plotted for different conditions. Arrows indicate the difference in variance to the control I-E^k/MCC data, numbers the corresponding square root. (b) Mean z_{SMLM} per cell was plotted for different conditions. Arrows indicate the difference to the control $I-E^k/MCC$ data. To calculate the mean distance of TCR microclusters from the glass surface we considered only localizations within microclusters (termed "only MCs") in experiments performed both at high and low densities of ICAM-1. (n = 15 cells per condition). Taken from (Velas et al. 2021).

3.3.5 Discussion

We applied here a novel 3D SMLM method to map and analyze the position of the TCR within the immunological synapse at isotropic localization precision below 15 nm, and put it in the context of IRM imaging. IRM contrast arises from interferences due to optical path-length differences between the beam reflected at the glass-water interface and beams reflected from surfaces within the sample. Recording 3D SMLM localization maps is fundamentally different from IRM. Using supercritical angle detection combined with defocused imaging, our method essentially determines the three-dimensional position of all visible dye molecules. We employed here an AlexaF647-conjugated single chain antibody fragment that specifically recognizes the TCR β subunit (Huppa, Axmann, Mörtelmaier, et al. 2010). In previous studies we have shown that labelling neither activates T cells nor impedes specific antigen recognition (Huppa, Axmann, Mörtelmaier, et al. 2010). Of note, we used TIR excitation in order to confine imaging to the synapse region. While the evanescent field was narrow enough to prevent contributions from TCRs at the top of the T cell, we could observe both the bottom and the top membranes of lamellipodia.

Indeed, there was in general a good qualitative agreement between the two imaging modalities. Substantial differences, however, arose when distal membrane regions contributed to the IRM contrast values. Then, contrast values did not unequivocally correspond to the axial membrane separation. This was especially observed in lamellipodia, where both the bottom and the top membrane contributed to the signal.

Two aspects of our study contain important immunological implications for understanding T cell antigen recognition:

1) What is the physical reason for the observation of TCR microclusters?

In TIR excitation, fluorescent molecules close to the glass coverslip naturally contribute with higher brightness than distal molecules. This effect is further amplified by the collection of supercritical angle fluorescence when using high NA objectives (Oheim, Salomon, and Brunstein 2020). Taken together, what appears as a bright spot in diffraction-limited fluorescence microscopy could be the consequence of increased density or of increased brightness of the fluorophores. Given the close contact between TCR microclusters and the surface (Cai et al. 2017) researchers became concerned, whether microclusters actually reflect TCR enrichment.

3D SMLM provides ground truth information on the origin of apparent TCR microclusters in diffraction-limited TIR microscopy, as it allows for disentangling molecular enrichment from brightness changes. We observed only marginal contributions from single molecule brightness increase; as brightness was largely attributable to molecular enrichment. This finding is in accord with our observation of a rather smooth interface between the SLB and the T cell membrane under activating conditions, so that there are globally only minor variations in the single molecule's z-distance in comparison to the TIR penetration depth.

2) Does the observed cleft size support CD45 segregation?

A prominent model for TCR triggering involves the balance in the activities of the kinase Lck and the phosphatase CD45 for ITAM phosphorylation. In this kinetic segregation model, proteins with bulky extracellular domains - such as the large phosphatase CD45 - are proposed to be segregated locally from the comparably short pMHC-TCR complexes (Davis and van der Merwe 2006). While there are ample of reports that would be consistent with this model (Chang et al. 2016; Santos et al. 2018; Choudhuri et al. 2005; Taylor et al. 2017; Fernandes, Ganzinger, Tzou, Jönsson, et al. 2019) the community has not reached a consensus yet (Al-Aghbar et al. 2018; Courtney et al. 2019; Cai et al. 2018).

One difficulty has been the precise measurement of the cleft size between the T cell surface and the opposing membrane. Given the dimension of the TCR-pMHC-CD4 ternary complex of 10 nm (Yin, Wang, and Mariuzza 2012) and our apparent distance measurements between TCR and I-Ek/MCC within TCR microclusters of 5 nm, the obtained distance undervalues the cleft size by 5 nm. Upon correcting for this effect, an average cleft size within the whole synapse ranging between 23 nm and 36 nm for the conditions shown in Figure 64b can be estimated. In addition to the average cleft size, however, distance fluctuations within the synapse were of the same order (Figure 64a), indicating the presence of multiple contact sites between the two membranes. Assuming an axial length of CD45R0, the smallest CD45 isoform, of approximately 22 nm (Chang et al. 2016), our measurements hence indicate the existence of numerous membrane contact sites that would be too narrow to host CD45, both for resting and activating conditions. In particular, an average cleft size of 30 nm together with an average surface roughness of 29 nm, as observed for scanning T cells at high ICAM-1 densities, render the presence of multiple CD45 exclusion zones likely. Similar data were recently reported for the tips of microvilli which showed segregation of the TCR and CD45 prior to T cell activation (Jung et al. 2021). Given that none of these scenarios promoted T cell activation it is possible that the ITAMs of these segregated TCRs are not accessible to kinases (Lanz et al. 2021). In addition, TCR-CD45 segregation may be too transient to trigger stable phosphorylation of TCR ITAMs. Kinetic data about protein mobility in conjunction with the super-resolution images would be needed in order to obtain a quantitative understanding of these key aspects of the TCR triggering process.

3.4 Conclusion

Within this thesis, a novel 3D single molecule localization microscopy method was developed and applied to study the topography of the immunological synapse. The method relies on extracting the 3D coordinates of each fluorophore from the shape of the point spread function upon defocusing. Such approach is similar to other point spread function engineering methods (von Diezmann, Shechtman, and Moerner 2017), however, doesn't require addition of other optical elements to the emission pathway, such as spatial light modulators, thereby keeping the experimental setup simple and more efficient in collection of photons (Zelger et al. 2020). The method is meant to be used for imaging close to the coverslip as there it achieves high localization precision due to the profound effect of depth-dependent supercritical angle fluorescence on the shape of the defocused point spread function. The detection of supercritical angle fluorescence is achieved simply by using an objective with high numerical aperture. Our single channel defocused imaging approach leverages the advantage of supercritical angle fluorescence better than other methods based on splitting of the supercritical angle fluorescence and undercritical angle fluorescence (Bourg et al. 2015; Deschamps, Mund, and Ries 2014). This was supported by calculations of the Cramér-Rao lower bounds for the two methods. Of note, optimal performance of the method regarding localization precision and accuracy can be achieved only with an accurate point spread function model. We have used a vectorial model of the point spread function including the effects of supercritical angle fluorescence (Axelrod 2012) and modified it with experimentally measured aberrations of the optical system (Quirin, Pavani, and Piestun 2012). Overall, the method achieves state-of-the-art localization precision of the single molecule localization microscopy techniques while conserving simplicity of its experimental implementation. Slightly better results regarding the localization precision and z range can be achieved using bi-plane imaging, however, at the cost of the complexity of the experimental system (Zelger et al. 2021).

In order to implement the method experimentally, we have designed and built a new microscopy system equipped for single molecule localization microscopy. As defocus magnitude is the most important parameter of the method, we have mounted the objective on a piezo stage that allows precise defocusing and have built a focus hold system to ensure that the defocus magnitude stays constant during the whole recording. The performance of the method was tested on a number of samples with a known ground truth. We have used fluorescently coated glass spheres to confirm no z bias of the method. 30 nm long DNA origami nanorulers were used to confirm high localization precision of the method, achieving about 10 nm in all three dimensions. Finally, to prove the performance of the method in cellular environment, we have successfully resolved the structure of nuclear pore complex in 3D.

Application of 3D single molecule localization microscopy to study the topography of the immunological synapse was one of the main motivations for this thesis. The positions of membrane bound T cell receptor molecules correlated well with interference reflection microscopy images of well adhered T cells, which allowed to cross-validate the two methods. The only differences arose in the regions of lamellipodia where the interference model is poorly defined due to the presence of multiple reflecting interfaces and tilted membranes (Limozin and Sengupta 2009).

Mapping the positions of T cell receptors and comparing the images with diffraction limited images of the immune synapse obtained by total internal reflection fluorescence



microscopy revealed that the T cell receptor microclusters appearing as bright spots correlate with regions of close proximity of the T cell receptors to the supported lipid bilayer. This raises a question about the true molecular enrichment of the T cell receptor in the microclusters (Cai et al. 2017) as the proximity of these regions to the coverslip could result in higher brightness due to detection of the supercritical angle fluorescence and the exponential decay of the exciting evanescent field. Our measurements revealed that this effect only contributes by around 20% to the higher intensity observed in diffraction limited images and that T cell receptor microclusters are 2-5 times enriched with T cell receptor molecules.

Finally, we quantified the average cleft sizes and their fluctuations within the synapses of activated and non-activated T cells. We observed smaller cleft sizes for activated cells with regions likely corresponding to the bound T cell receptors, qualifying for exclusion of the CD45 phosphatase. Despite the larger cleft sizes observed for non-activating T cells, higher fluctuations of these synapses indicate possible contact zones which would also qualify for exclusion of the CD45. It is therefore unclear, why these possible exclusion zones don't lead to activation of T cells. One possibility is that these zones are short-lived and the separation of the T cell receptor and CD45 doesn't last long enough to trigger activation. T cells have been shown to initiate contacts with antigen presenting cells via microvilli protrusions. These protrusions are highly dynamic and only get stabilized upon T cell activation (Cai et al. 2017). Another explanation would be that the T cell receptor can freely diffuse through the CD45 exclusion zones and only trapping of the T cell receptor in these tight contacts leads to the T cell receptor phosphorylation and T cell activation (Chen et al. 2021). Our implementation of the method provides a static picture of the synapse as it requires fixed cells. However, measuring stability or dynamics of these contacts in live cells could help in understanding why not all close contacts lead to T cell activation. Besides the super-resolution microscopy, our method can be used for 3D single molecule tracking as well, allowing to address dynamic aspects of the T cell receptor within the immune synapse. Single molecule tracking relies on connecting localizations of the same molecule over a period of time. In the case of diffusing molecules, extra care has to be taken to ensure that the recorded single molecule images are not distorted by the movement as this could lead to localization bias in z direction. This can be ensured by choosing a short illumination time in comparison to the molecule's diffusion.

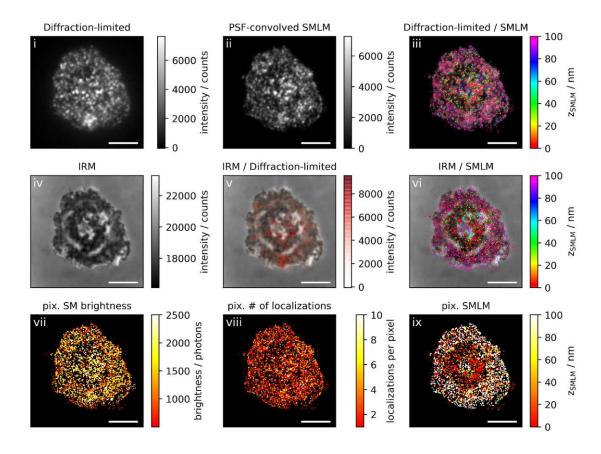
As an outlook, due to the simple implementation of the 3D single molecule localization microscopy via defocused imaging and single channel approach, the method can be easily adjusted for two-color 3D microscopy using a dichroic mirror and a second channel. It would be of great interest to the community to simultaneously observe the 3D distribution of the T cell receptor and the phosphatase CD45 in order to directly confirm or rule out their mutual exclusion in the close contacts.

Supplementary Gallery

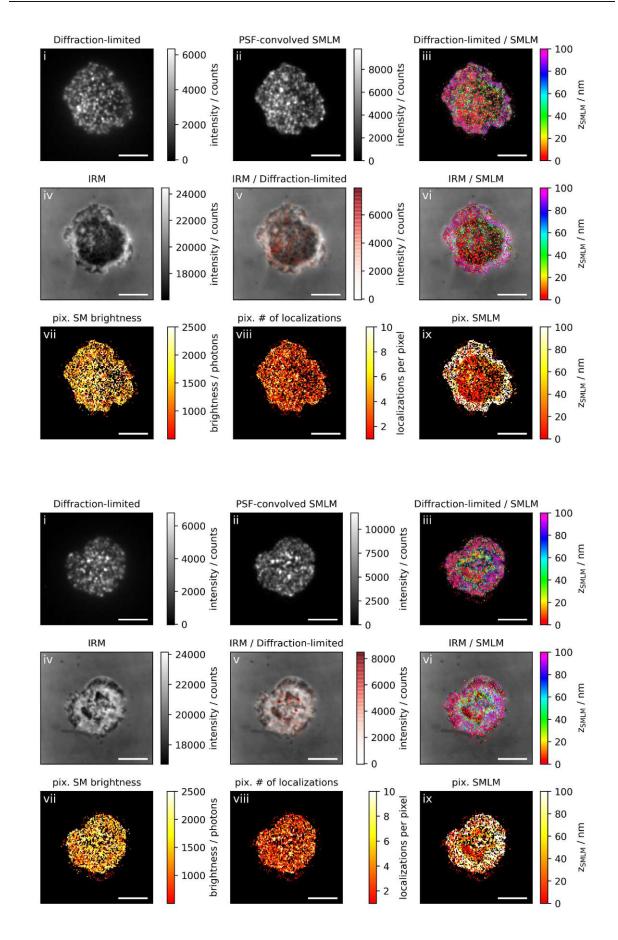
The Supplementary Gallery contains a set of 60 correlative 3D-SMLM, IRM and TIR microscopy images of T cells analyzed in section 3.3. The images are sorted according to activating or nonactivating conditions, ICAM-1 density and the timepoint of fixation post seeding.

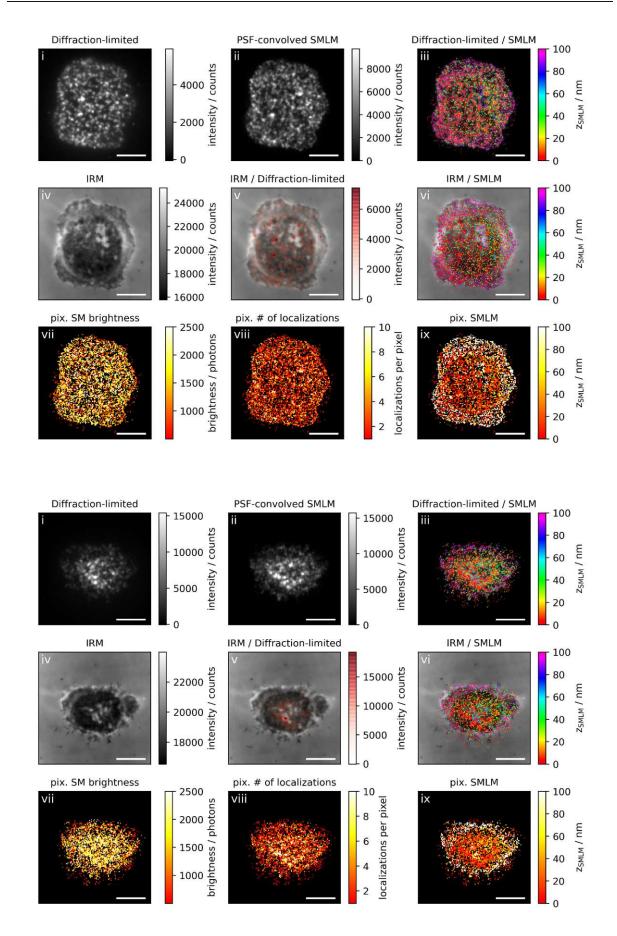
Activating conditions, high ICAM-1 density, fixation: 5-10 min post seeding

Correlative 3D-SMLM, IRM, and diffraction-limited TIR microscopy of the immunological synapse. T cells were activated on an SLB functionalized with I-Ek/MCC, B7-1 and high density of ICAM-1, and fixed 5-10 minutes post seeding. The T cell was imaged with IRM and fluorescence microscopy: (i) Diffraction-limited TIR image of the T cell. (ii) Reconstruction of the diffractionlimited image by convolving the 3D-SMLM image with the corresponding psf. (iii) Overlay of the diffraction-limited TIR image with the 3D-SMLM image. Color-code indicates distance to the coverslip z_{SMLM}. (iv) IRM image. (v) Overlay of the IRM image with the diffraction-limited image. (vi) Overlay of the IRM and the 3D-SMLM image. Bottom row images were generated by calculating the pixel-wise average of the 3D-SMLM images (pixel size of 146nm is consistent with diffraction-limited image) according to pixelated mean single molecule (SM) intensity (vii), pixelated number of localizations (viii) and pixelated mean z_{SMLM} (ix). Scale bars 5 μm. Taken from (Velas et al. 2021).



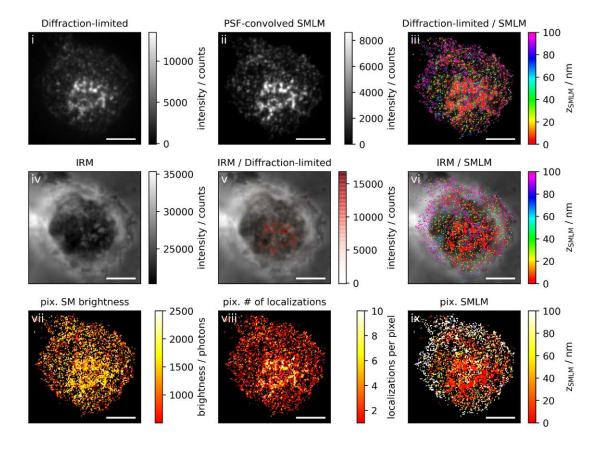




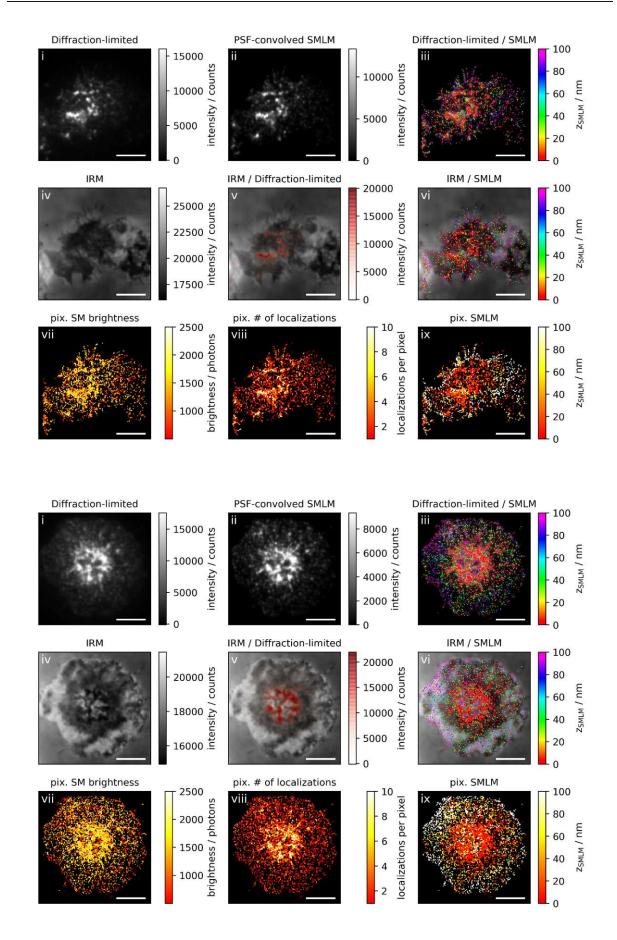


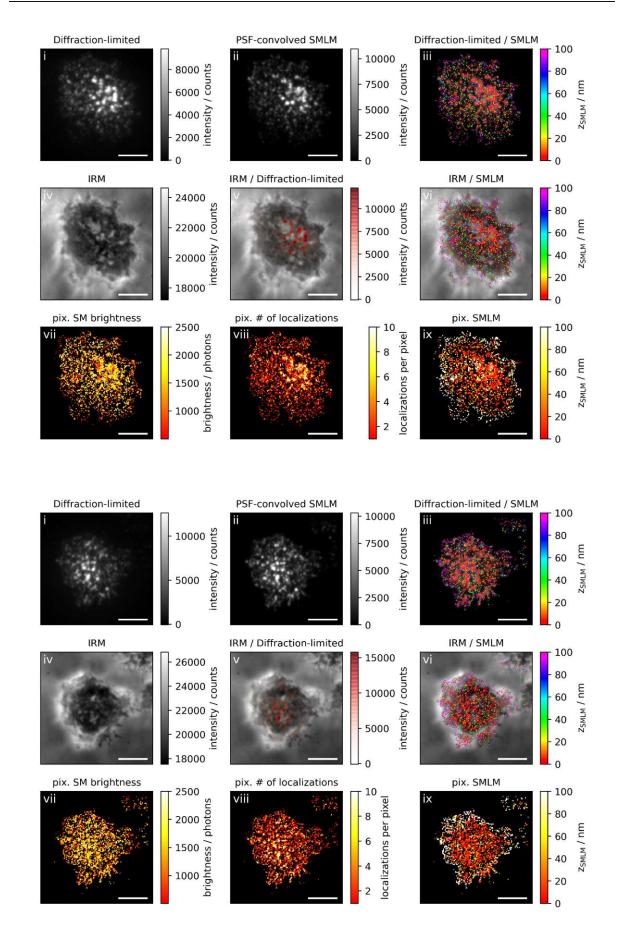
Activating conditions, high ICAM-1 density, fixation: 10 min post seeding

Correlative 3D-SMLM, IRM, and diffraction-limited TIR microscopy of the immunological synapse. T cells were activated on an SLB functionalized with I-Ek/MCC, B7-1 and high density of ICAM-1, and fixed 10 minutes post seeding. The T cell was imaged with IRM and fluorescence microscopy: (i) Diffraction-limited TIR image of the T cell. (ii) Reconstruction of the diffraction-limited image by convolving the 3D-SMLM image with the corresponding psf. (iii) Overlay of the diffractionlimited TIR image with the 3D-SMLM image. Color-code indicates distance to the coverslip z_{SMLM}. (iv) IRM image. (v) Overlay of the IRM image with the diffraction-limited image. (vi) Overlay of the IRM and the 3D-SMLM image. Bottom row images were generated by calculating the pixelwise average of the 3D-SMLM images (pixel size of 146nm is consistent with diffraction-limited image) according to pixelated mean single molecule (SM) intensity (vii), pixelated number of localizations (viii) and pixelated mean z_{SMLM} (ix). Scale bars 5 μm. Taken from (Velas et al. 2021).



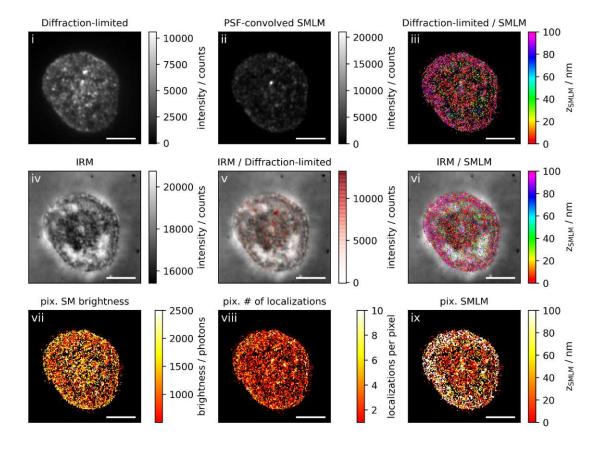




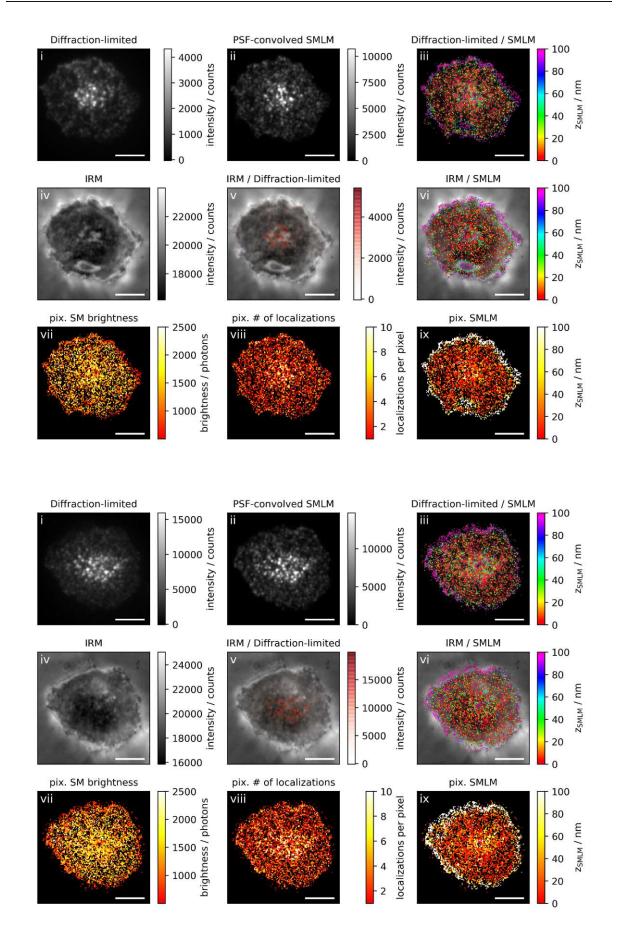


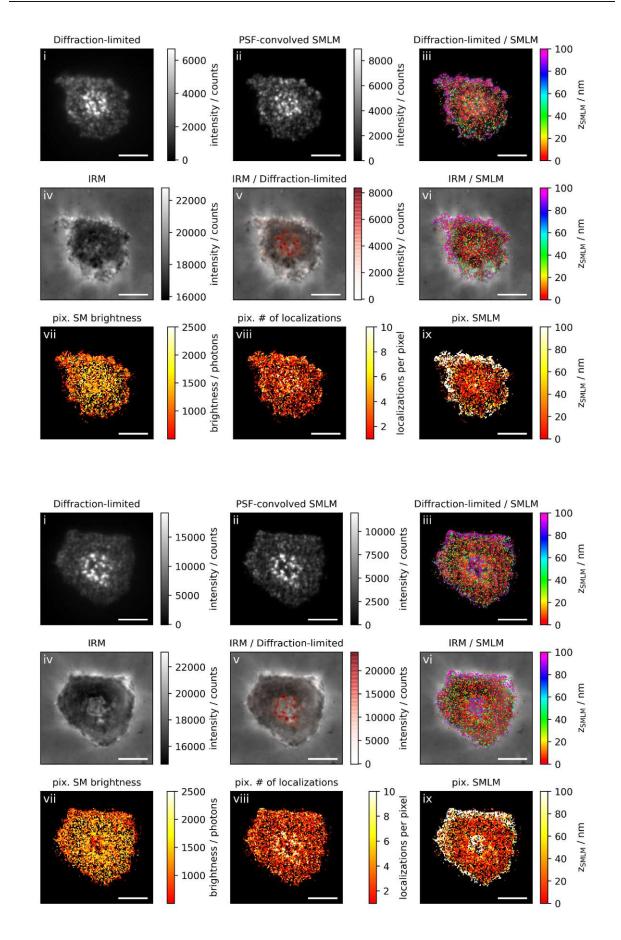
Activating conditions, high ICAM-1 density, fixation: 10-15 min post seeding

Correlative 3D-SMLM, IRM, and diffraction-limited TIR microscopy of the immunological synapse. T cells were activated on an SLB functionalized with I-Ek/MCC, B7-1 and high density of ICAM-1, and fixed 10-15 minutes post seeding. The T cell was imaged with IRM and fluorescence microscopy: (i) Diffraction-limited TIR image of the T cell. (ii) Reconstruction of the diffractionlimited image by convolving the 3D-SMLM image with the corresponding psf. (iii) Overlay of the diffraction-limited TIR image with the 3D-SMLM image. Color-code indicates distance to the coverslip z_{SMLM}. (iv) IRM image. (v) Overlay of the IRM image with the diffraction-limited image. (vi) Overlay of the IRM and the 3D-SMLM image. Bottom row images were generated by calculating the pixel-wise average of the 3D-SMLM images (pixel size of 146nm is consistent with diffraction-limited image) according to pixelated mean single molecule (SM) intensity (vii), pixelated number of localizations (viii) and pixelated mean z_{SMLM} (ix). Scale bars 5 μm. Taken from (Velas et al. 2021).



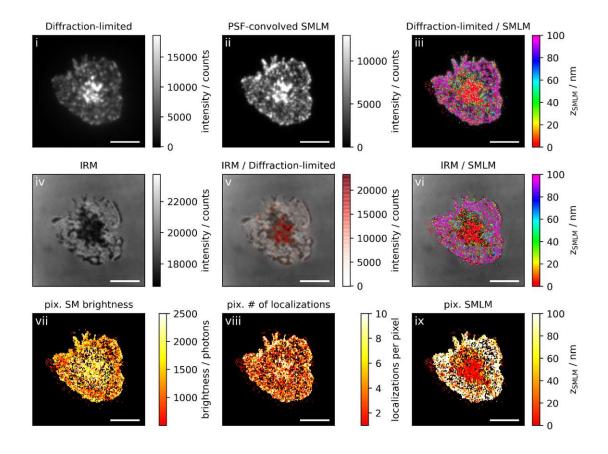


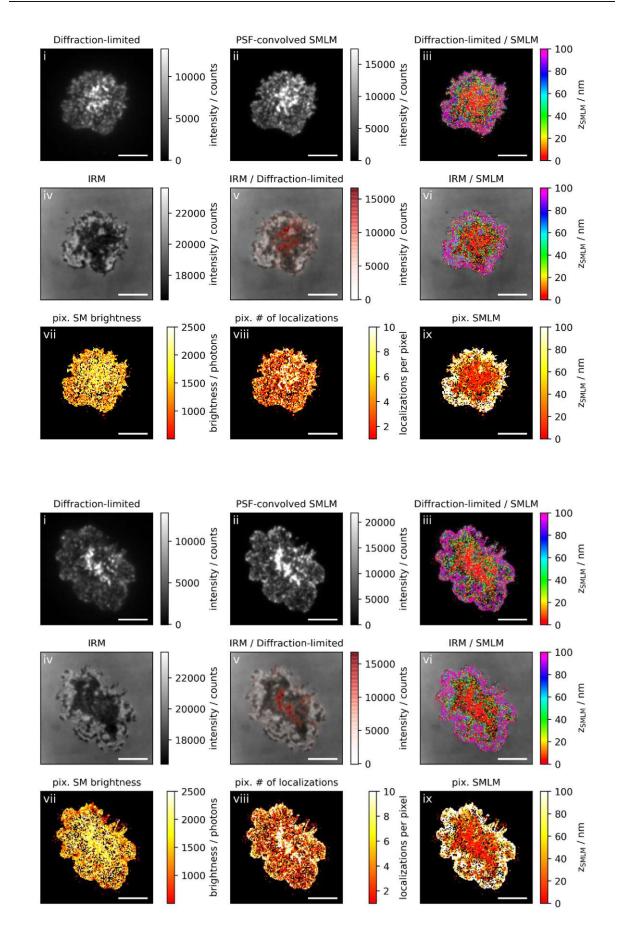


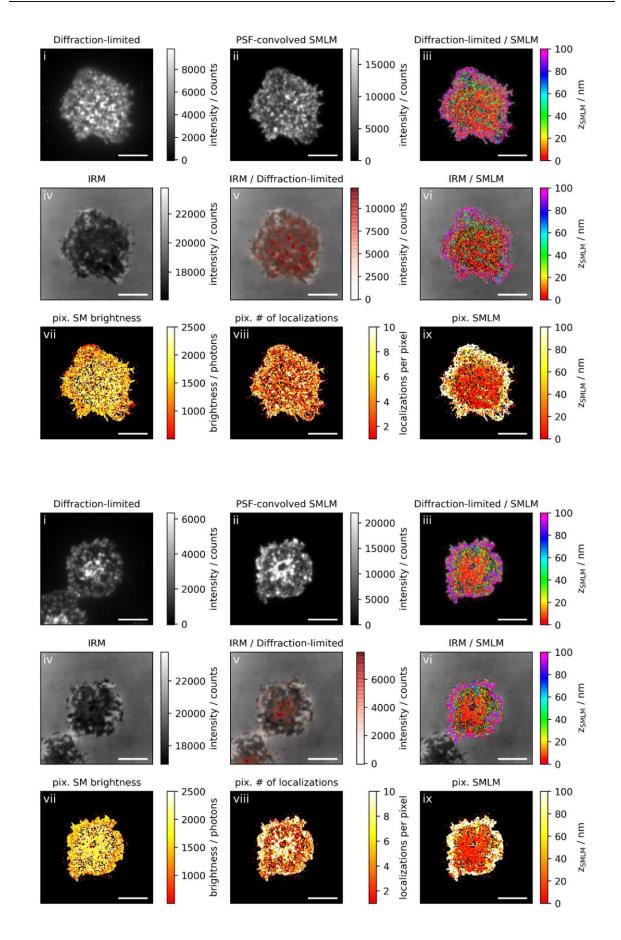


Activating conditions, low ICAM-1 density, fixation: 5-10 min post seeding

Correlative 3D-SMLM, IRM, and diffraction-limited TIR microscopy of the immunological synapse. T cells were activated on an SLB functionalized with I-Ek/MCC, B7-1 and low density of ICAM-1, and fixed 5-10 minutes post seeding. The T cell was imaged with IRM and fluorescence microscopy: (i) Diffraction-limited TIR image of the T cell. (ii) Reconstruction of the diffractionlimited image by convolving the 3D-SMLM image with the corresponding psf. (iii) Overlay of the diffraction-limited TIR image with the 3D-SMLM image. Color-code indicates distance to the coverslip z_{SMLM}. (iv) IRM image. (v) Overlay of the IRM image with the diffraction-limited image. (vi) Overlay of the IRM and the 3D-SMLM image. Bottom row images were generated by calculating the pixel-wise average of the 3D-SMLM images (pixel size of 146nm is consistent with diffraction-limited image) according to pixelated mean single molecule (SM) intensity (vii), pixelated number of localizations (viii) and pixelated mean z_{SMLM} (ix). Scale bars 5 μm. Taken from (Velas et al. 2021).







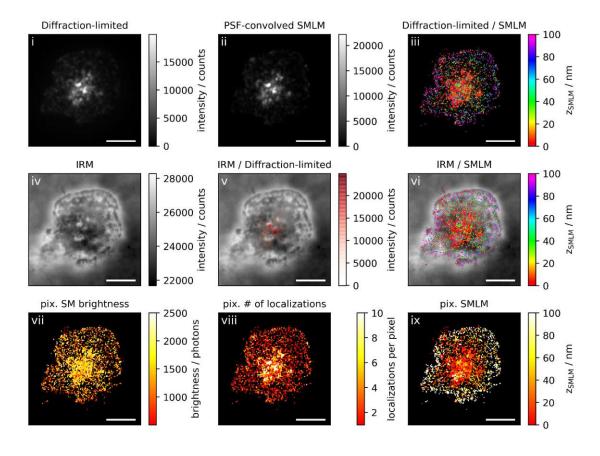
TU Sibliothek Die approbierte gedruckte Originalversion dieser Dissertation ist an der TU Wien Bibliothek verfügbar.

The approved original version of this doctoral thesis is available in print at TU Wien Bibliothek.

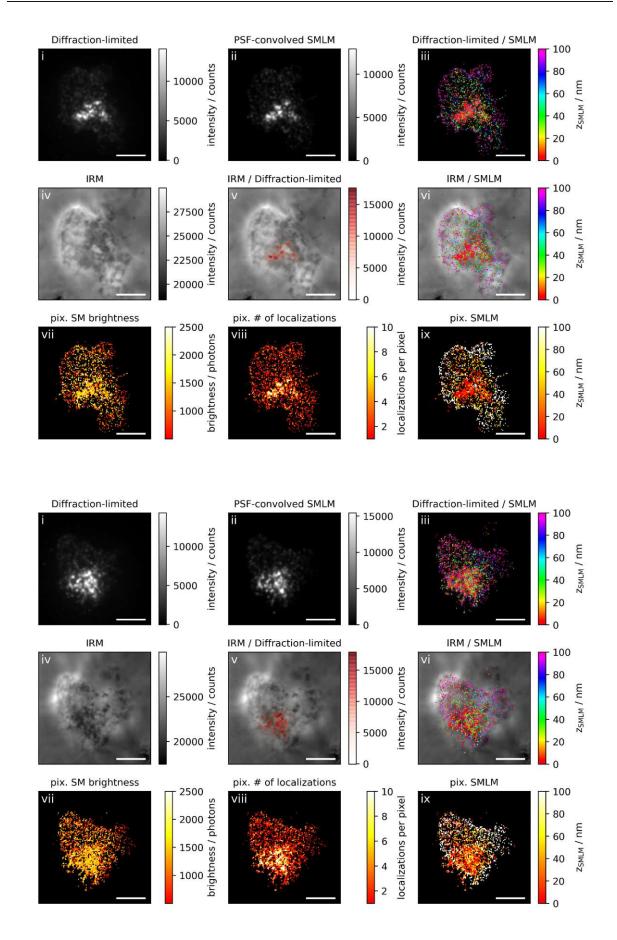
Chapter 4 **Appendix**

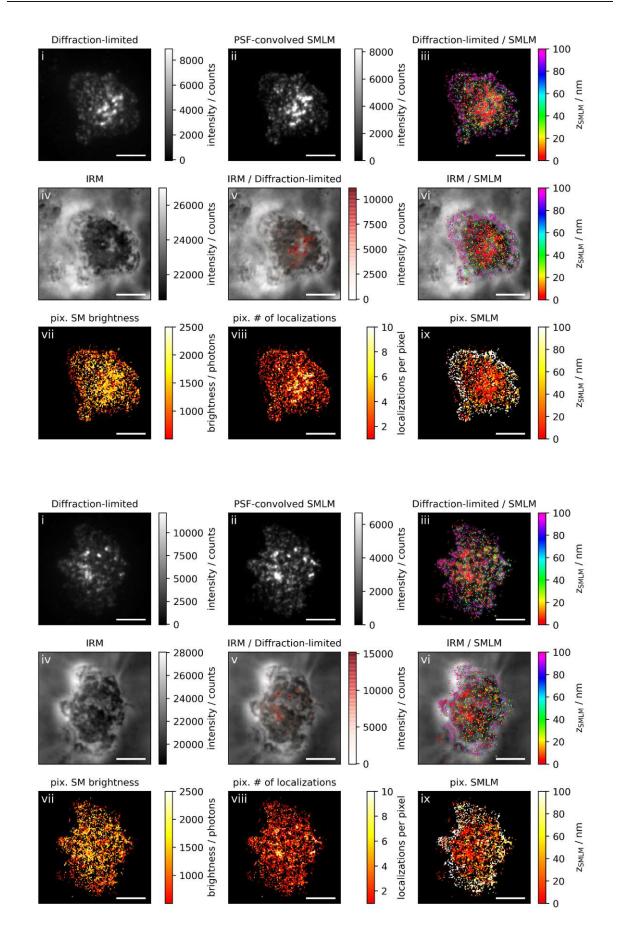
Activating conditions, low ICAM-1 density, fixation: 10 min post seeding

Correlative 3D-SMLM, IRM, and diffraction-limited TIR microscopy of the immunological synapse. T cells were activated on an SLB functionalized with I-Ek/MCC, B7-1 and low density of ICAM-1, and fixed 10 minutes post seeding. The T cell was imaged with IRM and fluorescence microscopy: (i) Diffraction-limited TIR image of the T cell. (ii) Reconstruction of the diffraction-limited image by convolving the 3D-SMLM image with the corresponding psf. (iii) Overlay of the diffractionlimited TIR image with the 3D-SMLM image. Color-code indicates distance to the coverslip z_{SMLM}. (iv) IRM image. (v) Overlay of the IRM image with the diffraction-limited image. (vi) Overlay of the IRM and the 3D-SMLM image. Bottom row images were generated by calculating the pixelwise average of the 3D-SMLM images (pixel size of 146nm is consistent with diffraction-limited image) according to pixelated mean single molecule (SM) intensity (vii), pixelated number of localizations (viii) and pixelated mean z_{SMLM} (ix). Scale bars 5 μm. Taken from (Velas et al. 2021).



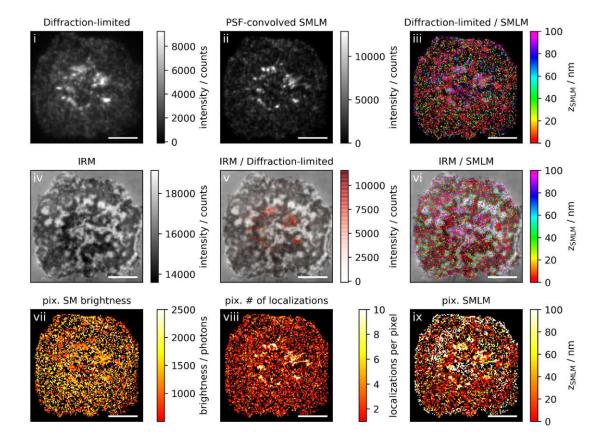




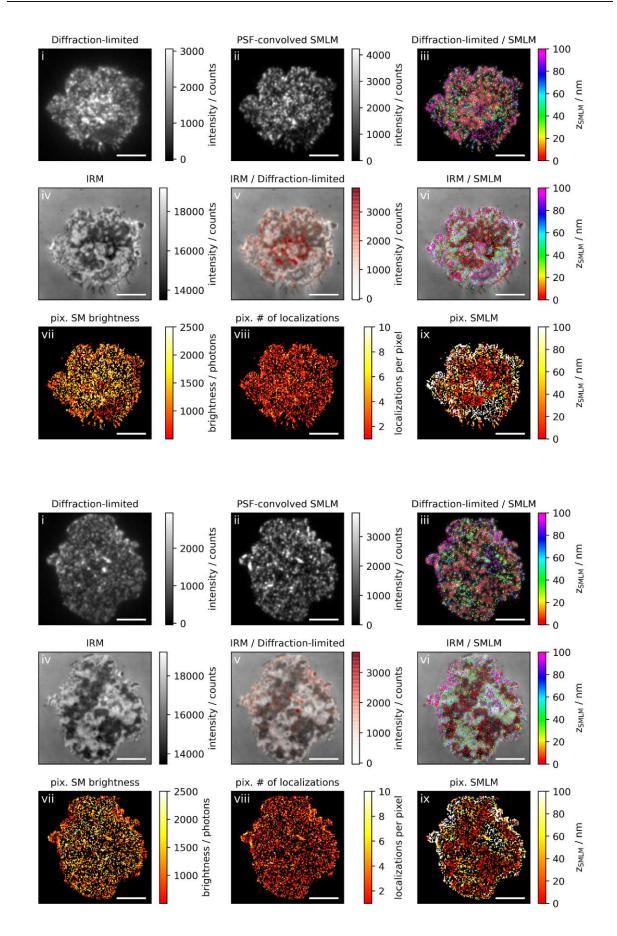


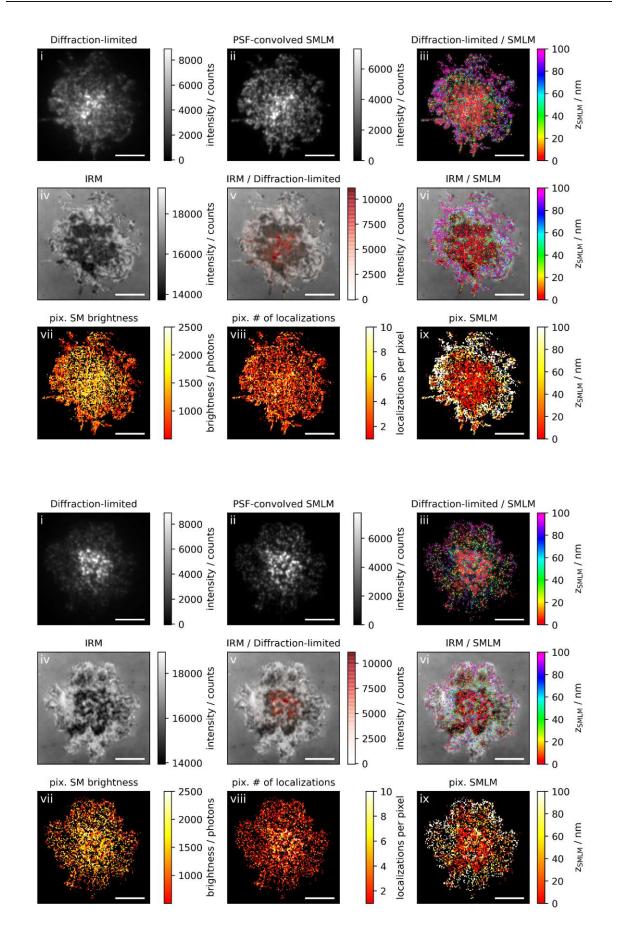
Activating conditions, low ICAM-1 density, fixation: 10-15 min post seeding

Correlative 3D-SMLM, IRM, and diffraction-limited TIR microscopy of the immunological synapse. T cells were activated on an SLB functionalized with I-Ek/MCC, B7-1 and low density of ICAM-1, and fixed 10-15 minutes post seeding. The T cell was imaged with IRM and fluorescence microscopy: (i) Diffraction-limited TIR image of the T cell. (ii) Reconstruction of the diffractionlimited image by convolving the 3D-SMLM image with the corresponding psf. (iii) Overlay of the diffraction-limited TIR image with the 3D-SMLM image. Color-code indicates distance to the coverslip z_{SMLM}. (iv) IRM image. (v) Overlay of the IRM image with the diffraction-limited image. (vi) Overlay of the IRM and the 3D-SMLM image. Bottom row images were generated by calculating the pixel-wise average of the 3D-SMLM images (pixel size of 146nm is consistent with diffraction-limited image) according to pixelated mean single molecule (SM) intensity (vii), pixelated number of localizations (viii) and pixelated mean z_{SMLM} (ix). Scale bars 5 μm. Taken from (Velas et al. 2021).



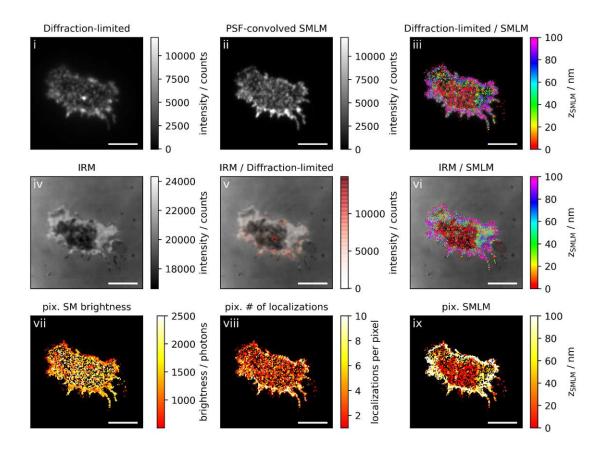


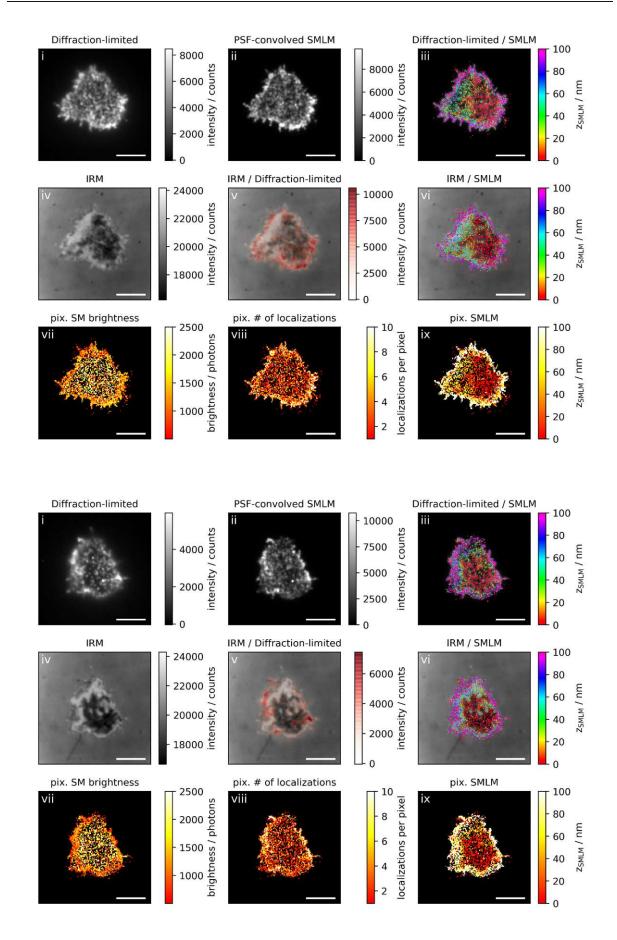


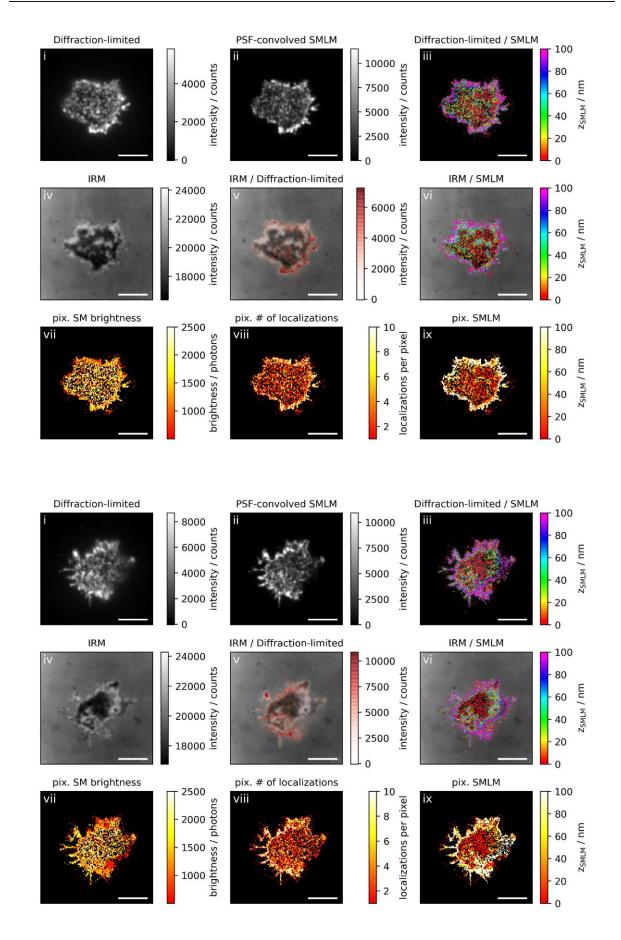


Non-activating conditions, high ICAM-1 density, fixation: 5-10 min post seeding

Correlative 3D-SMLM, IRM, and diffraction-limited TIR microscopy of the immunological synapse. T cells were seeded on an SLB functionalized with high density of ICAM-1, and fixed 5-10 minutes post seeding. The T cell was imaged with IRM and fluorescence microscopy: (i) Diffraction-limited TIR image of the T cell. (ii) Reconstruction of the diffraction-limited image by convolving the 3D-SMLM image with the corresponding psf. (iii) Overlay of the diffraction-limited TIR image with the 3D-SMLM image. Color-code indicates distance to the coverslip z_{SMLM}. (iv) IRM image. (v) Overlay of the IRM image with the diffraction-limited image. (vi) Overlay of the IRM and the 3D-SMLM image. Bottom row images were generated by calculating the pixel-wise average of the 3D-SMLM images (pixel size of 146nm is consistent with diffraction-limited image) according to pixelated mean single molecule (SM) intensity (vii), pixelated number of localizations (viii) and pixelated mean z_{SMLM} (ix). Scale bars 5 μm. Taken from (Velas et al. 2021).

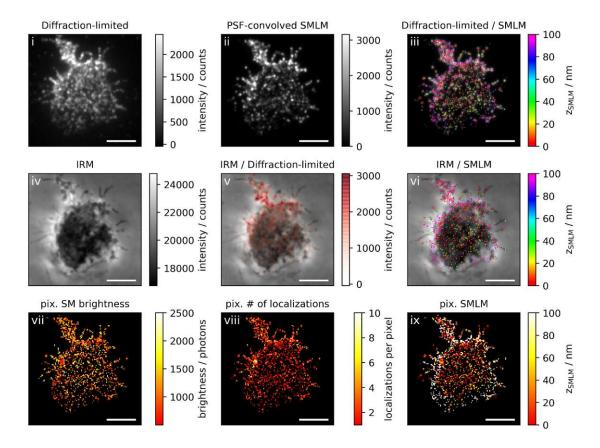


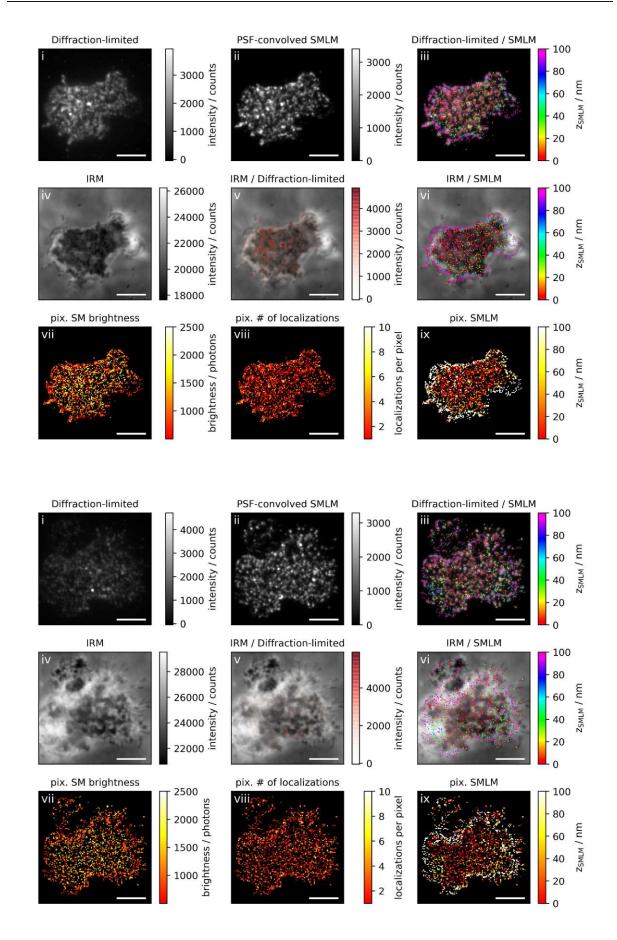


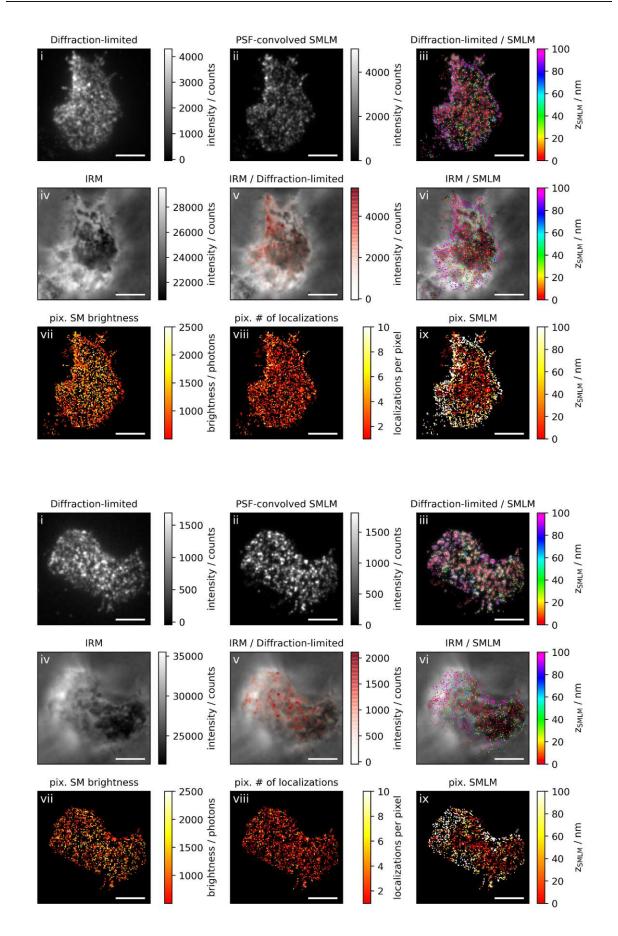


Non-activating conditions, high ICAM-1 density, fixation: 10 min post seeding

Correlative 3D-SMLM, IRM, and diffraction-limited TIR microscopy of the immunological synapse. T cells were seeded on an SLB functionalized with high density of ICAM-1, and fixed 10 minutes post seeding. The T cell was imaged with IRM and fluorescence microscopy: (i) Diffraction-limited TIR image of the T cell. (ii) Reconstruction of the diffraction-limited image by convolving the 3D-SMLM image with the corresponding psf. (iii) Overlay of the diffraction-limited TIR image with the 3D-SMLM image. Color-code indicates distance to the coverslip z_{SMLM}. (iv) IRM image. (v) Overlay of the IRM image with the diffraction-limited image. (vi) Overlay of the IRM and the 3D-SMLM image. Bottom row images were generated by calculating the pixel-wise average of the 3D-SMLM images (pixel size of 146nm is consistent with diffraction-limited image) according to pixelated mean single molecule (SM) intensity (vii), pixelated number of localizations (viii) and pixelated mean z_{SMLM} (ix). Scale bars 5 μm. Taken from (Velas et al. 2021).

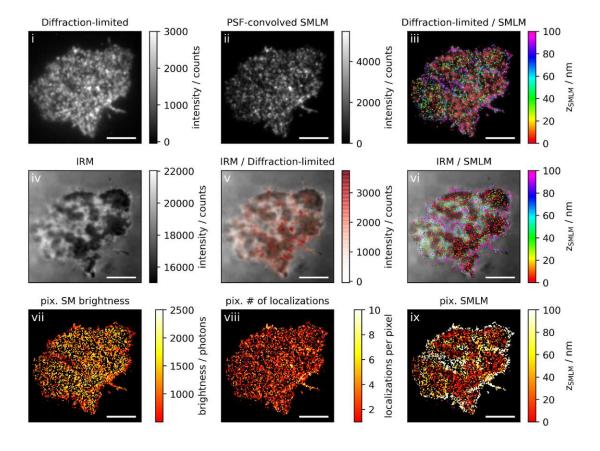




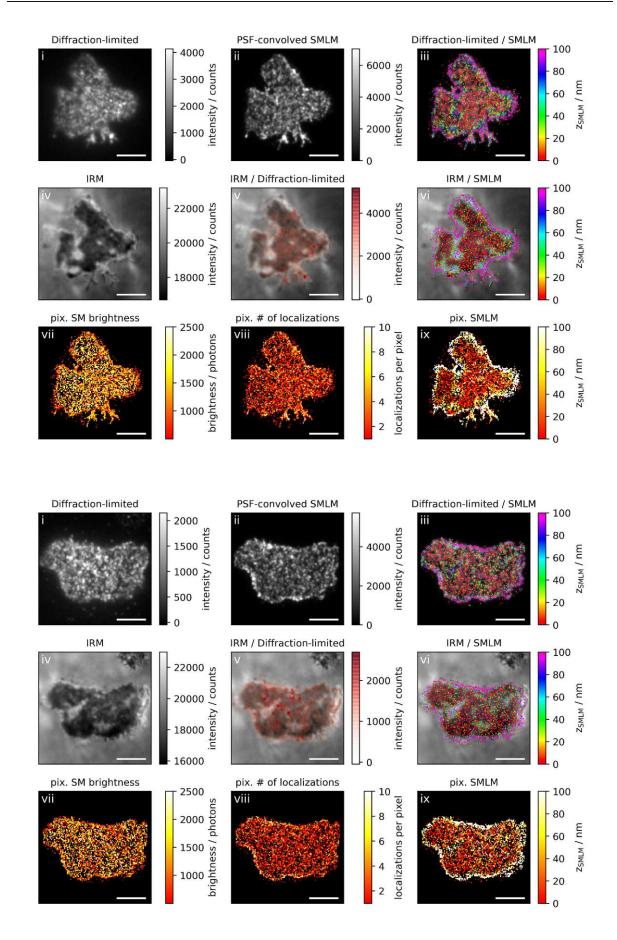


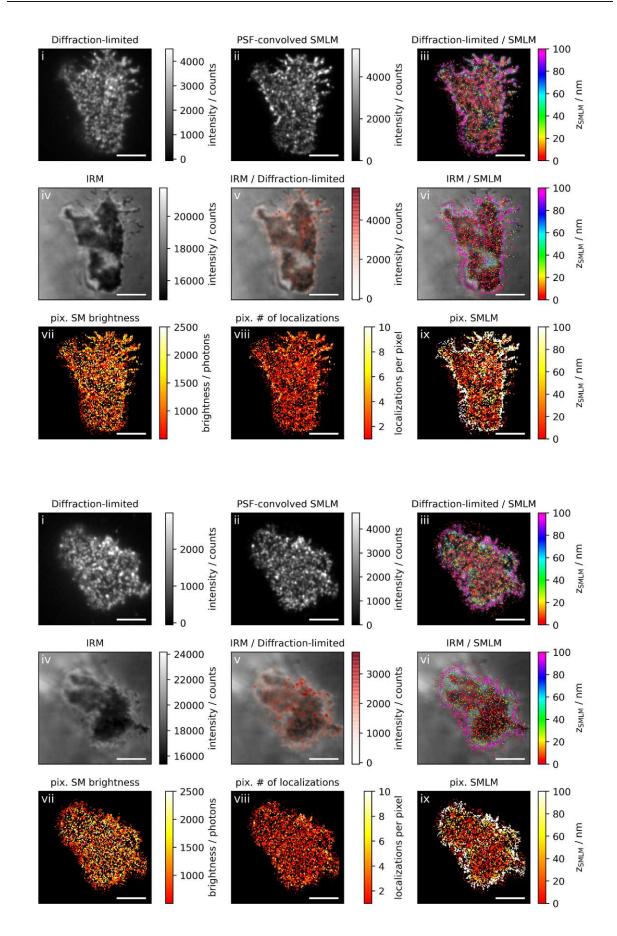
Non-activating conditions, high ICAM-1 density, fixation: 10-15 min post seeding

Correlative 3D-SMLM, IRM, and diffraction-limited TIR microscopy of the immunological synapse. T cells were seeded on an SLB functionalized with high density of ICAM-1, and fixed 10-15 minutes post seeding. The T cell was imaged with IRM and fluorescence microscopy: (i) Diffraction-limited TIR image of the T cell. (ii) Reconstruction of the diffraction-limited image by convolving the 3D-SMLM image with the corresponding psf. (iii) Overlay of the diffraction-limited TIR image with the 3D-SMLM image. Color-code indicates distance to the coverslip z_{SMLM}. (iv) IRM image. (v) Overlay of the IRM image with the diffraction-limited image. (vi) Overlay of the IRM and the 3D-SMLM image. Bottom row images were generated by calculating the pixel-wise average of the 3D-SMLM images (pixel size of 146nm is consistent with diffraction-limited image) according to pixelated mean single molecule (SM) intensity (vii), pixelated number of localizations (viii) and pixelated mean z_{SMLM} (ix). Scale bars 5 μm. Taken from (Velas et al. 2021).



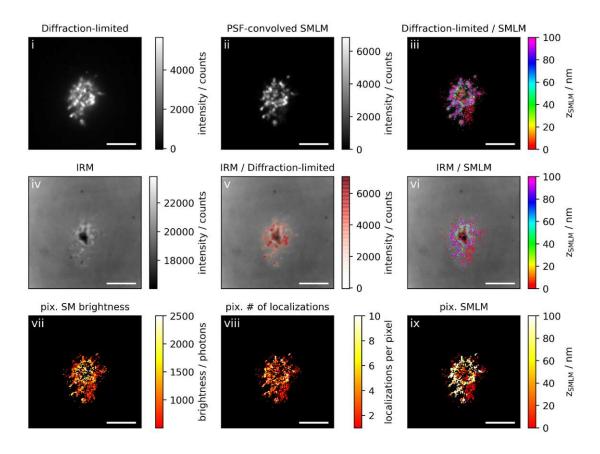


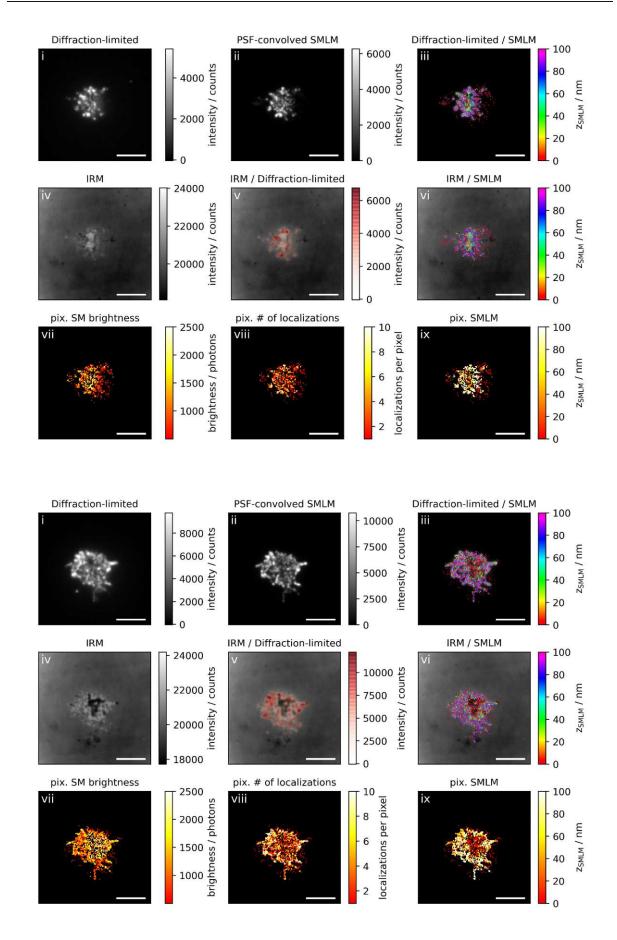


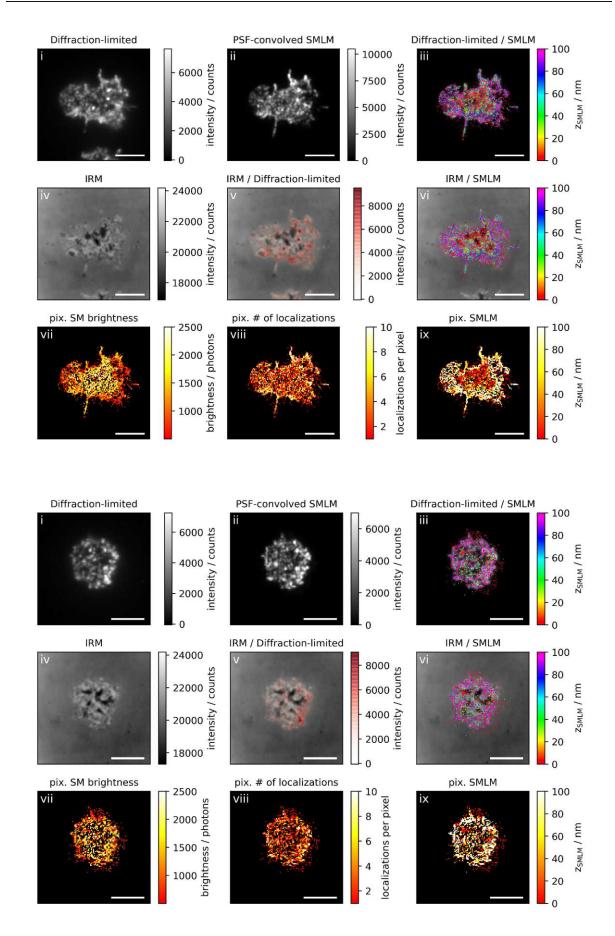


Non-activating conditions, low ICAM-1 density, fixation: 5-10 min post seeding

Correlative 3D-SMLM, IRM, and diffraction-limited TIR microscopy of the immunological synapse. T cells were seeded on an SLB functionalized with low density of ICAM-1, and fixed 5-10 minutes post seeding. The T cell was imaged with IRM and fluorescence microscopy: (i) Diffraction-limited TIR image of the T cell. (ii) Reconstruction of the diffraction-limited image by convolving the 3D-SMLM image with the corresponding psf. (iii) Overlay of the diffraction-limited TIR image with the 3D-SMLM image. Color-code indicates distance to the coverslip z_{SMLM}. (iv) IRM image. (v) Overlay of the IRM image with the diffraction-limited image. (vi) Overlay of the IRM and the 3D-SMLM image. Bottom row images were generated by calculating the pixel-wise average of the 3D-SMLM images (pixel size of 146nm is consistent with diffraction-limited image) according to pixelated mean single molecule (SM) intensity (vii), pixelated number of localizations (viii) and pixelated mean z_{SMLM} (ix). Scale bars 5 μm. Taken from (Velas et al. 2021).





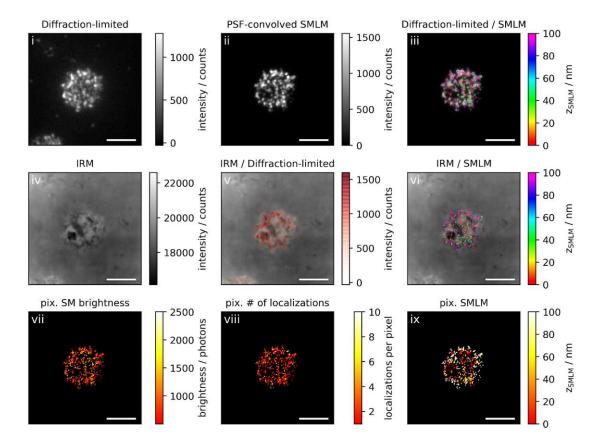


Chapter 4

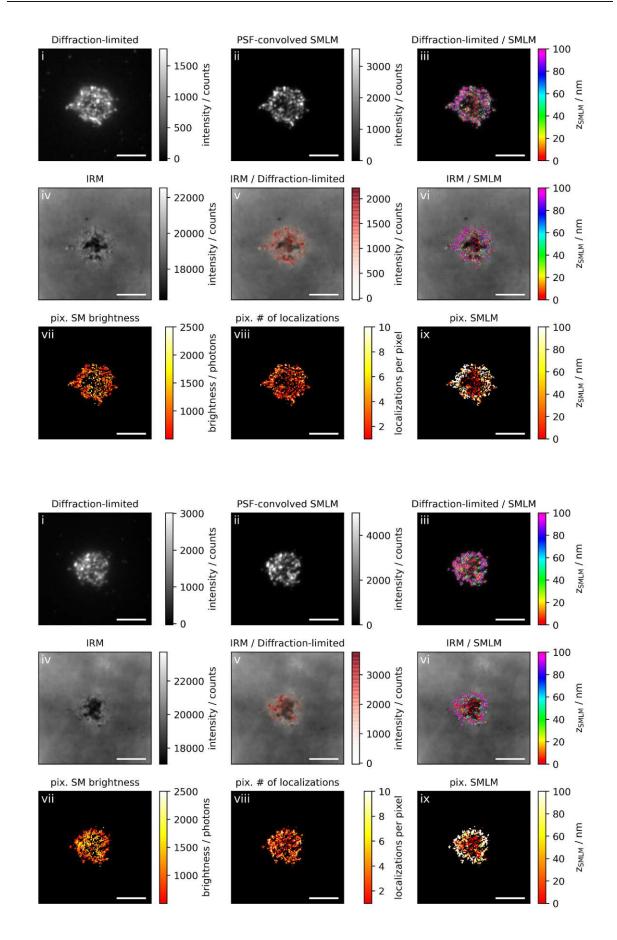
Non-activating conditions, low ICAM-1 density, fixation: 10 min post seeding

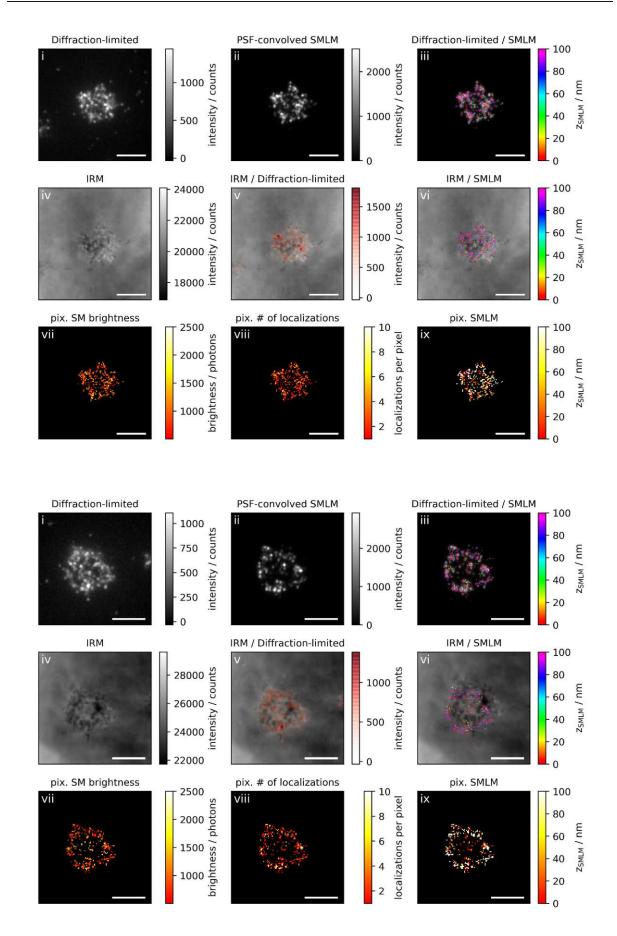
Appendix

Correlative 3D-SMLM, IRM, and diffraction-limited TIR microscopy of the immunological synapse. T cells were seeded on an SLB functionalized with low density of ICAM-1, and fixed 10 minutes post seeding. The T cell was imaged with IRM and fluorescence microscopy: (i) Diffraction-limited TIR image of the T cell. (ii) Reconstruction of the diffraction-limited image by convolving the 3D-SMLM image with the corresponding psf. (iii) Overlay of the diffraction-limited TIR image with the 3D-SMLM image. Color-code indicates distance to the coverslip z_{SMLM}. (iv) IRM image. (v) Overlay of the IRM image with the diffraction-limited image. (vi) Overlay of the IRM and the 3D-SMLM image. Bottom row images were generated by calculating the pixel-wise average of the 3D-SMLM images (pixel size of 146nm is consistent with diffraction-limited image) according to pixelated mean single molecule (SM) intensity (vii), pixelated number of localizations (viii) and pixelated mean z_{SMLM} (ix). Scale bars 5 μm. Taken from (Velas et al. 2021).





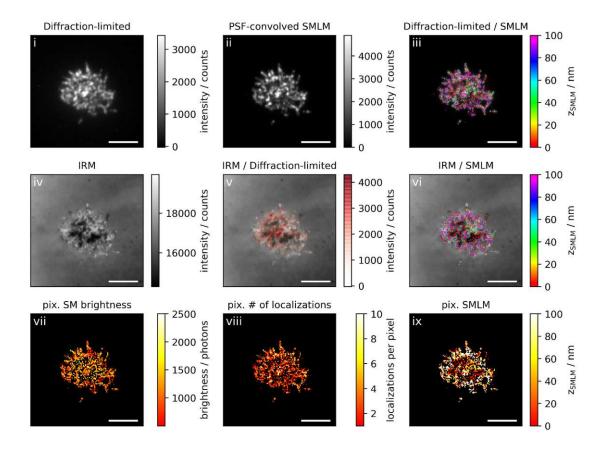




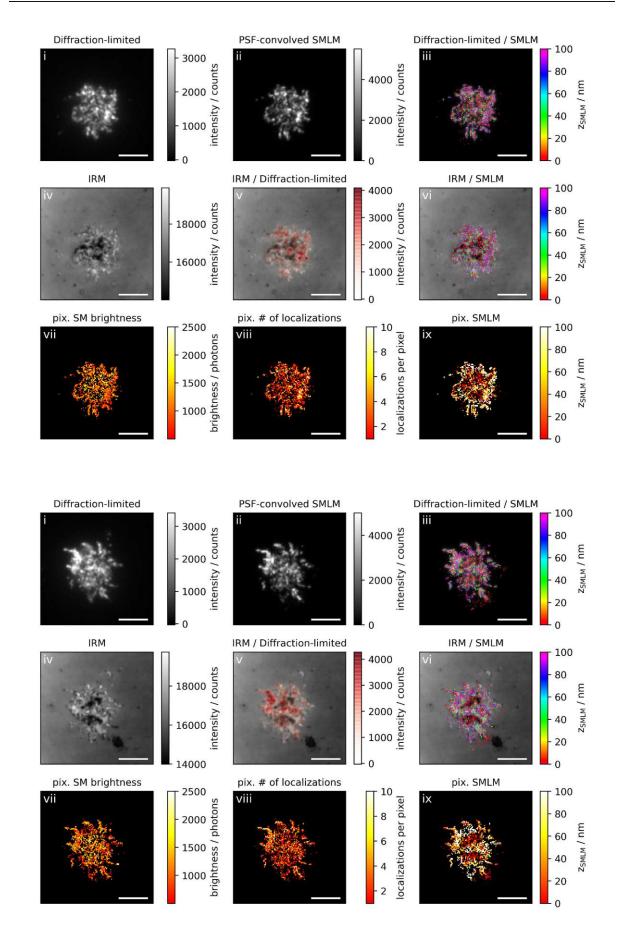
Chapter 4

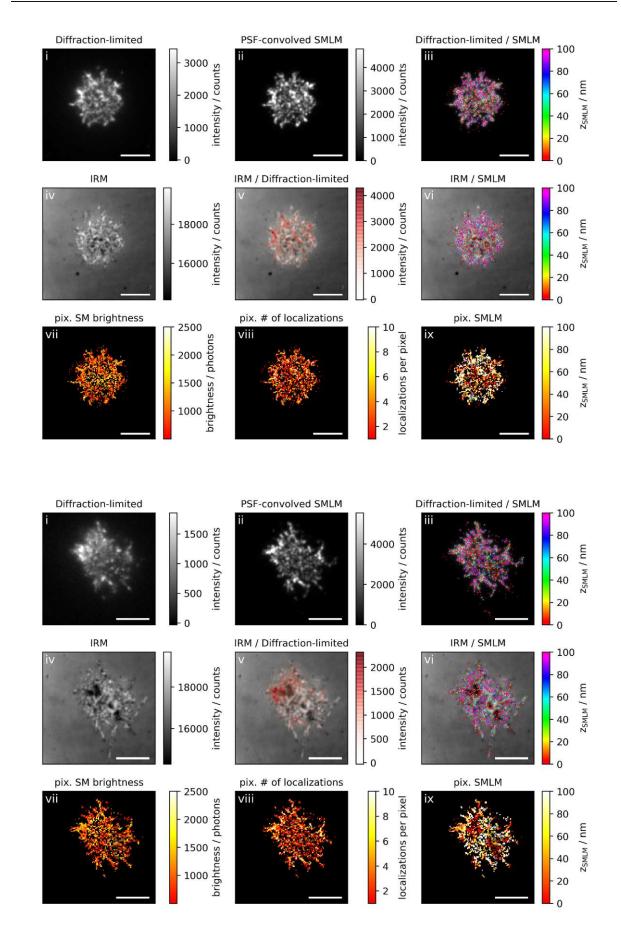
Non-activating conditions, low ICAM-1 density, fixation: 10-15 min post seeding

Correlative 3D-SMLM, IRM, and diffraction-limited TIR microscopy of the immunological synapse. T cells were seeded on an SLB functionalized with low density of ICAM-1, and fixed 10-15 minutes post seeding. The T cell was imaged with IRM and fluorescence microscopy: (i) Diffraction-limited TIR image of the T cell. (ii) Reconstruction of the diffraction-limited image by convolving the 3D-SMLM image with the corresponding psf. (iii) Overlay of the diffraction-limited TIR image with the 3D-SMLM image. Color-code indicates distance to the coverslip z_{SMLM}. (iv) IRM image. (v) Overlay of the IRM image with the diffraction-limited image. (vi) Overlay of the IRM and the 3D-SMLM image. Bottom row images were generated by calculating the pixel-wise average of the 3D-SMLM images (pixel size of 146nm is consistent with diffraction-limited image) according to pixelated mean single molecule (SM) intensity (vii), pixelated number of localizations (viii) and pixelated mean z_{SMLM} (ix). Scale bars 5 μm. Taken from (Velas et al. 2021).









List of Abbreviations

TCR T cell receptor

MHC Major histocompatibility complex

pMHC peptide-Major histocompatibility complex

APC Antigen presenting cell

STORM Stochastic optical reconstruction microscopy

SMLM Single molecule localization microscopy

SLB Supported lipid bilayer

TIRF Total internal reflection fluorescence

SAF Supercritical angle fluorescence

PRR Pattern recognition receptor

BCR B cell receptor

CDR Complementarity-determining region

ITAM Immunoreceptor tyrosine-based activation motif

LAT Linker for activated T cells

IP3 Inositol triphosphate

ER Endoplasmic reticulum

cSMAC Central supramolecular activation cluster

pSMAC Peripheral supramolecular activation cluster

dSMAC Distal supramolecular activation cluster

EDTA Ethylenediaminetetra-acetic acid

LED Light emitting diode

PSF Point spread function

FWHM Full width at half maximum

NA Numerical aperture

EM-CCD Electron-multiplying charge-coupled device

sCMOS Scientific complementary metal-oxide semiconductor

PALM Photoactivated localization microscopy

SIM Structured illumination microscopy

SOFI Super-resolution optical fluctuation imaging

PAINT Point accumulation in nanoscale topography

STED Stimulated emission depletion

SNR Signal to noise ratio

ROI Region of interest

LS Least-squares

MLE Maximum likelihood estimation

CRLB Cramér-Rao lower bound

UAF Undercritical angle fluorescence

IRM Interference reflection microscopy

RICM Reflection interference contrast microscopy

INA Illumination numerical aperture

PBS Phosphate buffer saline

HBSS Hanks' balanced salt solution

BSA Bovine serum albumin

DMEM Dulbecco's Modified Eagle Medium

NEAA Non-essential amino acids

DOPC 1,2-dioleoyl-sn-glycero-3-phosphocholine

DPPC 1,2-dipalmitoyl-sn-glycero-3-phosphocholine

1,2-dioleoyl-sn-glycero-3-[(N-(5-amino-1-arboxypentyl)iminodiacetic Ni-NTA-DGS

acid)succinyl] (nickel salt)

FCS Fetal calf serum

MCC Moth cytochrome C

SUV Small unilamellar vesicle

SALM Supercritical angle localization microscopy

DONALD Direct optical nanoscopy with axially localized detection

BFP Back focal plane

NPC Nuclear pore complex



List of Figures

Figure 1: Overview of the Immune system	6
Figure 2: Macrophages and dendritic cells	7
Figure 3: Overview of adaptive immunity	9
Figure 4: Schematic structure of an antibody molecule and the T cell receptor	10
Figure 5: Structure of the TCR-CD3 complex	12
Figure 6: Schematic structure of MHC class I and MHC class II molecules	13
Figure 7: Schematic structure of the TCR-CD3 complex and CD4 co-receptor	15
Figure 8: Scheme of signaling events	16
Figure 9: Formation of immunological synapse	17
Figure 10: Schematic of the kinetic proofreading model	18
Figure 11: Schematic of the kinetic segregation model	20
Figure 12: Schematic of conformational change model	21
Figure 13: Schematic of ITAM sequestration model	21
Figure 14: Schematic of mechanosensor model	22
Figure 15: Simulated patterns in the adhesion zone	24
Figure 16: Formation of a supported lipid bilayer,	26
Figure 17: Scheme of a T cell interacting with a supported lipid bilayer	27
Figure 18: Jablonski diagram of a fluorophore	29
Figure 19: Excitation and emission spectra of three fluorescent dyes	29
Figure 20: Schematic of an inverted fluorescence microscope	31
Figure 21: Penetration depth δ and normalized intensity at the coverslip	33
Figure 22: Abbe's diffraction limit	34
Figure 23: Process of SMLM	36
Figure 24: Fitting of the pixelated measured signal of a single molecule	37
Figure 25: Localization accuracy and precision	37
Figure 26: Experimental setup for biplane imaging	41
Figure 27: Overview of PSF engineering methods	42
Figure 28: Comparison of CRLB in x, y and z direction for standard, astigmatic, doutetrapod PSFs	
Figure 29: Principle of supercritical angle fluorescence emission	45
Figure 30: Schematic of four channel interference	46



Chapter 4

Figure 31: Mechanisms of transitions between ON- and OFF-states for different dyes	47
Figure 32: Overview of labeling strategies	49
Figure 33: Schematic of a RICM setup	51
Figure 34: Principle of IRM	52
Figure 35: Effects of illumination numerical aperture, multiple interfaces and curved surfaces	53
Figure 36: Comparison of SALM/DONALD and Off-focus imaging	71
Figure 37: Calculated dependency of the localization precision in x, y and z direction on the demagnitude	
Figure 38: Comparison of xy and z localization precisions	73
Figure 40: Addition of a focus hold system for stabilization of z-drift	76
Figure 41: Addition of Interference reflection microscopy to the experimental setup	77
Figure 42: Drift measurement of fluorescent beads along the x, y and z axis	78
Figure 43: Drift of the fluorescent beads after application of an x/y cross-corelative drift corre	
Figure 44: Noll Zernike term expansion for characterization of optical aberrations	79
Figure 45: Characterization of the aberrations of the experimental setup	81
Figure 46: Comparison of the achievable localization precisions for the simulated PSF retrieved the measured data and the aberration-free PSF	
Figure 47: Correction of z-bias caused by field aberrations	82
Figure 48: 3D SMLM on a glass sphere	84
Figure 49: 3D SMLM on 30 nm DNA origami nanorulers	86
Figure 50: 3D SMLM on nuclear pore complexes	88
Figure 51: Histogram of localization precision in x, y and z direction	89
Figure 52: Control experiment on a fluorescently labeled glass sphere	92
Figure 53: Histogram of localization precision in x, y and z direction	93
Figure 54: Correlative 3D SMLM and IRM within the immunological synapse	94
Figure 55: Release of intracellular calcium assessed via the median FURA-2 ratio	95
Figure 56: Histogram of zSMLM positions in the area of the lamellipodium	95
Figure 57: Correlative 3D SMLM, IRM, and diffraction-limited TIR microscopy of the immunol synapse	_
Figure 58: Correlative 3D SMLM, IRM, and diffraction-limited TIR microscopy of the immunol synapse	_
Figure 59: Intensity thresholding	99

Appendix

Chapter 4

Figure 60: Disentangling single molecule brightness and molecular enrichment in TCR microclusters99
Figure 61: Correlative 3D SMLM, IRM, and diffraction-limited TIR microscopy of the immunological synapse
Figure 62: Correlative 3D SMLM, IRM, and diffraction-limited TIR microscopy of the immunological synapse
Figure 63: Selecting the appropriate parameters for correction of overcounts
Figure 64: Contact analysis for T cells recorded under activating and non-activating conditions 105

Bibliography

Abbas, AK, AH Lichtman, and P Shiv. 2015. 'Cellular and molecular immunology, 8 edn: Elsevier'. Abbe, Ernst. 1873. 'Beiträge zur Theorie des Mikroskops und der mikroskopischen Wahrnehmung', Archiv für mikroskopische Anatomie, 9: 413-68.

- Abraham, Anish V, Sripad Ram, Jerry Chao, ES Ward, and Raimund J Ober. 2009. 'Quantitative study of single molecule location estimation techniques', Optics express, 17: 23352-73.
- Abraham, Vivek C., Vijaykumar Krishnamurthi, D. Lansing Taylor, and Frederick Lanni. 1999. 'The Actin-Based Nanomachine at the Leading Edge of Migrating Cells', Biophysical Journal, 77: 1721-32.
- Adler, Jeremy, Andrew I Shevchuk, Pavel Novak, Yuri E Korchev, and Ingela Parmryd. 2010. 'Plasma membrane topography and interpretation of single-particle tracks', Nature methods, 7: 170-
- Al-Aghbar, Mohammad Ameen, Yeh-Shiu Chu, Bing-Mae Chen, and Steve R. Roffler. 2018. 'High-Affinity Ligands Can Trigger T Cell Receptor Signaling Without CD45 Segregation', Frontiers in Immunology, 9.
- Allan, Daniel B, Thomas Caswell, Nathan C. Keim, Casper M. van der Wel, and Ruben W. Verweij. 2021. 'trackpy: Trackpy v0.5.0', Zenodo: http://doi.org/10.5281/zenodo.4682814.
- Andresen, Martin, Andre C Stiel, Simon Trowitzsch, Gert Weber, Christian Eggeling, Markus C Wahl, Stefan W Hell, and Stefan Jakobs. 2007. 'Structural basis for reversible photoswitching in Dronpa', Proceedings of the National Academy of Sciences, 104: 13005-09.
- Annibale, Paolo, Stefano Vanni, Marco Scarselli, Ursula Rothlisberger, and Aleksandra Radenovic. 2011. 'Identification of clustering artifacts in photoactivated localization microscopy', Nature methods, 8: 527-28.
- Axelrod, D., T. P. Burghardt, and N. L. Thompson. 1984. 'Total internal reflection fluorescence', Annu Rev Biophys Bioeng, 13: 247-68.
- Axelrod, Daniel. 2001. 'Selective imaging of surface fluorescence with very high aperture microscope objectives', Journal of biomedical optics, 6: 6-13.
- ——. 2012. 'Fluorescence excitation and imaging of single molecules near dielectric-coated and bare surfaces: a theoretical study', Journal of microscopy, 247: 147-60.
- Backer, Adam S, Mikael P Backlund, Matthew D Lew, and W Esco Moerner. 2013. 'Single-molecule orientation measurements with a quadrated pupil', Optics letters, 38: 1521-23.
- Balagopalan, L., N. P. Coussens, E. Sherman, L. E. Samelson, and C. L. Sommers. 2010. 'The LAT story: a tale of cooperativity, coordination, and choreography', Cold Spring Harb Perspect Biol, 2: a005512.
- Balagopalan, L., E. Sherman, V. A. Barr, and L. E. Samelson. 2011. 'Imaging techniques for assaying lymphocyte activation in action', Nat Rev Immunol, 11: 21-33.
- Betzig, Eric, George H Patterson, Rachid Sougrat, O Wolf Lindwasser, Scott Olenych, Juan S Bonifacino, Michael W Davidson, Jennifer Lippincott-Schwartz, and Harald F Hess. 2006. 'Imaging intracellular fluorescent proteins at nanometer resolution', Science, 313: 1642-45.
- Blom, Hans, and Jerker Widengren. 2017. 'Stimulated emission depletion microscopy', Chemical reviews, 117: 7377-427.
- Born, Max, and Emil Wolf. 2013. Principles of optics: electromagnetic theory of propagation, interference and diffraction of light (Elsevier).
- Borroto, Aldo, Irene Arellano, Raquel Blanco, Manuel Fuentes, Alberto Orfao, Elaine P Dopfer, Marek Prouza, Miloslav Suchànek, Wolfgang W Schamel, and Balbino Alarcón. 2014. 'Relevance of Nck–CD3ε interaction for T cell activation in vivo', *The Journal of Immunology*, 192: 2042-53.
- Bossi, Mariano, Jonas Fölling, Vladimir N Belov, Vadim P Boyarskiy, Rebecca Medda, Alexander Egner, Christian Eggeling, Andreas Schönle, and Stefan W Hell. 2008. 'Multicolor far-field fluorescence nanoscopy through isolated detection of distinct molecular species', Nano letters, 8: 2463-68.

Botcherby, Edward J, Rimas Juskaitis, Martin J Booth, and Tony Wilson. 2007. 'Aberration-free optical refocusing in high numerical aperture microscopy', Optics letters, 32.

- Bourg, Nicolas, Céline Mayet, Guillaume Dupuis, Thomas Barroca, Pierre Bon, Sandrine Lécart, Emmanuel Fort, and Sandrine Lévêque-Fort. 2015. 'Direct optical nanoscopy with axially localized detection', *Nature Photonics*, 9: 587-93.
- Brameshuber, M., F. Kellner, B. K. Rossboth, H. Ta, K. Alge, E. Sevcsik, J. Gohring, M. Axmann, F. Baumgart, N. R. J. Gascoigne, S. J. Davis, H. Stockinger, G. J. Schutz, and J. B. Huppa. 2018. 'Monomeric TCRs drive T cell antigen recognition', Nat Immunol, 19: 487-96.
- Brian, Adrienne A, and Harden M McConnell. 1984. 'Allogeneic stimulation of cytotoxic T cells by supported planar membranes', Proceedings of the National Academy of Sciences, 81: 6159-
- Bunnell, Stephen C, Valarie A Barr, Claudette L Fuller, and Lawrence E Samelson. 2003. 'Highresolution multicolor imaging of dynamic signaling complexes in T cells stimulated by planar substrates', Science's STKE, 2003: pl8-pl8.
- Cabriel, Clément, Nicolas Bourg, Guillaume Dupuis, and Sandrine Lévêque-Fort. 2018. 'Aberrationaccounting calibration for 3D single-molecule localization microscopy', Optics letters, 43: 174-77.
- Cai, En, Kyle Marchuk, Peter Beemiller, Casey Beppler, Matthew G Rubashkin, Valerie M Weaver, Audrey Gérard, Tsung-Li Liu, Bi-Chang Chen, Eric Betzig, Frederic Bartumeus, and Matthew F Krummel. 2017. 'Visualizing dynamic microvillar search and stabilization during ligand detection by T cells', Science (New York, NY), 356.
- Cai, Haogang, James Muller, David Depoil, Viveka Mayya, Michael P. Sheetz, Michael L. Dustin, and Shalom J. Wind. 2018. 'Full control of ligand positioning reveals spatial thresholds for T cell receptor triggering', Nature Nanotechnology, 13: 610–17.
- Campi, G., R. Varma, and M. L. Dustin. 2005. 'Actin and agonist MHC-peptide complex-dependent T cell receptor microclusters as scaffolds for signaling', J Exp Med, 202: 1031-6.
- Cartwright, Adam N. R., Jeremy Griggs, and Daniel M. Davis. 2014. 'The immune synapse clears and excludes molecules above a size threshold', Nature communications, 5: 5479.
- Chakraborty, Arup K, and Arthur Weiss. 2014. 'Insights into the initiation of TCR signaling', Nature immunology, 15: 798-807.
- Chang, V. T., R. A. Fernandes, K. A. Ganzinger, S. F. Lee, C. Siebold, J. McColl, P. Jonsson, M. Palayret, K. Harlos, C. H. Coles, E. Y. Jones, Y. Lui, E. Huang, R. J. C. Gilbert, D. Klenerman, A. R. Aricescu, and S. J. Davis. 2016. 'Initiation of T cell signaling by CD45 segregation at 'close contacts", Nat Immunol, 17: 574-82.
- Chao, Jerry, E Sally Ward, and Raimund J Ober. 2016. 'Fisher information theory for parameter estimation in single molecule microscopy: tutorial', JOSA A, 33: B36-B57.
- Cheezum, Michael K, William F Walker, and William H Guilford. 2001. 'Quantitative comparison of algorithms for tracking single fluorescent particles', Biophysical Journal, 81: 2378-88.
- Chen, Kevin Y, Edward Jenkins, Markus Körbel, Aleks Ponjavic, Anna H Lippert, Ana Mafalda Santos, Nicole Ashman, Caitlin O'Brien-Ball, Jemma McBride, and David Klenerman. 2021. 'Trapping or slowing the diffusion of T cell receptors at close contacts initiates T cell signaling', Proceedings of the National Academy of Sciences, 118: e2024250118.
- Cheng, Ching-Ya, and Chia-Lung Hsieh. 2017. 'Background estimation and correction for highprecision localization microscopy', ACS Photonics, 4: 1730-39.
- Choudhuri, Kaushik, Jaime Llodra, Eric W. Roth, Jones Tsai, Susana Gordo, Kai W. Wucherpfennig, Lance C. Kam, David L. Stokes, and Michael L. Dustin. 2014. 'Polarized release of T-cellreceptor-enriched microvesicles at the immunological synapse', Nature, 507: 118-23.
- Choudhuri, Kaushik, David Wiseman, Marion H Brown, Keith Gould, and P Anton van der Merwe. 2005. 'T-cell receptor triggering is critically dependent on the dimensions of its peptide-MHC ligand', Nature, 436: 578-82.

Cordoba, Shaun-Paul, Kaushik Choudhuri, Hao Zhang, Marcus Bridge, Alp Bugra Basat, Michael L Dustin, and P Anton van der Merwe. 2013. 'The large ectodomains of CD45 and CD148 regulate their segregation from and inhibition of ligated T-cell receptor', Blood, The Journal of the American Society of Hematology, 121: 4295-302.

- Courtney, A. H., W. L. Lo, and A. Weiss. 2018. 'TCR Signaling: Mechanisms of Initiation and Propagation', Trends Biochem Sci, 43: 108-23.
- Courtney, Adam H., Alexey A. Shvets, Wen Lu, Gloria Griffante, Marianne Mollenauer, Veronika Horkova, Wan-Lin Lo, Steven Yu, Ondrej Stepanek, Arup K. Chakraborty, and Arthur Weiss. 2019. 'CD45 functions as a signaling gatekeeper in T cells', Science Signaling, 12: eaaw8151.
- Curtis, A. S. G. 1964. 'The Mechanism of Adhesion of Cells to Glass: A Study by Interference Reflection Microscopy', Journal of Cell Biology, 20: 199-215.
- Daniels, Mark A, Emma Teixeiro, Jason Gill, Barbara Hausmann, Dominique Roubaty, Kaisa Holmberg, Guy Werlen, Georg A Holländer, Nicholas RJ Gascoigne, and Ed Palmer. 2006. 'Thymic selection threshold defined by compartmentalization of Ras/MAPK signalling', Nature, 444: 724-29.
- Davis, S. J., and P. A. van der Merwe. 2006. 'The kinetic-segregation model: TCR triggering and beyond', Nat Immunol, 7: 803-9.
- Dertinger, T., R. Colyer, G. Iyer, S. Weiss, and J. Enderlein. 2009. 'Fast, background-free, 3D superresolution optical fluctuation imaging (SOFI)', Proc Natl Acad Sci U S A, 106: 22287-92.
- Deschamps, Joran, Markus Mund, and Jonas Ries. 2014. '3D superresolution microscopy by supercritical angle detection', Optics express, 22: 29081-91.
- Deschout, Hendrik, Francesca Cella Zanacchi, Michael Mlodzianoski, Alberto Diaspro, Joerg Bewersdorf, Samuel T Hess, and Kevin Braeckmans. 2014. 'Precisely and accurately localizing single emitters in fluorescence microscopy', Nature methods, 11: 253-66.
- Dickson, Robert M, David J Norris, Yih-Ling Tzeng, and WE Moerner. 1996. 'Three-dimensional imaging of single molecules solvated in pores of poly (acrylamide) gels', Science, 274: 966-68.
- Diekmann, Robin, Maurice Kahnwald, Andreas Schoenit, Joran Deschamps, Ulf Matti, and Jonas Ries. 2020. 'Optimizing imaging speed and excitation intensity for single-molecule localization microscopy', Nature methods, 17: 909-12.
- Dobrucki, Jurek W, and Ulrich Kubitscheck. 2017. 'Fluorescence microscopy', Fluoresc. Microsc. From Princ. to Biol. Appl, 2: 85-132.
- Dong, De, Lvqin Zheng, Jianquan Lin, Bailing Zhang, Yuwei Zhu, Ningning Li, Shuangyu Xie, Yuhang Wang, Ning Gao, and Zhiwei Huang. 2019. 'Structural basis of assembly of the human T cell receptor-CD3 complex', Nature, 573: 546-52.
- Dustin, M. L., D. E. Golan, D. M. Zhu, J. M. Miller, W. Meier, E. A. Davies, and P. A. van der Merwe. 1997. 'Low affinity interaction of human or rat T cell adhesion molecule CD2 with its ligand aligns adhering membranes to achieve high physiological affinity', J Biol Chem, 272: 30889-
- Dustin, Michael L, and John A Cooper. 2000. 'The immunological synapse and the actin cytoskeleton: molecular hardware for T cell signaling', *Nature immunology*, 1: 23-29.
- Enderlein, Jörg. 1995. 'Maximum-likelihood criterion and single-molecule detection', Applied optics, 34: 514-26.
- Enderlein, Jörg, and Martin Böhmer. 2003. 'Influence of interface-dipole interactions on the efficiency of fluorescence light collection near surfaces', Optics letters, 28: 941-43.
- Ester, Martin, Hans-Peter Kriegel, Jörg Sander, and Xiaowei Xu. 1996. "A density-based algorithm for discovering clusters in large spatial databases with noise." In kdd, 226-31.
- Fernandes, R. A., K. A. Ganzinger, J. C. Tzou, P. Jonsson, S. F. Lee, M. Palayret, A. M. Santos, A. R. Carr, A. Ponjavic, V. T. Chang, C. Macleod, B. C. Lagerholm, A. E. Lindsay, O. Dushek, A. Tilevik, S. J. Davis, and D. Klenerman. 2019. 'A cell topography-based mechanism for ligand discrimination by the T cell receptor', *Proc Natl Acad Sci U S A*, 116: 14002-10.

Fernandes, Ricardo A, Chao Yu, Alexandre M Carmo, Edward J Evans, P Anton van der Merwe, and Simon J Davis. 2010. 'What controls T cell receptor phosphorylation?', Cell, 142: 668-69.

- Fernandes, Ricardo A., Kristina A. Ganzinger, Justin C. Tzou, Peter Jönsson, Steven F. Lee, Matthieu Palayret, Ana Mafalda Santos, Alexander R. Carr, Aleks Ponjavic, Veronica T. Chang, Charlotte Macleod, B. Christoffer Lagerholm, Alan E. Lindsay, Omer Dushek, Andreas Tilevik, Simon J. Davis, and David Klenerman. 2019. 'A cell topography-based mechanism for ligand discrimination by the T cell receptor', Proceedings of the National Academy of Sciences, 116: 14002-10.
- Fritzsche, M., R. A. Fernandes, V. T. Chang, H. Colin-York, M. P. Clausen, J. H. Felce, S. Galiani, C. Erlenkamper, A. M. Santos, J. M. Heddleston, I. Pedroza-Pacheco, D. Waithe, J. B. de la Serna, B. C. Lagerholm, T. L. Liu, T. L. Chew, E. Betzig, S. J. Davis, and C. Eggeling. 2017. 'Cytoskeletal actin dynamics shape a ramifying actin network underpinning immunological synapse formation', Sci Adv, 3: e1603032.
- Fritzsche, Marco, and Michael L Dustin. 2018. 'Organization of immunological synapses and kinapses.' in, Structural Biology in Immunology (Elsevier).
- Fu, Yan, Peter W Winter, Raul Rojas, Victor Wang, Matthew McAuliffe, and George H Patterson. 2016. 'Axial superresolution via multiangle TIRF microscopy with sequential imaging and photobleaching', *Proceedings of the National Academy of Sciences*, 113: 4368-73.
- Furukawa, Tatsuhiko, Michiyasu Itoh, Neil X Krueger, Michel Streuli, and Haruo Saito. 1994. 'Specific interaction of the CD45 protein-tyrosine phosphatase with tyrosine-phosphorylated CD3 zeta chain', Proceedings of the National Academy of Sciences, 91: 10928-32.
- Gahlmann, Andreas, Jerod L Ptacin, Ginni Grover, Sean Quirin, Lexy von Diezmann, Marissa K Lee, Mikael P Backlund, Lucy Shapiro, Rafael Piestun, and WE Moerner. 2013. 'Quantitative multicolor subdiffraction imaging of bacterial protein ultrastructures in three dimensions', Nano letters, 13: 987-93.
- Ganti, Raman S, Wan-Lin Lo, Darren B McAffee, Jay T Groves, Arthur Weiss, and Arup K Chakraborty. 2020. 'How the T cell signaling network processes information to discriminate between self and agonist ligands', Proceedings of the National Academy of Sciences, 117: 26020-30.
- Geiger, Benjamin, Zafrira Avnur, Thomas E Kreis, and Joseph Schlessinger. 1984. 'The dynamics of cytoskeletal organization in areas of cell contact', The Cytoskeleton: 195-234.
- Geisler, Claudia, Thomas Hotz, Andreas Schönle, Stefan W Hell, Axel Munk, and Alexander Egner. 2012. 'Drift estimation for single marker switching based imaging schemes', Optics express, 20: 7274-89.
- Gibson, Sarah Frisken, and Frederick Lanni. 1991. 'Experimental test of an analytical model of aberration in an oil-immersion objective lens used in three-dimensional light microscopy', *JOSA A*, 8: 1601-13.
- Gil, Diana, Wolfgang W. A. Schamel, María Montoya, Francisco Sánchez-Madrid, and Balbino Alarcón. 2002. 'Recruitment of Nck by CD3 Reveals a Ligand-Induced Conformational Change Essential for T Cell Receptor Signaling and Synapse Formation', Cell, 109: 901-12.
- Gizeli, Electra, and Johanna Glad. 2004. 'Single-step formation of a biorecognition layer for assaying histidine-tagged proteins', Analytical chemistry, 76: 3995-4001.
- Göhring, Janett, Florian Kellner, Lukas Schrangl, René Platzer, Enrico Klotzsch, Hannes Stockinger, Johannes B Huppa, and Gerhard J Schütz. 2021. 'Temporal analysis of T-cell receptorimposed forces via quantitative single molecule FRET measurements', Nature communications, 12: 1-14.
- Goodman, Joseph W. 2005. 'Introduction to Fourier Optics, Roberts & Co', Publishers, Englewood, Colorado.
- Grakoui, A., S. K. Bromley, C. Sumen, M. M. Davis, A. S. Shaw, P. M. Allen, and M. L. Dustin. 1999. 'The immunological synapse: a molecular machine controlling T cell activation', Science, 285:
- Gray, Noah. 2009. 'Knowing the limit', Nature Cell Biology, 11: S8-S8.



Greengard, Adam, Yoav Y Schechner, and Rafael Piestun. 2006. 'Depth from diffracted rotation', *Optics letters*, 31: 181-83.

- Grimm, Jonathan B, Brian P English, Heejun Choi, Anand K Muthusamy, Brian P Mehl, Peng Dong, Timothy A Brown, Jennifer Lippincott-Schwartz, Zhe Liu, and Timothée Lionnet. 2016. 'Bright photoactivatable fluorophores for single-molecule imaging', Nature methods, 13: 985-88.
- Grover, Ginni, Sean Quirin, Callie Fiedler, and Rafael Piestun. 2011. 'Photon efficient double-helix PSF microscopy with application to 3D photo-activation localization imaging', Biomedical Optics Express, 2: 3010-20.
- Groves, Jay T, and Michael L Dustin. 2003. 'Supported planar bilayers in studies on immune cell adhesion and communication', Journal of immunological methods, 278: 19-32.
- Gustafsson, Mats GL. 2000. 'Surpassing the lateral resolution limit by a factor of two using structured illumination microscopy', *Journal of microscopy*, 198: 82-87.
- Hajj, Bassam, Mohamed El Beheiry, Ignacio Izeddin, Xavier Darzacq, and Maxime Dahan. 2014. 'Accessing the third dimension in localization-based super-resolution microscopy', Physical Chemistry Chemical Physics, 16: 16340-48.
- Hanser, Bridget M, Mats GL Gustafsson, DA Agard, and John W Sedat. 2004. 'Phase-retrieved pupil functions in wide-field fluorescence microscopy', Journal of microscopy, 216: 32-48.
- Hashimoto-Tane, Akiko, and Takashi Saito. 2016. 'Dynamic Regulation of TCR-Microclusters and the Microsynapse for T Cell Activation', Frontiers in Immunology, 7: 255.
- Hashimoto-Tane, Akiko, Tadashi Yokosuka, Kumiko Sakata-Sogawa, Machie Sakuma, Chitose Ishihara, Makio Tokunaga, and Takashi Saito. 2011. 'Dynein-Driven Transport of T Cell Receptor Microclusters Regulates Immune Synapse Formation and T Cell Activation', Immunity, 34: 919-31.
- Heilemann, Mike, Sebastian Van De Linde, Anindita Mukherjee, and Markus Sauer. 2009. 'Superresolution imaging with small organic fluorophores', Angewandte Chemie International Edition, 48: 6903-08.
- Heilemann, Mike, Sebastian Van De Linde, Mark Schüttpelz, Robert Kasper, Britta Seefeldt, Anindita Mukherjee, Philip Tinnefeld, and Markus Sauer. 2008. 'Subdiffraction-resolution fluorescence imaging with conventional fluorescent probes', Angewandte Chemie International Edition, 47: 6172-76.
- Hell, Stefan, and Ernst HK Stelzer. 1992. 'Properties of a 4Pi confocal fluorescence microscope', JOSA A, 9: 2159-66.
- Hell, Stefan W, and Jan Wichmann. 1994. 'Breaking the diffraction resolution limit by stimulated emission: stimulated-emission-depletion fluorescence microscopy', Optics letters, 19: 780-
- Hellmeier, Joschka, Rene Platzer, Alexandra S. Eklund, Thomas Schlichthaerle, Andreas Karner, Viktoria Motsch, Magdalena C. Schneider, Elke Kurz, Victor Bamieh, Mario Brameshuber, Johannes Preiner, Ralf Jungmann, Hannes Stockinger, Gerhard J. Schütz, Johannes B. Huppa, and Eva Sevcsik. 2021. 'DNA origami demonstrate the unique stimulatory power of single pMHCs as T cell antigens', Proceedings of the National Academy of Sciences, 118: e2016857118.
- Hess, Samuel T, Thanu PK Girirajan, and Michael D Mason. 2006. 'Ultra-high resolution imaging by fluorescence photoactivation localization microscopy', Biophysical Journal, 91: 4258-72.
- Hoerter, John AH, Joanna Brzostek, Maxim N Artyomov, Steven M Abel, Javier Casas, Vasily Rybakin, Jeanette Ampudia, Carina Lotz, Janet M Connolly, and Arup K Chakraborty. 2013. 'Coreceptor affinity for MHC defines peptide specificity requirements for TCR interaction with coagonist peptide–MHC', Journal of Experimental Medicine, 210: 1807-21.
- Holler, Phillip D, and David M Kranz. 2003. 'Quantitative analysis of the contribution of TCR/pepMHC affinity and CD8 to T cell activation', *Immunity*, 18: 255-64.



Hu, J., R. Lipowsky, and T. R. Weikl. 2013. 'Binding constants of membrane-anchored receptors and ligands depend strongly on the nanoscale roughness of membranes', Proc Natl Acad Sci U S A, 110: 15283-8.

- Huang, Bo, Sara A Jones, Boerries Brandenburg, and Xiaowei Zhuang. 2008. 'Whole-cell 3D STORM reveals interactions between cellular structures with nanometer-scale resolution', Nature methods, 5: 1047-52.
- Huang, Bo, Wengin Wang, Mark Bates, and Xiaowei Zhuang. 2008. 'Three-dimensional superresolution imaging by stochastic optical reconstruction microscopy', Science, 319: 810-13.
- Huang, Jun, Mario Brameshuber, Xun Zeng, Jianming Xie, Qi-jing Li, Yueh-hsiu Chien, Salvatore Valitutti, and Mark M Davis. 2013. 'A single peptide-major histocompatibility complex ligand triggers digital cytokine secretion in CD4+ T cells', Immunity, 39: 846-57.
- Huppa, J. B., M. Gleimer, C. Sumen, and M. M. Davis. 2003. 'Continuous T cell receptor signaling required for synapse maintenance and full effector potential', Nat Immunol, 4: 749-55.
- Huppa, Johannes B, Markus Axmann, Manuel A Mörtelmaier, Björn F Lillemeier, Evan W Newell, Mario Brameshuber, Lawrence O Klein, Gerhard J Schütz, and Mark M Davis. 2010. 'TCRpeptide-MHC interactions in situ show accelerated kinetics and increased affinity', Nature, 463: 963-67.
- Huppa, Johannes B., Markus Axmann, Manuel A. Mortelmaier, Bjorn F. Lillemeier, Evan W. Newell, Mario Brameshuber, Lawrence O. Klein, Gerhard J. Schütz, and Mark M. Davis. 2010. 'TCRpeptide-MHC interactions in situ show accelerated kinetics and increased affinity', Nature, 463: 963-67.
- Irvine, Darrell J, Marco A Purbhoo, Michelle Krogsgaard, and Mark M Davis. 2002. 'Direct observation of ligand recognition by T cells', Nature, 419: 845-49.
- Izeddin, Ignacio, Mohamed El Beheiry, Jordi Andilla, Daniel Ciepielewski, Xavier Darzacq, and Maxime Dahan. 2012. 'PSF shaping using adaptive optics for three-dimensional singlemolecule super-resolution imaging and tracking', Optics express, 20: 4957-67.
- Juette, Manuel F, Travis J Gould, Mark D Lessard, Michael J Mlodzianoski, Bhupendra S Nagpure, Brian T Bennett, Samuel T Hess, and Joerg Bewersdorf. 2008. 'Three-dimensional sub-100 nm resolution fluorescence microscopy of thick samples', Nature methods, 5: 527-29.
- Jung, Y., I. Riven, S. W. Feigelson, E. Kartvelishvily, K. Tohya, M. Miyasaka, R. Alon, and G. Haran. 2016. 'Three-dimensional localization of T-cell receptors in relation to microvilli using a combination of superresolution microscopies', Proc Natl Acad Sci U S A, 113: E5916-E24.
- Jung, Yunmin, Lai Wen, Amnon Altman, and Klaus Ley. 2021. 'CD45 pre-exclusion from the tips of T cell microvilli prior to antigen recognition', Nature communications, 12: 1-16.
- Jungmann, Ralf, Christian Steinhauer, Max Scheible, Anton Kuzyk, Philip Tinnefeld, and Friedrich C Simmel. 2010. 'Single-molecule kinetics and super-resolution microscopy by fluorescence imaging of transient binding on DNA origami', Nano letters, 10: 4756-61.
- Kao, H Pin, and AS1225486 Verkman. 1994. 'Tracking of single fluorescent particles in three dimensions: use of cylindrical optics to encode particle position', Biophysical Journal, 67: 1291-300.
- Kay, Steven M. 1998. 'Fundamentals of statistical signal processing. detection theory, volume ii', Printice Hall PTR: 1545-5971.
- Khan, Javed Mohammed, Harish Reddy Cheruku, Joo Chuan Tong, and Shoba Ranganathan. 2011. 'MPID-T2: a database for sequence—structure—function analyses of pMHC and TR/pMHC structures', Bioinformatics, 27: 1192-93.
- Kiessling, Volker, and Lukas K Tamm. 2003. 'Measuring distances in supported bilayers by fluorescence interference-contrast microscopy: polymer supports and SNARE proteins', Biophysical Journal, 84: 408-18.
- Kim, Sun Taek, Koh Takeuchi, Zhen-Yu J Sun, Maki Touma, Carlos E Castro, Amr Fahmy, Matthew J Lang, Gerhard Wagner, and Ellis L Reinherz. 2009. 'The αβ T cell receptor is an anisotropic mechanosensor', Journal of Biological Chemistry, 284: 31028-37.



Kjer-Nielsen, Lars, Craig S Clements, Anthony W Purcell, Andrew G Brooks, James C Whisstock, Scott R Burrows, James McCluskey, and Jamie Rossjohn. 2003. 'A structural basis for the selection of dominant αβ T cell receptors in antiviral immunity', *Immunity*, 18: 53-64.

- Klein, Teresa, Sven Proppert, and Markus Sauer. 2014. 'Eight years of single-molecule localization microscopy', *Histochemistry and cell biology*, 141: 561-75.
- Klotzsch, Enrico, and Gerhard J Schütz. 2013. 'Improved ligand discrimination by force-induced unbinding of the T cell receptor from peptide-MHC', Biophysical Journal, 104: 1670-75.
- Koretzky, Gary A, Joel Picus, Terrie Schultz, and Arthur Weiss. 1991. 'Tyrosine phosphatase CD45 is required for T-cell antigen receptor and CD2-mediated activation of a protein tyrosine kinase and interleukin 2 production', Proceedings of the National Academy of Sciences, 88: 2037-41.
- Kühner, Martin, and Erich Sackmann. 1996. 'Ultrathin hydrated dextran films grafted on glass: preparation and characterization of structural, viscous, and elastic properties by quantitative microinterferometry', Langmuir, 12: 4866-76.
- Lakowicz, Joseph R. 2013. Principles of fluorescence spectroscopy (Springer science & business media).
- Lang, Kathrin, and Jason W Chin. 2014. 'Cellular incorporation of unnatural amino acids and bioorthogonal labeling of proteins', *Chemical reviews*, 114: 4764-806.
- Lanz, Anna-Lisa, Giulia Masi, Nicla Porciello, André Cohnen, Deborah Cipria, Dheeraj Prakaash, Štefan Bálint, Roberto Raggiaschi, Donatella Galgano, David K. Cole, Marco Lepore, Omer Dushek, Michael L. Dustin, Mark S. P. Sansom, Antreas C. Kalli, and Oreste Acuto. 2021. 'Allosteric activation of T cell antigen receptor signaling by quaternary structure relaxation', Cell Reports, 36: 109531.
- Laugel, Bruno, Hugo A van den Berg, Emma Gostick, David K Cole, Linda Wooldridge, Jonathan Boulter, Anita Milicic, David A Price, and Andrew K Sewell. 2007. 'Different T cell receptor affinity thresholds and CD8 coreceptor dependence govern cytotoxic T lymphocyte activation and tetramer binding properties', Journal of Biological Chemistry, 282: 23799-810.
- Lee, Hsiao-lu D, Steffen J Sahl, Matthew D Lew, and WE Moerner. 2012. 'The double-helix microscope super-resolves extended biological structures by localizing single blinking molecules in three dimensions with nanoscale precision', Applied Physics Letters, 100:
- Lee, Kyeong-Hee, Amy D Holdorf, Michael L Dustin, Andrew C Chan, Paul M Allen, and Andrey S Shaw. 2002. 'T cell receptor signaling precedes immunological synapse formation', Science, 295: 1539-42.
- Lee, Sang Hak, Murat Baday, Marco Tjioe, Paul D Simonson, Ruobing Zhang, En Cai, and Paul R Selvin. 2012. 'Using fixed fiduciary markers for stage drift correction', Optics express, 20: 12177-83.
- Lelek, Mickaël, Melina T Gyparaki, Gerti Beliu, Florian Schueder, Juliette Griffié, Suliana Manley, Ralf Jungmann, Markus Sauer, Melike Lakadamyali, and Christophe Zimmer. 2021. 'Singlemolecule localization microscopy', Nature Reviews Methods Primers, 1: 1-27.
- Li, Yiming, Markus Mund, Philipp Hoess, Joran Deschamps, Ulf Matti, Bianca Nijmeijer, Vilma Jimenez Sabinina, Jan Ellenberg, Ingmar Schoen, and Jonas Ries. 2018. 'Real-time 3D single-molecule localization using experimental point spread functions', Nature methods, 15: 367-69.
- Limozin, L., M. Bridge, P. Bongrand, O. Dushek, P. A. van der Merwe, and P. Robert. 2019. 'TCRpMHC kinetics under force in a cell-free system show no intrinsic catch bond, but a minimal encounter duration before binding', Proc Natl Acad Sci U S A, 116: 16943-48.
- Limozin, Laurent, and Kheya Sengupta. 2007. 'Modulation of vesicle adhesion and spreading kinetics by hyaluronan cushions', Biophysical Journal, 93: 3300-13.
- ———. 2009. 'Quantitative reflection interference contrast microscopy (RICM) in soft matter and cell adhesion', Chemphyschem, 10: 2752-68.
- Lin, Yu, Jane J Long, Fang Huang, Whitney C Duim, Stefanie Kirschbaum, Yongdeng Zhang, Lena K Schroeder, Aleksander A Rebane, Mary Grace M Velasco, and Alejandro Virrueta. 2015.



- 'Quantifying and optimizing single-molecule switching nanoscopy at high speeds', PLoS One, 10: e0128135.
- Liss, Viktoria, Britta Barlag, Monika Nietschke, and Michael Hensel. 2015. 'Self-labelling enzymes as universal tags for fluorescence microscopy, super-resolution microscopy and electron microscopy', Scientific reports, 5: 1-13.
- Liu, B., W. Chen, B. D. Evavold, and C. Zhu. 2014. 'Accumulation of dynamic catch bonds between TCR and agonist peptide-MHC triggers T cell signaling', Cell, 157: 357-68.
- Liu, Wenjie, Kimani C Toussaint Jr, Chukwuemeka Okoro, Dazhao Zhu, Youhua Chen, Cuifang Kuang, and Xu Liu. 2018. 'Breaking the Axial Diffraction Limit: A Guide to Axial Super-Resolution Fluorescence Microscopy', Laser & Photonics Reviews, 12: 1700333.
- Liu, Y., L. Blanchfield, V. P. Ma, R. Andargachew, K. Galior, Z. Liu, B. Evavold, and K. Salaita. 2016. 'DNA-based nanoparticle tension sensors reveal that T-cell receptors transmit defined pN forces to their antigens for enhanced fidelity', Proc Natl Acad Sci U S A, 113: 5610-5.
- Luescher, Immanuel F, Eric Vivier, Andreas Layer, Jérôme Mahiou, François Godeau, Bernard Malissen, and Pedro Romero. 1995. 'CD8 modulation of T-cell antigen receptor-ligand interactions on living cytotoxic T lymphocytes', Nature, 373: 353-56.
- Lukyanov, Konstantin A, Dmitry M Chudakov, Sergey Lukyanov, and Vladislav V Verkhusha. 2005. 'Photoactivatable fluorescent proteins', Nature Reviews Molecular Cell Biology, 6: 885-90.
- Ma, V. P., Y. Liu, L. Blanchfield, H. Su, B. D. Evavold, and K. Salaita. 2016. 'Ratiometric Tension Probes for Mapping Receptor Forces and Clustering at Intermembrane Junctions', Nano Lett, 16: 4552-9.
- Ma, Zhengyu, Kim A Sharp, Paul A Janmey, and Terri H Finkel. 2008. 'Surface-anchored monomeric agonist pMHCs alone trigger TCR with high sensitivity', PLoS biology, 6: e43.
- Macdonald, Patrick J, Susan Gayda, Richard A Haack, Qiaoqiao Ruan, Richard J Himmelsbach, and Sergey Y Tetin. 2018. 'Rhodamine-derived fluorescent dye with inherent blinking behavior for super-resolution imaging', *Analytical chemistry*, 90: 9165-73.
- Manley, Suliana, Jennifer M Gillette, George H Patterson, Hari Shroff, Harald F Hess, Eric Betzig, and Jennifer Lippincott-Schwartz. 2008. 'High-density mapping of single-molecule trajectories with photoactivated localization microscopy', Nature methods, 5: 155-57.
- Mashanov, GI, D Tacon, AE Knight, M Peckham, and Justin E Molloy. 2003. 'Visualizing single molecules inside living cells using total internal reflection fluorescence microscopy', Methods, 29: 142-52.
- McEvoy, Ann L, Hiofan Hoi, Mark Bates, Evgenia Platonova, Paula J Cranfill, Michelle A Baird, Michael W Davidson, Helge Ewers, Jan Liphardt, and Robert E Campbell. 2012. 'mMaple: a photoconvertible fluorescent protein for use in multiple imaging modalities', PLoS One, 7: e51314.
- McKeithan, T. W. 1995. 'Kinetic proofreading in T-cell receptor signal transduction', Proc Natl Acad Sci U S A, 92: 5042-6.
- Meuer, Stefan C, Oreste Acuto, Rebecca E Hussey, James C Hodgdon, Kathleen A Fitzgerald, Stuart F Schlossman, and Ellis L Reinherz. 1983. 'Evidence for the T3-associated 90K heterodimer as the T-cell antigen receptor', Nature, 303: 808-10.
- Michie, Megan S, Ralph Götz, Christian Franke, Matthew Bowler, Nikita Kumari, Valentin Magidson, Marcia Levitus, Jadranka Loncarek, Markus Sauer, and Martin J Schnermann. 2017. 'Cyanine conformational restraint in the far-red range', Journal of the American Chemical Society, 139: 12406-09.
- Middendorff, Claas v, Alexander Egner, Claudia Geisler, StefanW Hell, and Andreas Schönle. 2008. 'Isotropic 3D Nanoscopy based on single emitter switching', Optics express, 16: 20774-88.
- Mlodzianoski, Michael J, Manuel F Juette, Glen L Beane, and Joerg Bewersdorf. 2009. 'Experimental characterization of 3D localization techniques for particle-tracking and super-resolution microscopy', Optics express, 17: 8264-77.



Moerner, WE, and David P Fromm. 2003. 'Methods of single-molecule fluorescence spectroscopy and microscopy', REVIEW OF SCIENTIFIC INSTRUMENTS, 74: 3597-619.

- Moertelmaier, Manuel, Mario Brameshuber, Mario Linimeier, Gerhard J Schütz, and Hannes Stockinger. 2005. 'Thinning out clusters while conserving stoichiometry of labeling', Applied Physics Letters, 87: 263903.
- Monks, C. R., B. A. Freiberg, H. Kupfer, N. Sciaky, and A. Kupfer. 1998. 'Three-dimensional segregation of supramolecular activation clusters in T cells', Nature, 395: 82-6.
- Mortensen, Kim I, L Stirling Churchman, James A Spudich, and Henrik Flyvbjerg. 2010. 'Optimized localization analysis for single-molecule tracking and super-resolution microscopy', Nature *methods*, 7: 377-81.
- Murphy, Kenneth, and Casey Weaver. 2016. Janeway's immunobiology (Garland science).
- Mustelin, T., K. M. Coggeshall, and A. Altman. 1989. 'Rapid activation of the T-cell tyrosine protein kinase pp56lck by the CD45 phosphotyrosine phosphatase', Proc Natl Acad Sci U S A, 86: 6302-6.
- Natarajan, Kannan, Andrew C McShan, Jiansheng Jiang, Vlad K Kumirov, Rui Wang, Huaying Zhao, Peter Schuck, Mulualem E Tilahun, Lisa F Boyd, and Jinfa Ying. 2017. 'An allosteric site in the T-cell receptor Cβ domain plays a critical signalling role', Nature communications, 8: 1-14.
- Nehme, Elias, Daniel Freedman, Racheli Gordon, Boris Ferdman, Lucien E Weiss, Onit Alalouf, Tal Naor, Reut Orange, Tomer Michaeli, and Yoav Shechtman. 2020. 'DeepSTORM3D: dense 3D localization microscopy and PSF design by deep learning', Nature methods, 17: 734-40.
- Neubert, Franziska, Gerti Beliu, Ulrich Terpitz, Christian Werner, Christian Geis, Markus Sauer, and Sören Doose. 2018. 'Bioorthogonal click chemistry enables site-specific fluorescence labeling of functional NMDA receptors for super-resolution imaging', Angewandte Chemie International Edition, 57: 16364-69.
- Nielsen, Morten M, Deborah A Witherden, and Wendy L Havran. 2017. 'yδ T cells in homeostasis and host defence of epithelial barrier tissues', Nature Reviews Immunology, 17: 733-45.
- Noll, Robert J. 1976. 'Zernike polynomials and atmospheric turbulence', JOSA, 66: 207-11.
- Norcross, MA. 1984. "A synaptic basis for T-lymphocyte activation." In Annales de l'Institut Pasteur/Immunologie, 113-34. Elsevier.
- Nye, Jeffrey A, and Jay T Groves. 2008. 'Kinetic control of histidine-tagged protein surface density on supported lipid bilayers', Langmuir, 24: 4145-49.
- Ober, Raimund J, Sripad Ram, and E Sally Ward. 2004. 'Localization accuracy in single-molecule microscopy', Biophysical Journal, 86: 1185-200.
- Oettgen, Hans C, Carolyn L Pettey, W Lee Maloy, and Cox Terhorst. 1986. 'A T3-like protein complex associated with the antigen receptor on murine T cells', *Nature*, 320: 272-75.
- Oheim, Martin, Adi Salomon, and Maia Brunstein. 2020. 'Supercritical Angle Fluorescence Microscopy and Spectroscopy', Biophysical Journal, 118: 2339-48.
- Onnis, Anna, and Cosima T. Baldari. 2019. 'Orchestration of Immunological Synapse Assembly by Vesicular Trafficking', *Frontiers in Cell and Developmental Biology*, 7: 110.
- Ovesný, Martin, Pavel Křížek, Josef Borkovec, Zdeněk Švindrych, and Guy M Hagen. 2014. 'ThunderSTORM: a comprehensive ImageJ plug-in for PALM and STORM data analysis and super-resolution imaging', Bioinformatics, 30: 2389-90.
- Pageon, Sophie V., Thibault Tabarin, Yui Yamamoto, Yuanqing Ma, John S. Bridgeman, André Cohnen, Carola Benzing, Yijun Gao, Michael D. Crowther, Katie Tungatt, Garry Dolton, Andrew K. Sewell, David A. Price, Oreste Acuto, Robert G. Parton, J. Justin Gooding, Jérémie Rossy, Jamie Rossjohn, and Katharina Gaus. 2016. 'Functional role of T-cell receptor nanoclusters in signal initiation and antigen discrimination', Proceedings of the National Academy of Sciences, 113: E5454-63.
- Parthasarathy, Raghuveer. 2012. 'Rapid, accurate particle tracking by calculation of radial symmetry centers', Nature methods, 9: 724-26.



Pavani, Sri Rama Prasanna, Jennifer G DeLuca, and Rafael Piestun. 2009. 'Polarization sensitive, three-dimensional, single-molecule imaging of cells with a double-helix system', Optics express, 17: 19644-55.

- Pavani, Sri Rama Prasanna, Michael A Thompson, Julie S Biteen, Samuel J Lord, Na Liu, Robert J Twieg, Rafael Piestun, and William E Moerner. 2009. 'Three-dimensional, single-molecule fluorescence imaging beyond the diffraction limit by using a double-helix point spread function', Proceedings of the National Academy of Sciences, 106: 2995-99.
- Platzer, René, and Johannes B Huppa. 2020. 'T-Cell Antigen Recognition-Lessons from the Past and Projections into the Future', eLS: 1-26.
- Platzer, René, Benedikt K Rossboth, Magdalena C Schneider, Eva Sevcsik, Florian Baumgart, Hannes Stockinger, Gerhard J Schütz, and Mario Brameshuber. 2021. 'Overcoming Overcounting Artifacts in Super-Resolution Microscopy', Microscopy on Wiley Analytical Science: 20.
- Polliack, A, N Lampen, BD Clarkson, E De Harven, Z Bentwich, FP Siegal, and HG Kunkel. 1973. 'Identification of human B and T lymphocytes by scanning electron microscopy', The Journal of experimental medicine, 138: 607-24.
- Prabhat, Prashant, Sripad Ram, E Sally Ward, and Raimund J Ober. 2004. 'Simultaneous imaging of different focal planes in fluorescence microscopy for the study of cellular dynamics in three dimensions', IEEE transactions on nanobioscience, 3: 237-42.
- ———. 2006. "Simultaneous imaging of several focal planes in fluorescence microscopy for the study of cellular dynamics in 3D." In Three-Dimensional and Multidimensional Microscopy: Image Acquisition and Processing XIII, 60900L. International Society for Optics and Photonics.
- Prezhdo, Oleg V, and Yuriy V Pereverzev. 2009. 'Theoretical aspects of the biological catch bond', Accounts of chemical research, 42: 693-703.
- Purbhoo, Marco A, Darrell J Irvine, Johannes B Huppa, and Mark M Davis. 2004. 'T cell killing does not require the formation of a stable mature immunological synapse', Nature immunology, 5: 524-30.
- Quirin, Sean, Sri Rama Prasanna Pavani, and Rafael Piestun. 2012. 'Optimal 3D single-molecule localization for superresolution microscopy with aberrations and engineered point spread functions', Proceedings of the National Academy of Sciences, 109: 675-79.
- Rädler, Joachim, and Erich Sackmann. 1993. 'Imaging optical thicknesses and separation distances of phospholipid vesicles at solid surfaces', Journal de Physique II, 3: 727-48.
- Ram, Sripad, Dongyoung Kim, Raimund J Ober, and E Sally Ward. 2012. '3D single molecule tracking with multifocal plane microscopy reveals rapid intercellular transferrin transport at epithelial cell barriers', Biophysical Journal, 103: 1594-603.
- Ram, Sripad, Prashant Prabhat, Jerry Chao, E Sally Ward, and Raimund J Ober. 2008. 'High accuracy 3D quantum dot tracking with multifocal plane microscopy for the study of fast intracellular dynamics in live cells', Biophysical Journal, 95: 6025-43.
- Razvag, Yair, Yair Neve-Oz, Julia Sajman, Meital Reches, and Eilon Sherman. 2018. 'Nanoscale kinetic segregation of TCR and CD45 in engaged microvilli facilitates early T cell activation', Nature communications, 9: 1-17.
- Richter, Ralf P, Rémi Bérat, and Alain R Brisson. 2006. 'Formation of solid-supported lipid bilayers: an integrated view', Langmuir, 22: 3497-505.
- Ries, Jonas, Charlotte Kaplan, Evgenia Platonova, Hadi Eghlidi, and Helge Ewers. 2012. 'A simple, versatile method for GFP-based super-resolution microscopy via nanobodies', Nature methods, 9: 582-84.
- Rodriguez, Erik A, Robert E Campbell, John Y Lin, Michael Z Lin, Atsushi Miyawaki, Amy E Palmer, Xiaokun Shu, Jin Zhang, and Roger Y Tsien. 2017. 'The growing and glowing toolbox of fluorescent and photoactive proteins', Trends in biochemical sciences, 42: 111-29.
- Rossboth, Benedikt, Andreas M. Arnold, Haisen Ta, René Platzer, Florian Kellner, Johannes B. Huppa, Mario Brameshuber, Florian Baumgart, and Gerhard J. Schütz. 2018. 'TCRs are randomly

- distributed on the plasma membrane of resting antigen-experienced T cells', Nature Immunology, 19: 821-27.
- Rossy, J., D. M. Owen, D. J. Williamson, Z. Yang, and K. Gaus. 2013. 'Conformational states of the kinase Lck regulate clustering in early T cell signaling', Nat Immunol, 14: 82–89.
- Roy, Rahul, Sungchul Hohng, and Taekjip Ha. 2008. 'A practical guide to single-molecule FRET', *Nature methods*, 5: 507-16.
- Ruckstuhl, Thomas, Jörg Enderlein, Stefan Jung, and Stefan Seeger. 2000. 'Forbidden light detection from single molecules', Analytical chemistry, 72: 2117-23.
- Ruckstuhl, Thomas, and Dorinel Verdes. 2004. 'Supercritical angle fluorescence (SAF) microscopy', Optics express, 12: 4246-54.
- Ruozi, Barbara, Daniela Belletti, Andrea Tombesi, Giovanni Tosi, Lucia Bondioli, Flavio Forni, and Maria Angela Vandelli. 2011. 'AFM, ESEM, TEM, and CLSM in liposomal characterization: a comparative study', International journal of nanomedicine, 6: 557.
- Rust, Michael J, Mark Bates, and Xiaowei Zhuang. 2006. 'Sub-diffraction-limit imaging by stochastic optical reconstruction microscopy (STORM)', Nature methods, 3: 793-96.
- Sacek, Vladimir. 2006. http://optics.udjat.nl/zernike expansion schemes.htm.
- Sage, Daniel, Thanh-An Pham, Hazen Babcock, Tomas Lukes, Thomas Pengo, Jerry Chao, Ramraj Velmurugan, Alex Herbert, Anurag Agrawal, and Silvia Colabrese. 2019. 'Super-resolution fight club: assessment of 2D and 3D single-molecule localization microscopy software', Nature methods, 16: 387-95.
- Santos, Ana Mafalda, Aleks Ponjavic, Marco Fritzsche, Ricardo A. Fernandes, Jorge Bernardino de la Serna, Martin J. Wilcock, Falk Schneider, Iztok Urbančič, James McColl, Consuelo Anzilotti, Kristina A. Ganzinger, Meike Aßmann, David Depoil, Richard J. Cornall, Michael L. Dustin, David Klenerman, Simon J. Davis, Christian Eggeling, and Steven F. Lee. 2018. 'Capturing resting T cells: the perils of PLL', *Nature Immunology*, 19: 203–05.
- Sauer, Markus, and Mike Heilemann. 2017. 'Single-Molecule Localization Microscopy in Eukaryotes', *Chemical Reviews*, 117: 7478–509.
- Schilling, Jörg, Kheya Sengupta, Stefanie Goennenwein, Andreas R Bausch, and Erich Sackmann. 2004. 'Absolute interfacial distance measurements by dual-wavelength reflection interference contrast microscopy', *Physical Review E*, 69: 021901.
- Schmidt, Thomas, GJ Schütz, W Baumgartner, HJ Gruber, and H Schindler. 1996. 'Imaging of single molecule diffusion', *Proceedings of the National Academy of Sciences*, 93: 2926-29.
- Schmied, Jürgen J, Carsten Forthmann, Enrico Pibiri, Birka Lalkens, Philipp Nickels, Tim Liedl, and Philip Tinnefeld. 2013. 'DNA origami nanopillars as standards for three-dimensional superresolution microscopy', Nano letters, 13: 781-85.
- Schnitzbauer, Joerg, Maximilian T Strauss, Thomas Schlichthaerle, Florian Schueder, and Ralf Jungmann. 2017. 'Super-resolution microscopy with DNA-PAINT', Nature protocols, 12:
- Scomparin, C, S Lecuyer, M Ferreira, Thierry Charitat, and B Tinland. 2009. 'Diffusion in supported lipid bilayers: Influence of substrate and preparation technique on the internal dynamics', The European Physical Journal E, 28: 211-20.
- Sharonov, Alexey, and Robin M Hochstrasser. 2006. 'Wide-field subdiffraction imaging by accumulated binding of diffusing probes', Proceedings of the National Academy of Sciences, 103: 18911-16.
- Shechtman, Yoav, Steffen J Sahl, Adam S Backer, and William E Moerner. 2014. 'Optimal point spread function design for 3D imaging', Physical Review Letters, 113: 133902.
- Shechtman, Yoav, Lucien E Weiss, Adam S Backer, Steffen J Sahl, and WE Moerner. 2015. 'Precise three-dimensional scan-free multiple-particle tracking over large axial ranges with tetrapod point spread functions', Nano letters, 15: 4194-99.
- Shtengel, Gleb, James A Galbraith, Catherine G Galbraith, Jennifer Lippincott-Schwartz, Jennifer M Gillette, Suliana Manley, Rachid Sougrat, Clare M Waterman, Pakorn Kanchanawong, and



- Michael W Davidson. 2009. 'Interferometric fluorescent super-resolution microscopy resolves 3D cellular ultrastructure', Proceedings of the National Academy of Sciences, 106: 3125-30.
- Simoncelli, Sabrina, Juliette Griffié, David J. Williamson, Jack Bibby, Cara Bray, Rose Zamoyska, Andrew P. Cope, and Dylan M. Owen. 2020. 'Multi-color Molecular Visualization of Signaling Proteins Reveals How C-Terminal Src Kinase Nanoclusters Regulate T Cell Receptor Activation', Cell Reports, 33: 108523.
- Sivankutty, Siddharth, Iván Coto Hernández, Nicolas Bourg, Guillaume Dupuis, and Sandrine Lévêque-Fort. 2020. 'Supercritical angle fluorescence for enhanced axial sectioning in STED microscopy', Methods, 174: 20-26.
- Smith, Ana-Sunčana, Kheya Sengupta, Stefanie Goennenwein, Udo Seifert, and Erich Sackmann. 2008. 'Force-induced growth of adhesion domains is controlled by receptor mobility', Proc Natl Acad Sci U S A, 105: 6906-11.
- Smith, Carlas, Max Huisman, Marijn Siemons, David Grünwald, and Sjoerd Stallinga. 2016. 'Simultaneous measurement of emission color and 3D position of single molecules', Optics express, 24: 4996-5013.
- Smith, Carlas S, Nikolai Joseph, Bernd Rieger, and Keith A Lidke. 2010. 'Fast, single-molecule localization that achieves theoretically minimum uncertainty', Nature methods, 7: 373-75.
- Su, X., J. A. Ditlev, E. Hui, W. Xing, S. Banjade, J. Okrut, D. S. King, J. Taunton, M. K. Rosen, and R. D. Vale. 2016. 'Phase separation of signaling molecules promotes T cell receptor signal transduction', Science, 352: 595-9.
- Swamy, M., K. Beck-Garcia, E. Beck-Garcia, F. A. Hartl, A. Morath, O. S. Yousefi, E. P. Dopfer, E. Molnar, A. K. Schulze, R. Blanco, A. Borroto, N. Martin-Blanco, B. Alarcon, T. Hofer, S. Minguet, and W. W. Schamel. 2016. 'A Cholesterol-Based Allostery Model of T Cell Receptor Phosphorylation', Immunity, 44: 1091-101.
- Sykulev, Yuri, Michael Joo, Irina Vturina, Theodore J Tsomides, and Herman N Eisen. 1996. 'Evidence that a single peptide–MHC complex on a target cell can elicit a cytolytic T cell response', *Immunity*, 4: 565-71.
- Tahmasbi, Amir, Sripad Ram, Jerry Chao, Anish V Abraham, Felix W Tang, E Sally Ward, and Raimund J Ober. 2014. 'Designing the focal plane spacing for multifocal plane microscopy', Optics express, 22: 16706-21.
- Takakura, Hideo, Yongdeng Zhang, Roman S Erdmann, Alexander D Thompson, Yu Lin, Brian McNellis, Felix Rivera-Molina, Shin-nosuke Uno, Mako Kamiya, and Yasuteru Urano. 2017. 'Long time-lapse nanoscopy with spontaneously blinking membrane probes', Nature *biotechnology*, 35: 773-80.
- Tamm, Lukas K, and Harden M McConnell. 1985. 'Supported phospholipid bilayers', Biophysical Journal, 47: 105-13.
- Taylor, Marcus J., Kabir Husain, Zev J. Gartner, Satyajit Mayor, and Ronald D. Vale. 2017. 'A DNA-Based T Cell Receptor Reveals a Role for Receptor Clustering in Ligand Discrimination', Cell, 169: 108-19.e20.
- Thauland, Timothy J, and David C Parker. 2010. 'Diversity in immunological synapse structure', Immunology, 131: 466-72.
- Thevathasan, Jervis Vermal, Maurice Kahnwald, Konstanty Cieśliński, Philipp Hoess, Sudheer Kumar Peneti, Manuel Reitberger, Daniel Heid, Krishna Chaitanya Kasuba, Sarah Janice Hoerner, and Yiming Li. 2019. 'Nuclear pores as versatile reference standards for quantitative superresolution microscopy', Nature methods, 16: 1045-53.
- Thill, Peter A, Arthur Weiss, and Arup K Chakraborty. 2016. 'Phosphorylation of a tyrosine residue on Zap70 by Lck and its subsequent binding via an SH2 domain may be a key gatekeeper of T cell receptor signaling in vivo', *Molecular and cellular biology*, 36: 2396-402.
- Thorn, Kurt. 2017. 'Genetically encoded fluorescent tags', Molecular biology of the cell, 28: 848-57. Trebak, M., and J. P. Kinet. 2019. 'Calcium signalling in T cells', Nat Rev Immunol, 19: 154-69.



Turkowyd, Bartosz, David Virant, and Ulrike Endesfelder. 2016. 'From single molecules to life: microscopy at the nanoscale', Analytical and bioanalytical chemistry, 408: 6885-911.

- Uno, Shin-nosuke, Mako Kamiya, Akihiko Morozumi, and Yasuteru Urano. 2018. 'A green-lightemitting, spontaneously blinking fluorophore based on intramolecular spirocyclization for dual-colour super-resolution imaging', Chemical Communications, 54: 102-05.
- Uno, Shin-nosuke, Mako Kamiya, Toshitada Yoshihara, Ko Sugawara, Kohki Okabe, Mehmet C Tarhan, Hiroyuki Fujita, Takashi Funatsu, Yasushi Okada, and Seiji Tobita. 2014. 'A spontaneously blinking fluorophore based on intramolecular spirocyclization for live-cell super-resolution imaging', Nature chemistry, 6: 681-89.
- Valitutti, S., S. Müller, M. Cella, E. Padovan, and A. Lanzavecchia. 1995. 'Serial triggering of many Tcell receptors by a few peptide-MHC complexes', Nature, 375: 148-51.
- van de Linde, S., A. Loschberger, T. Klein, M. Heidbreder, S. Wolter, M. Heilemann, and M. Sauer. 2011. 'Direct stochastic optical reconstruction microscopy with standard fluorescent probes', Nat Protoc, 6: 991-1009.
- van Oers, Nicolai SC, Nigel Killeen, and Arthur Welss. 1994. 'ZAP-70 is constitutively associated with tyrosine-phosphorylated TCR ζ in murine thymocytes and lymph node T cells', *Immunity*, 1: 675-85.
- Van Oers, NS, Wen Tao, Julian D Watts, Pauline Johnson, Ruedi Aebersold, and Hung Sia Teh. 1993. 'Constitutive tyrosine phosphorylation of the T-cell receptor (TCR) zeta subunit: regulation of TCR-associated protein tyrosine kinase activity by TCR zeta', Molecular and cellular biology, 13: 5771-80.
- van Weerd, Jasper, Marcel Karperien, and Pascal Jonkheijm. 2015. 'Supported lipid bilayers for the generation of dynamic cell-material interfaces', Advanced healthcare materials, 4: 2743-79.
- Varma, R., G. Campi, T. Yokosuka, T. Saito, and M. L. Dustin. 2006. 'T cell receptor-proximal signals are sustained in peripheral microclusters and terminated in the central supramolecular activation cluster', Immunity, 25: 117-27.
- Velas, Lukas, Mario Brameshuber, Johannes B Huppa, Elke Kurz, Michael L Dustin, Philipp Zelger, Alexander Jesacher, and Gerhard J Schütz. 2021. 'Three-Dimensional single molecule localization microscopy reveals the topography of the immunological synapse at isotropic precision below 15 nm', Nano letters, 21: 9247-55.
- Von Appen, Alexander, Jan Kosinski, Lenore Sparks, Alessandro Ori, Amanda L DiGuilio, Benjamin Vollmer, Marie-Therese Mackmull, Niccolo Banterle, Luca Parca, and Panagiotis Kastritis. 2015. 'In situ structural analysis of the human nuclear pore complex', Nature, 526: 140-43.
- von Diezmann, Alex, Yoav Shechtman, and WE Moerner. 2017. 'Three-dimensional localization of single molecules for super-resolution imaging and single-particle tracking', Chemical reviews, 117: 7244-75.
- Wang, Feng, Katharina Beck-García, Carina Zorzin, Wolfgang WA Schamel, and Mark M Davis. 2016. 'Inhibition of T cell receptor signaling by cholesterol sulfate, a naturally occurring derivative of membrane cholesterol', Nature immunology, 17: 844-50.
- Wange, Ronald L. 2000. LAT, the linker for activation of T cells: a bridge between T cell-specific and general signaling pathways', Science's STKE, 2000: re1-re1.
- Weikl, Thomas R, and Reinhard Lipowsky. 2004. 'Pattern formation during T-cell adhesion', Biophysical Journal, 87: 3665-78.
- Weikl, Thomas R., Mesfin Asfaw, Heinrich Krobath, Bartosz Różycki, and Reinhard Lipowsky. 2009. 'Adhesion of membranes via receptor-ligand complexes: Domain formation, binding cooperativity, and active processes', Soft Matter, 5.
- Wombacher, Richard, Meike Heidbreder, Sebastian Van De Linde, Michael P Sheetz, Mike Heilemann, Virginia W Cornish, and Markus Sauer. 2010. 'Live-cell super-resolution imaging with trimethoprim conjugates', *Nature methods*, 7: 717-19.
- Wooldridge, Linda, Hugo A van den Berg, Meir Glick, Emma Gostick, Bruno Laugel, Sarah L Hutchinson, Anita Milicic, Jason M Brenchley, Daniel C Douek, and David A Price. 2005.

- Interaction between the CD8 coreceptor and major histocompatibility complex class I stabilizes T cell receptor-antigen complexes at the cell surface', Journal of Biological Chemistry, 280: 27491-501.
- Xie, J., J. B. Huppa, E. W. Newell, J. Huang, P. J. Ebert, Q. J. Li, and M. M. Davis. 2012. 'Photocrosslinkable pMHC monomers stain T cells specifically and cause ligand-bound TCRs to be 'preferentially' transported to the cSMAC', Nat Immunol, 13: 674-80.
- Xu, C., E. Gagnon, M. E. Call, J. R. Schnell, C. D. Schwieters, C. V. Carman, J. J. Chou, and K. W. Wucherpfennig. 2008. 'Regulation of T cell receptor activation by dynamic membrane binding of the CD3epsilon cytoplasmic tyrosine-based motif', Cell, 135: 702-13.
- Xu, Ke, Guisheng Zhong, and Xiaowei Zhuang. 2013. 'Actin, spectrin, and associated proteins form a periodic cytoskeletal structure in axons', Science, 339: 452-56.
- Yan, Qi, and Marcel P Bruchez. 2015. 'Advances in chemical labeling of proteins in living cells', Cell and tissue research, 360: 179-94.
- Yin, Y., X. X. Wang, and R. A. Mariuzza. 2012. 'Crystal structure of a complete ternary complex of Tcell receptor, peptide-MHC, and CD4', Proc Natl Acad Sci U S A, 109: 5405-10.
- Yokosuka, Tadashi, Kumiko Sakata-Sogawa, Wakana Kobayashi, Michio Hiroshima, Akiko Hashimoto-Tane, Makio Tokunaga, Michael L Dustin, and Takashi Saito. 2005. 'Newly generated T cell receptor microclusters initiate and sustain T cell activation by recruitment of Zap70 and SLP-76', *Nature immunology*, 6: 1253-62.
- Yu, Cheng-han, and Jay T Groves. 2010. 'Engineering supported membranes for cell biology', Medical & biological engineering & computing, 48: 955-63.
- Zelger, P., K. Kaser, B. Rossboth, L. Velas, G. J. Schütz, and A. Jesacher. 2018. 'Three-dimensional localization microscopy using deep learning', Optics Express, 26: 33166-79.
- Zelger, Philipp, Lisa Bodner, Martin Offterdinger, Lukas Velas, Gerhard J Schütz, and Alexander Jesacher. 2021. 'Three-dimensional single molecule localization close to the coverslip: a comparison of methods exploiting supercritical angle fluorescence', Biomedical Optics Express, 12: 802-22.
- Zelger, Philipp, Lisa Bodner, Lukas Velas, Gerhard J. Schütz, and Alexander Jesacher. 2020. 'Defocused imaging exploits supercritical-angle fluorescence emission for precise axial single molecule localization microscopy', Biomedical Optics Express, 11: 775-90.
- Zhang, Bo, Josiane Zerubia, and Jean-Christophe Olivo-Marin. 2007. 'Gaussian approximations of fluorescence microscope point-spread function models', Applied optics, 46: 1819-29.



Curriculum Vitae

Mgr. Lukáš Veľas

Born: 26.3.1993, Humenné, Slovakia

Nationality: Slovak

E-mail: lukas.velas@gmail.com

LinkedIN: https://cz.linkedin.com/in/lukasvelas

Education

TU Wien, Faculty of Physics, Vienna, Austria

since 2017, PhD degree in Technical Physics

Doctoral thesis: Three-dimensional super-resolution microscopy of the immunological synapse

Charles University, Faculty of Mathematics and Physics, Prague, Czechia

- 2015 2017, master's degree in Biophysics and Chemical Physics, summa cum laude
- Master's thesis: Influence of lipid composition and model peptides on lateral organization of lipid layers

Charles University, Faculty of Mathematics and Physics, Prague, Czechia

- 2012 2015, bachelor's degree in General Physics
- Bachelor's thesis: Monitoring the effect of medically important drugs on activity of human Pglycoprotein using fluorescent probes

Professional Experience

Project Assistant – Institute of Applied Physics, TU Wien

- since October 2017, MSCA ITN fellowship in prof. Gerhard Schuetz's biophysical group
- Tasks: Advanced fluorescence microscopy super-resolution microscopy, cell culture, fluorescence labelling of cells, imaging, chemical preparation of samples, data analysis, programming, simulations

Research Assistant – J Heyrovsky Institute of Physical Chemistry of the CAS, Prague

- April 2016 September 2017, part-time contract in prof. Martin Hof's fluorescence group
- Tasks: Fluorescence lifetime imaging, chemical preparation of samples, data analysis, programming, simulations

Work Experience Student - The James Cook University Hospital, Middlesbrough, UK

- July 2015, Department of Medical Physics
- Tasks: Observation of routine activities at the departments of Clinical Measurments, Radiotherapy Physics and Nuclear Medicine. Contribution to a project: "Validation of a new Tomotherapy MV CT reconstruction mode"

Research Assistant - Royal Veterinary College, University of London, UK

- October 2013 and August 2014, part-time contract
- Tasks: collection of data and statistical analysis for a project in the field of animal health



Publications

Velas, L., Brameshuber, M., Huppa, J. B., Kurz, E., Dustin, M. L., Zelger, P., Jesacher, A., & Schütz, G. J. (2021). Three-Dimensional Single Molecule Localization Microscopy Reveals the Topography of the Immunological Synapse at Isotropic Precision below 15 nm. Nano letters, 21(21), 9247-9255

- Zelger, P., Bodner, L., Offterdinger, M., Velas, L., Schütz, G. J., & Jesacher, A. (2021). Threedimensional single molecule localization close to the coverslip: a comparison of methods exploiting supercritical angle fluorescence. Biomedical Optics Express, 12(2), 802-822.
- Zelger, P., Bodner, L., Velas, L., Schütz, G. J., & Jesacher, A. (2020). Defocused imaging exploits supercritical-angle fluorescence emission for precise axial single molecule localization microscopy. *Biomedical optics express*, 11(2), 775-790.
- Vinklárek, I. S., Vel'as, L., Riegerová, P., Skála, K., Mikhalyov, I., Gretskaya, N., Hof, M. & Šachl, R. (2019). Experimental evidence of the existence of interleaflet coupled nanodomains: An MC-FRET study. *The Journal of Physical Chemistry Letters*, 10(9), 2024-2030.
- Zelger, P., Kaser, K., Rossboth, B., Velas, L., Schütz, G. J., & Jesacher, A. (2018). Threedimensional localization microscopy using deep learning. Optics express, 26(25), 33166-33179

Dissemination

- Talk at the Austrian Cluster for Tissue Regeneration, April 2022, Vienna, Austria
- Poster at the Biophysical Society Annual Meeting 2022, February 2022, San Francisco, USA
- Poster at the 13th European Biophysics Conference, July 2021, Vienna, Austria
- Talk at the 3rd European CAR T-cell Meeting, February 2021, Virtual meeting
- Poster at the Biophysical Society Annual Meeting 2021, February 2021, Virtual meeting
- Poster at the Biophysical Society Annual Meeting 2020, February 2020, San Diego, USA
- Poster at the XXII Annual Linz Winter Workshop, February 2020, Linz, Austria
- Poster at the XXI Annual Linz Winter Workshop, February 2019, Linz, Austria •
- Talk at the EBSA Biophysics Course, June 2018, La Grande Motte, France
- Poster at the 8th Regional Biophysics Conference, May 2018, Zreče, Slovenia
- Poster at the XX Annual Linz Winter Workshop, February 2018, Linz, Austria

